Hydrodynamic Flow Fluctuations in $\sqrt{s_{\mathrm{NN}}} = 5.02$ TeV PbPb Collisions

By

James R. Castle

Submitted to the Department of Physics and Astronomy and the
Graduate Faculty of the University of Kansas
in partial fulfillment of the requirements for the degree of
Doctor of Philosophy

Committee members

Dr. Stephen J. Sanders, Chairperson

Dr. Daniel Tapia Takaki

Dr. Alice L. Bean

Dr. Ian Lewis

Dr. Christopher G. Elles

Date defended: July 13, 2017

The Thesis Committee for James R. Castle certifies
that this is the approved version of the following thesis :

Hydrodynamic Flow Fluctuations in $\sqrt{s_{\mathrm{NN}}} = 5.02$ TeV PbPb Collisions

Dr. Stephen J. Sanders, Chairperson

Date approved: July 24, 2017

Abstract

The collective, anisotropic expansion of the medium created in ultrarelativistic heavy-ion collisions, known as flow, is characterized through a Fourier expansion of the final-state azimuthal particle density. In the Fourier expansion, flow harmonic coefficients v_n correspond to shape components in the final-state particle density, which are a consequence of similar spatial anisotropies in the initial-state transverse energy density of a collision. Flow harmonic fluctuations are studied for PbPb collisions at $\sqrt{s_{\mathrm{NN}}} = 5.02$ TeV using the CMS detector at the CERN LHC. Flow harmonic probability distributions $p(v_n)$ are obtained using particles with $0.3 < p_{\mathrm{T}} < 3.0$ GeV/c and $|\eta| < 1.0$ by removing finite-multiplicity resolution effects from the observed azimuthal particle density through an unfolding procedure. Cumulant elliptic flow harmonics ($n = 2$) are determined from the moments of the unfolded $p(v_2)$ distributions and used to construct observables in 5% wide centrality bins up to 60% that relate to the initial-state spatial anisotropy. Hydrodynamic models predict that fluctuations in the initial-state transverse energy density will lead to a non-Gaussian component in the elliptic flow probability distributions that manifests as a negative skewness. A statistically significant negative skewness is observed for all centrality bins as evidenced by a splitting between the higher-order cumulant elliptic flow harmonics. The unfolded $p(v_2)$ distributions are transformed assuming a linear relationship between the initial-state spatial anisotropy and final-state flow and are fitted with elliptic power law and Bessel Gaussian parametrizations to infer information on the nature of initial-state fluctuations. The elliptic power law parametrization is found to provide a more accurate description of the fluctuations than the Bessel-Gaussian parametrization. In

addition, the event-shape engineering technique, where events are further divided into classes based on an observed ellipticity, is used to study fluctuation-driven differences in the initial-state spatial anisotropy for a given collision centrality that would otherwise be destroyed by event-averaging techniques. Correlations between the first and second moments of $p(v_n)$ distributions and event ellipticity are measured for harmonic orders $n = 2-4$ by coupling event-shape engineering to the unfolding technique.

Acknowledgements

First and foremost, I want to thank my adviser, Dr. Stephen Sanders, for his extraordinary guidance throughout my graduate studies. From essential research skills to planning my future career, Dr. Sanders has provided sound advice time and time again. When I first began working for him, he once said to me, "I'm going to be giving you a lot of grief over the next few years, so you might as well start calling me Steve." Thank you for all the "grief," Steve, I am very fortunate to have worked for and with you.

I want to thank the United States Department of Energy for funding my research and multiple visits to CERN.

I want to thank all of my collaborators in the CMS Heavy Ion and AlCa groups. Particularly, I want to thank Quan Wang and Maxime Guilbaud for their help in getting my analysis off the ground and through the CMS pipeline. I want to thank Marco Musich for helping me to become an expert on tracker alignment and beamspot calibrations; those projects would not have succeeded without his guidance. Lastly, I want to thank Raghav Kunnawalkam Elayavalli, Chris Ferraioli, and Matthew Nguyen for helping me to retain my sanity during the 2015 PbPb run.

I want to thank all of my colleagues at the University of Kansas. First, thank you to those that came before me, Chris, Danny, Pat, and Robert, who helped me overcome the steep learning curve that comes with working on CMS. I want to thank those still here with me, Ayman, Christian, Cole, Erich, Hussein, James, Justin, Samuel, Sinan, Tim, and Will, for making this institution feel like a home for the past five years.

I want to thank Dr. Linda Weber for initially sparking my interest in physics in high school and Dr. Matthew Zacate for further feeding the flames by taking me to work at ISOLDE Hall at CERN as an undergraduate. I would not be where I am today if it were not for your influence and mentorship.

I want to thank my mother and father, Ruth and Greg Castle, for raising me to be the man I am today. Whether it was being told countless times while growing up to, "look it up in the dictionary and then *you* tell *me*," or to, "just Google it and then *you* tell *me*," you secretly instilled me with the ability and desire to independently seek out the answers to my questions. I consider this to be one of my most valuable skills, which has played a significant role in my successes to this day. I also want to thank my sister, Emily Castle, for the countless times she's offered to read over my writing and correct my horrible grammar.

Lastly, and most importantly, I want to thank my wife, Jennifer Castle. I'm a lucky man to have found someone who is as loving and supportive as you, even while living 650 miles away from each other. Thank you for keeping my feet on the ground while my head was in the clouds, for planning surprise trips out to Kansas, and for surprise-delivering me pizza when you knew I'd had a bad day. Thank you for choosing to spend your life with me, I cannot wait to come home. *"We live happily forever, so the story goes..."*

Contents

List of Figures

List of Tables

Chapter 1

Introduction

Ultrarelativistic heavy-ion collisions at the Relativistic Heavy-Ion Collider (RHIC) and the Large Hadron Collider (LHC) create a hot, dense state of matter that consists of strongly-interacting quarks and gluons, the so-called Quark-Gluon Plasma [1, 2, 3, 4, 5, 6]. In early theoretical developments, the QGP was believed to behave as a gas, but has since been shown to instead behave as a nearly perfect fluid [1, 2, 3, 4]. This fluid behavior mostly preserves shape components in the overlap region of the two colliding nuclei, which are reflected in the final-state particle spectra. These shape components are characterized using a Fourier expansion of the initial-state transverse energy density profile and final-state azimuthal particle density, respectively. For non-central collisions, the lenticular shape of the overlap region, as illustrated in Fig. 1.1, results in a dominant second-order term in the Fourier expansion. The second-order terms corresponds to an elliptic shape and, for the final-state spectra, is referred to elliptic flow.

Since the colliding nuclei are quantum systems, the positions of the nucleons within each nucleus fluctuate on a collision-by-collision basis. These quantum fluctuations result in drastically different initial-state shape components for collisions with same impact parameters. Quantum fluctuations additionally allow for stronger contributions from higher-order Fourier components, such as the third-order (triangular) term. Given that the largest contribution to the uncertainties in theoretical predictions of heavy-ion collisions come from an imprecise knowledge of the physics of the

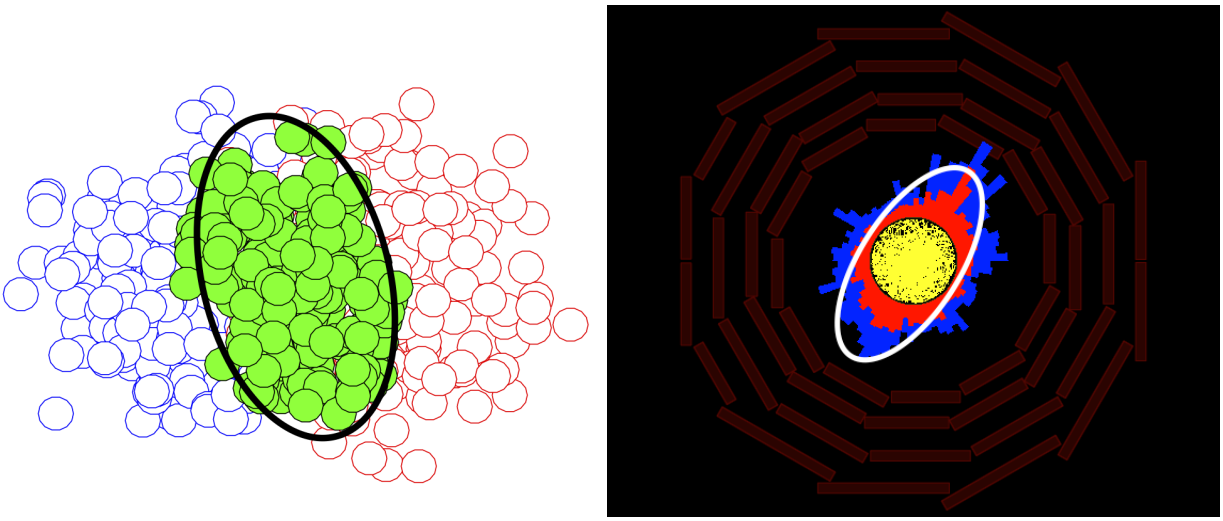

Figure 1.1: (Left) A Glauber simulation [88, 89, 90] of a PbPb collision at $\sqrt{s_{\mathrm{NN}}} = 5.02$ TeV with a strong elliptic shape. A solid black line illustrates the dominant second-order term in the Fourier expansion. (Right) A CMS event display of a PbPb collision at $\sqrt{s_{\mathrm{NN}}} = 5.02$ TeV with a strong elliptic shape in the final-state azimuthal particle density. A white line illustrated the dominant second-order term in the Fourier expansion.

initial stages, this begs the question: can these initial-state spatial fluctuations be quantified experimentally and how can this information be used to constrain the theoretical understanding of the physics governing the early stages of the QGP? To answer this question, the nature of the initial-state spatial fluctuations is studied in this thesis through detailed inspection of the event-by-event fluctuation of the final-state Fourier components. The following sections provide an introduction to the theory behind ultrarelativistic heavy-ion collisions and how experiments today are probing their properties.

1.1 Quantum chromodynamics

Quantum Chromo-Dynamics (QCD) [7] is the theory that governs strong interactions, *i.e.*, interactions between quarks and gluons. Quarks and gluons are the building blocks of the protons and neutrons that form the structures of atoms and molecules we observe in the universe today. In QCD field theory, quarks and gluons carry "color" charge and the strength of strong interactions is

described by the strong coupling constant

$$\alpha_s(|q^2|) = \frac{12\pi}{(11n - 2f)\ln\left[|q^2c^2|/\Lambda^2_{\mathrm{QCD}}\right]}, \tag{1.1}$$

where n is the number of color charges, f is the number of quark flavors, q is the momentum transfer of an interaction, and Λ_{QCD} defines the scale of QCD [8, 9]. As can be seen from Eq. (1.1) α_s is dependent on the momentum transfer of the interaction, meaning that α_s is a running coupling constant (see Fig. 1.2). One of the greatest successes of QCD is the concept of asymptotic freedom [8, 9], which states that at short distances, or large energies, quarks and gluons are weakly bound. In this regime, perturbative QCD becomes a valid theory for predicting observables through an expansion of processes in increasing orders of α_s. Conversely, at long distances and low energies, the coupling strength between color charges becomes increasingly strong, to the point where new particles will be pulled from the vacuum in order to screen any isolated color charge; this phenomenon is known as confinement [10].

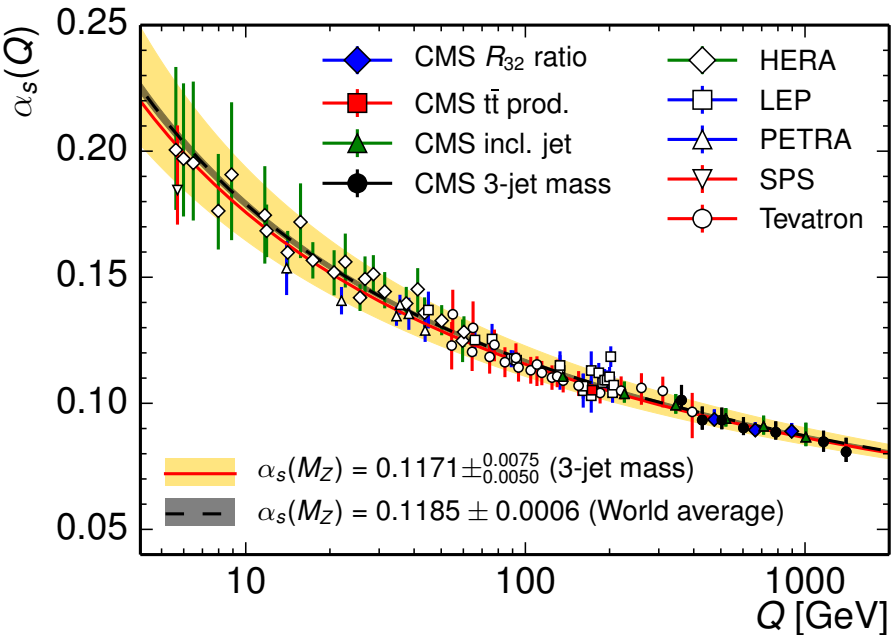

Figure 1.2: Overview of the measurements of the running strong coupling from experiments using a variety of collision systems and energies [11].

Despite the numerous successes of numerical lattice QCD calculations [12] (*e.g.*, describing the hadron spectrum [13]), there are still aspects of standard QCD matter where analytical understanding is lacking. For example, the concepts of confinement and chiral symmetry breaking [14] lack rigorous theoretical understanding. In order to gain further insight into these concepts, QCD matter can be studied under extreme temperature and density conditions, where asymptotic freedom is approximately valid and chiral symmetry is nearly restored, and by probing the phase boundary with normal QCD matter. A schematic of the QCD phase diagram is shown in Fig. 1.3. Relativistic heavy-ion colliders are today exploring QCD matter in the limit of asymptotic freedom by producing a phase of QCD matter known as the Quark-Gluon Plasma (QGP).

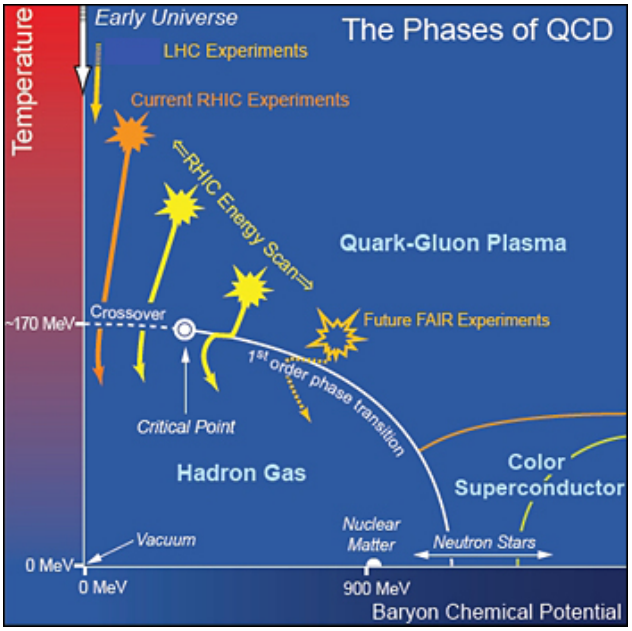

Figure 1.3: QCD matter phase diagram [15].

1.2 Quark gluon plasma

Lattice QCD calculations predict the formation of a QGP at energy densities $\varepsilon \sim 1$ GeV/fm^3 [16]. Heavy-ion collisions at the BNL RHIC and the CERN LHC produce energy densities well above this threshold, on the order of 14 GeV/fm^3 [17]. The first measurements at RHIC showed that azimuthal anisotropies in the final-state particle spectra can be reproduced using relativistic hy-

drodynamics. This discovery implied that the formation of the QGP phase happens at extremely short time scales and the QGP medium reaches a local thermal equilibrium on a similar time scale. Moreover, since the final-state particle spectra anisotropies resemble initial-state shape components in the overlap geometry of the collisions, the ratio of the shear viscosity to entropy density of the medium must be small. This means that initial-state information is mostly preserved as the medium evolves in time. Additional observations of this medium have shown a strong suppression of high-energy back-to-back partons, an effect not present in scaled-up "QCD vacuum" states such as achieved with proton-on-proton (pp) collisions. These observations suggest that the partons are interacting strongly with the produced medium and losing energy as a result. In a similar vein, a suppression of quarkonia bound states ($q\bar{q}$) is observed relative to QCD vacuum states. This suppression is one of the earliest predicted signatures of the QGP [18]. Moreover, the enhancement of final-state particles carrying a strange quark is a strong signature of the QGP, as strange quarks are predicted to reach chemical equilibrium faster in the presence of a QGP than with a QCD vacuum [19].

1.3 Heavy-ion collisions

Experiments colliding heavy ions at relativistic velocities date back to the 1970's at Lawrence Berkley National Laboratory. Here, the Bevatron was capable of accelerating beams of heavy ions (deuterons, alpha particles, and Nitrogen) to energies of $\sim$2 GeV/A to collide with fixed targets [20]. Much later, in the 1980's, two machines capable of accelerating heavy ions to higher energies came online. The first was the Alternating Gradient Synchrotron (AGS) at Brookhaven National Laboratory (BNL), which was a fixed target facility capable of accelerating heavy ions (*e.g.*, ^{16}O and ^{28}Si) to energies of $\sim$15 GeV/A [21]. The second was the Super Proton Synchrotron (SPS) at the European Organization for Nuclear Research (CERN). The SPS facility was also home to fixed-target experiments and was capable of accelerating a wider spectrum of heavy ions (up to Pb) to energies of $\sim$200 GeV/A [22]. Presently there are two colliders in the world carrying out ultrarelativistic heavy-ion experiments, the BNL RHIC and the CERN LHC. The RHIC machine is

capable of colliding a wide array of ions (up to U) to center-of-mass per colliding nucleon energies of $\sqrt{s_{\mathrm{NN}}} = 200$ GeV [23]. The LHC operates at much larger center-of-mass energies, but limits its scope to colliding lead-on-lead (PbPb) or proton-on-lead (pPb) ions. For PbPb collisions, the LHC is designed to reach a center-of-mass energy of $\sqrt{s_{\mathrm{NN}}} = 5.5$ TeV [24].

A collision between two heavy ions can be factorized into several stages, as depicted in Fig. 1.4. A summary of each stage in terms of the Lorentz-invariant quantity proper time τ is as follows [25]:

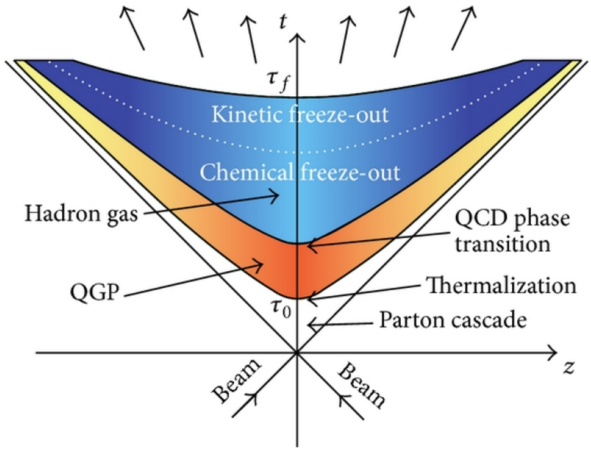

Figure 1.4: Space-time representation of the evolution of a heavy-ion collision [25]. Time is represented by the Lorentz-invariant quantity proper time $\tau = \sqrt{t^2 - z^2/c^2}$, where z is the direction of the ion's momentum. Figure taken from Ref. [26].

- $\tau < 0$ fm/c: Nuclei are circulating in the accelerator traveling at ultrarelativistic velocities. As a consequence, the nuclei are Lorentz contracted in the longitudinal direction and appear as "pancakes" in the laboratory frame of reference. For example Pb nuclei in the LHC at $\sqrt{s_{\mathrm{NN}}} = 5.02$ TeV have a Lorentz γ-factor of $\sim$2700.

- $0 < \tau \lesssim 1$ fm/c: Nuclei collide and constituent partons are liberated in a series of hard and soft processes. The terms "hard" and "soft" refer to the scale of the processes. Hard processes are characterized by a relatively large momentum transfer or mass scale. By the uncertainty principle, the time scale for such processes is on the order of the inverse of the

momentum transfer. Therefore, harder processes develop earlier in the collision. Liberated partons rapidly approach local thermal equilibrium during this time.

- $1 \lesssim \tau \lesssim 20$ fm/c: The QGP phase is formed and remains in a local thermal equilibrium as it expands and cools. The constituent partons are strongly interacting and the evolution of this medium is described well using relativistic hydrodynamics. Eventually the system cools to the point where partons coalesce back into hadrons.

- $\tau \sim 20$ fm/c: The mean free path of hadrons is now on the order of the size of the system and interactions between the hadrons effectively cease. This stage is known as "hadron freeze out." The final state continues expanding until it is eventually picked up by detectors.

Experimentalists study the final-state particles and infer information about the various stages of these collisions. The following sections provide descriptions of both the initial state of heavy-ion collisions and examples of some of the important observables inspected in the final state.

1.3.1 The initial state

Precise understanding of the pre-collision and thermalization stages is one of the most fundamental open problems in the study of the QGP. The question that remains to be answered fully is how the initial state of an ultrarelativistic heavy-ion collision evolves into a system that is described using hydrodynamics. Considering the pre-collision stage, deep inelastic scattering measurements at HERA have shown that the density of partons within a nucleus rapidly grow with increasing $\sqrt{s}$ [27]. The nucleus occupies a transverse area of $S_A = \pi R_A^2$ where R_A is the nuclear radius, which goes as $R_A \sim A^{1/3}$. The uncertainty principle dictates that a parton with transverse momentum Q occupies a length $\sim 1/Q$ and therefore an area $\sim 1/Q^2$. This area can be probed with a cross section $\sigma \sim \alpha_s(Q^2)/Q^2$, where $\alpha_s(Q^2)$ is the strong coupling constant. If the density of partons is large enough such that

$$N_A \sim \frac{S_A}{\sigma} \sim \frac{\pi}{\alpha_s(Q^2)} R_A^2 Q^2, \tag{1.2}$$

then the partons will begin to overlap and interact [28, 29, 30]. This effect is known as "gluon saturation" and prevents parton densities from growing further. The momentum scale at which this occurs is called the saturation scale. Beyond the precise knowledge of the nuclear wave functions before the moment of impact, the underlying mechanism that causes the system to thermalize on the order of 1 fm/c is unknown. Whether or not gluon saturation is present in the pre-collision state and the mechanism for thermalization each have a direct consequence on the observables outlined in the following section. Precision measurements of these final-state observables help to answer the open questions on the nature of the initial state.

1.3.2 Final-state observables

Before an in-depth description of the observables, it is worth defining common variables in heavy-ion measurements that comprise experimental observables. Detectors in high energy physics typically consist of two types of subsystems, trackers and calorimeters. Trackers are used to measure the trajectories of charged particles emitted from collisions. When placed in a magnetic field, the curvature of the trajectories provides a measurement of the charged particle momentum. The momentum component transverse to the beam direction is denoted by p_{T}. Calorimeters are designed with dense material to stop incident particles and measure their energy, typically through scintillation. Transverse energy measured by a calorimeter is defined as $E_{\mathrm{T}} = \sum_i E_i \sin\theta_i$, where E_i is the energy measured by the i^{th} calorimeter element and θ_i is the element's polar angle measured from the beam direction. The azimuthal angle ϕ is measured in the plane transverse to the beam direction and, depending on the particle species, is measured using either a tracker or a calorimeter. In addition, the spatial coordinate pseudorapidity η is used to describe the polar angle θ and is defined as $\eta = -\ln\tan\left(\theta/2\right)$. For more detailed information on the subsystems that comprise a detector, see Chapter 3.

Given that nuclei are extended objects, the size of the interaction region in a collision is dependent on the impact parameter b, which is defined as the distance between the centers of the colliding nuclei. Since the impact parameter is not experimentally accessible, it is often estimated

by the transverse energy deposited in the detector, which is expected to increase monotonically with system size (decreasing b). The transverse energy for this estimate is measured usually in the forward region to avoid autocorrelations with other measurements. The observable "centrality" is defined as a percentile of the total nucleus-nucleus cross section (as measured by forward calorimeters) and is commonly reported as an estimate of the collision impact parameter [31].

1.3.2.1 Charged particle multiplicity

The measured final-state energy density can be related to the initial state of the medium in these collisions. For example, measurements of charged particle multiplicity as a function of system size are sensitive to the contribution from hard and soft scatterings during the collision. Final-state multiplicity contributions are often modeled such that the particle yield from hard processes is proportional to the number of nucleon-nucleon collisions, while the yield from soft processes is proportional to the number of nucleons in the interaction region (participants) [32]:

$$\frac{dN_{\mathrm{ch}}}{d\eta} \propto AN_{\mathrm{part}} + BN_{\mathrm{coll}}. \tag{1.3}$$

Charged particle density measurements provide a test case for how well the initial state can be modeled in terms of competing processes. Theoretical models can be broken into two classes, the first of which is a two-component model similar to Eq. (1.3) based on perturbative QCD and soft processes [33, 34]. The second class consists of gluon saturation models with different parametrizations of the gluon saturation scale. Figure 1.5 shows an example measurement by the ALICE collaboration of the charged particle density at mid-rapidity ($\eta = 0$) as a function of the average number of participants for PbPb collisions at $\sqrt{s_{\mathrm{NN}}} = 5.02$ TeV. Here, various models of initial-state contributions are fit to the data and a single model cannot be selected to capture the behavior across all system sizes within the limit set by statistical uncertainties.

The scope of this measurement can be broadened by observing the particle density behavior as a function of collision energy. Figure 1.6 shows an exponential increase in the particle density

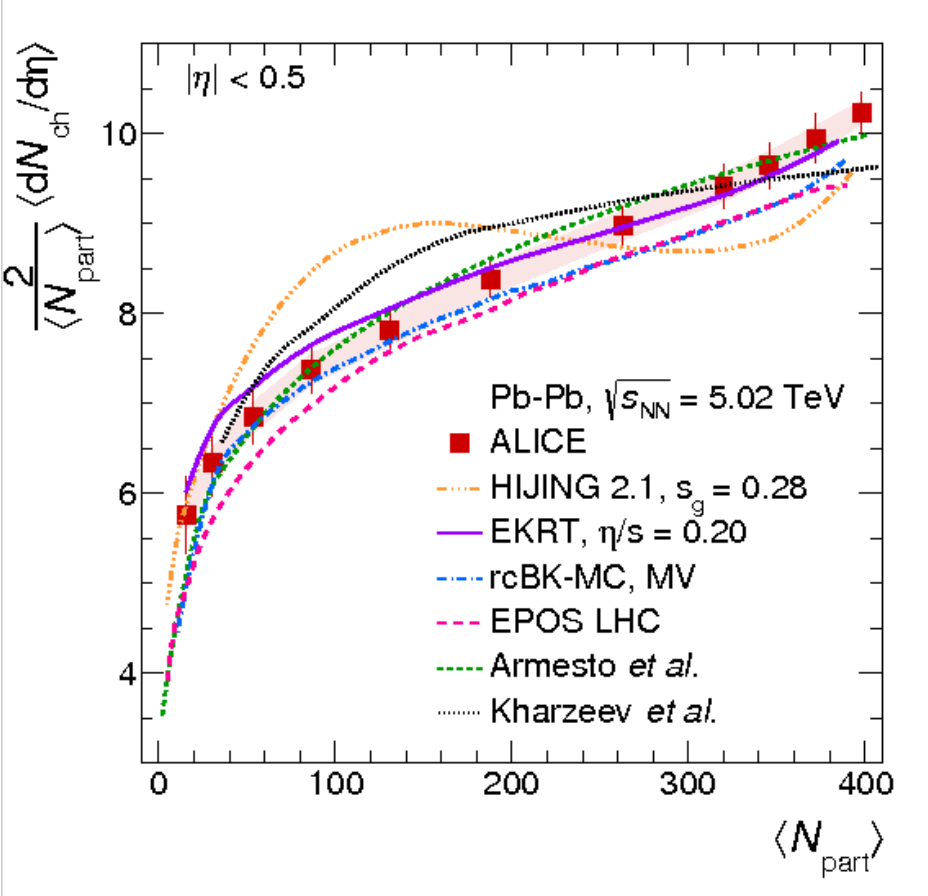

Figure 1.5: Charged particle density at mid-rapidity measured by the ALICE collaboration [35] as a function of the average number of participants for PbPb collisions at $\sqrt{s_{\mathrm{NN}}} = 5.02$ TeV. Various models of initial-state contributions (see Ref. [35]) are compared to the data and it is difficult to select a single model to capture the behavior across all system sizes within the limit set by statistical uncertainties.

at midrapidity across several decades of collision energy and a variety of collision systems from pp to central AA. The LHC era brings a steep rise in multiplicity, a feature that is qualitatively understood by a significant increase in the number of hard processes that comes with an increase in $\sqrt{s_{\mathrm{NN}}}$ [36]. Regardless of collision energy, the N_{part}-scaled charged particle densities in AA collisions are systematically larger than those in pp collisions. This observation indicates that the charged particle densities in AA collisions cannot simply be described by charged particle densities in pp collisions scaled by the number of participant nucleons.

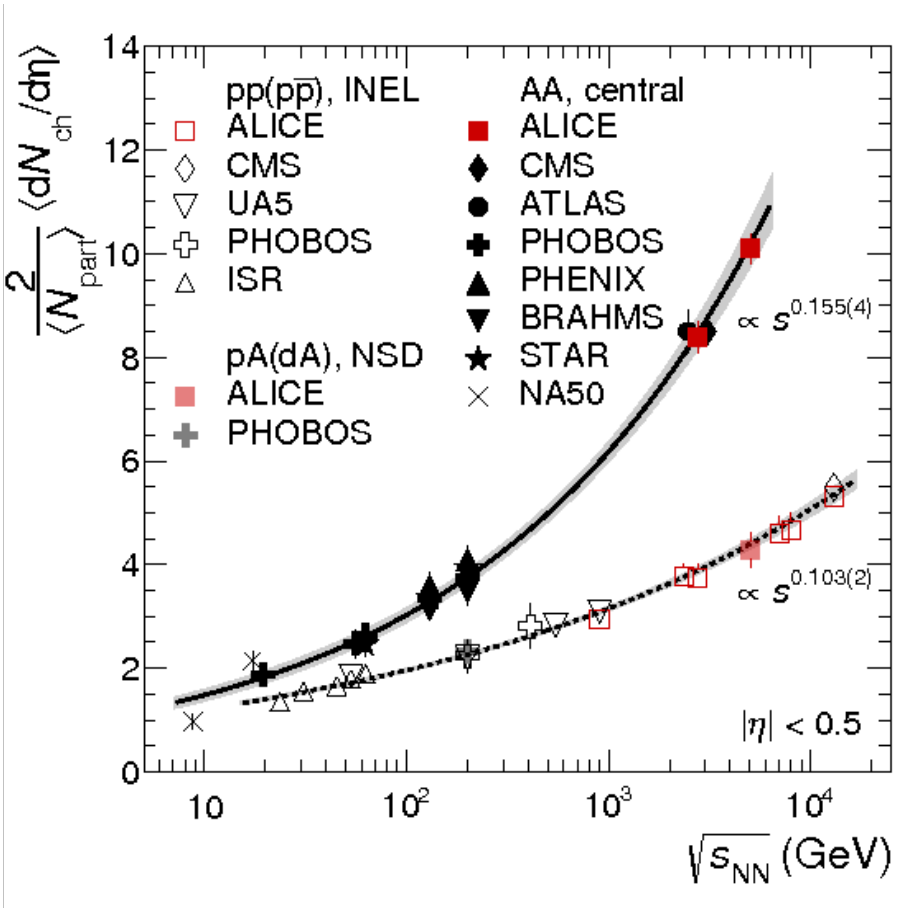

Figure 1.6: Charged particle density at mid-rapidity measured as a function of center-of-mass collision energy from Ref. [35] and references therein. Measurements are reported for a variety of collision systems spanning from pp to central AA. Dotted lines represent power law fits to the respective pp and AA trends.

1.3.2.2 Correlations and flow

The QGP is found to behave as a nearly perfect fluid with a shear viscosity to entropy density ratio η/s that is on the order of the lowest possible value for a quantum fluid [37, 38]. The fluid-like properties of the QGP are inferred from studies of its collective phenomena, which are described well using relativistic hydrodynamic models [39]. Large pressure gradients from strong interactions and subsequent hydrodynamic evolution result in the transfer of spatial asymmetries in the initial-state to a final-state anisotropy in momentum space for the emitted particles [40, 41]. This momentum anisotropy is reflected in an azimuthally anisotropic outgoing particle density. While the presence of a non-zero viscosity will degrade the correspondence between initial- and final-state anisotropies [42, 39], studies of the azimuthal anisotropy of outgoing particle densities make it possible to infer properties of the initial state of the medium as well as its transport properties during its time evolution.

The spatial anisotropy in the initial-state transverse profile of the collision can be expanded into Fourier-shape "eccentricity" harmonics $\vec{\varepsilon}_n$ [43], examples of which include elliptic ($n = 2$) and triangular ($n = 3$) terms. While the overlapping geometry of the two nucleons results in a dominant elliptic term for non-central collisions, quantum fluctuations of the transverse energy density of a collisions cause the eccentricity vectors to fluctuate in magnitude and orientation with respect to the plane defined by the beam direction and impact parameter (the reaction plane) on an event-by-event basis [41, 44, 45]. The concept of initial-state fluctuations is the focus of this thesis and is discussed further in Chapter 2.

Anisotropies in the initial-state density distribution result in an azimuthally anisotropic distribution of outgoing particles, with

$$\frac{dN}{d\phi} \propto 1 + 2\sum_{n=1}^{\infty}\left(v_{n,x}\cos n\phi + v_{n,y}\sin n\phi\right). \tag{1.4}$$

In the Fourier expansion, v_n denotes the magnitude of the n^{th}-order flow vector $\vec{v}_n \equiv (v_{n,x}, v_{n,y})$ with respect to the n^{th}-order symmetry plane defined by $\Phi_n = \frac{1}{n}\tan^{-1}\left(v_{n,y}/v_{n,x}\right)$. Viscous hydro-

dynamic calculations suggest that the v_n coefficients scale linearly with ε_n for $n \leq 3$ with proportionality constants that are sensitive to properties of the medium such as the equation of state and η/s [46, 47, 48].

With the dramatic increase in collision energy and experimental acceptance, measurements of flow harmonic coefficients at the LHC have reached a new level of precision. Flow harmonic coefficients from v_2 to v_6 have been measured using a variety of methods including event-plane correlations [49], multi-particle correlations [50], and Lee Yang zeros (LYZ) [51, 52] to yield both integrated and differential measurements in both transverse momentum p_{T} and η. Figure 1.7 shows examples of yield-weighted v_n coefficient measurements by the CMS collaboration for particles with $0.3 < p_{\mathrm{T}} < 3.0$ GeV/c and $|\eta| < 0.8$ in PbPb collisions at $\sqrt{s_{\mathrm{NN}}} = 2.76$ TeV as a function of centrality [53]. The harmonics show a hierarchy such that the v_2 coefficient dominates while the subsequent higher-order coefficient signals decrease with increasing n. This dampening of higher orders is sensitive to the shear viscosity of the medium, where larger η/s values will further suppress higher-order anisotropies.

The shear viscosity of the medium can be probed further by measuring the elliptic flow coefficients for different particle species. Such measurements have been carried out both at RHIC [54, 55, 56, 57, 58, 59, 60] and the LHC [61]. A mass ordering is observed at low p_{T} ($p_{\mathrm{T}} < 3$ GeV/c) such that lower mass particle species have a stronger v_2 signal. This behavior is shown in Fig. 1.8 for PbPb collisions at $\sqrt{s_{\mathrm{NN}}} = 2.76$ TeV and is attributed to an interplay between the collective radial expansion of emitted particles (radial flow) and elliptic flow that alters v_2 values according to particle mass [61]. The mass ordering can be used in hydrodynamic model calculations to constrain the initial conditions and fluid properties of the medium. For example, model calculations using VISHNU [62], a model that describes the expansion of the medium with viscous hydrodynamics and the late hadron gas stage with the Boltzmann equation, show that smaller values of η/s are more consistent with the observed mass ordering [61].

Beyond the low-p_{T} flow region ($p_{\mathrm{T}} < 3$ GeV/c), measurements are extended to higher p_{T} values where collective effects are no longer valid. In the high-p_{T} region ($p_{\mathrm{T}} > 10$ GeV/c) non-zero

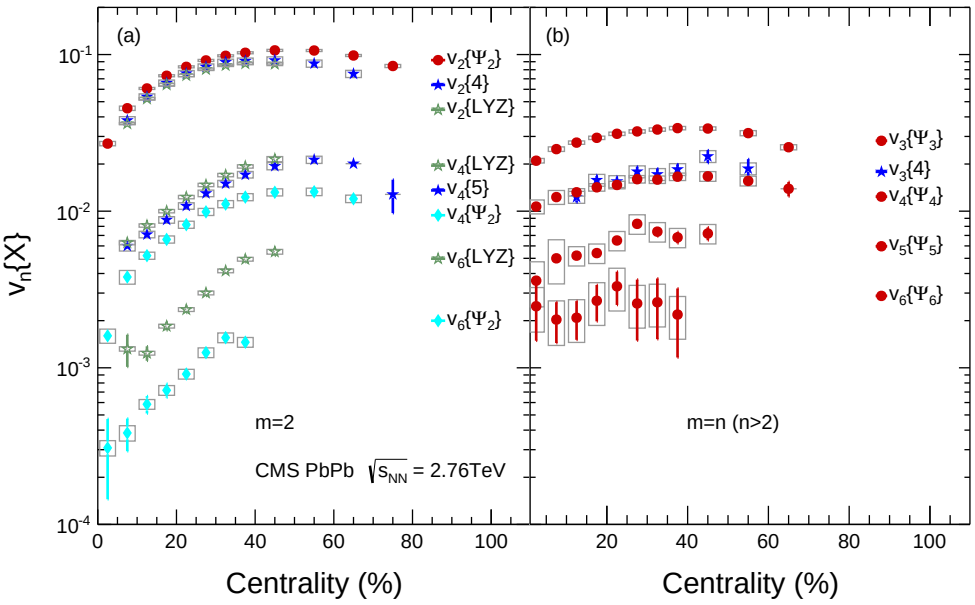

Figure 1.7: Yield-weighted v_n coefficient measurements by the CMS collaboration [53] for particles with $0.3 < p_T < 3.0$ GeV/c and $|\eta| < 0.8$ in PbPb collisions at $\sqrt{s_{NN}} = 2.76$ TeV as as a function of centrality. Measurements were obtained using event-plane correlations ($v_n\{\Psi_m\}$), m-particle correlations ($v_n\{m\}$), and LYZ ($v_n\{\text{LYZ}\}$).

flow signals are related to a path length difference for partons traversing the strongly interacting medium [63]. This path length difference leads to varying energy losses for the partons [64]. Coupling high-p_T v_n measurements to hard-probe measurements such as jet suppression (Sec. 1.3.2.3) help to reveal subtleties by adding a path length dependence to the parton evolution through the medium [65]. Figure 1.9 shows an example measurement by the CMS collaboration [63] of v_2 coefficients up to 60 GeV/c for PbPb collisions at $\sqrt{s_{NN}} = 2.76$ TeV. Here it can be seen for all centralities that there is a steep rise in flow signal up to 3 GeV/c that is well understood by collective hydrodynamics. As p_T increases past the flow region, signals begin to fall at a rapid rate which becomes more moderate around 10 GeV/c. A statistically significant non-zero signal is observed for all centralities up to 40 GeV/c. Currently, there does not exist a model that can simultaneously replicate v_2 behavior at high p_T and jet suppression. Further constraints of leading theoretical models can be made by including initial-state fluctuations in calculations. This information is obtained by measuring odd-order harmonics such as v_3 at high p_T [66] and by the measurements performed

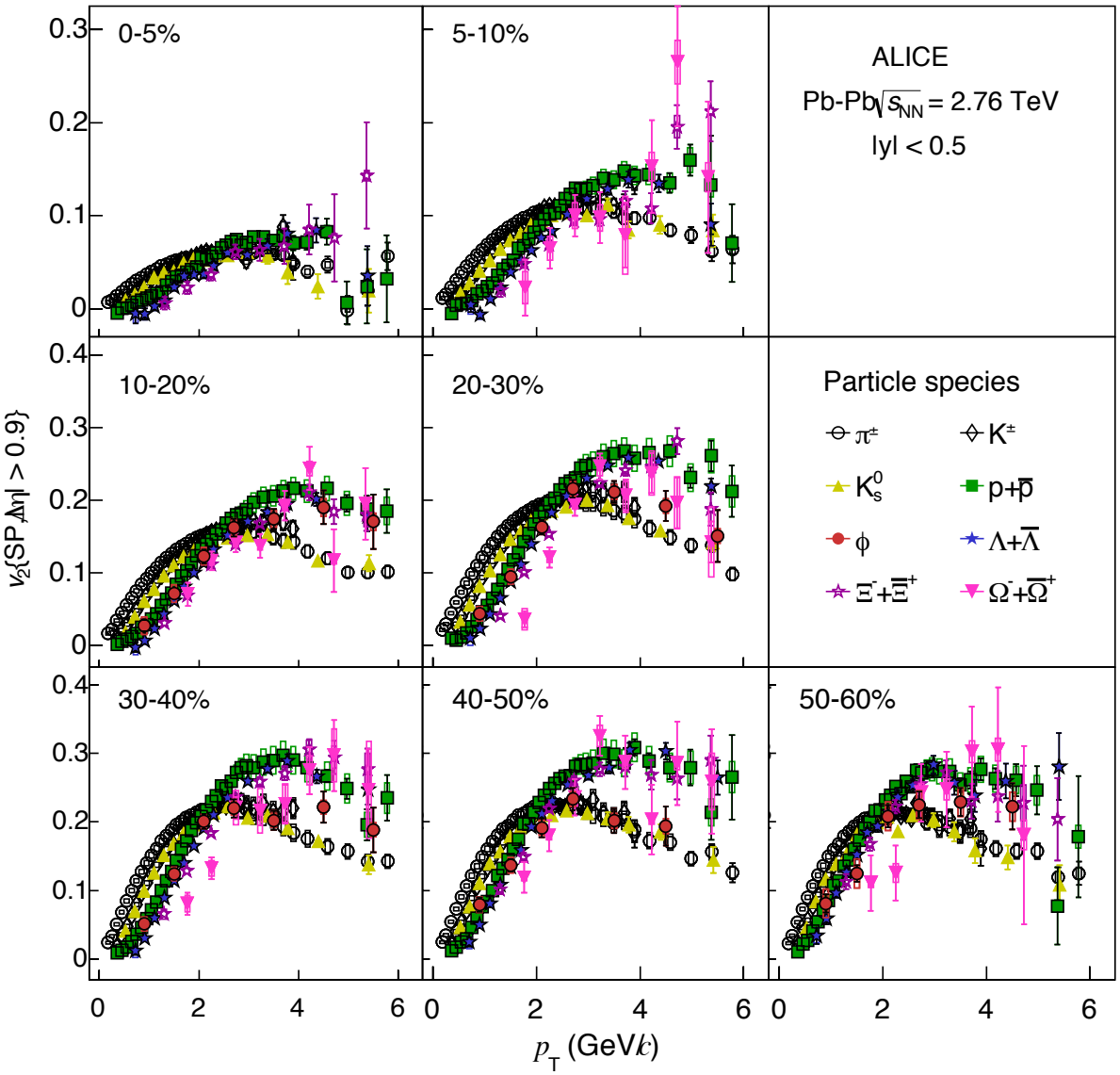

Figure 1.8: Differential flow of for different particle species with $|\eta| < 0.9$ in PbPb collisions at $\sqrt{s_{\rm NN}} = 2.76$ TeV as measured by the ALICE collaboration [61]. Behavior is shown for different centrality classes and in each case a mass ordering is observed where lighter particles have stronger elliptic flow signals.

in this thesis.

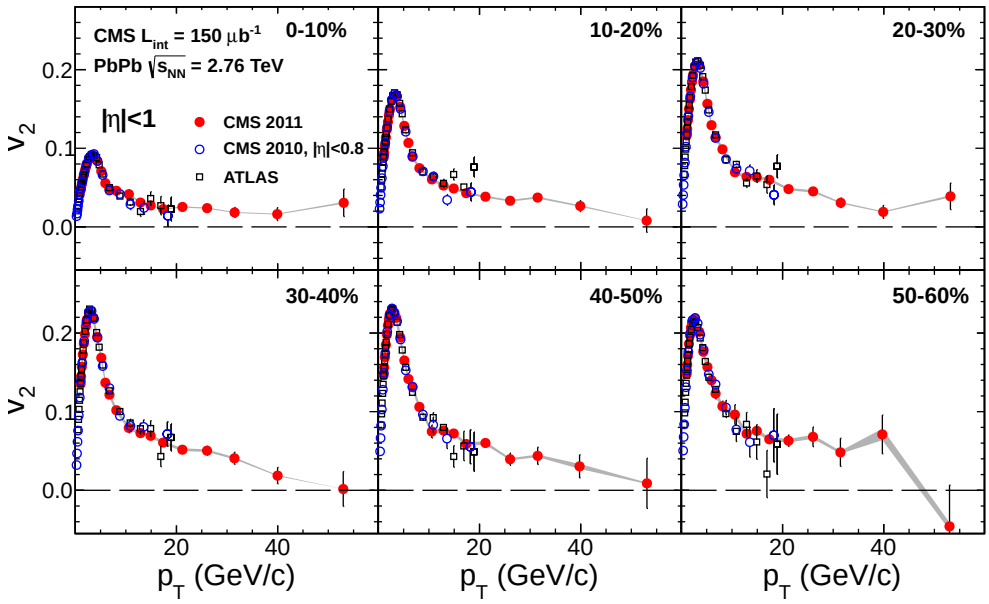

Figure 1.9: Elliptic flow coefficients measured in PbPb collisions at $\sqrt{s_{\mathrm{NN}}} = 2.76$ TeV up to $p_{\mathrm{T}} \approx 60$ GeV/c by the CMS collaboration [63] for centralities up to 60% and $|\eta| < 1$. Elliptic flow signals show a rise up to $p_{\mathrm{T}} \approx 3$ GeV/c and then begin to rapidly decrease as p_{T} extends past the flow region.

In addition to flow measurements, spatial correlations between emitted particles are used to probe early time scales in heavy-ion collisions. The observation of long-range particle correlations in rapidity indicate a common origin in the initial stages of the medium [67]. The first observation of long range correlations came out of AuAu collisions at RHIC [68, 69]. Here, significant correlations were observed in the $(\Delta\phi, \Delta\eta)$ difference of particle pairs that extended over several units of rapidity for $\Delta\phi = 0°$ and $180°$. This behavior was given the name "the Ridge." One of the surprising results that came out of the LHC heavy-ion run was the observation of ridge-like structures in high-multiplicity pPb and pp collisions [70, 71, 72, 73, 74, 75]. The formation of a QGP phase was not expected in pPb collisions and, as a result, collective effects were not anticipated in measurements. Figure 1.10 shows an example of the ridge behavior in pPb collisions at $\sqrt{s_{\mathrm{NN}}} = 5.02$ TeV as reported by the CMS collaboration [73]. This observation has sparked great interest and has spawned much discussion on collectivity in small systems. The question remains unanswered on whether or not a QGP phase is formed in high-multiplicity pPb and pp

collisions [76, 77, 78, 79, 80, 81, 82, 83, 84, 85, 86].

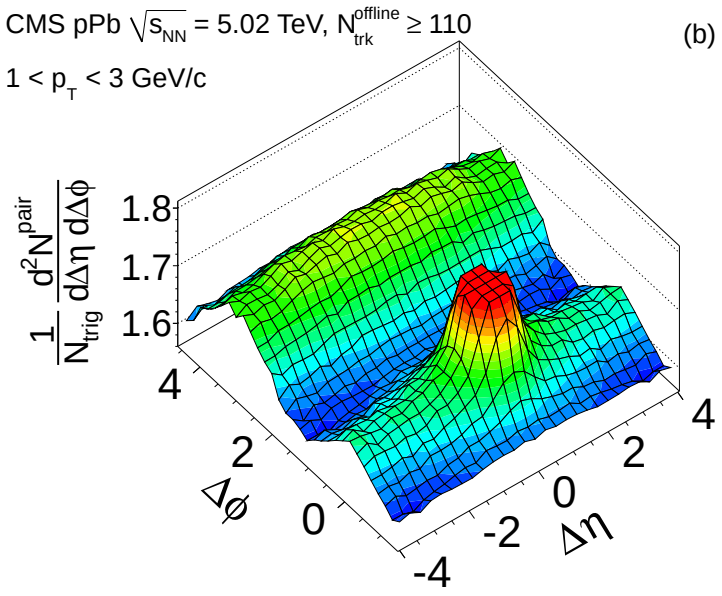

Figure 1.10: Two-particle correlations in $(\Delta\phi, \Delta\eta)$ for high-multiplicity ($N_{\mathrm{ch}} > 110$) pPb events at $\sqrt{s_{\mathrm{NN}}} = 5.02$ TeV as reported by the CMS collaboration [73]. The ridge behavior is observed when $\Delta\phi \sim 0$ and correlations persist out at large $\Delta\eta$ values.

1.3.2.3 Hard probes

The name "hard probes" refers to particles whose origins lie in the hard scatterings during a collision. Hard probes of the medium created in a heavy-ion collisions include particles with large p_{T}, jets, and heavy-flavor mesons. These probes are a powerful tool to characterize the QGP medium because they are created very early in a collision and the large scale in mass/energy/p_{T} of these probes places them in the realm of perturbative QCD. This, in turn, provides a solid theoretical foundation to separate production mechanisms from medium effects. A common experimental observable employed to study effects from the presence of the medium is the nuclear modification factor R_{AA} [87]. In this observable, particle yields or cross sections are compared to a cases where

nuclear effects are not expected, such as in pp collisions,

$$R_{\mathrm{AA}}(y, p_{\mathrm{T}}) = \frac{\frac{d^2N^{\mathrm{AA}}}{dydp_{\mathrm{T}}}}{\langle N_{\mathrm{coll}} \rangle \frac{d^2N^{\mathrm{pp}}}{dydp_{\mathrm{T}}}}, \tag{1.5}$$

$$R_{\mathrm{AA}}(y, p_{\mathrm{T}}) = \frac{\frac{d^2\sigma^{\mathrm{AA}}}{dydp_{\mathrm{T}}}}{T_{\mathrm{AA}} \frac{d^2\sigma^{\mathrm{pp}}}{dydp_{\mathrm{T}}}}, \tag{1.6}$$

where each fraction contains a normalization factor in the denominator. In the case of particle yields (Eq. (1.5), the fraction is normalized by $\langle N_{\mathrm{coll}} \rangle$ and for cross sections(Eq. (1.6) it is normalized by the nuclear thickness function $T_{\mathrm{AA}} = \langle N_{\mathrm{coll}} \rangle / \sigma_{\mathrm{pp}}^{\mathrm{inelastic}}$. These normalization factors are usually computed using a model tuned to the data such as the Glauber model [88, 89, 90]. With these normalizations, the absence of medium effects will yield a ratio of 1.

The observed suppression of high p_{T} particles was one of the measurements that motivated the presence of a QGP in heavy-ion collisions [91, 92, 93, 94, 95]. Figure 1.11 gives a comprehensive overview of the charged particle yield nuclear modification factor, measured up to $p_{\mathrm{T}} \approx 400$ GeV/c, as reported by the CMS collaboration [96] for a variety of collision systems and energies (and experiments). The nuclear modification factor shows a characteristic behavior as a function of p_{T} across all independent measurements. A local maximum in R_{AA} is observed at $p_{\mathrm{T}} \approx 2$ GeV/c while a local minimum is observed at $p_{\mathrm{T}} \approx 9$ GeV/c. This behavior is qualitatively understood to be a competition between several phenomena including radial flow (enhancement) [97], nuclear parton distribution function effects (model dependent) [98], parton energy loss (suppression) [64], and the Cronin effect (enhancement) [99, 100]. The Cronin effect is understood as a nuclear enhancement of high-p_{T} hadrons from multiple coherent nuclear interactions in the collision. Charged particle R_{AA} measurements provide a great test-case for competing models as the dependence on kinematic variables like p_{T} is sensitive to how well they balance these competing effects.

Perhaps one of the most important of the hard probes of the medium created in heavy-ion collisions are jets. Jets are narrow cones of hadrons resulting from the fragmentation of a colored object. Fragmentation is a consequence of confinement and thus makes jets the closest observable

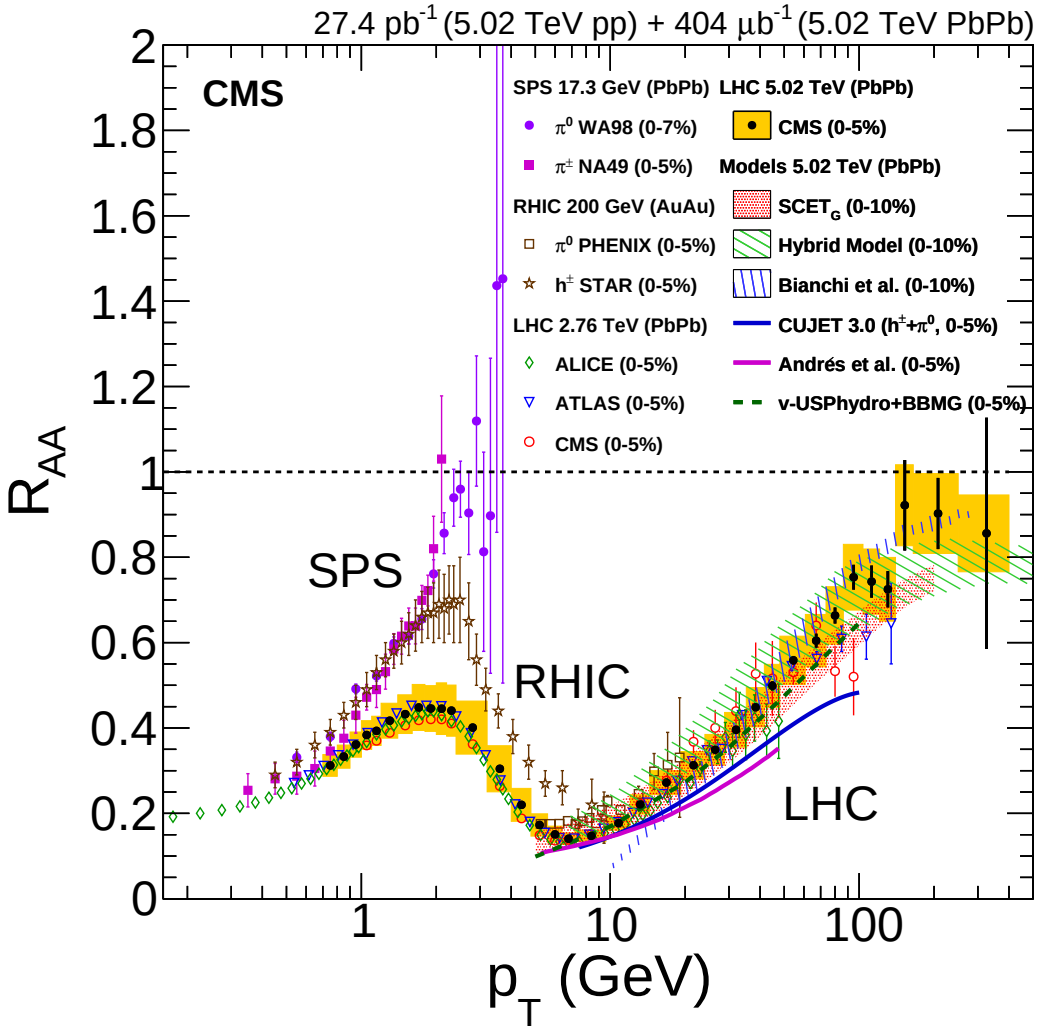

Figure 1.11: Comprehensive scan of particle production yields as measured by multiple experiments across different beam energies and collision systems. Summary reported by the CMS collaboration, see Ref. [96] and references therein.

to partons that can be properly defined [101]. Given the colored origins of jets, they make an excellent tool to study the mechanisms of energy loss in and the density of the medium. The LHC era brought fourth a new era of precision jet reconstruction with the increase in collision energy and the dramatic increase in calorimeter acceptance. One of the first measurements to come out of the LHC era was the energy imbalance of dijets and their distribution in azimuth [5, 6, 102]. The energy imbalance is quantified by

$$A_j = \frac{p_{\mathrm{T},1} - p_{\mathrm{T},2}}{p_{\mathrm{T},1} + p_{\mathrm{T},2}}, \tag{1.7}$$

where $p_{\mathrm{T},1}$ is the transverse momentum of the "leading" jet (the jet with the largest E_{T}) and $p_{\mathrm{T},2}$ is the transverse momentum of the "subleading" jet (the largest E_{T} jet in the hemisphere opposite the leading jet). This measurement is shown in Fig. 1.12 by the ATLAS collaboration [5] for PbPb collisions at $\sqrt{s_{\mathrm{NN}}} = 2.76$ TeV. Here, a significant increase in the energy imbalance is observed without azimuthal decorrelation of the two jets. These measurements are considered to be strong evidence of the QGP and also provide an estimate of the energy loss from medium effects by examining the average imbalance $\left\langle p_{\mathrm{T},2}/p_{\mathrm{T},1} \right\rangle$. Other measurements for jets include jet R_{AA} [103, 104, 105] which show a similar suppression as charged particles.

Similar to jets, heavy quarks also play an important role in characterizing the medium created in heavy ion collisions. With a mass that is larger than the temperature of the medium ($k_{\mathrm{B}}T \approx 300$ MeV at LHC energies [108]), heavy quarks are neither created nor destroyed by the medium, but solely by the initial hard scatterings of the collision. Therefore, heavy quarks will experience both energy loss and collective flow of the medium. Studies of the yields and azimuthal anisotropies of heavy flavor bound states therefore shed light on both the thermalization and hydrodynamic behavior of the medium. This is achieved by examining the nuclear modification factor and elliptic flow of heavy flavor states, studies of which have been carried out both at RHIC [109, 110] and the LHC [111, 112, 113, 114, 115, 116, 117, 118, 119, 120, 121, 122, 123]. Figure 1.13 shows an example of these measurements for D mesons ($c\bar{q}$) by the ALICE collaboration at $\sqrt{s_{\mathrm{NN}}} = 2.76$ TeV [118]. Here, a statistically significant non-zero v_2 is observed as a function of p_{T} and is complimented by a strong suppression of D meson states. The flow signal is

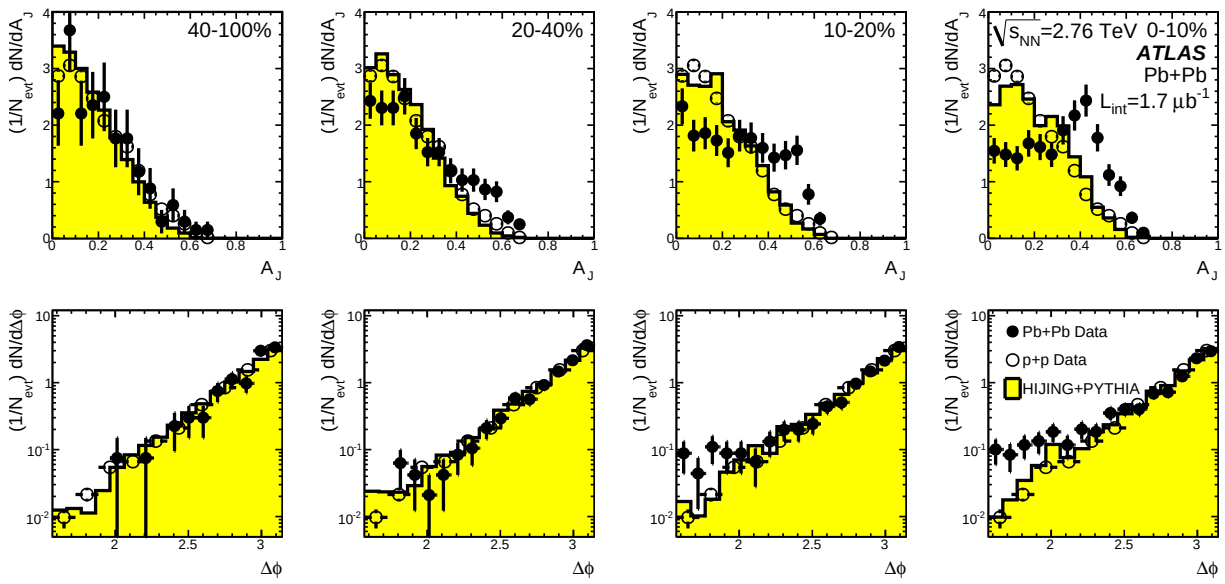

Figure 1.12: Dijet energy asymmetry (Eq. (1.7)) measured by the ATLAS collaboration [5] for PbPb collisions at $\sqrt{s_{\mathrm{NN}}} = 2.76$ TeV compared to pp collisions and HIJING+PYTHIA [106, 107] simulations with the absence of jet quenching. Jet opening angle $\Delta\phi$ is also presented to show that there is a significant dijet energy imbalance without azimuthal decorrelation of the two jets. The columns represent different centrality ranges, reported in percentages, where the trend moves from peripheral (left) to central (right) collisions.

related to a difference in path length for quarks emitted in-plane or out-of-plane, resulting in different energy losses for the quarks, and manifests as a final-state azimuthal anisotropy in momentum space [124, 125]. The strong suppression of D mesons yields is also related to energy loss in the medium, but adds a mass scale to the problem to provide further constraints. As can be seen in the left and right panels of Fig. 1.13, the experimental uncertainties need to be reduced to better constrain model calculations.

1.3.2.4 Quarkonia

One of the first predicted signatures of the QGP was the suppression of quarkonia bound states [18]. This suppression is a consequence of a screening of the color charge for quark-antiquark pairs surrounded by a high density of colored partons in a strongly interacting medium. This color screening results in a dissociation of the quark-antiquark pair and, at the time of hadronization, can lead to the constituent quarks pairing off with different partons. The suppression of charmonium states

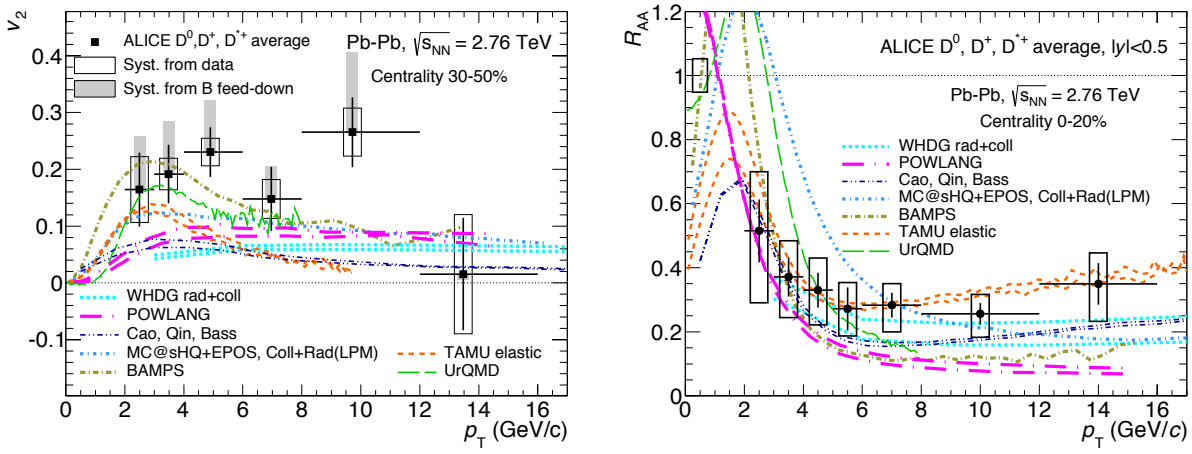

Figure 1.13: D meson R_{AA} and v_2 as measured by the ALICE collaboration at $\sqrt{s_{\mathrm{NN}}} = 2.76$ TeV [118]. A statistically significant v_2 signal is complimented by a strong suppression of D meson states.

(*e.g* J/ψ and $\psi(2S)$) was first observed at SPS [126, 127, 128] and RHIC [129, 130]. However, the observed suppression was not considered as definitive evidence for the QGP because there are several competing mechanisms from cold nuclear matter (CNM) effects, which can alter the production rate of charmonia states including:

- As the quark-antiquark pair escapes the environment, it undergoes multiple scatterings that can result in a dissociation of the pair [131, 132, 133].
- The parton distribution function for a nucleon can be altered by the surrounding nucleons, resulting in a modification of the gluon density within. This effect can alter the production rate of heavy quarks within a collision [134, 135].
- There is evidence that points to a secondary production mechanism for quark-antiquark pairs through a state of chemical equilibrium at the phase boundary of the QGP [136, 137, 138]. This production mechanism is known as "recombination" and can counterbalance suppression effects.

The LHC era brought forth an increase in statistics for charmonia states as well as access to higher mass states such as bottomonia ($b\bar{b}$). Quarkonia have been studied extensively by AL-

ICE [139, 140, 141, 142, 143, 144, 138, 145, 146, 147, 148, 121], CMS [148, 149, 150, 151, 122], ATLAS [152, 153], and LHCb [154, 155].

Suppression of quarkonia states is often studied through the nuclear modification factor. Figure 1.14 provides an example measurement of the R_{AA} for $\Upsilon(1S)$ and $\Upsilon(2S)$ states by the CMS collaboration for PbPb collisions at $\sqrt{s_{\mathrm{NN}}} = 2.76$ TeV [156]. Here, a strong suppression of states is observed as a function of centrality (reported in terms of N_{part}) with no indication of dependence on p_{T} or rapidity. Measurements by ALICE show a similar suppression for $\Upsilon(1S)$ at forward rapidity [147]. These measurements provide valuable input to help constrain theoretical models; more precise measurements are needed to fully understand the observed suppressions and their respective rapidity/p_{T}/centrality dependence [157, 158, 159].

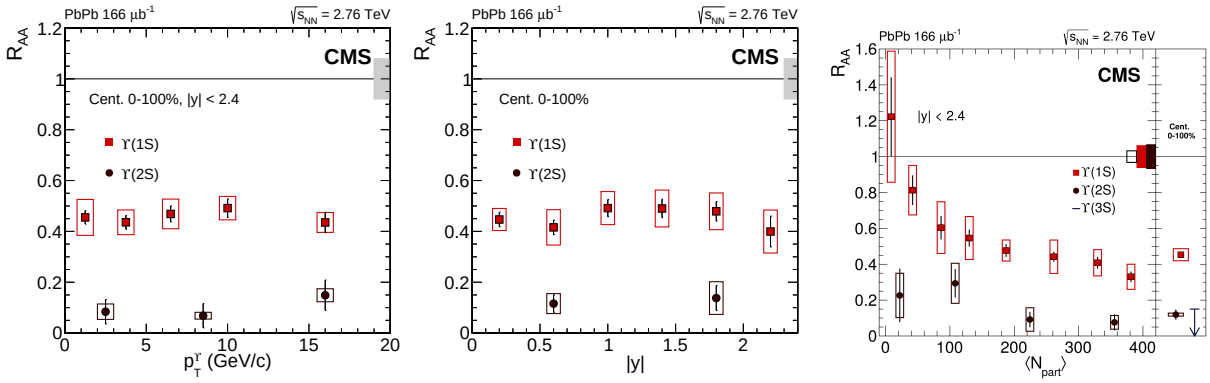

Figure 1.14: Upsilon R_{AA} as a function of p_{T} (left), $|y|$ (center), and $\langle N_{\mathrm{part}} \rangle$ (right) as measured by the CMS collaboration for PbPb collisions at $\sqrt{s_{\mathrm{NN}}} = 2.76$ TeV [156].

In addition to studying medium effects, quarkonia states are also used to probe nuclear parton distribution functions through ultra-peripheral collisions (UPCs). A UPC is a non-hadronic interaction where a photon emitted from one nucleus interacts with a target nucleus. In addition to colliding protons and nuclei, RHIC and the LHC also serve as photon-ion colliders. The source of photons for these collisions is understood from the Weizsäcker-Williams approximation [160, 161], which relates the electric field of a point charge to a semi-classical flux of photons. At relativistic velocities, electric field lines are Lorentz contracted and become increasingly dense in the plane transverse to the momentum of the nucleus. A Fourier transform of the electric field

results in a strong flux of photons in the same plane. These photons can interact with a target nucleus coherently, where the nucleus is excited and remains intact, or incoherently, where the excitation results in a dissociation of the nucleus. The measurement of coherent and incoherent cross sections of charmonia states is a powerful tool in discriminating models for nuclear parton distributions and what effects play an important role. This discriminatory power is illustrated in Fig. 1.15 where measurements of coherent J/ψ photoproduction are shown with several initial-state models [162, 163]. The two data points are able to successfully reject up to eight competing models and have also provided the first experimental evidence for gluon shadowing [164].

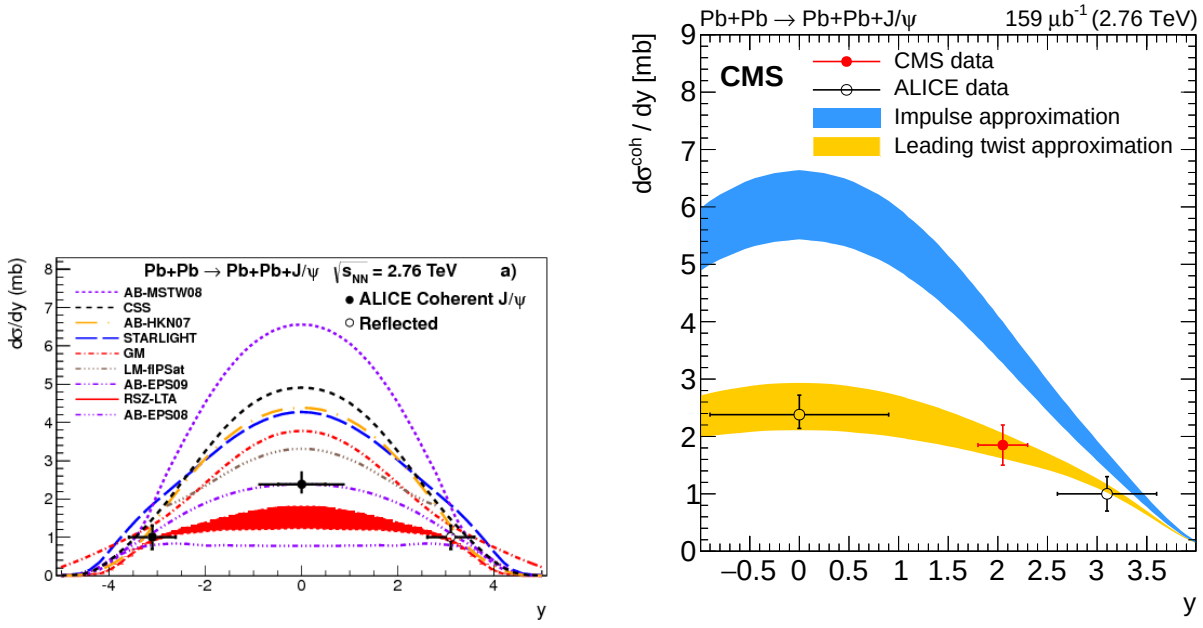

Figure 1.15: (Left) Coherent J/ψ photoproduction cross section as a function of rapidity as measured by ALICE in PbPb UPC collisions at $\sqrt{s_{\mathrm{NN}}} = 2.76$ TeV [162]. The two data points show a strong preference toward the AB-EPS09 model. (Right) Coherent J/ψ photoproduction cross section as a function of rapidity as measured by CMS in PbPb UPC collisions at $\sqrt{s_{\mathrm{NN}}} = 2.76$ TeV [163]

1.4 The big picture

One of the major physics goals in heavy-ion collisions is to determine quantitative properties of the QGP. While relativistic viscous hydrodynamics has been shown to be a successful tool to describe

the bulk dynamics of the QGP, the equations governing these dynamics require an input initial condition. Given the uncertainty in the physics governing the initial state of the collision, the standard in the field today is to construct models of the initial stages of heavy-ion collisions based on the physics that is known, propagate the assumed initial conditions using relativistic viscous hydrodynamics, and use the agreement with final-state measurements to constrain the models.

The hydrodynamic evolution of the QGP is but one of the stages of a heavy-ion collision. During the time evolution of a collision, there will come a point where the hydrodynamic description breaks down and kinetic models become more appropriate. The point at which this occurs is around hadron freeze out. The modern approach to modeling heavy-ion collisions is to use so-called "hybrid models" [165, 166, 167, 168, 169, 170, 171], which factorize a collision into separate stages, each governed by different physics. As time propagates in the hybrid models, there comes a point where two stages are approximately valid and the "final state" of the early stage becomes the "initial state" for the subsequent stage. With this approach, constraining any one stage of the model will affect the outcome of all subsequent stages. For example, when considering the initial-state spatial anisotropy in the transverse profile of the collision, the assumption in what contributes to this anisotropy alters the collision eccentricity values. Assuming that the sole source of the anisotropy is the participant nucleons of the collision leads to smaller predicted eccentricity values than if the substructures of the nucleons were considered [170]. Moreover, the presence gluon saturation will also affect the contribution to the eccentricity from the substructures of nucleons [172, 173]. These, in turn, result in different values of the viscosity of the QGP medium that are needed to match final-state flow measurements. As a consequence, other bulk observables from the model will also be affected, such as final-state particle yields and the interactions of hard probes with the medium.

In the hydrodynamic stage, the variables necessary to specify the initial conditions are the energy density, flow velocity, and viscosity. To obtain these conditions, models make assumptions on the following collision properties:

- The longitudinal profile: Is the longitudinal flow boost invariant and independent of the

transverse expansion of the medium [174]?

- The transverse profile: What are the dominant sources of the initial azimuthal anisotropy? Do the nucleon substructures contribute to this anisotropy and, if so, are gluon saturation effects considered?

- The fluctuations in the transverse profile: What is the nature of the fluctuations, are they Gaussian or not? Does the model account for these fluctuations at all?

- The total energy/entropy: What are the dominant sources of entropy production in the collision and do they match final-state particle production?

- The initial flow velocity distributions: What are the initial flow velocities in the transverse and longitudinal profiles of the collisions?

Measurements performed in this thesis will have the largest impact on model assumptions made on the anisotropy in the transverse profile a collision and its event-by-event fluctuations. This is achieved by studying the probabilistic behavior of the final-state fluctuations in the flow harmonic coefficients for PbPb collisions at $\sqrt{s_{\mathrm{NN}}} = 5.02$ TeV. The inclusion of this fluctuation behavior into models therefore provides additional constraints on the understanding of the initial state of ultrarelativistic heavy-ion collisions.

Probability distributions that describe the event-by-event fluctuation of the elliptic flow harmonic $p(v_2)$ are determined by removing finite-multiplicity resolution effects from measured $p\left(v_2^{\mathrm{obs}}\right)$ distributions using a statistical unfolding technique [175]. The moments of the unfolded distributions are used in a cumulant expansion [176, 50, 177] to construct cumulant flow harmonics. Hydrodynamic studies have shown that the cumulant elliptic flow harmonics can be directly related to the cumulant ellipticity harmonics of the underlying $p(\varepsilon_2)$ distributions [178]. In addition, the cumulant flow harmonics provide an estimate of the skewness of the elliptic flow probability distributions with respect to the reaction plane, a quantity that is sensitive to deviations from the Gaussian model of eccentricity fluctuations [178, 44]. Precision measurements of cumulant elliptic flow harmonics and skewness estimates are presented based on the moments of unfolded $p(v_2)$ distributions

for 5% wide centrality bins, each with an integrated η (p_{T}) range $|\eta| < 1.0$ ($0.3 < p_{\mathrm{T}} < 3.0$ GeV/c). Unfolded distributions are transformed assuming a linear relationship between ellipticity and elliptic flow and fitted with Bessel-Gaussian and elliptic power law parametrizations to infer information on the underlying ellipticity distributions. The unfolding technique is also coupled to the event-shape engineering technique [179, 180], where events are further classified by their "shape" observed in the forward region, to probe correlations amongst different-order harmonics.

1.5 Overview of this thesis

This thesis is organized into eight chapters designed to introduce the hot, dense QCD matter created in heavy-ion collisions and probe in detail the aspect of initial-state spatial asymmetry fluctuations. Following the introduction of this chapter, Chapter 2 further discusses the concept of initial-state spatial asymmetry fluctuations and theoretical motivations for their study. Chapter 3 provides an in-depth discussion of the experimental apparatus used, the CMS detector at the CERN LHC. Chapter 4 discusses the acquisition of data for this analysis and the selection criteria used to suppress unrelated phenomena. Chapter 5 provides a detailed overview of the analysis technique used to extract the distributions of elliptic flow harmonics. Chapter 6 outlines the systematic studies used in this analysis to ascertain residual biases from unrelated physics phenomena. Chapter 7 presents the primary findings of this analysis in terms of the measured quantities and their physics impact. Chapter 8 presents the conclusions of this analysis and discusses prospects for future studies. Lastly, Appendix A provides a detailed derivation of the cumulant expansion for flow harmonics, Appendix B gives prescriptions for deriving analytic response matrices, and Appendix C contains a comprehensive set of plots that show the unfolding performance for all distributions obtained in this analysis using both D'Agostini iteration and SVD unfolding techniques.

Chapter 2

Participant eccentricity fluctuations

The observation of a non-zero average v_3 value (Fig. 2.1, for example) at RHIC [41] was a clear signal that the quantum nature of the overlap geometry of a heavy-ion collision has an impact on the observed final-state particle anisotropies. Quantum fluctuations in the positions of the nucleons and their substructure within the nucleus imply that, for a given impact parameter, the initial profile of a collision cannot be described using a single eccentricity harmonic (Eq. (2.10)), but rather a distribution of possible eccentricity harmonics $\varepsilon_n \rightarrow p(\varepsilon_n)$. The importance of initial-state eccentricity fluctuations was introduced in Sec. 1.3.2.2. Fluctuations can be studied by measuring odd-order flow harmonics, as odd-order harmonics are expected to vanish in the absence of fluctuations [181]. In addition, the distributions of event-by-event flow harmonic coefficients can be used to infer information on the underlying eccentricity distributions [182].

For central to mid-central collisions, fluctuations in the participant eccentricity can be described by a two-dimensional (2D) Gaussian function [44], with

$$p\left(\vec{\varepsilon}_n\right) = \frac{1}{2\pi\delta_{\varepsilon_n}^2} \exp\left[-\frac{\left(\vec{\varepsilon}_n - \langle\vec{\varepsilon}_n^{\mathrm{RP}}\rangle\right)^2}{2\delta_{\varepsilon_n}^2}\right]. \tag{2.1}$$

Here, $\langle\vec{\varepsilon}_n^{\mathrm{RP}}\rangle$ represents the average eccentricity vector that is associated with the reaction plane and δ_{ε_n} quantifies the fluctuations-induced "width" of the distribution. While this parametrization

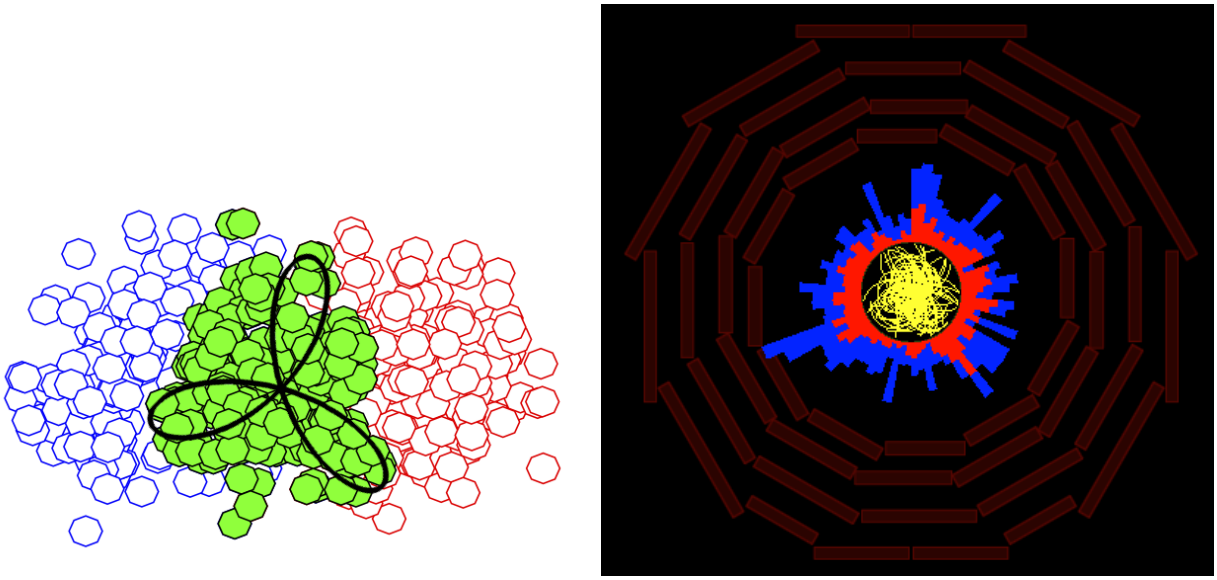

Figure 2.1: (Left) A Glauber simulation of a PbPb collisions with a strong ε_3 signal A solid black line illustrates the $\cos 3\phi$ triangular term in the Fourier decomposition. (Right) A CMS event display of a PbPb collision with a strong v_3 signal.

works well for central collisions, it fails to describe the fluctuation behavior in more peripheral collisions [182, 183], as illustrated in Fig 2.2. If the flow response depends linearly on the participant eccentricity, the fluctuations of the flow vectors can be similarly described by a 2D Gaussian for central collisions, with

$$p\left(\vec{v}_n\right) = \frac{1}{2\pi\delta_{v_n}^2} \exp\left[-\frac{\left(\vec{v}_n - \langle\vec{v}_n^{\mathrm{RP}}\rangle\right)^2}{2\delta_{v_n}^2}\right], \tag{2.2}$$

where $\langle\vec{v}_n^{\mathrm{RP}}\rangle$ and δ_{v_n} are flow analogs to the eccentricity parametrization described in Eq. (2.1). The probability distribution of the magnitude of flow is obtained by integrating out the ϕ-dependence of Eq. (2.2) [44, 184], leading to

$$p\left(v_n\right) = \frac{v_n}{\delta_{v_n}^2} \exp\left[-\frac{(v_n)^2 + \langle v_n^{\mathrm{RP}}\rangle^2}{2\delta_{v_n}^2}\right] I_0\left(\frac{v_n\langle v_n^{\mathrm{RP}}\rangle}{\delta_{v_n}^2}\right), \tag{2.3}$$

where I_0 is the modified Bessel function of the first kind. This functional form is known as a

Bessel-Gaussian.

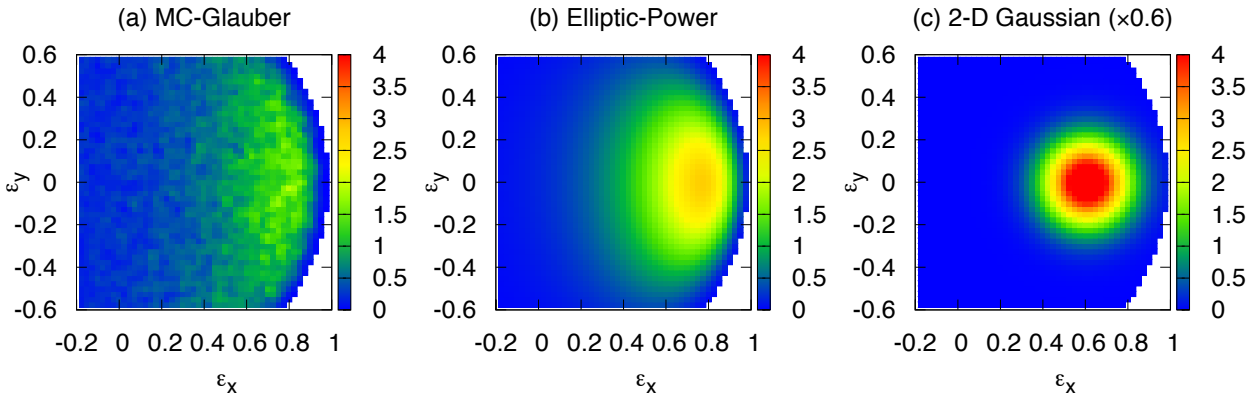

Figure 2.2: (Left) The transverse distribution of participant eccentricity vectors for 40 000 peripheral events generated in Ref. [182] using the Monte-Carlo Glauber model. (Middle) A fit to the left panel using an elliptic power law parametrization (Eq. (2.14)). (Right) A fit to the left panel using a 2D Gaussian parametrization (Eq. (2.1)). Here, the elliptic power law parametrization provides a better description of the distribution of participant eccentricity vectors.

Properties of $p\left(v_n\right)$ distributions have been inferred from studies using event-averaged values. For example, m-particle azimuthal correlation measurements are commonly used to probe the moments of $p(v_n)$ distributions. Within a m-particle correlation analysis the cosine average of all combinations of m particles in an event is calculated and, in the absence of "non-flow" effects such as resonance decays and dijet correlations, corresponds to the m^{th}-order moment of the underlying $p(v_n)$ distribution [44],

$$\left\langle v_n^{2k}\right\rangle \equiv \int v_n^{2k} p\left(v_n\right) dv_n = \left\langle \cos \sum_{j=1}^{k} n\left(\phi_{2j} - \phi_{2j-1}\right) \right\rangle + \text{non-flow}, \tag{2.4}$$

where $2k = m$. The m-particle azimuthal correlation analysis is extended with a cumulant expansion to construct cumulant flow harmonics [176, 50, 177]. Cumulants are a set of quantities that describe the behavior of a probability distribution and are determined by the moments of the distribution. Cumulants are obtained through a series expansion of the "cumulant-generating function" [185], which is shown for an arbitrary probability distribution in Appendix A. The cumulant-generating function is built from the natural logarithm of the "moment-generating function," which,

in this case, is Fourier-Laplace transform of the $\vec{v}_n$ vectors from Eq. (1.4) [178],

$$G_n(k) \equiv \log M_n(k) = \log\left(\int_0^{2\pi} \frac{d\phi}{2\pi} \langle e^{\vec{k}\cdot\vec{v}_n}\rangle\right), \tag{2.5}$$

where $\vec{k}$ is a generic vector and $M_n(\vec{k}) \equiv \langle e^{\vec{k}\cdot\vec{v}_n}\rangle$ is the moment-generating function. When considering the magnitude of flow, the moment-generating function is first integrated over the azimuthal angle before building the cumulant-generating function. The m^{th} order cumulant flow harmonic is obtained from the m^{th}-order term in a taylor expansion of $G_n(k)$ [50]

$$\frac{d^m}{dk^m} \log I_0(k v_n\{m\})\bigg|_{k=0} \equiv \frac{d^m}{dk^m} \log G_n(k)\bigg|_{k=0}. \tag{2.6}$$

The cumulant expansion has the advantage compared to using the moments of the m-particle azimuthal correlations in that cumulants of higher orders naturally eliminate correlations of a lower order [177]. In other words, higher-order cumulant measurements naturally suppress non-flow correlations and provide more robust flow measurements. The first non-vanishing orders of cumulant flow harmonics are [44]:

$$\begin{aligned}
v_n\{2\}^2 &\equiv \langle v_n^2\rangle, \\
v_n\{4\}^4 &\equiv -\langle v_n^4\rangle + 2\langle v_n^2\rangle^2, \\
v_n\{6\}^6 &\equiv \left(\langle v_n^6\rangle - 9\langle v_n^4\rangle\langle v_n^2\rangle + 12\langle v_n^2\rangle^3\right)/4, \\
v_n\{8\}^8 &\equiv -\left(\langle v_n^8\rangle - 16\langle v_n^6\rangle\langle v_n^2\rangle - 18\langle v_n^4\rangle^2 + 144\langle v_n^4\rangle\langle v_n^2\rangle^2 - 144\langle v_n^2\rangle^4\right)/33 \\
&\vdots
\end{aligned} \tag{2.7}$$

The cumulant flow harmonics are derived assuming that the underlying fluctuation behavior is Gaussian and isotropic [50]. With this assumption, the cumulants flow harmonics then have the form [186]:

$$v_n\{2k\} = \begin{cases} \sqrt{\langle v_n^{\text{RP}}\rangle^2 + 2\delta_{v_n}^2}, & k = 1 \\ \langle v_n^{\text{RP}}\rangle, & k > 1 \end{cases}. \tag{2.8}$$

A detailed derivation of the cumulant flow harmonics from Eqs. (2.7) and (2.8) is show in Appendix A.

The initial-state eccentricity values are obtained similarly through a cumulant expansion of the initial-state entropy density [43]. Here, the cumulant generating function $W(\vec{k})$ is defined such that

$$\exp\left(W(\vec{k})\right) \equiv \int d^2\vec{x}\, e^{i\vec{k}\cdot\vec{x}} \rho(\vec{x}), \tag{2.9}$$

where $\rho(\vec{x})$ is the transverse entropy density. The first non-vanishing orders of eccentricities are:

$$\varepsilon_1 e^{i\Phi_1} \equiv -\frac{\left\{r^3 e^{i\phi}\right\}}{r^3}, \quad \varepsilon_2 e^{2i\Phi_2} \equiv -\frac{\left\{r^2 e^{2i\phi}\right\}}{r^2}, \quad \varepsilon_3 e^{3i\Phi_3} \equiv -\frac{\left\{r^3 e^{3i\phi}\right\}}{r^3}, \tag{2.10}$$

where ε_n and Φ_n denote the amplitudes and phases of the n^{th}-order eccentricity, respectively, and curly brackets denote averages over the transverse entropy density in a single event.

Recently, the ATLAS collaboration introduced a new experimental method to extract the $p(v_n)$ probability distribution directly using an unfolding technique [175], allowing for detailed studies of the behavior of flow (and, ultimately, eccentricity) fluctuations through precise extraction of the cumulants. The observation that $v_n\{4\} \approx v_n\{6\} \approx v_n\{8\}$ in PbPb collisions suggests that the flow fluctuations are nearly Gaussian in nature [44, 187, 188, 189]. However, there is great interest in the field to observe a breakdown in the Gaussian model of fluctuations, as this behavior is predicted by hydrodynamic models [178, 190]. A fine-structure splitting between $v_n\{4\}$ and $v_n\{6\}$ has been observed by ATLAS based on direct m-particle cumulant measurements [189].

In a recent hydrodynamic study [178], $p(v_2)$ distributions were found to have a negative skewness with respect to the reaction plane, which results from the fluctuating initial-state ellipticities and a linear flow response. Within this hydrodynamic study, skewness estimates were derived from the $p(v_2)$ distributions obtained by ATLAS for PbPb collisions at $\sqrt{s_{\text{NN}}} = 2.76$ TeV energies [175]. While the theoretical predictions were consistent with the derived skewness, the derived results contain large statistical uncertainties. A direct measurement of the skewness estimate is needed to constrain experimental uncertainties. A non-zero skewness with respect to the reaction plane is a

signature of non-Gaussian fluctuations. The standardized skewness used to express this deviation from a Gaussian behavior is a dimensionless quantity and, for elliptic flow, can be expressed as

$$\gamma_1 = \frac{\left\langle \left(v_2 - \langle v_2^{\mathrm{RP}} \rangle \right)^3 \right\rangle}{\left(\sqrt{\left\langle (v_2)^2 \right\rangle - \langle v_2 \rangle^2} \right)^3} \tag{2.11}$$

where the flow harmonics are determined with respect to the reaction plane. Since this plane is not experimentally accessible, it was proposed in Ref. [178] to estimate the standardized skewness of Eq. (2.11) in terms of the cumulant flow harmonics, with

$$\gamma_1^{\mathrm{exp}} \equiv -6\sqrt{2} v_2\{4\}^2 \frac{v_2\{4\} - v_2\{6\}}{\left(v_2\{2\}^2 - v_2\{4\}^2 \right)^{3/2}}. \tag{2.12}$$

Hydrodynamic calculations find this estimate to be in good agreement with the actual skewness up to 60% centrality [178].

Beyond the extraction of cumulants from the moments of $p(v_n)$ distributions, the distributions themselves can be used to infer the nature of $p(\varepsilon_n)$ distributions. If the flow response is assumed to be linear with $v_n = k_n\, \varepsilon_n$, then functional parametrizations of $p(\varepsilon_n)$ can be transformed and fitted to measured $p(v_n)$ distributions, with

$$p(\varepsilon_n) = p\left(\frac{v_n}{k_n} \right) = k_n\, p(v_n), \tag{2.13}$$

where k_n is the flow response coefficient. One particular parametrization that has gained theoretical favor in the recent years is the elliptic power law parametrization [191]

$$p(\varepsilon_n) = \frac{2\alpha\varepsilon_n}{\pi} (1-\varepsilon_0^2)^{\alpha+1/2} \int_0^\pi \frac{(1-\varepsilon_n^2)^{\alpha-1} d\phi}{(1-\varepsilon_0\varepsilon_n\cos\phi)^{2\alpha+1}}, \tag{2.14}$$

where ε_0 is approximately equal to the mean eccentricity with respect to the reaction plane and α describes the size of the eccentricity fluctuations. This function is a result of the assumption that the

initial energy density profile of the collision is a superposition of N point-like, independent sources, with the α term being approximately proportional to N. The elliptic power law parametrization was shown to describe the eccentricity distributions in pp, pPb, and PbPb collisions well using the MC-Glauber and MC-KLN initial-state models [45]. In cases where $\alpha \gg 1$ and $\varepsilon_0 \ll 1$ the universal elliptic power law distribution reduces to a Bessel-Gaussian distribution.

Beyond the m-particle correlation analysis, there exist different experimental techniques that probe moments of the underlying $p(v_n)$ fluctuation behavior. For example, the scalar product method [192, 193] for flow analysis provides an unambiguous measure of the root-mean-square (RMS) of the underlying $p(v_n)$ distribution, while the event-plane method mentioned in Sec. 1.3.2.2 provides a measure of a flow value between the mean and the RMS of the underlying $p(v_n)$ distribution. While these techniques are standard in flow measurements, the unfolding technique outlined in Chapter 5 measures the event-by-event flow harmonic coefficient fluctuation behavior itself and brings analyses into an era of precision fluctuation studies.

Chapter 3

Experimental setup

3.1 The LHC machine

The LHC is a 26.7 km circumference accelerator located ∼100 m underground between the Swiss and French border at CERN. Since the discovery of the Higgs in 2012 [194, 195], the primary focus of the LHC has shifted towards revealing physics beyond the Standard Model. The LHC is designed to reach center-of-mass energies up to 14 TeV for pp collisions. To study exotic events with high precision, the LHC aims for a peak luminosity of $L = 10^{34}$ cm^{2}s^{-1} [196]. The number of events produced per unit time for a given process is given by

$$\frac{dN_{\text{Events}}}{dt} = L\sigma, \tag{3.1}$$

where L is the machine luminosity and σ is the cross section for the process of interest. The machine luminosity is dependent on parameters related to the beam profile. For a Gaussian beam distribution in a circular collider, the luminosity can be expressed as

$$L = \frac{N_b^2 n_b f_{\text{rev}} \gamma_r}{,} 4\pi\varepsilon_n \beta^* F \tag{3.2}$$

where N_b is the number of particles within a bunch, n_b is the number of bunches per beam, which is driven by the spacing between bunches in the accelerator, f_{rev} is the revolution frequency for a bunch, γ_r is the relativistic gamma factor, ε_n is the normalized transverse beam emittance, F is a reduction factor from the non-zero crossing angle at the collision point, and β^* determines the transverse beam size at the collision point.

The collision rate at the LHC is driven by the spacing between bunches in the accelerator. At peak operating conditions bunch spacing can be as small as 25 ns [196]. Bunches are first formed

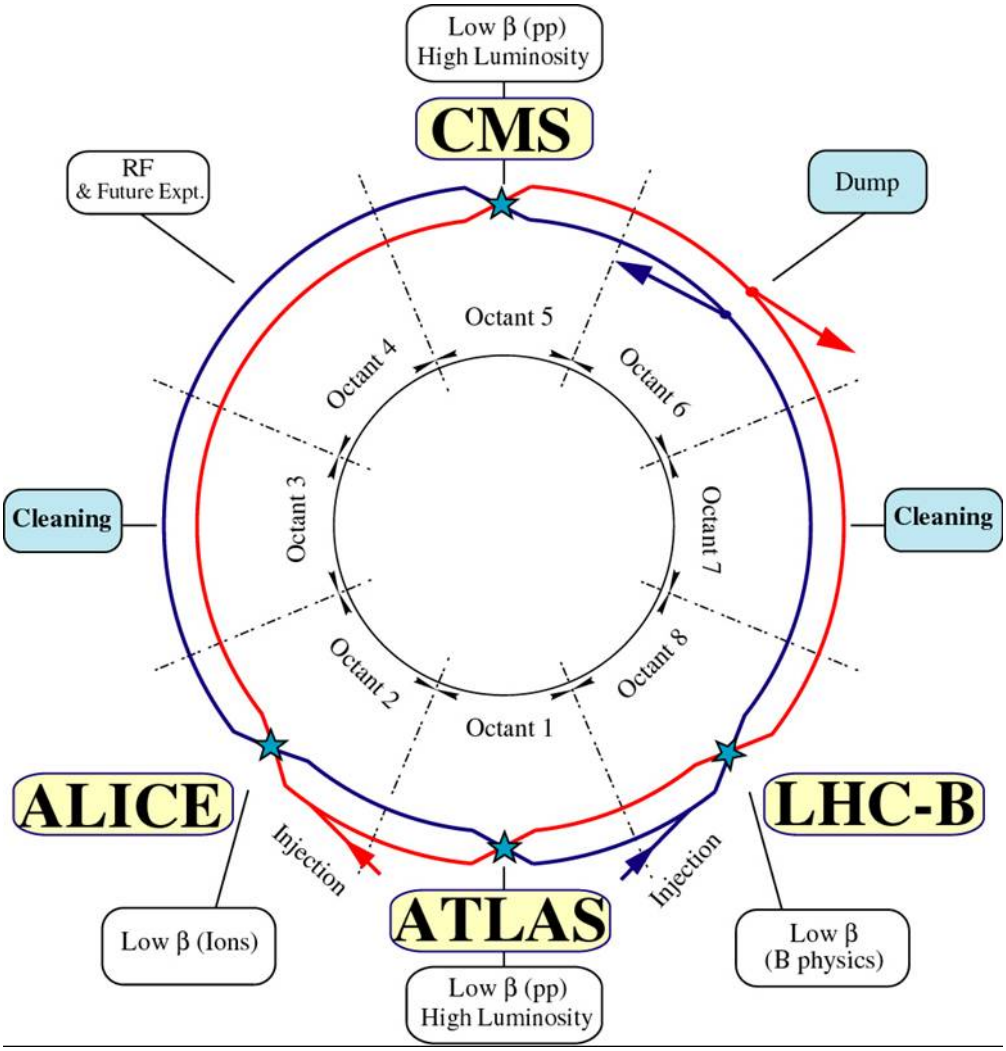

Figure 3.1: A schematic view of the LHC ring and the contents of its octants. Schematic taken from Ref. [196].

in the Proton Synchrotron (PS) at CERN and accelerated up to 26 GeV/A in energy. Bunches are

then passed to a secondary loop, SPS, where they are accelerated up to 450 GeV/A. After SPS, bunches are finally fed into the LHC where they undergo a final acceleration up to the current operational energy (13 TeV for pp, 5.02 TeV for PbPb, and 8.16 TeV for pPb). There are four points in the LHC ring where bunches collide and the main experiments sit, as depicted in Fig. 3.1. Two of experiments are general-purpose detectors, CMS and ATLAS, designed to operate at the peak LHC luminosity. The remaining experiments are specialized detectors, LHCb and ALICE, designed to study B-physics and heavy-ion physics, respectively.

The LHC primarily operates colliding protons to achieve its physics goals. However, on the order of one month out of the year, it switches to colliding PbPb or pPb bunches to study high density QCD physics [197, 198]. This thesis focuses on PbPb collisions at $\sqrt{s_{\mathrm{NN}}} = 5.02$ TeV as recorded by the CMS experiment during the 2015 year run. A detailed overview of the CMS detector is provided in subsequent sections.

3.2 The CMS detector

The Compact Muon Solenoid (CMS) is a general-purpose detector located at interaction point 5 on the LHC ring in Cessey, France. In the early conceptual designs for the experiment, one of the driving goals was to achieve a precise measurement of the momentum of muons. To achieve this goal, CMS uses a 13 m long, 5.9 m inner diameter super conducting solenoid capable of producing a 4 T magnetic field. This powerful magnetic field provides the bending power necessary to measure high-momentum (TeV scale) muons. The CMS detector is cylindrical in shape, having a length of 21.6 m and a diameter of 14.6 m [199]. Overall, the detector weighs 12 500 tons. A schematic drawing of the detector is given in Fig. 3.2.

CMS uses a global coordinate system oriented such that the x-axis points toward the center of the LHC ring, the y-axis points vertically upward, and the z-axis points in the direction of the beam. The radial coordinate r as well as the azimuthal angle ϕ from the x-axis are measured in the xy plane. The Lorentz-invariant spatial coordinate η, as defined in Sec. 1.3.2, is used instead of the polar angle θ to specify the direction of outgoing particles.

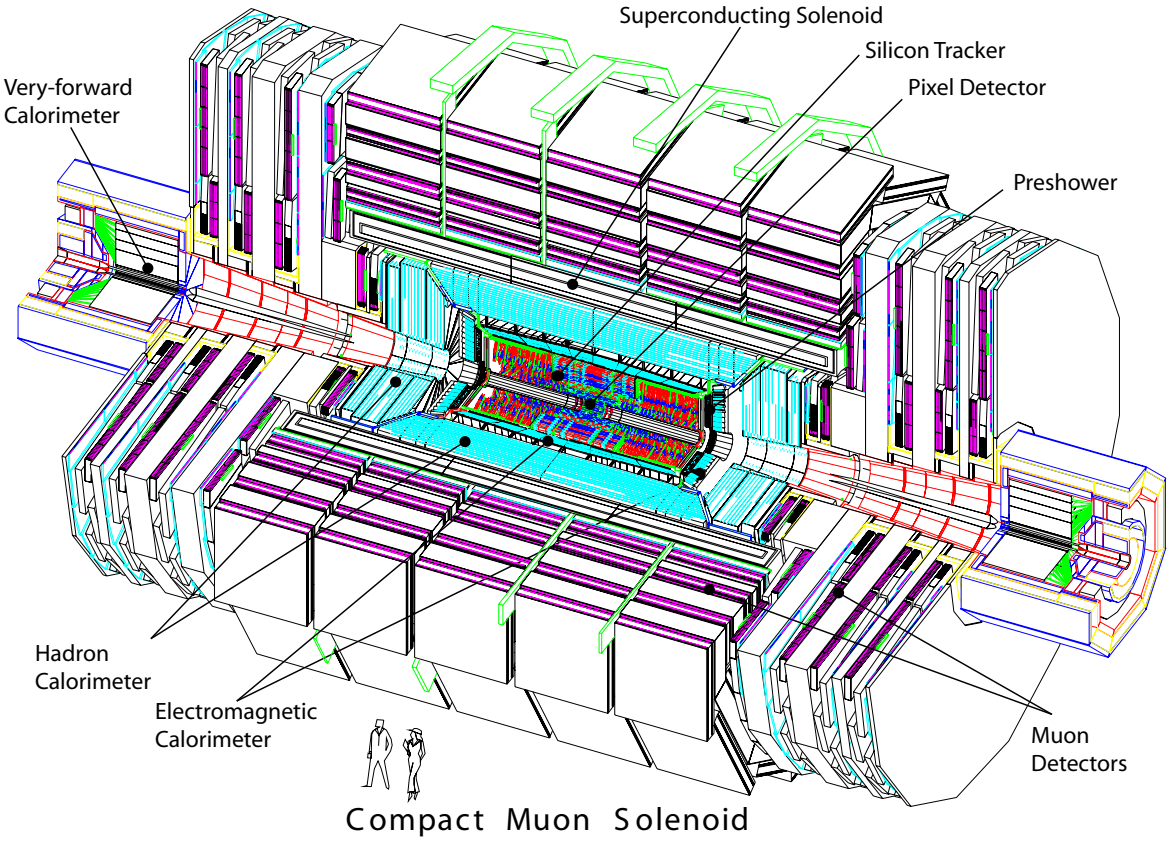

Figure 3.2: A full-scale view of the CMS detector and its subsystems. The ZDCs and CASTOR calorimeters are not shown in this figure. Figure taken from Ref. [199].

The inner bore of the solenoid is large enough to include multiple subsystems to extend the detection capabilities of the experiment. With that, CMS is organized into an onion-like structure with different layers of detection technologies. Within the magnet, closest to the beam line, sits the silicon tracking system. The silicon tracker is designed to measure the trajectories of a large volume of charged particles emitted in a collision with extreme precision. Occupying the layer surrounding the tracking system is an electromagnetic calorimeter (ECAL). The ECAL system uses lead tungstate crystals to initiate showers of light from incident electrons and photons. This scintillation light is collected and used to measure the energy and position of the incident particles. A hadronic calorimeter (HCAL) is positioned in the next layer surrounding ECAL. Similar to ECAL, HCAL uses brass scintillator plates to initiate showers of light from incident hadrons (mostly pions) and measure their positions and energies. The silicon tacker, ECAL, and HCAL occupy the volume of the bore of the magnet, but there exists one additional layer outside the magnet containing the muon systems. Embedded within the steel return yoke of the magnet are muon chambers utilizing various detection technologies capable of extending the trajectories of muons beyond those measured by the tracking system. Each of these subsystems compose the central CMS detector and consist of a central cylindrical shell ("barrel") hermetically sealed by circular disks ("endcaps") that provide full azimuthal acceptance and a wide coverage in η.

In addition to the barrel and endcap systems, CMS has several extensions to measure energy in the very forward region. Beyond the reach of the endcaps of HCAL sit forward hadronic calorimeters (HFs) that use iron and quartz fibers to initiate and measure scintillation of incident hadrons. Moving further forward, on the negative-η side of the experiment, is the Centauro And Strange Object Research (CASTOR) calorimeter that uses alternating tungsten and quartz plates to measure the energy of both electromagnetic and hadronic particles traversing the calorimeter. Lastly, sitting $\pm$140 m from the center of CMS sit the Zero Degree Calorimeters (ZDCs). The ZDCs use alternating plates of tungsten and quartz fibers to measure very forward photons and neutrons resulting from hard scattering, electromagnetic, and diffractive events. All subsystems of the CMS detector are discussed in more detail in the following subsections.

3.2.1 Tracker

The CMS tracker occupies a cylindrical volume 5.8 m in length and 2.5 m in diameter, with its axis closely aligned to the LHC beam line. The tracker utilizes both silicon pixel and strip technologies to measure charged particle trajectories with extreme precision. A schematic slice of the CMS tracker is shown in Fig. 3.3.

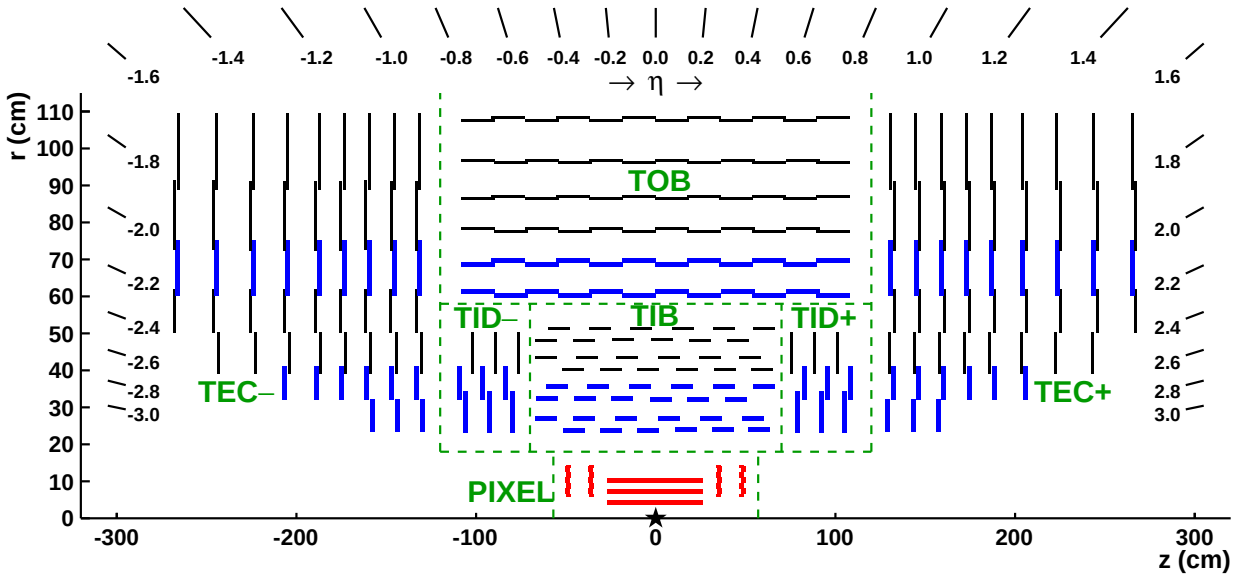

Figure 3.3: Schematic view of the silicon tracking system in the CMS detector. Schematic taken from Ref. [200]. Bold blue lines denote double-sided strip modules.

The pixel tracker consists of 1440 modules organized into three coaxial barrel layers located at radii of 4.4, 7.3, and 10.2 cm. The barrel layers are complimented by two endcap disks on both sides of the barrel located at $|z| = 34.5$ cm and 46.5 cm from the origin. The pixel detector measures the interaction of charged particles with its sensors and records these "hits" in the three dimensions. Each hit has a measurement resolution of ~ 10 μm and 20–40 μm in the transverse and longitudinal directions, respectively [200].

Surrounding the pixel tracker is the strip tracker, which extends out to a radius of 110 cm. The strip tracker consists of 15 148 silicon strip modules organized into 10 coaxial barrel layers complimented by three small and nine large endcap disks. The strip tracker is comprised of four subsystems: the Tracker Inner Barrel (TIB), the Tracker Outer Barrel (TOB), the Tracker Inner

Disks (TID), and the Tracker EndCaps (TEC). The TIB and TID are located within $r < 55$ cm and $|z| < 118$ cm. The TIB consists of four concentric barrel layers (staggered modules comprise one layer in Fig. 3.3) while the TID provide three disks on each end of the TIB. Both the TIB and TID provide hit measurements in $r\phi$ with a resolution between 13–38 μm. The TOB is located at $r > 55$ cm and $|z| < 118$ cm with six concentric barrel layers. The TEC are located between $124 < |z| < 282$ cm and consist of nine disks. Each of the disks contain up to seven concentric rings of strip modules. Both the TOB and TEC provide hit measurements in $r\phi$ with resolutions between 18–47 μm.

Hit position resolutions are studied through simulation. Events are first generated containing the "true" trajectories for each particle and then reconstructed using GEANT4 [201] to mimic detector effects as the particles traverse through the material. Resolutions are estimated by examining track residuals, which are the differences between reconstructed track parameters and the generated track parameters. For all track parameters, the resolution is defined as the half-width of the distribution of track residuals centered at the most probable value of the residuals. Residuals are binned in the η and ϕ of the generated tracks to explore the location resolution of the tracker based on the technology used to detect hits and the arrangement of the modules. An example of the p_{T} resolution for single isolated pions as a function of η is shown in Fig. 3.4.

3.2.1.1 The prompt calibration loop

To ensure a higher quality of data, CMS uses a low-latency series of calibration workflows that run immediately after data is collected. This series of workflows is known as the Prompt Calibration Loop (PCL) and is illustrated in Fig. 3.5. As data are collected, the main physics dataset is stored on a disk buffer for up to 48 hours. At the same time, a subset of the physics data is siphoned off into "Express" and "Calibration" streams. These streams undergo reconstruction that takes on the order of two hours and are input into various calibration workflows that determine near real-time conditions of the detector. Workflows that are run during the PCL include: beamspot, silicon-strip bad-channel, silicon-strip gains, and silicon-pixel-large-structure alignment calibrations. Part of

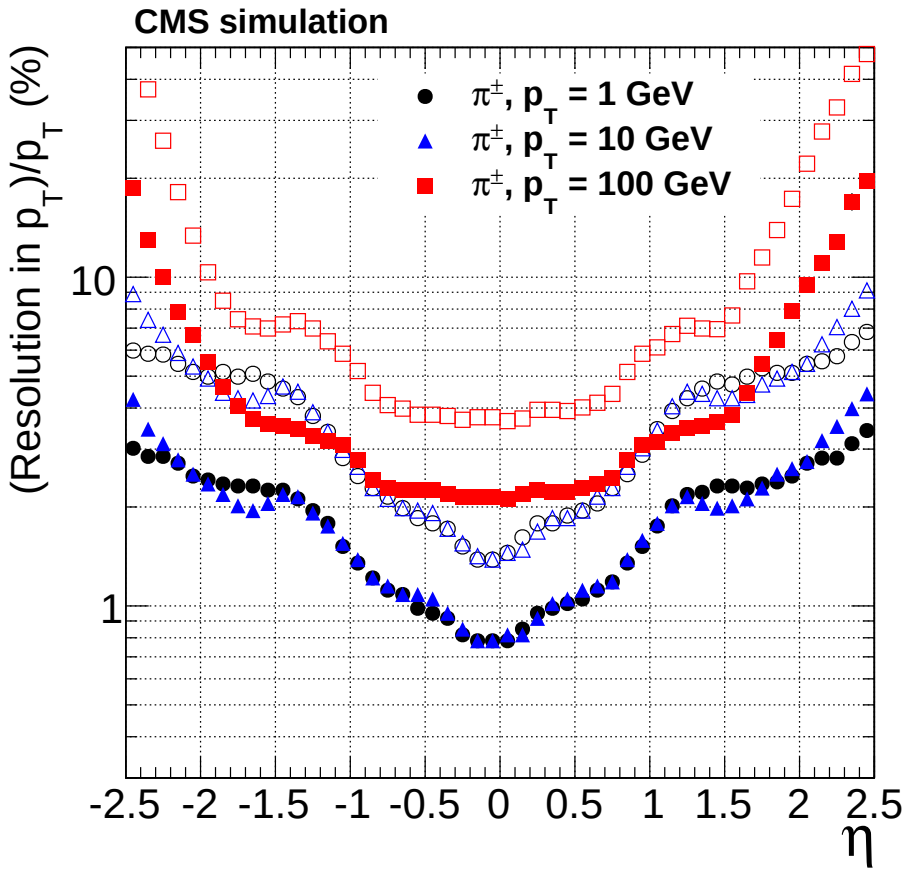

Figure 3.4: Resolution in p_T as a function of pseudorapidity for single isolated pions with p_T of 1, 10, and 100 GeV. For each bin in η, the closed (open) symbols represent the half-width for 68% (90%) confidence intervals, where points are centered at the mode of the distribution of residuals. Plot taken from Ref. [200].

the work of this thesis was to build the streams for beamspot and alignment calibration workflows in terms of the types of events and the statistics needed for a reliable calibration. The details of this work are discussed further in Secs. 3.2.1.2 and 3.2.1.3.

Upon completion of the calibration workflows, updated conditions are then stored in an offline conditions database to be accessed at a later time for analysis purposes. After 48 hours, the primary physics dataset is released to undergo "prompt reconstruction" that utilizes the most recent detector calibrations. This workflow allows for analyses to be run quickly over a well-calibrated dataset. In addition, special skims are created over the physics datasets, dropping a majority of the event content irrelevant to detector calibrations, and stored at CERN for more detailed "offline" calibrations.

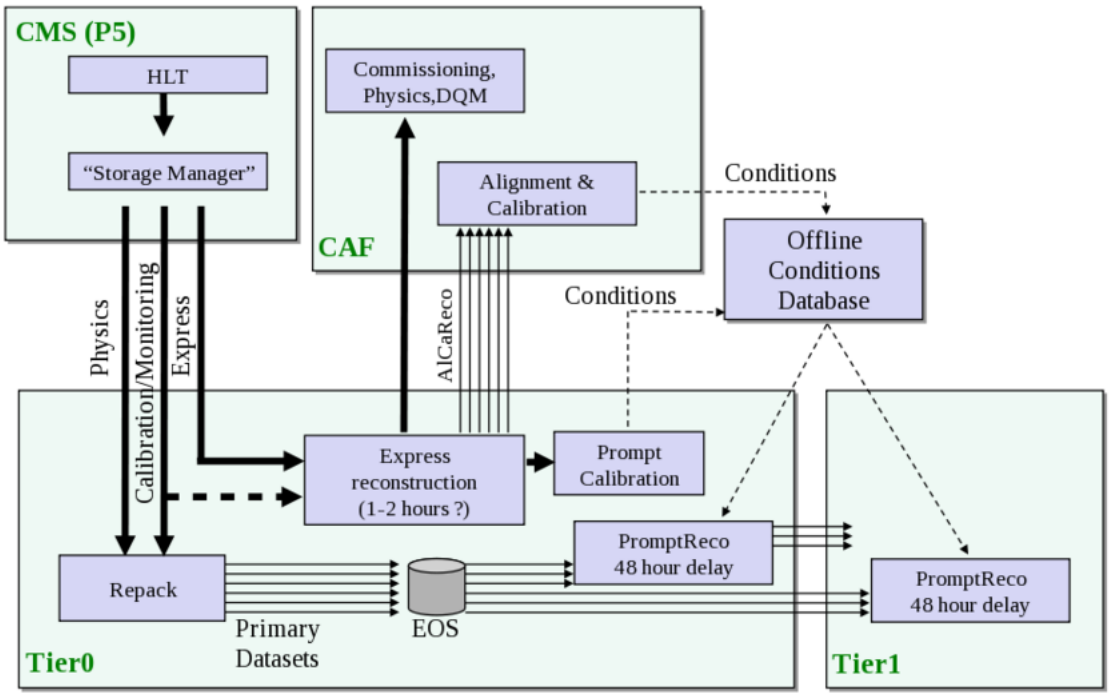

Figure 3.5: The prompt calibration loop: The main physics dataset is stored on a disk buffer for up to 48 hours. Subsets of the data undergo fast reconstruction and are input to calibration algorithms. The resulting conditions are stored in an offline conditions database to be used in the reconstruction of the physics dataset. Schematic taken from Ref. [202].

3.2.1.2 Beamspot calibration

The three-dimensional (3D) profile of the luminous region surrounding the interaction point in the CMS detector is referred to the beamspot. As an accelerator operates at higher luminosities, the probability of bunch crossings with multiple interactions (pileup events) becomes more significant. Within each pileup event, the positions of all interactions (pp, pA, or AA) are called primary vertices. The centroid of the beamspot gives reconstruction algorithms a starting point when deciding the location of all primary vertices in events as well as constrains their locations within the profile [200]. In addition, the beamspot greatly assists in finding the primary interaction point in low multiplicity events, where the vertex resolution increases.

The centroid of the CMS beamspot is determined in two ways. The first method considers the correlation between track transverse impact parameter relative to the origin d_0 and azimuthal angle ϕ when the beamspot is displaced from its nominal position. Track d_0 can be parametrized by [203]

$$d_0\left(\phi, z_p\right) = x_0 \sin\phi + \frac{dx}{dz} z_p \sin\phi - y_0 \cos\phi - \frac{dy}{dz} z_p \cos\phi, \tag{3.3}$$

where z_p is the longitudinal track position at minimum approach, x_0, y_0 are the positions of the beam at $z = 0$, and $\frac{dx}{dz}$ and $\frac{dy}{dz}$ are the beam slopes in x and y with respect to z. The beam position fitter is an iterative χ^2 minimizer where the χ^2 has the form [203]

$$\chi^2 = \sum_{i=1}^{N_{\text{Tracks}}} \left(\frac{d_{0i} - \left(x_0 \sin\phi_i + \frac{dx}{dz} z_{pi} \sin\phi_i - y_0 \cos\phi_i - \frac{dy}{dz} z_{pi} \cos\phi_i \right)}{\sigma_i} \right)^2. \tag{3.4}$$

Track contributions are weighted by their error σ_i and a statistical precision of 5 μm can be achieved using $\sim$ 1000 tracks [200]. The second method extracts the mean position in x, y, and z through a likelihood fit to the 3D distribution of vertex positions over events collected.

Simulations using the two methods show that they provide consistent results [203, 200]. The d_0-ϕ fit is more precise in low multiplicity events, but cannot return the parameters beyond the transverse positions of the beamspot and the slopes with respect to z. The likelihood fit is capable

of returning the parameters that the d_0-ϕ fit cannot. Therefore, both methods are used to measure the beamspot: the d_0-ϕ is used to measure the center of the beamspot in the transverse plane and the beam slopes with respect to z while the 3D likelihood fit is used to measure the longitudinal position of the beamspot and its RMS widths in all directions (σ_x, σ_y, and σ_z).

As part of this thesis, work was done to set up and ensure beamspot calibrations were made during heavy-ion operation at CMS. A dedicated heavy-ion contact was needed with the new implementation of the PCL. Given the different event topologies and LHC running conditions during heavy-ion operations, the default setup from proton-proton collisions could not simply be copied over for PbPb collisions. With the larger track multiplicities per event, the event rates siphoned into the express and calibration streams were chosen as not to flood express reconstruction while still providing enough data for a successful calibration. During data collection the PCL was closely monitored to ensure that the failure rate was minimized and that the fits were returning reasonable results. In addition, when data collection ceased, average beamspot parameters over all collected events were calculated and sent to the Monte-Carlo (MC) generation team so that event simulation could be tuned to match the same tracker occupancy as during data collection.

3.2.1.3 Tracker alignment calibration

The set of parameters that describe the geometric properties of the modules comprising the silicon tracker is referred to as the "tracker geometry." Precise knowledge of the tracker geometry is crucial for physics analyses as systematic misalignments limit the tracker performance. Distortions in the tracker geometry can be introduced by temperature fluctuations within the detector and by the ramping of the magnetic field during a power cycle of the detector. Large misalignments in the tracker geometry introduce significant systematic uncertainties for tracking-sensitive physics analyses. For example, b-tagging performance has been shown to deteriorate in the presence of a misaligned tracker [204, 205] and the tracking performance in charged particle nuclear modification factor studies [96] is sensitive to misalignment.

In setting up the tracker geometry, a local right handed coordinate system is defined for each

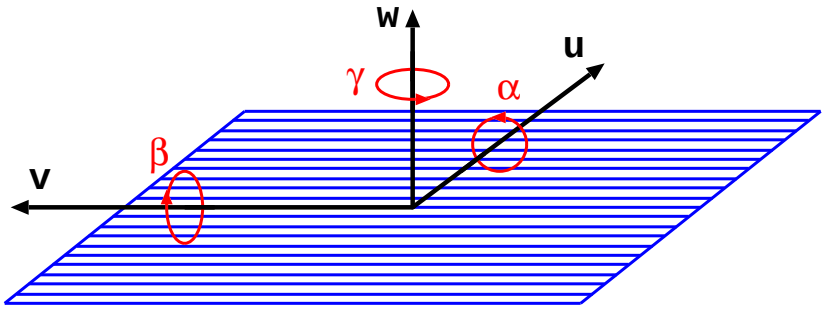

Figure 3.6: Example of the local coordinate system defined for each module considered in alignment of the tracker [206]. The u and v axes are defined in the plane of the module where u points along the more precisely measured axis of the module. The w axis is normal to the plane of the module. Three angles α, β, and γ denote rotation angles about the respective u, v, and w axes.

module within the tracker [206]. Three orthogonal basis vectors $(\vec{u},\vec{v},\vec{w})$ span the active area of each module. The vector $\vec{u}$ points along the more precisely measured direction in the module (*e.g.* the $r\phi$ direction in the BPIX). The vector $\vec{v}$ points away from the readout objects, orthogonal to $\vec{u}$ in the plane of the module. The vector $\vec{w}$ is normal to the plane of the module and its origin is located at the center of the module material. In addition, three angles α, β, and γ represent respective rotations about the u, v, and w axes. Two local track angles ψ and ζ are defined with respect to the normal of the module plane in the uw and vw planes respectively. A sketch of the local coordinate system can be found in Fig. 3.6.

To the first order, the set of orthogonal basis vectors and rotation angles describe the tracker geometry well. However, a deviation from planarity is expected in these modules and the specifications for the construction of these modules require that such deviations must be less than 100 μm [207]. To account for shape deformations in the modules, the sensor shape is parametrized as a sum of modified Legendre polynomials up to the second order [206]

$$\begin{aligned} w(u_r,v_r) =& w + w_{10}\cdot u_r + w_{01}\cdot v_r + \\ & w_{20}\cdot(u_r^2 - 1/3) + w_{11}\cdot(u_r\cdot v_r) + w_{02}\cdot(v_r^2 - 1/3). \end{aligned} \tag{3.5}$$

The parameters w_{11}, w_{20}, and w_{02} define the surface deformations of the sensors, which are illustrated in Fig. 3.7.

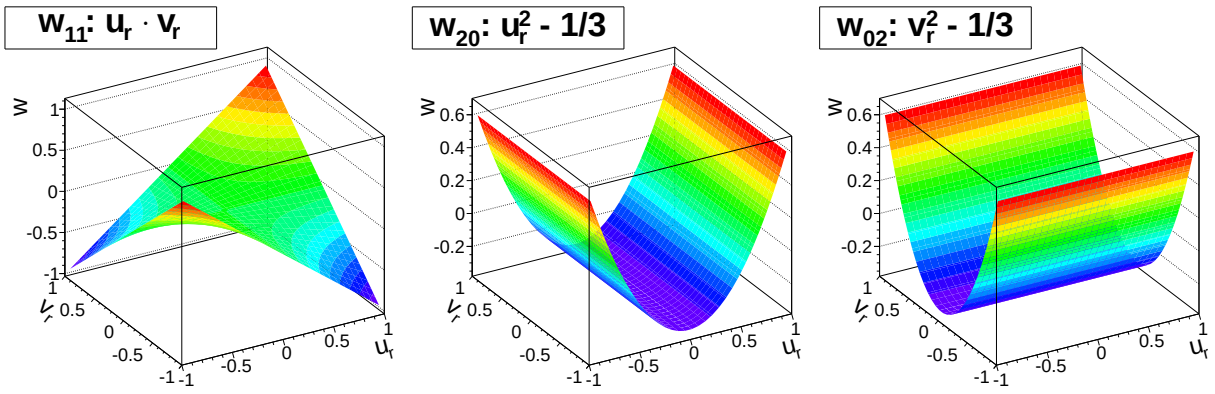

Figure 3.7: Example surface deformations of the sensors that show how deviations from planar modules are considered when aligning the tracker. Schematic taken from Ref. [206].

The standard approach in track-based alignment is to minimize the sum of the squares of the normalized track residuals over many tracks. A track residual is the difference between the measured trajectories of tracks and their predicted trajectories based on the current tracker geometry. If the assumed geometry is incorrect, then the distribution of track residuals over many tracks will broaden. The χ^2 function to be minimized is [206]

$$\chi^2(\mathbf{p},\mathbf{q}) = \sum_{j}^{N_{\text{Tracks}}} \sum_{i}^{N_{\text{Meas.}}} \left(\frac{m_{ij} - f_{ij}(\mathbf{p},\mathbf{q_j})}{\sigma_{ij}} \right)^2, \tag{3.6}$$

where m_{ij} corresponds to the measurements (the hit positions on the modules), σ_{ij} corresponds to the associated uncertainties on the measurements, and f_{ij} is the predicted track trajectory, which is a function of the tracker geometry $\mathbf{p}$ and the track parameters $\mathbf{q_j}$. The χ^2 function in Eq. (3.6) assumes that the measurements are independent. Often, alignment corrections can be assumed to be small and f_{ij} can be linearized. Following linearization, the χ^2 minimization reduces to a linear set of equations

$$\mathbf{Ca} = \mathbf{b}, \tag{3.7}$$

where $\mathbf{C}$ is the Hessian matrix of the linearized f_{ij}, $\mathbf{a}^T = (\Delta\mathbf{p}, \Delta\mathbf{q})$ is a vector that contains the change in alignment parameters and the corrections to all tracks used, and $\mathbf{b}$ is the gradient of the linearized f_{ij}. If the corrections are large, then the linearization precision is limited and the

procedure must be iterated. To approach solving Eq. (3.7) CMS utilizes a global-fit [208] using the program MILLEPEDE II [209].

Very often, the matrix $\mathbf{C}$ in Eq. (3.7) is ill-conditioned as a result of "weak modes," or linear combinations of track parameters that do not (or minimally) change the overall χ^2 in Eq. (3.6). Weak modes can be understood as coherent changes in the alignment parameters being compensated by changes in track parameters. For example, an overall translation in the tracker could be compensated by an overall shift for all track impact parameters. What makes the alignment problem more difficult is that even small contributions from weak modes can lead to large distortions in the resulting tracker geometry. Weak modes are controlled by including more information into the χ^2 calculation of Eq. (3.6). This is achieved by including tracks with different topologies into the global fit. Track topologies that control weak modes include muons from cosmic rays, straight tracks recorded during 0 T operation, and muons from resonance decays. Once a new set of alignment parameters have been returned from MILLEPEDE II, they must be validated to determine the impact on physics performance. There are three primary validation workflows that are used to assess the quality of alignment: primary vertex, distribution of median residual (DMR), and $Z \to \mu^+\mu^-$ validations.

In a primary vertex validation, primary vertices are refitted under the new alignment using all tracks except for a single "probe" track. After reconstruction the compatibility of the probe track is assessed in terms of the track's transverse and longitudinal impact parameters as a function of probe track η and ϕ. With a perfectly aligned detector, the averages of these parameters over many events and tracks are expected to be 0. In the presence of a misaligned detector, biases in these distributions will arise. An example primary vertex validation from 2011 proton-proton operations can be seen in Fig. 3.8.

In a DMR validation, tracks are refit under the new alignment and the distribution of median residuals from each measurement for each module is inspected. Only modules with more than 30 measurements are inspected in these validations. The median is less sensitive to non-alignment related biases [206], such as multiple scatterings, and is an ideal candidate to study the resolution

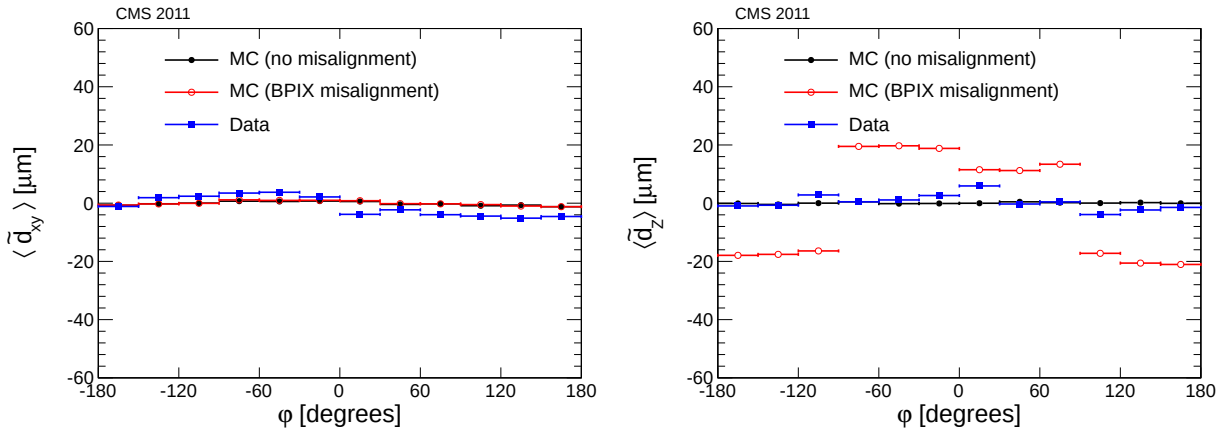

Figure 3.8: Example primary vertex validation from 2011 proton-proton operations [206]. Average longitudinal and transverse impact parameters for probe tracks are plotted as a function of their respective η and ϕ. In the ideal, aligned MC case, the averages are close to 0 for all kinematic variables. The effect of misalignment will be to bias the impact parameters away from 0.

of the newly obtained alignment. With a perfectly aligned detector, the DMR will be centered at 0 with a very narrow width. A width of 0 is unobtainable, as there is an intrinsic resolution to the alignment algorithm. The effect of a misaligned detector will be to broaden the DMR significantly. An example DMR validation from 2011 proton-proton operations can be seen in Fig. 3.9.

In a $Z \to \mu^+\mu^-$ validation, tracks are refitted using the newly obtained alignment and distributions of Z candidates are constructed in bins of muon η and ϕ. In each bin, the distributions are fit with a Voigtian function [210] and an exponential to model the resonant peak and background respectively. The mass of the Z candidates is extracted from the mean of the Voigtian function and plotted against the daughter muon η and ϕ. With a perfectly aligned detector, the mass of the Z boson will not depend on the location of the daughter muons, but misalignments in the tracker will bias these distributions. An example $Z \to \mu^+\mu^-$ validation from 2011 proton-proton operations can be seen in Fig. 3.10.

As part of this thesis, work was done to set up dedicated alignment workflows for heavy-ion operations both during PCL operation and later offline calibrations. A dedicated heavy-ion expert was needed to handle the event content difference in heavy-ion verses proton-proton collisions. Heavy-ion collisions generally produce many more particles than in proton-proton collisions and

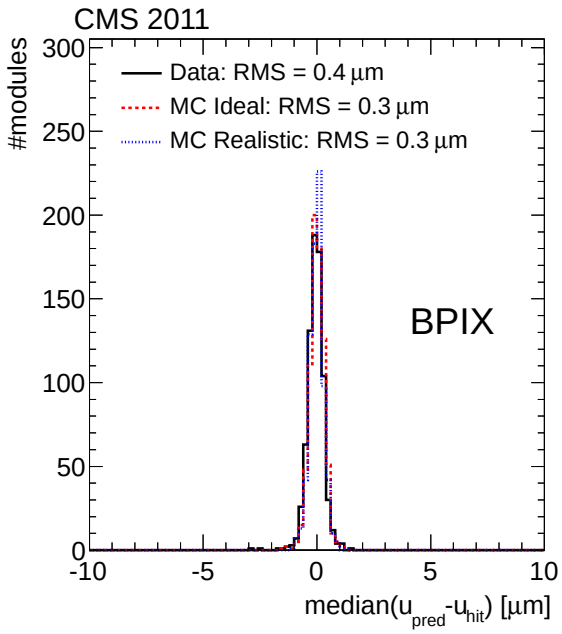

Figure 3.9: Example DMR validation for the barrel section of the pixel tracker from 2011 proton-proton operations [206]. In the ideal, aligned MC case, the distribution is centered at 0 with a width on the order of the resolution of the module. The effects from misalignment will broaden and/or shift this distribution about 0.

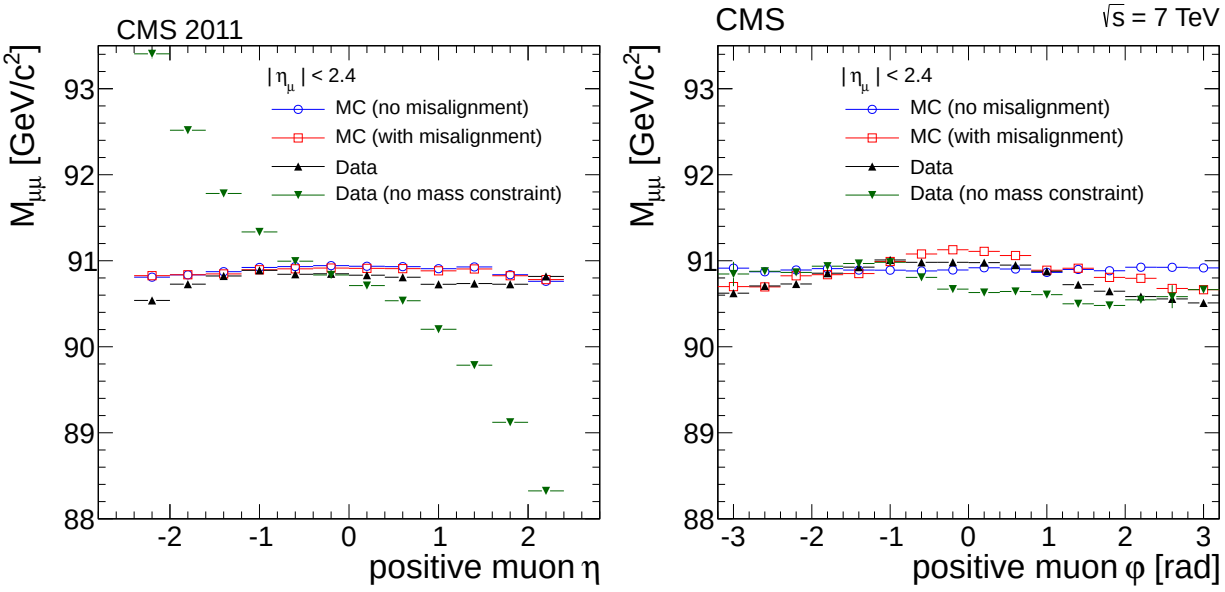

Figure 3.10: Example $Z \to \mu^+\mu^-$ validation from 2011 proton-proton operations [206]. The mass of the Z candidates is plotted as a function of the positive daughter muon's η and ϕ for different alignment scenarios. In the ideal, aligned MC case, there is no strong bias as a function the kinematic variables, however when misalignments are introduced, biases arise in the mass distributions.

not all of these tracks are useful in alignment efforts. Heavy-ion events are dominated by soft (low-momentum) tracks and suppressed resonance yields combined with low signal-to-noise ratios. General track selection had to be modified to suppress the soft tracks, which are more susceptible to non-alignment related effects, and to maximize the resonance yields. Dedicated filters for PbPb and pPb data collection were developed to this aim. In addition, work was done to assure that the massive influx of tracks did not overload alignment algorithms at PCL by tuning the rates in the express and calibration streams.

In 2015 alignment at PCL was not in place so the calibrations were performed in a semi-automated process to keep calibrations as close to real-time as possible. Work was done to assist in setting up the semi-automated processes that queried the storage manager for when data acquisition runs were finished and, if they passed a threshold in number of events, the data were then sent to a worker node to manually run an alignment. The contact for alignment was then notified by e-mail if large movements were seen in the tracker and a new alignment was needed to be uploaded in the conditions database. The CMS magnet experienced issues with the filtration of its cold box in 2015, requiring many cycles of the magnet. The semi-automated PCL alignment procedure allowed for a fast response time, but motivated full integration into PCL. In 2016 the PCL alignment became fully automated and was running successfully during the collection of pPb data later that year.

3.2.2 ECAL

The electromagnetic calorimeter consists of 61 200 lead tungstate ($PbWO_4$) crystals mounted in a central barrel region complimented by an endcap on both sides. There are 7324 crystals in each endcap region. To prevent the misidentification of two closely spaced photons from the decay of a neutral pion as a single high-energy photon, a preshower detector is placed in front of each of the endcap regions. A schematic view of the ECAL is shown in Fig. 3.11.

The barrel region of ECAL has a granularity of 360-fold in ϕ and (2×85)-fold in η, providing coverage for $|\eta| < 1.479$. The crystals in the barrel are mounted such that their axes make a small angle (3°) with respect to the vector pointing back to the nominal interaction point. This mounting

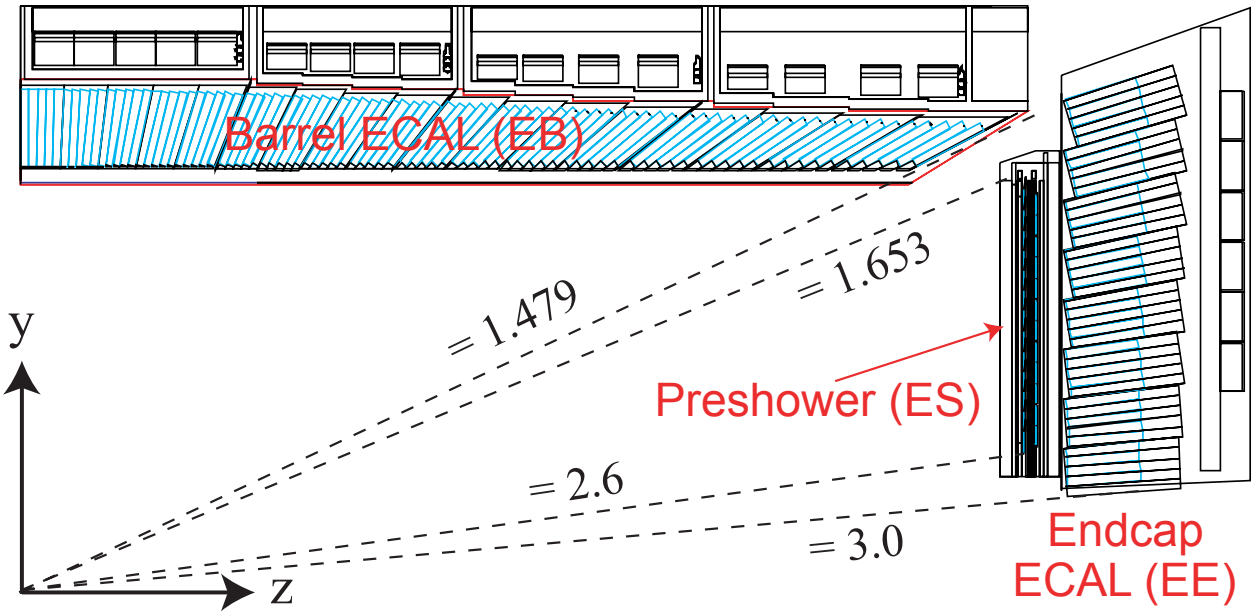

Figure 3.11: Schematic view of ECAL showing the location and coverage of the barrel, endcap, and preshower detectors. Schematic taken from Ref. [204].

is chosen to avoid cracks in the calorimeter that are aligned with incident particle trajectories. The size of each crystal is 22×22 mm^2 and 26×26 mm^2 for the front and rear faces respectively and a length of 230 mm [211]. Avalanche photodiodes (APDs) are used as photodetectors in this region.

The endcap regions of ECAL provide coverage for $1.479 < |\eta| < 3.0$ and are split into two halves called "Dees." Each Dee contains 3662 crystals that are grouped into units of 5×5 "supercrystals." The supercrystals are organized such that there are 138 standard supercrystals within the Dees and 18 partial supercrystals along the circumference of each Dee. To avoid cracks along a particle's trajectory, the supercrystals are oriented such that there is a small angle(2–8°) with respect to the vector pointing back to the nominal interaction point. The endcap crystals have a size of 28.62×28.62 mm^2 and 30×30 mm^2 in the front and rear faces respectively and a length of 220 mm [211]. The endcaps use vacuum phototriodes (VPTs) as photodetectors.

The energy resolution for ECAL can be parametrized by [204]

$$\left(\frac{\sigma}{E}\right)^2 = \left(\frac{S}{\sqrt{E}}\right)^2 + \left(\frac{N}{E}\right)^2 + C^2, \tag{3.8}$$

where S denotes a stochastic contribution, N denotes a noise contribution, and C denotes a scale contribution. The stochastic term has itself three primary sources: photostatistics in the APDs and VPTs, event-by-event fluctuations in the lateral shower containment, and energy resolution in the preshower detector. The noise term also has three primary sources: noise from electronics, noise from digitization, and noise from pileup events. Lastly, the scale term has three primary contributions as well: non-uniform light collection in the longitudinal direction, miscalibration, and energy leakage from the crystals. An example of the total ECAL energy resolution during test beam commissioning as a function of electron energy is shown in Fig. 3.12

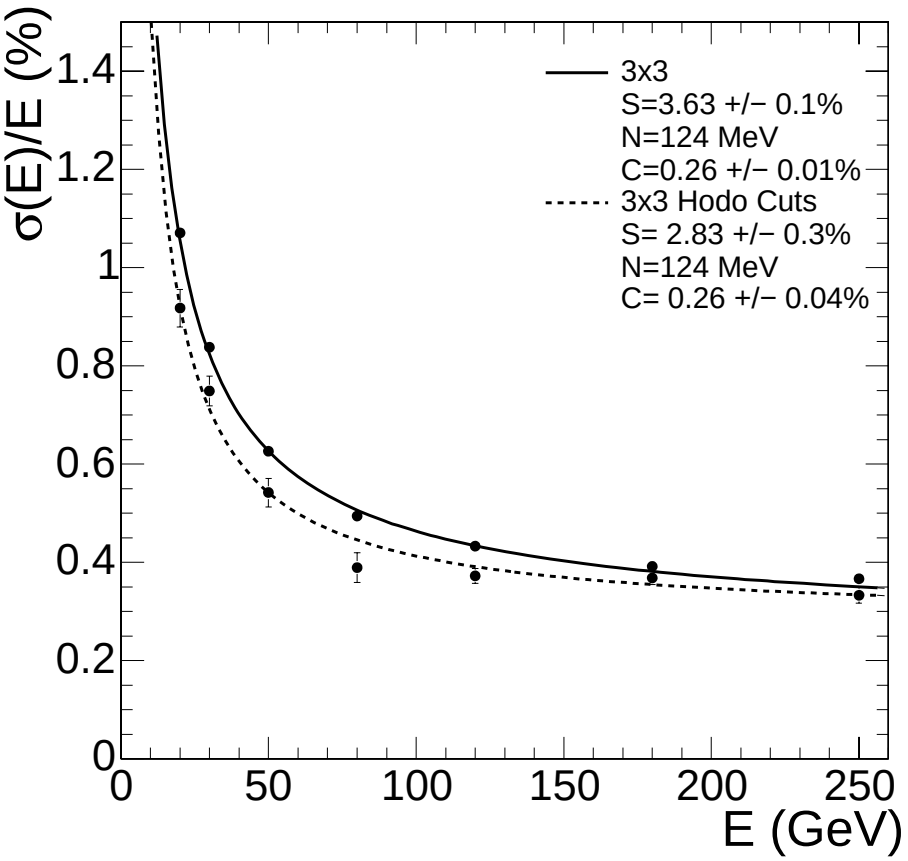

Figure 3.12: ECAL energy resolution as a function of electron energy recorded during a test beam commissioning [204]. The solid and dashed lines correspond to different event selection and electron reconstruction schemes.

3.2.3 HCAL

The Hadronic Calorimeter measures the position, energy, and arrival time of hadrons through the use of successive scintillator and absorber materials. Four subsystems comprise HCAL, which extend coverage both inside and outside of the magnetic field of the solenoid. Located within the magnetic field are the barrel (HB) and endcap (HE) subsystems, while the outer barrel (HO) and forward (HF) subsystems are located outside the solenoid within the return flux where the magnetic field is significantly smaller. A schematic view of HCAL and its subsystems is shown in Fig. 3.13.

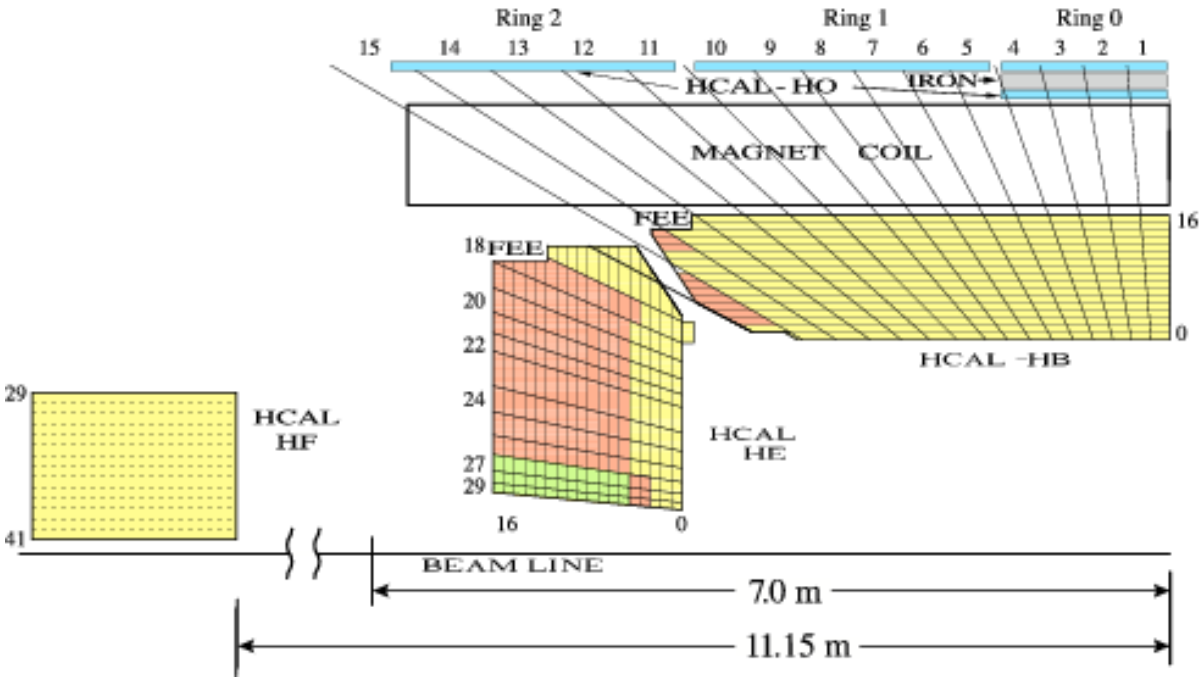

Figure 3.13: Schematic slice of HCAL and its subsystems in the *rz* plane. Colors represent different longitudinal ("depth") segmentations. Schematic taken from Ref. [199].

The HB subsystem provides a coverage in η of $|\eta| < 1.4$ and is split into two half barrel sections that span $1777.0 < r < 2876.5$ mm from the beam line. Each half barrel is split into 18 identical wedges of size 20° in ϕ. Within each wedge are brass alloy absorber plates and active plastic scintillator plates of size $\Delta\eta \times \Delta\phi = 0.087 \times 0.087$ rad. There are 17 layers of scintillator plates that are alternately stacked with absorber plates to form 16 projective "towers" in η of size $\Delta\eta \times \Delta\phi = 0.087 \times 0.087$ rad for each half barrel [211]. The net optical signal for each tower

is converted to an electrical signal by pixelated hybrid photodiodes mounted at the ends of the barrel section. The HE subsystem is interlocked with the HB and provides a coverage in η of $1.3 < |\eta| < 3.0$. Similar to the HB, the HE is split into 18 wedges in ϕ and the brass absorber plates have the same $\Delta\eta \times \Delta\phi = 0.087 \times 0.087$ rad size up to $|\eta| = 1.74$. There are 19 layers of active plastic scintillators in the HE and the size of the absorber plates (and thus the towers) is increased up to $\Delta\eta = 0.35$ when $|\eta| > 1.74$ [211].

The HO subsystem has a coverage in η of $|\eta| < 1.26$ and extends the radial reach of HCAL to $r = 4097.0$ mm. The HO consists of additional layers of scintillators beyond the solenoid coils and is divided into five rings longitudinally. Each ring has a length of 2.54 m in z. The central ring, located at $z = 0$, consists of two layers of active plastic scintillators, while the remaining rings contain only one. The $\Delta\eta \times \Delta\phi$ tower size in HO matches that of HB. The HF subsystem extends the reach of HCAL to $2.9 < |\eta| < 5.0$ and is located at $|z| = \pm 11.2$ m from the nominal interaction point. The HF is split into 18 identical wedges in ϕ, which do not project back to the interaction point. Each wedge consists of steel absorber plates and quartz fibers to measure Cherenkov light from incident particles [211].

The performance of HCAL can be assessed by inspecting the jet energy resolution for the various subsystems. Jet reconstruction assumes that particles from a jet are concentrated in a conical region characterized by a radius $R^2 = \Delta\eta^2 + \Delta\phi^2$. Given the finite granularity of the detector, jet cones reconstructed by HCAL will have a measured energy that fluctuates around the exact energy of the parton shower. Similar to Eq. (3.8), the jet energy resolution can be parametrized by [211]

$$\frac{\sigma\left(\frac{E_{\mathrm{T}}^{\mathrm{rec}}}{E_{\mathrm{T}}^{\mathrm{MC}}}\right)}{\left\langle\frac{E_{\mathrm{T}}^{\mathrm{rec}}}{E_{\mathrm{T}}^{\mathrm{MC}}}\right\rangle} = \frac{a}{E_{\mathrm{T}}^{\mathrm{MC}}} \oplus \frac{b}{\sqrt{E_{\mathrm{T}}^{\mathrm{MC}}}} \oplus c, \tag{3.9}$$

where a describes energy fluctuations in the cone of the jet, b describes the stochastic response of the calorimeter, and c describes residual non-uniformities and non-linearities in the detector response. The energy resolution can be obtained by simulating QCD dijet events using the

PYTHIA [106] event generator. Here, generator-level information is digitized and then reconstructed to introduce detector-level effects. Distributions of the ratio of E_{T} for reconstructed jets relative to generated jets are fitted using Eq. (3.9) to extract the resolution width. The result of this assessment is shown in Fig. 3.14 where the jet energy resolution for different η windows that span all subsystems of HCAL is plotted as a function of p_{T} of the generated jet.

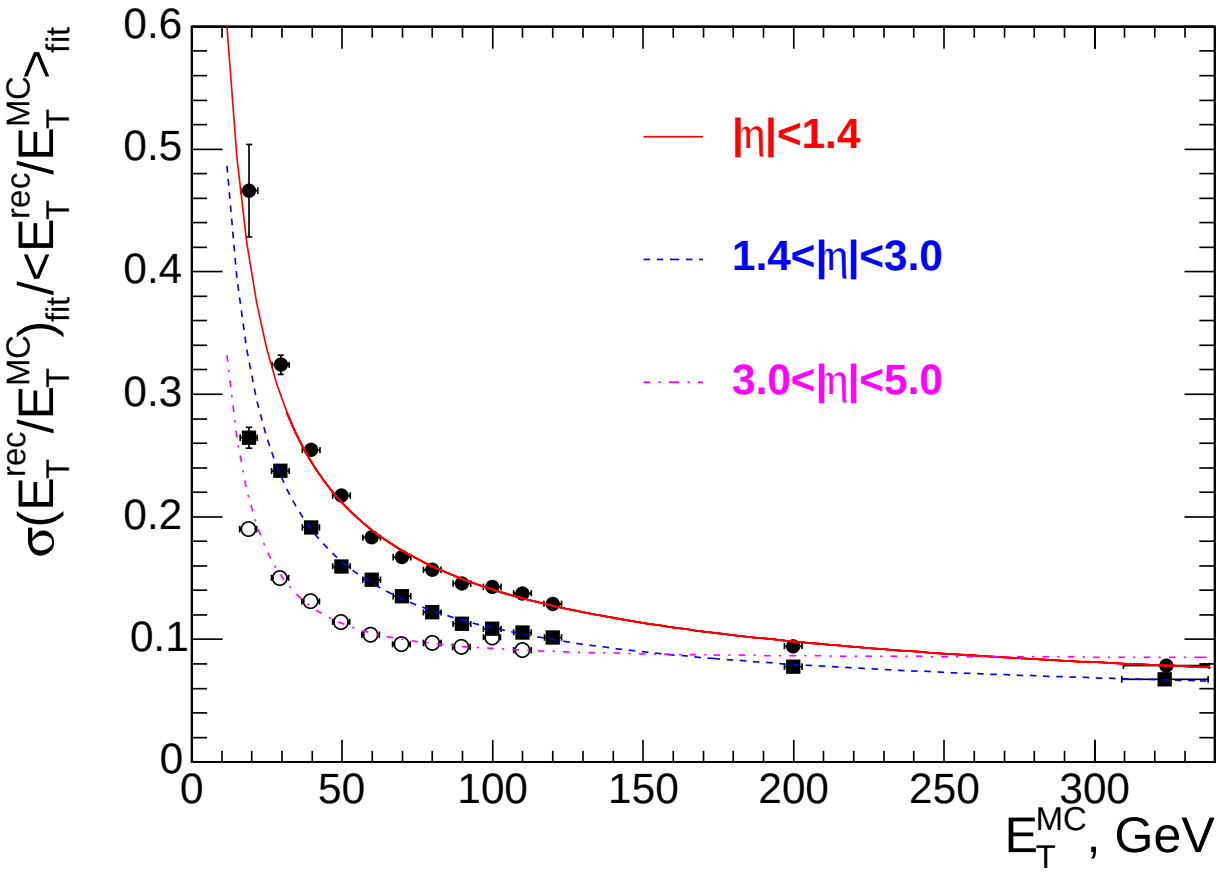

Figure 3.14: Jet energy resolution for different η windows that span all subsystems of HCAL. Jet energy resolutions are obtained through MC studies that compare reconstructed jet energies to generated jet energies [211].

3.2.4 Muons

The muon system is comprised of barrel (MB) and endcap (ME) subsystems embedded within the return yoke of the magnet. Muons are detected using three technologies: drift tubes (DTs), cathode strip chambers (CSCs), and resistive plate capacitors (RPCs). The MB and ME provide

full acceptance in ϕ and cover an η range of $|\eta| < 2.4$. A schematic view of the muon systems and the organization of the detector technologies is shown in Fig. 3.15.

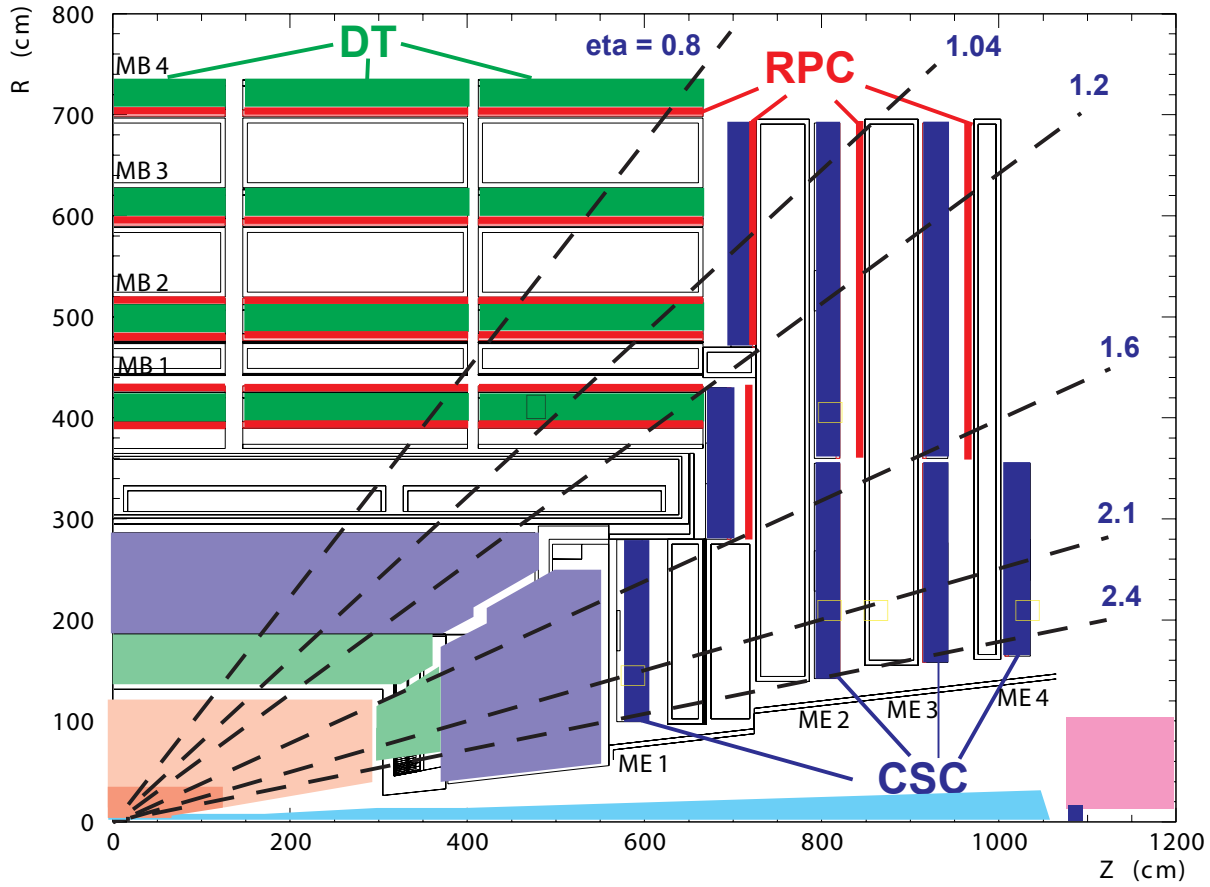

Figure 3.15: Schematic view of the muon subsystems. Schematic taken from Ref. [211].

The MB subsystem is organized into four cylindrical stations MB1–MB4, located at respective radii of 4.0, 4.9, 5.9, and 7.0 m from the beam line [211]. Each station is segmented into five wheels of longitudinal length 2.5 m, following the five wheels of the return yoke. Each wheel is split into 12 azimuthal sectors that cover 30° each and house rectangular detection chambers. The chamber boundaries for the different stations are staggered to prevent loss of acceptance for high p_{T} muons. In the MB region, the muon rate and fringe field from the magnet is low so DTs are used as the primary detection technology. For MB1–MB3, the 12 sectors form "superlayers" that consist of 12 DT planes. In order of increasing radius, the drift tubes are organized into four $r\phi$ measuring planes, four z measuring planes, and then four more $r\phi$ measuring planes [211]. The

superlayers in MB4 do not contain any z measuring planes. Each DT chamber also has at least one RPC coupled to it to improve timing resolution. In MB1 and MB2, DT chambers are sandwiched in r between two RPC chambers while MB3 and MB4 have one RPC coupled to their inner radius.

The ME subsystem is split into four disks (ME1–ME4), each consisting of 2–3 concentric rings. The innermost disk ME1 consists of three rings, while the remaining disks consist of only two. Within each ring are 36 muon detection chambers. The innermost rings of ME2–ME4 are an exception to this pattern, and contain only 18 chambers. Chambers are trapezoidal in shape and overlapped in ϕ to prevent holes in acceptance. The ME utilizes both CSC and RPC technologies to detect forward muons. The CSCs provide fast spatial measurements of muons while RPCs are used in tandem to resolve any ambiguities. Forward RPC chambers only cover up to $|\eta| < 1.6$, while CSC chambers provide coverage up to $|\eta| < 2.4$ [211]. In later stages of CMS, the RPC coverage will be extended up to $|\eta| < 2.1$.

Each of the detection technologies have distinct strengths in their performance. Drift tubes in the MB have a spatial resolution of $\approx$200 μm and a ϕ resolution of $\approx$1 mrad coupled to a timing resolution of 5 ns [211, 212]. The DTs are most sensitive to stray magnetic fields and are thus restricted to the MB region. Cathode strip chambers have a spatial resolution of $\approx$200 μm and a ϕ resolution of $\approx$10 mrad coupled to a timing resolution of 6 ns [211, 212]. With a similar performance as the DTs, CSCs are placed in the endcaps where the fringe magnetic field is stronger. The RPCs have a spatial resolution that is on the order of the size of the chamber which, on average, is $\approx$1 cm in both the MB and ME [213]. The RPCs make up for their spatial resolution with an excellent timing resolution of 3 ns [212]. Thus, RPCs are placed in both the MB and ME to aid in resolving any ambiguities in measurements from the other detection technologies.

Muons are measured using both the silicon tracker and the muon systems. A muon's p_{T} measured using solely the muon systems is determined from the bending angle of the muon once it exits the coils of the magnet. This, in itself, is a limited measurement, but is further complicated by multiple scattering effects in the steel before reaching the first muon chamber. At low p_{T} (< 200 GeV/c) the momentum resolution for muons is an order of magnitude larger for the

muons systems when compared to the muon momentum resolution in the tracker. At high p_T the momentum resolution of the tracker becomes increasingly limited, similar to the behavior for pions illustrated in Fig. 3.4. By combining hits in the silicon tracker with multiple hits in the muon chambers, the best momentum resolution for muons is achieved, as shown in Fig. 3.16.

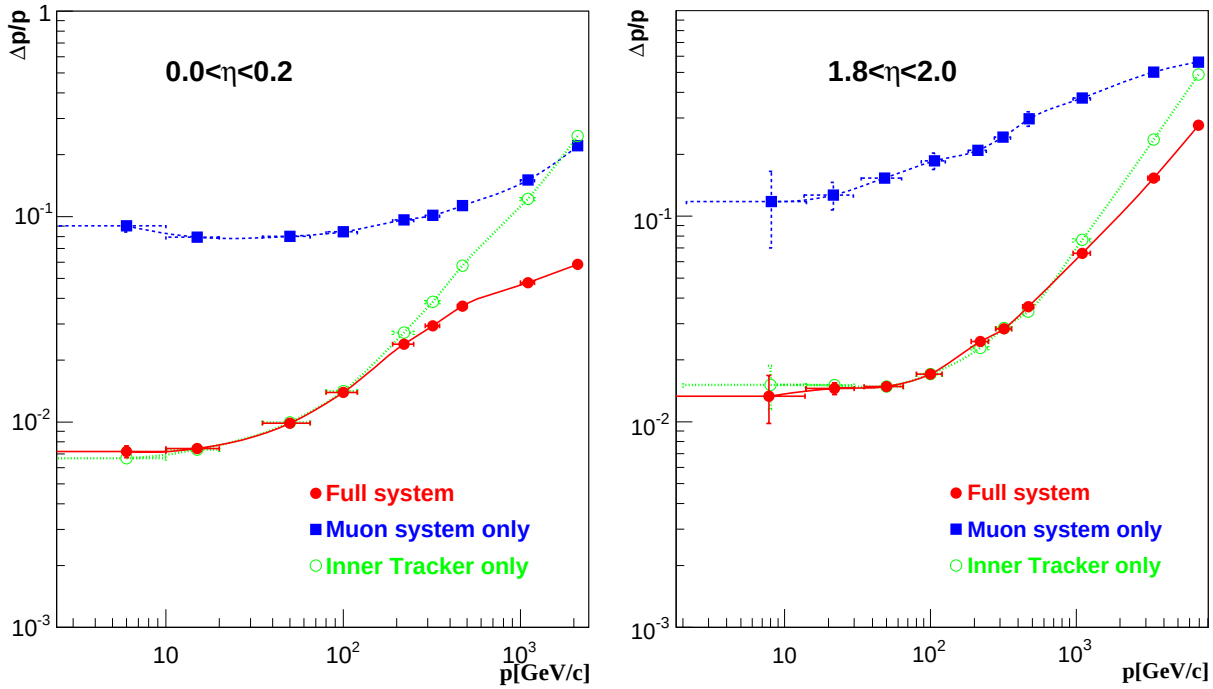

Figure 3.16: Momentum resolution for muons measured using the silicon tracker only, the muon systems only, and the combination of both systems. The left panel shows the resolution for centrally produced muons while the right panel shows the resolution for forward muons. Figure taken from Ref. [211].

3.2.5 CASTOR

In the forward region, beyond the acceptance of the central CMS detector, is the CASTOR calorimeter. In conjunction with other forward detectors, CASTOR is included in the CMS experiment to extend coverage into the very forward region where a majority of the energy flow from inelastic collisions is deposited. The CASTOR calorimeter is both an electromagnetic and hadronic calorimeter that measures Cherenkov light emitted as particles traverse the calorimeter. To initiate and capture these signals, CASTOR utilizes successive plates of tungsten (absorber) and quartz (ac-

tive medium) mounted at 45° with respect to the nominal particle trajectories [211]. A schematic of the CASTOR calorimeter is shown in Fig. 3.17.

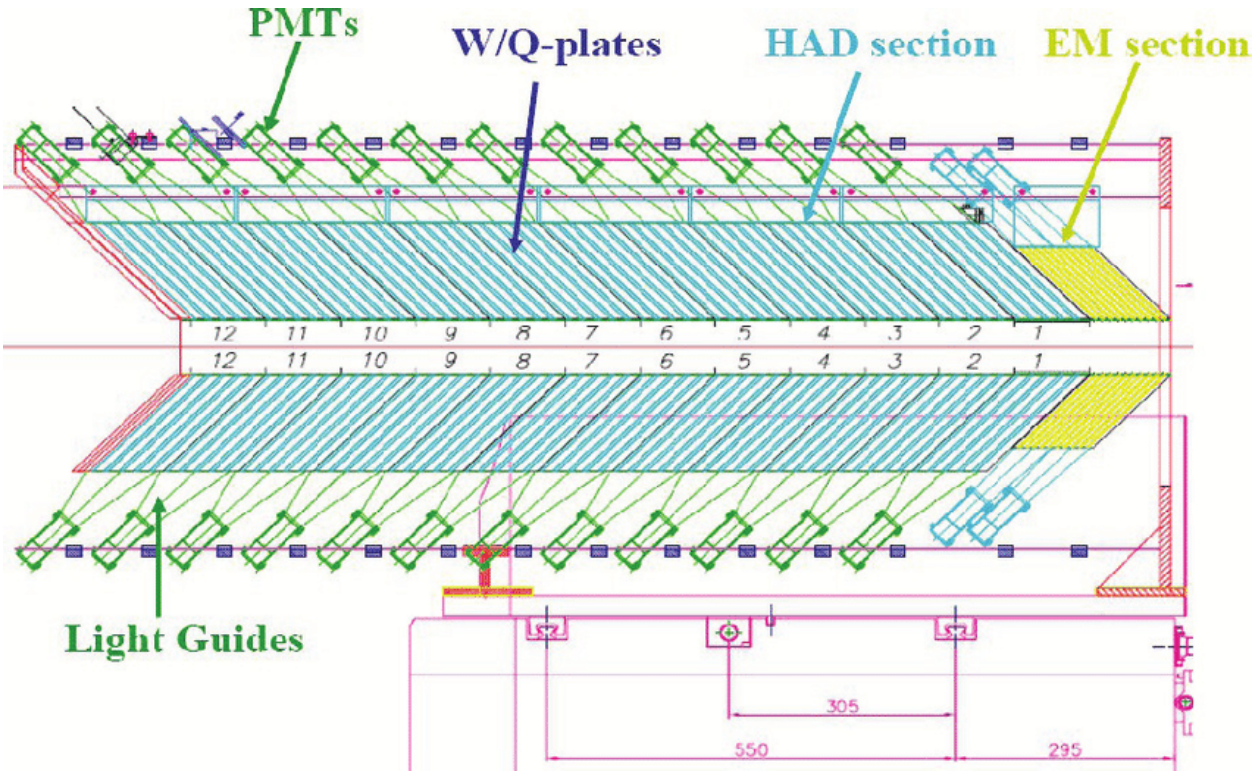

Figure 3.17: Schematic view of CASTOR. Schematic taken from Ref. [214].

The CASTOR calorimeter is located 1437 cm away from the nominal interaction point and provides an η coverage of $-6.6 < \eta < -5.2$. The calorimeter is longitudinally split into 12 slices called Reading Units (RUs), each divided into 16 azimuthal sectors of size $\phi = 22.5°$. Within CASTOR are an electromagnetic section and a hadronic section. The electromagnetic section provides a coverage of $-6.5 < \eta < -5.3$ and consists of two RU samplings of 2 mm quartz plates sandwiched between 5 mm tungsten plates. The hadronic section provides a coverage of $-6.4 < \eta < -5.15$ and consists of 10 RU samplings 4 mm quartz plates sandwiched between 10 mm tungsten plates. Cherenkov light is collected in the quartz plates and passed through internal reflection to PMTs at ends of each RU. There are two stages of CASTOR: Stage I consists of the electromagnetic and six hadronic RUs and is geared toward pp physics, while Stage II contains the remaining four hadronic RUs and is geared toward heavy-ion physics.

Before final design, the relative energy resolution of detection technologies for CASTOR were tested at SPS [211]. Here, electron beams of varying energy were used to examine the resolution when using quartz plates vs. quartz fibers, foil vs. glass reflectors in light guides, and PMTs vs. APD photodetectors. The results of various combinations are shown in Fig. 3.18. The resolutions were fitted using Eq. (3.8) both with and without the constant scale term. In each case both parametrizations describe the data well.

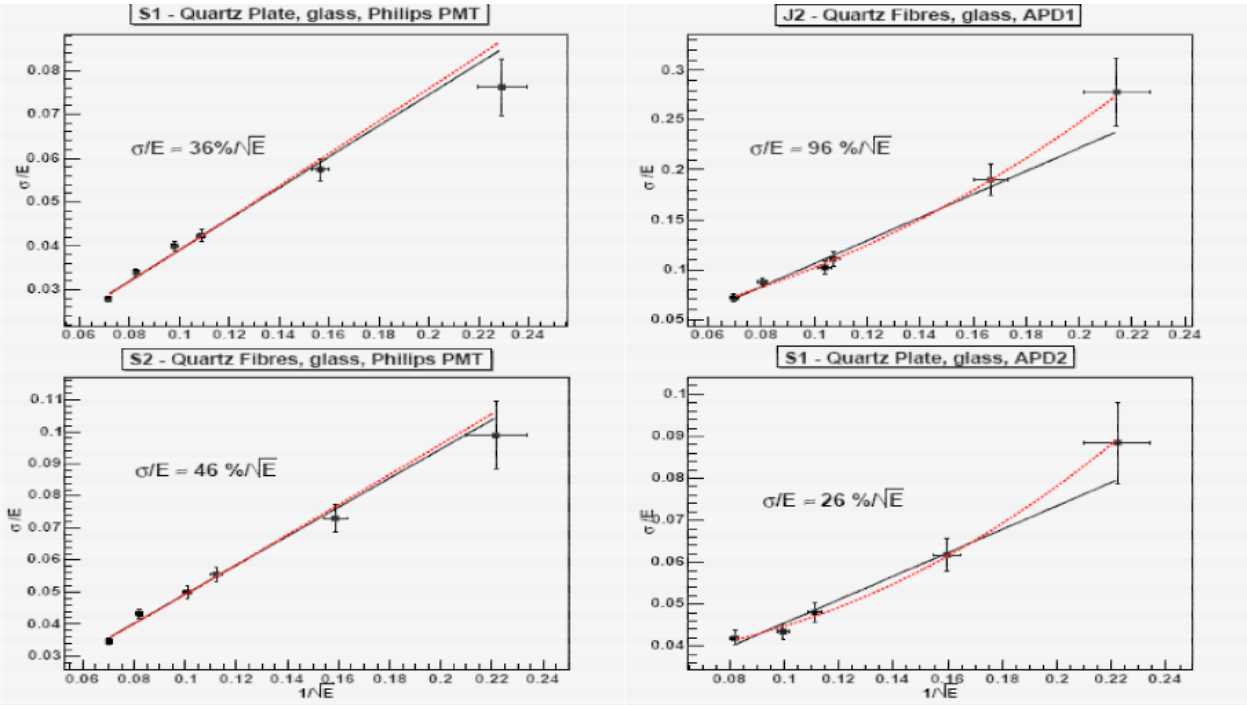

Figure 3.18: Energy resolution of CASTOR. Figure taken from Ref. [211].

3.2.6 ZDC

In the very forward region, ± 140 m from the nominal interaction point, sit Zero Degree Calorimeters (ZDCs). The ZDC is a sampling detector that measures Cherenkov light emitted by particles traversing its absorber/active medium and is designed to primarily detect forward photons and neutrons in heavy-ion and low-luminosity pp collisions. The ZDCs are managed by the nuclear research group at KU. Beyond the measurement of very-forward particles, signals in the ZDC are also used to discriminate collisions at the interaction point from background events arising from

beam-halo interactions. In addition, forward energy measurements with the ZDC combined with energy and multiplicity measurements at mid rapidity provide an additional method for determining event centrality in heavy-ion collisions. A schematic of the ZDC is provided in Fig. 3.19.

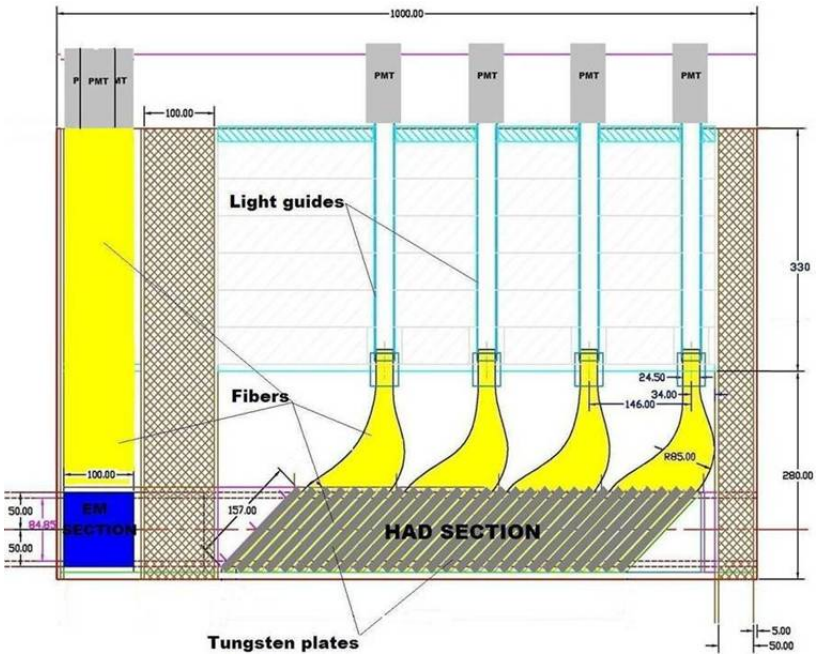

Figure 3.19: Schematic view of the ZDC with the beam direction moving from the left to the right. Schematic taken from Ref. [211].

The ZDCs are each housed inside neutral particle absorber units that protect the LHC dipole magnets. Each calorimeter is comprised of an electromagnetic and a hadronic section that provide an η coverage of $8.5 < \eta < \infty$. The electromagnetic section consists of 33 alternating layers of 2 mm thick tungsten plates and 0.7 mm diameter quartz fibers oriented 90° with respect to the beam direction [215]. The quartz fibers are segmented into five readout towers that couple to respective PMTs to amplify the signal. The hadronic section consists of 24 alternating layers of 15.5 mm thick tungsten plates oriented 45° from the beam direction [215] as illustrated in Fig. 3.19, The quartz fibers are segmented into four readout towers that couple to respective PMTs.

In the ZDC's early phases, test measurements were carried out in the SPS H2 beam at CERN. Here, a 400 GeV proton beam was steered onto a primary target to produce a secondary beam with energies ranging from 10–350 GeV. To test the energy resolution of the electromagnetic sec-

tion, positron beams for seven different energies between 10–150 GeV were used. The resolution widths were obtained from Gaussian fits and parametrized using Eq. (3.8) without the stochastic term [216]. The resulting ZDC energy resolution for positrons is shown in the left panel of Fig. 3.20. To test the energy resolution of the combined electromagnetic and hadronic sections, four beams of positive pions with energies between 150–350 GeV were used. The energy resolution widths were obtained from Landau fits and parametrized using Eq. (3.8) without the noise term [216]. The resulting combined energy resolutions are shown in the right panel of Fig. 3.20. One conclusion drawn from these tests was that GEANT4 simulations of the ZDC response are in good agreement with test measurements [216].

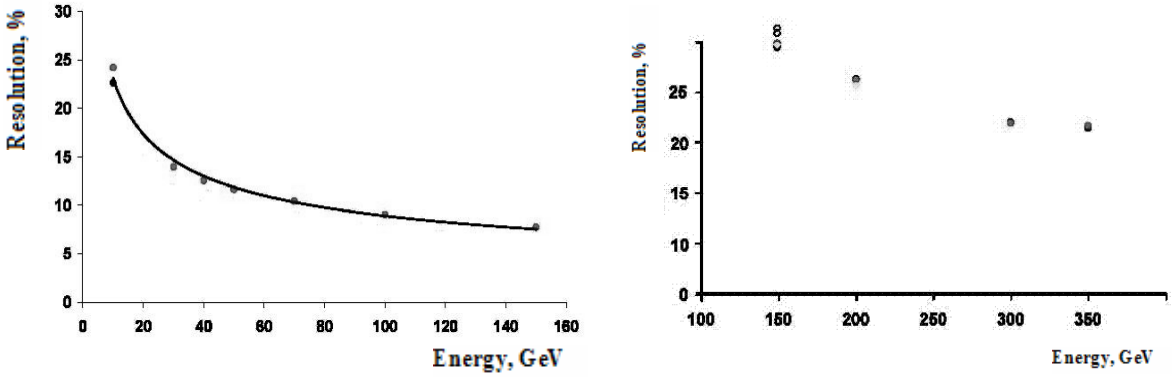

Figure 3.20: (Left) Positron energy resolution for the electromagnetic section of the ZDC. The energy resolution is parametrized with Eq. (3.8) without the stochastic term. (Right) Positive pion energy resolution for the combined electromagnetic and hadronic sections of the ZDC. The combined energy resolution is parametrized with Eq. (3.8) without the noise term. Figures taken from Ref. [216].

3.2.7 Detector scope

The analysis on which this thesis is based uses only two of the detector subsystems in CMS: the HF calorimeters and the silicon tracker. The HF calorimeters are used (in conjunction with LHC beam pickup monitors) to trigger minimum-bias events during data collection and to measure the total inelastic cross section for centrality calibrations. The role of the HF calorimeters in data collection

and calibration is discussed further in Chapter 4. In addition, the HF calorimeters are used to estimate the ellipticity of an event in the event-shape engineering technique, which is described in Sec. 5.3. The silicon tracker is used to measure the trajectories of charged particles emitted in a collision, the azimuthal angles of which are crucial for this analysis. Further discussion of charged-particle tracks is provided in Chapter 4.

While the other detector subsystems are not used in the current analysis, each could be used in future extensions. To begin, all calorimeter subsystems can be used in the event-shape engineering technique to estimate event ellipticity. The CASTOR and ZDC calorimeters are best suited for this purpose because they are located several units of pseudorapidity from the silicon tracker. This separation suppresses contamination from non-flow related phenomenon when correlating flow measured by the silicon tracker to event ellipticity. The ECAL and HCAL subsystems are best suited to extend this analysis to measure the flow of identified particle species. The Particle Flow Algorithm [217, 218] is used in CMS to identify the species of a particle based on the momentum measured by the silicon tracker and the energy deposited in either the ECAL or the HCAL subsystems. Lastly, the muon systems can be used to measure the flow of quarkonia states [140] through their leptonic decay channel (e.g., $\mathrm{J}/\psi \to \mu^+\mu^-$) by measuring and identifying the daughter muons from the parent quarkonia state.

Chapter 4

Data and event selection

4.1 Event selection

The minimum-bias trigger used in this analysis is triggered by coincident signals from both ends of the CMS detector using the HF detectors. In addition, the trigger is required to be in coincidence with the presence of both colliding bunches at the interaction point, as measured by the CMS beam pick-up timing system. This requirement largely suppresses events due to noise (*e.g* cosmic rays, double-firing triggers, and beam backgrounds). The minimum bias trigger is fully efficient for the centrality range 0-90%.

Events are further selected offline by requiring at least three hits in both HF calorimeters with at least 3 GeV of energy in each cluster to reject electromagnetic interactions. Events are also required to have a reconstructed primary vertex, containing at least two tracks, located within 15 cm of the nominal collision point along the beam axis. In addition, vertices are filtered on their pixel cluster compatibility. This is achieved by scanning the z axis around the reconstructed vertex and determining how many pixel clusters are compatible with a vertex at that position. A quality score is determined by the number of compatible pixel clusters such that a score of 0 indicates a poorly reconstructed vertex and increasing values indicate a higher quality of reconstructed vertex. This filter removes the bottom 1% of vertices with poor compatibility and suppresses contamination from pileup events.

4.2 Track selection

Tracks are divided into two types, each with their own selection: pixel and general tracks. Pixel tracks allow for reliable p_{T} measurements down to ≈0.3 GeV/c, which is important for flow studies in heavy-ion collisions. Tracks that have $p_{\mathrm{T}} < 2.4$ GeV/c and have between three and six hits in the pixel tracker are tagged as pixel tracks. All remaining tracks are considered general tracks. A high-purity reconstruction algorithm [219] is used for all track types to reduce the fraction of mis-reconstructed tracks. All pixel track quality cuts described above are summarized in table 4.1.

Table 4.1: Pixel track quality cuts

Offline Track Cut	Value
$p_{\mathrm{T}} < 2.4$ GeV/c and $N_{Hits} = 3-6$	True
High purity	True
$\left\lvert d_z/\sigma_{d_z}\right\rvert$	< 8
$\chi^2/dof/N_{\mathrm{Layers}}$	< 12

General tracks are required to be compatible with the primary vertex, having a longitudinal association significance (d_z/σ_{d_z}) and impact parameter significance (d_0/σ_{d_0}) less than three. In addition, the relative error for the p_{T} of each track, $\sigma_{p_{\mathrm{T}}}/p_{\mathrm{T}}$, is required to be less than 10% and tracks are required to have at least 11 hits along their trajectory in the pixel and strip trackers. To reduce the number of misidentified tracks, the χ^2 associated with fitting the track trajectory through the different pixel and strip layers divided by the total number of degrees of freedom must be less that 0.15 times the total number of layers with hits along the trajectory of the track. All general track quality cuts described above are summarized in table 4.2.

4.3 Centrality calibration

To estimate the total inelastic cross section for PbPb collisions collected in 2015, the same minimum bias trigger and event selection criteria in Sec. 4.1 were used. Events are divided into bins of fractions of the total inelastic cross section according to the transverse energy measured by the HF calorimeters. Figure 4.1 shows the distribution of E_{T} values measured by the HF calorimeters for

Table 4.2: General track quality cuts

Offline Track Cut	Value
High purity	True
$\left\|d_z/\sigma_{d_z}\right\|$	< 3.0
$\left\|d_0/\sigma_{d_0}\right\|$	< 3.0
$\sigma_{p_{\mathrm{T}}}/p_{\mathrm{T}}$	< 0.10
N_{Hits}	> 11
$\chi^2/dof/N_{\mathrm{Layers}}$	< 0.15
$p_{\mathrm{T}} > 2.4$ GeV/c and algoBit = 4 – 7	True

a large sample of minimum bias PbPb events collected in 2015. The distribution of E_{T} values is divided into 200 bins of equal area, each corresponding to 0.5% of the total inelastic cross section. Even after event selection, minimum bias events still contain residual biases that are not related to hadronic interactions. The two most prominent sources of uncertainty on the cross section measurement are event selection efficiency and electromagnetic interaction (e.g., UPC) contamination. The total systematic uncertainty from these sources is estimated to be 1%. This results in the bins corresponding to the most peripheral events (99–100%) being empty (HF measures $E_{\mathrm{T}} = 0$).

4.4 Tracking performance

Tracking performance is evaluated in terms of tracking efficiency, "fake" (mis-reconstructed) reconstruction rates, and multiple reconstruction rates in different bins of centrality, p_{T}, and η. To determine the tracking performance, a large sample of PYTHIA + HYDJET events were generated and propagated through GEANT4 to simulate detector effects. A brief description of how each term is determined is as follows:

- Tracking efficiency: fraction of simulated charged particles that can be associated ("matched") with a reconstructed track.
- Fake track rate: the fraction of the reconstructed tracks that do not have an associated simulated charged particle partner.

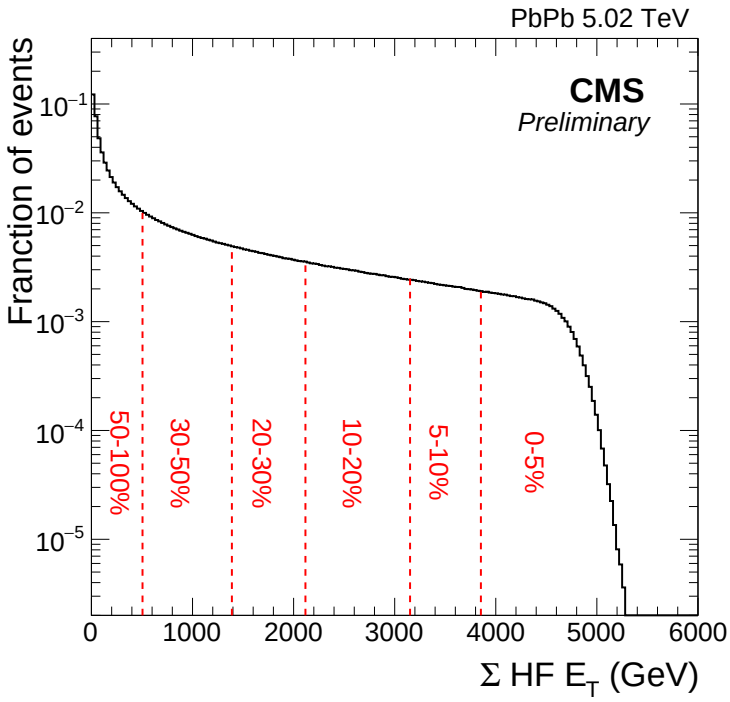

Figure 4.1: The distribution of E_{T} measured by the HF calorimeters for a large sample of minimum bias events PbPb events collected in 2015. Vertical lines denote bin boundaries of fractions of the total inelastic cross section.

- Multiple reconstruction rate: the fraction of the simulated primary charged particles that are associated with more than one reconstructed track.

Primary track reconstruction has a combined geometric acceptance and efficiency exceeding 60% for $p_{\mathrm{T}} \approx 1.0$ GeV/c and $|\eta| < 1.0$. When track p_{T} is below 1 GeV/c, the acceptance and efficiency steadily drops, reaching approximately 40% at $p_{\mathrm{T}} \approx 0.3$ GeV/c. The efficiency is not strongly dependent on centrality and the rate of misidentified tracks is smaller than 8% for the most central events. A summary of the tracking performance for the track selection discussed in Sec. 4.2 is shown in Fig. 4.2.

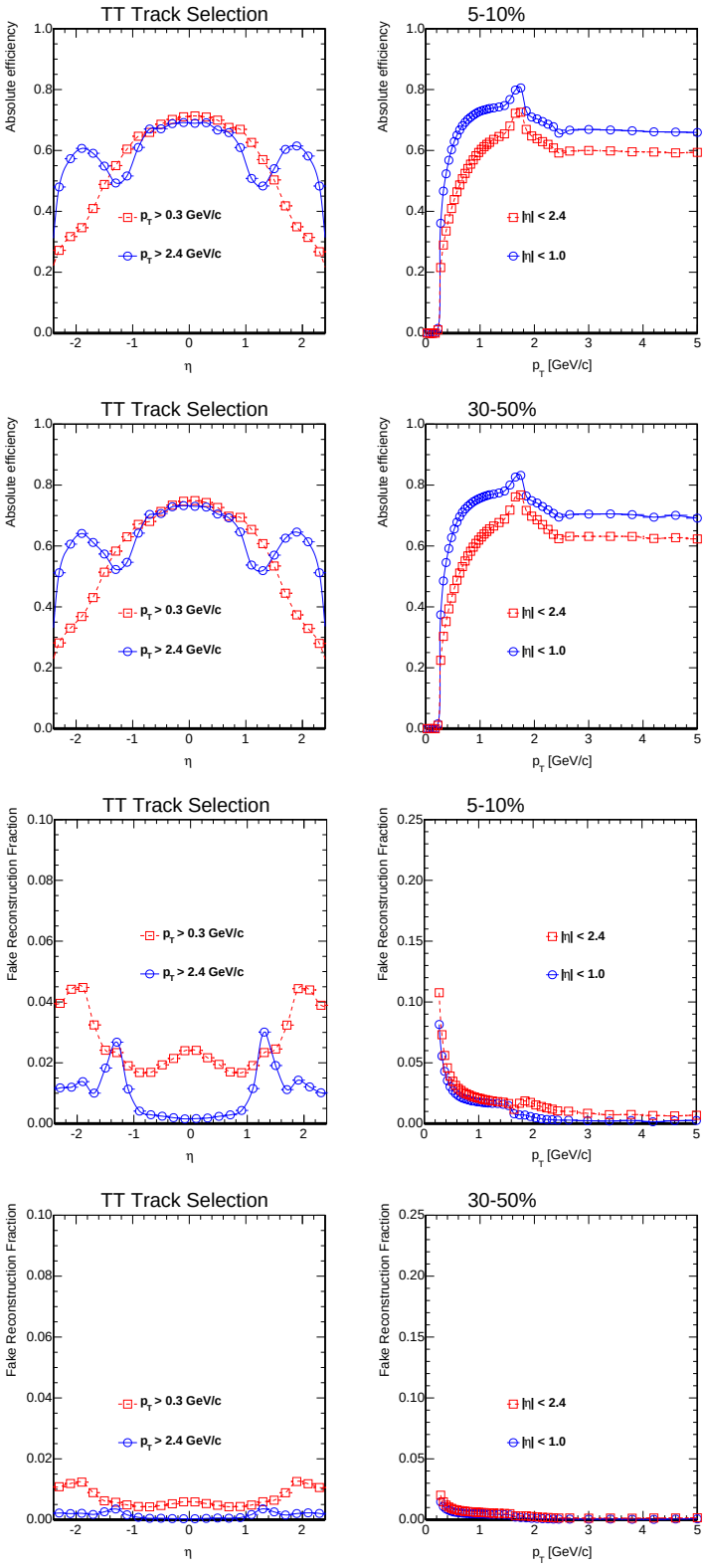

Figure 4.2: Tracking efficiency and fake reconstruction rates in different centrality, p_{T} and η ranges are presented. Track selections are discussed in Sec. 4.2 with track p_{T} greater than 0.3 GeV and η range between -2.4 and 2.4.

Chapter 5

Analysis

5.1 Event-by-event flow observables

Since only a finite number of particles are emitted in a given collision, the v_n coefficients in Eq. (1.4) can only be estimated on an event-by-event basis. Based on experiment, it is possible to calculate

$$\begin{aligned} v_{n,x}^{\text{raw}} &= \left|\vec{v}_n^{\text{raw}}\right| \cos n\Psi_n^{\text{raw}} = \langle \cos n\phi \rangle, \\ v_{n,y}^{\text{raw}} &= \left|\vec{v}_n^{\text{raw}}\right| \sin n\Psi_n^{\text{raw}} = \langle \sin n\phi \rangle, \\ \left|\vec{v}_n^{\text{raw}}\right| &= \sqrt{(v_{n,x}^{\text{raw}})^2 + (v_{n,y}^{\text{raw}})^2}, \end{aligned} \tag{5.1}$$

where $\langle \ldots \rangle$ denotes an average over all particles in a given range of phase space and Ψ_n^{raw} is the n^{th} order event plane angle defined as

$$\Psi_n^{\text{raw}} = \frac{1}{n} \tan^{-1} \left[\frac{\sum_i \sin n\phi_i}{\sum_i \cos n\phi_i} \right], \tag{5.2}$$

where sums run over the number of particles. On average, the event plane angle points in the same direction as the n^{th}-order symmetry plane, but the finite number of particles used cause it to fluctuate on an event-by-event basis. In the limit of large particle multiplicities, and in the absence of non-flow effects, the event-estimated flow values approach the true underlying flow values for each event. The estimate v_n^{raw} values are collected over all events and used to construct $p(v_n^{\text{obs}})$

counting distributions.

Before counting the event v_n^{raw} value, potential biases from non-uniform detector acceptance must be removed. To recover first-order effects that arise with non-uniform detector acceptances, tracks are weighted by their inverse tracking efficiencies. In doing so, Eq. (5.1) becomes

$$\begin{aligned} v_{n,x}^{\text{raw}} &= \frac{\sum_i w_i \cos n\phi_i}{\sum_i w_i}, \\ v_{n,y}^{\text{raw}} &= \frac{\sum_i w_i \sin n\phi_i}{\sum_i w_i} \end{aligned} \tag{5.3}$$

where $w_i = 1/\varepsilon_i(p_{\text{T}}, \eta)$ are the absolute tracking efficiencies discussed in Sec. 4.4. In addition to track reweighting, a standard recentering procedure [49] is applied to each centrality class to suppress further non-uniform detector biases. Since the orientation of the impact parameter is random on an event-by-event basis, the overall distribution of flow vectors should be isotropic and centered at 0. In the recentering technique, an average flow vector $\vec{v}_n^{\text{det}}$ is calculated over all events and then subtracted from the raw flow vector (Eq. (5.3)) on an event-by-event basis:

$$\begin{aligned} \vec{v}_n^{\text{det}} &= \frac{\sum_i^{N_{\text{Events}}} \vec{v}_{n,i}^{\text{raw}}}{N_{\text{Events}}}, \\ \vec{v}_n^{\text{obs}} &= \vec{v}_n^{\text{raw}} - \vec{v}_n^{\text{det}}. \end{aligned} \tag{5.4}$$

Holes in acceptance and detector inefficiencies will lead to a preferred direction ($\vec{v}_n^{\text{det}}$) for the flow vectors that is not related to the underlying flow physics. The recentering procedure largely corrects for this effect.

Finite particle multiplicities result in a statistical smearing of the measured $\vec{v}_n^{\text{obs}}$ vector about the true $\vec{v}_n$ vector associated with the event on an event-by-event basis. This, in turn, results in a $p\left(\vec{v}_n^{\text{obs}}\right)$ distribution that is statistically smeared about the true underlying $p(\vec{v}_n)$ behavior. It is of interest to remove the smearing effects from the observed distributions to allow for detailed studies of event-by-event fluctuations in the v_n coefficients. There are several approaches to remove smearing effects from event-by-event flow observables. Traditionally, smearing effects are removed using the event-averaged techniques described in Chapter 2. The technique used in this

analysis is to unfold these smearing effects, details of which are discussed in Sec. 5.2.

5.2 Unfolding the observed $p(v_n)$ distribution

The finite number of particles emitted per event places a limit on how well flow harmonics can be reconstructed on an event-by-event basis. As a consequence, the observed flow vectors are statistically smeared about the true underlying event flow vectors by a response function $p\left(\vec{v}_n^{\,\mathrm{obs}}|\vec{v}_n\right)$. The response function is a measure of the probability that, for a given event, one observes a $\vec{v}_n^{\,\mathrm{obs}}$ vector while the underlying $\vec{v}_n$ vector is of a different direction and/or magnitude. Therefore, the distribution of observed flow vectors can be expressed as a convolution of the underlying flow behavior and the response function

$$p\left(\vec{v}_n^{\,\mathrm{obs}}\right) = p\left(\vec{v}_n^{\,\mathrm{obs}}|\vec{v}_n\right) * p\left(\vec{v}_n\right). \tag{5.5}$$

The amount of smearing is driven by the number of particles used to determine the measured $\vec{v}_n^{\,\mathrm{obs}}$ vector. The effect of smearing is illustrated in Fig. 5.1 where $p\left(\left|\vec{v}_2^{\,\mathrm{obs}}\right|\right)$ is plotted for varying event multiplicities. It can be seen that the smearing effects tend to broaden the observed distribution and shift its mean to larger values. The smearing effect becomes more prominent as particle multiplicities approach 0. Using the event/track selection outlined in Chapter 4, particle multiplicities range between 100 and 2500 in this analysis.

In order to extract the distribution of underlying flow vectors, the smearing effects must be removed from the observed flow vector distribution. One technique of deconvolution, also known as unfolding, is to construct the response function using either a data-driven or a model-dependent approach, invert this function, and then apply it to the observed distribution. In data, it is typical to work with flow vector magnitudes and binned data, so the convolution can be rewritten as

$$p\left(v_{n,i}^{\mathrm{obs}}\right) = p\left(v_{n,i}^{\mathrm{obs}}|v_{n,j}\right) * p\left(v_{n,j}\right), \tag{5.6}$$

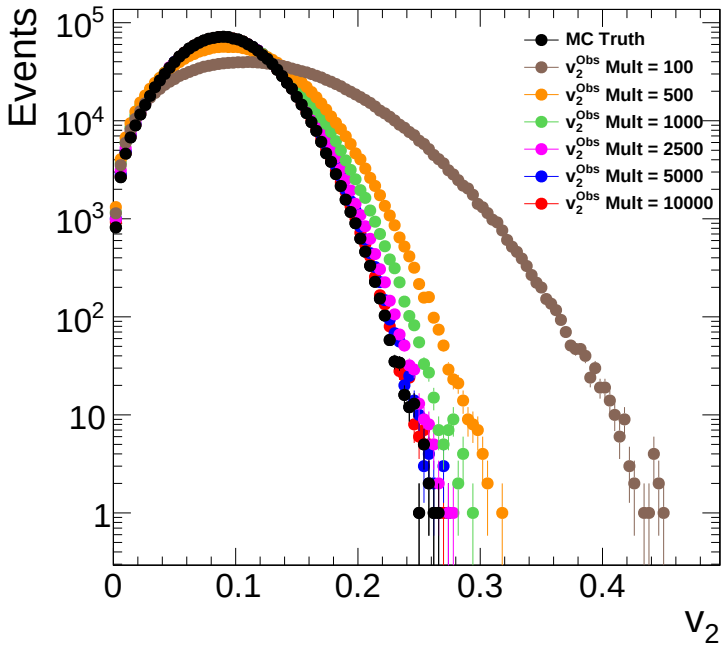

Figure 5.1: Toy MC simulation of how a finite particle multiplicity affects the reconstruction of an underlying flow distribution. Statistical smearing has the effect of broadening the observed distribution and shifting the mean to a larger value than that of the true underlying distribution. For large particle multiplicities (> 5000) the observed and underlying distributions are approximately equal. Smearing effects become exponentially lager as the particle multiplicity decreases.

where $p\left(v_{n,i}^{\text{obs}}|v_{n,j}\right)$ corresponds to the response matrix. This response matrix is often ill conditioned and cannot be inverted simply. There are several approaches to this type of problem that are commonly used in high-energy physics, such as D'Agostini iteration [220, 221, 222] and SVD Tikhonov regularization [223]. This analysis uses the D'Agostini iterative technique to remove the smearing effects from the measured $p\left(v_{n,i}^{\text{obs}}\right)$ distribution. However, before any unfolding technique can be used, the response matrix must first be built. The following subsections outline how response matrices are built in this analysis and how they are used in unfolding.

5.2.1 Building the response function

A critical step in this analysis is determining the correct response matrix to describe the smearing effects present in the observed $p\left(v_n^{\text{obs}}\right)$ distribution. To do so, events are first classified into separate centrality bins, each requiring its own response matrix, as the v_2 coefficients are dependent on the collision impact parameter. Thus, binning in centrality allows for the study of the fluctuations and their dependence on system size. A data-driven technique to build the response matrix was introduced by the ATLAS collaboration in Ref. [175] and is used in this analysis. This technique is only valid for symmetric collision systems such as for PbPb collisions.

The first step for a given class of events is to divide the track collection into two symmetric subevents. Tracks are measured using the silicon tracker and subevents are chosen based on pseudorapidity. All tracks with $\eta > 0$ are placed into subevent a while all tracks with $\eta < 0$ are placed into subevent b. For each subevent, flow vectors are calculated using Eqs. (5.1) and (5.4) to build the respective $p\left(\vec{v}_n^{\text{obs}}\right)$ distributions. Given that $v_n(\eta)$ is symmetric about $\eta = 0$, on average, the physical flow signal cancels in the distribution of subevent flow vector differences from each subevent $p\left(\vec{v}_n^{\text{obs},a} - \vec{v}_n^{\text{obs},b}\right)$ and the resulting distribution will contain the residual effects from statistical smearing. In addition, non-flow contributions that are correlated between the subevents will, on average, cancel in the subevent difference distribution, but uncorrelated contributions will remain. The uncorrelated non-flow contributions effectively broaden the subevent difference distribution and leave the mean unchanged [224]. The uncorrelated non-flow effects will be unfolded

in addition to the statistical smearing effects. The sensitivity of this analysis technique to non-flow is explored further in a study using the HIJING event generator, results of which are discussed in Sec. 7.1.

With the assumption that the subevent difference distribution is an accurate description of the smearing effects present in data, it can then be used to build the response matrix. For centrality intervals up to 50%, the subevent difference distribution is described well by a 2D Gaussian centered at 0 and, for more peripheral events it is better described by a 2D non-standardized Student's t-distribution centered at zero. This fit performance is illustrated in Fig. 5.3 where a sample 2SE difference distribution is taken from a central and peripheral centrality bin and their respective x and y projections are fitted with both a 1D Gaussian and Student's t-distribution. The widths (standard deviation) of these distributions are driven by the number of particles used to determine the subevent flow vectors. As the number of particles decreases, the smearing width increases exponentially, as shown in Fig. 5.2. The Student's t-distribution is a probability distribution that arises when a small sample size is used to estimate the mean of a normally distributed distribution and therefore provides a better fit for small multiplicities. In the limit where the sample size approaches infinity, the Student's t-distribution becomes a Gaussian distribution.

Before the subevent difference distribution can be used to build the response function, it must first be transformed to properly account for the sample sizes used. Because there are half as many tracks in each subevent compared to the full event, the smearing effects are different. For Gaussian random variables, the standard deviation of a population is inversely proportional to the square root of the sample size. In addition, the variance of a distribution obtained from the difference between two Gaussian random variables can be expressed as $\sigma^2_{a-b} = \sigma^2_a + \sigma^2_b$. Since, on average, the number of tracks in each subevent is half that of the full event and that the variances of the subevent distributions are equal, the smearing width obtained from the subevent difference distribution will be a factor of two larger than that for the full event. The mean is not affected by the sample size difference. Therefore, transforming the subevent difference distribution by a factor of $1/2$, where $p\left(\vec{v}_n^{\,\mathrm{obs},a} - \vec{v}_n^{\,\mathrm{obs},b}\right) \rightarrow p\left(\left[\vec{v}_n^{\,\mathrm{obs},a} - \vec{v}_n^{\,\mathrm{obs},b}\right]/2\right)$, will provide a more accurate

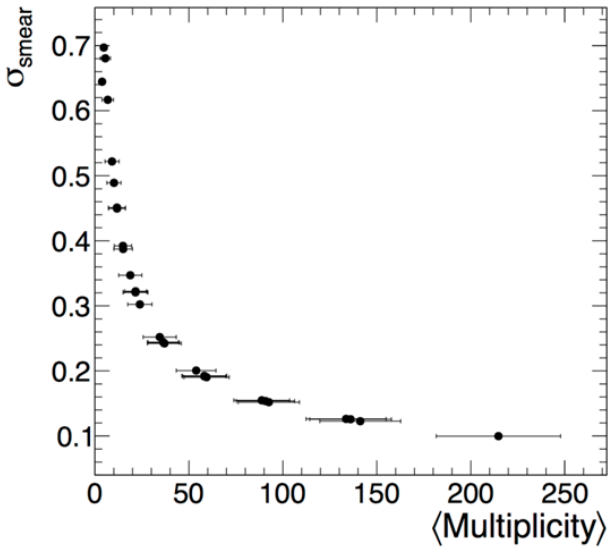

Figure 5.2: Smearing width obtained from the standard deviation of low-multiplicity $p\left(\vec{v}_n^{\text{obs},a} - \vec{v}_n^{\text{obs},b}\right)$ distributions as a function of mean event multiplicity.

description of the smearing present in the full event. This transformation is applied in Fig. 5.3.

Once the subevent difference distributions have been transformed to describe the smearing for the full event, they can be used to build the response matrix. There are two ways that these distributions can be used: with an analytic fit, or directly. The default response matrices for this analysis are those built from the subevent difference distributions directly. The following subsection outlines how to build a response matrix in this way, while Appendix B discusses how to build analytic response matrices by assuming either a Gaussian or Student's t-distribution.

5.2.1.1 Data-driven response matrix

The transformed subevent difference distribution is a measure of the smearing effects for the full event,

$$p\left(\left[\vec{v}_n^{\text{obs},a} - \vec{v}_n^{\text{obs},b}\right]/2\right) = p\left(\vec{s}\right) = p\left(\vec{v}_n^{\text{obs}} - \vec{v}_n\right), \tag{5.7}$$

where $\vec{s} = \vec{v}_n^{\text{obs}} - \vec{v}_n$ is the "smearing vector." The response matrix is constructed by first assuming the form of the underlying $p(\vec{v}_n)$ behavior. In cases of complete physical ignorance of the underlying behavior, it is acceptable to use a uniform distribution [220]. In this analysis, the assumed form

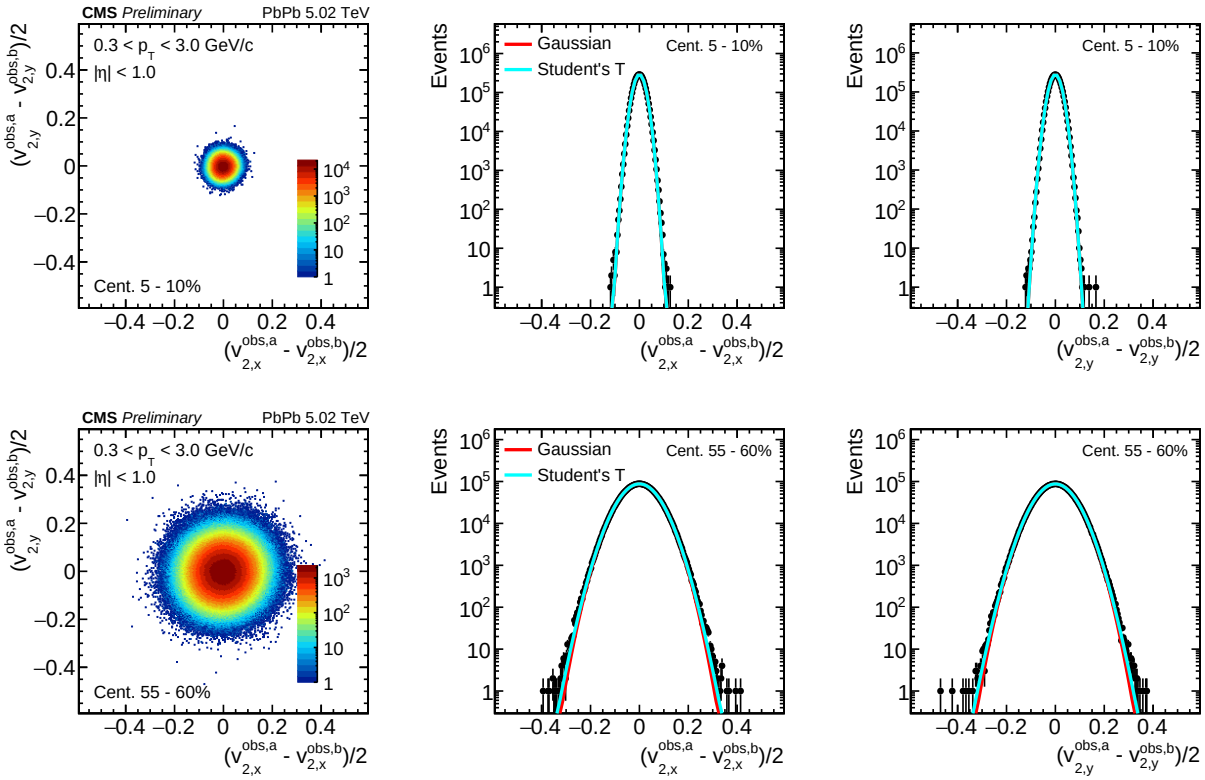

Figure 5.3: (Top row) Fit performance of a Gaussian and Student's t-distribution to the transformed subevent difference distributions for events in the 0-5% centrality class. Distributions are fitted using a binned likelihood technique. Due to the large number of tracks in each subevent, the Gaussian and Student's t-functions both describe the data well. (Bottom row) Fit performance of a Gaussian and Student's t-distribution to the rescaled subevent difference distributions for events in the 55-60% centrality class. In this case, the number of tracks for each subevent has fallen below the limit where the central limit theorem is applicable and Student's t-functions becomes the more accurate description of the data, yielding a fit χ^2/dof on the order of unity.

of the $p(\vec{v}_n)$ behavior was taken as the distribution of observed flow vectors. Given that particle multiplicities for most centrality classes are large, the smearing effects are relatively small and the observed flow vector distributions are similar to the respective underlying distributions. The consequences of the assumed form of the $p(\vec{v}_n)$ distribution are discussed in Secs. 5.2.2 and 6.1.4.

With an assumed form for the $p(\vec{v}_n)$ behavior and a measured $p(\vec{s})$ distribution, the response matrix is then built on an event-by-event basis. This is achieved by sampling a random flow vector based on the assumed $p(\vec{v}_n)$ behavior and sampling a random smearing vector from the $p(\vec{s})$ distribution. Adding these two vectors together provides an estimator for the observed flow vector for the event. This procedure is then repeated up to the number of events used to build the $p(\vec{s})$ distribution. By keeping the magnitudes of the vectors, each iteration will provide one entry of v_n^{obs} and v_n to the response matrix in Eq. (5.6).

5.2.2 D'Agostini iteration unfolding

The default method for unfolding in this analysis is D'Agostini iteration with early stopping, as outlined in Refs. [220, 221, 222]. As the name suggests, this technique is an iterative approach that utilizes Bayes' theorem to invert the response matrix. The RooUnfold [225] package for the ROOT data analysis framework [226] contains software for this unfolding technique and is utilized in this analysis. The unfolding workflow can be summarized by

$$\hat{p}\left(v_{n,i}\right)^{iter+1} = \sum_j \hat{M}_{ij}^{iter} p\left(v_{n,j}^{\text{obs}}\right), \tag{5.8}$$

where $\hat{p}\left(v_{n,i}\right)^{iter+1}$ is a vector that represents an estimator for the true, underlying distribution, $p\left(v_{n,j}^{\text{obs}}\right)$ is a vector that represents the measured distribution, and $\hat{M}_{ij}^{iter}$ is the "unfolding matrix." In this case, binned data are represented by vectors and matrices. This procedure requires two inputs: the measured $p\left(v_{n,j}^{\text{obs}}\right)$ vector and the response matrix. The unfolding matrix is constructed using the response matrix determined in Sec. 5.2.1.1 and a "prior," which is taken initially as a projection onto the v_n axis of the response matrix. The initial prior corresponds to the assumed

form of $p(v_n)$ from Sec. 5.2.1.1. The unfolding matrix has the form

$$\hat{M}_{ij}^{iter} = \frac{p\left(v_{n,j}^{\text{obs}}|v_{n,i}\right)\hat{p}\left(v_{n,i}\right)^{iter}}{\left[\sum_l p\left(v_{n,j}^{\text{obs}}|v_{n,l}\right)\hat{p}\left(v_{n,l}\right)^{iter}\right]\left[\sum_m p\left(v_{n,m}^{\text{obs}}|v_{n,i}\right)\right]}, \tag{5.9}$$

where $\hat{p}\left(v_{n,i}\right)^0$ is the initial prior and $p\left(v_{n,j}^{\text{obs}}|v_{n,i}\right)$ is the response matrix. Each application of the unfolding matrix to the observed vector produces an estimator of the underlying $p(v_n)$ distribution based on the prior. Since the initial prior is an assumed quantity, this setup naturally suggests to proceed iteratively by updating the prior in the unfolding matrix with the output estimator $\hat{p}\left(v_{n,i}\right)$ from the previous iteration. If run until convergence, the procedure will output a Maximum Likelihood Estimate (MLE) of the underlying $p(v_n)$ distribution. If the initial prior is close to the underlying $p(v_n)$ distribution, the procedure will converge after a few iterations.

Given that the response matrix is often ill conditioned, as the method proceeds out to more iterations, the procedure becomes increasingly sensitive to statistical fluctuations in the measured $p(v_n^{\text{obs}})$ distribution. This will give rise to unphysical oscillations in the unfolded distribution to overcompensate for these fluctuations. These features can be suppressed by stopping iterations before convergence and additionally by choosing an initial prior that better represents the underlying $p(v_n)$ behavior.

The criteria for iteration cutoff is obtained by examining the "smeared space." This is achieved by applying the response matrix ("refolding") to each unfolding iteration and comparing the result to the observed distribution. The motivation for this is seen in Eq. (5.6) by replacing the $p\left(v_{n,j}\right)$ distribution with a distribution obtained from an unfolding iteration. If the unfolding procedure is close to the MLE of the underlying $p\left(v_{n,j}\right)$ behavior, then refolding will reproduce the measured $p\left(v_{n,i}^{\text{obs}}\right)$ distribution. For this analysis, iterations are stopped when the χ^2/dof test statistic between the refolded and observed distributions is less than 1.2. In general, a χ^2/dof near 1.0 signifies a good fit. The choice of $\chi^2/dof \leq 1.2$ to determine when to stop iterating is arbitrary and can potentially bias results. The effects of this bias are considered as a systematic uncertainty

and are studied in detail in Sec. 6.1.4.

Figure 5.4 shows an example unfolding performance of a $p(v_2)$ distribution for mid-central events. Smearing effects are relatively small for these bins, but several aspects of the unfolding problem are illustrated in this figure:

- Panel A shows the response matrix obtained using the methods described in Secs. 5.2.1 and 5.2.1.1. Here, each entry represents a pair of v_n and v_n^{obs} values determined from the initial prior and the smearing distribution.

- Panel B shows both the observed and final unfolded distributions. The observed distribution is unfolded using the response matrix in panel A. The color of the unfolded distribution indicates how many iterations were used before the the smeared-space χ^2/dof value was less than 1.2.

- Panel C shows the correlation matrix **R** for the final unfolded distribution in panel B. The unfolding procedure and non-diagonal response matrix induce bin-to-bin correlations in the unfolded distribution. The correlation matrix is obtained from the covariance matrix used in the RooUnfold framework to propagate errors. To convert the covariance matrix into a correlation matrix, the following transformation [210] was used

$$\mathbf{R} = \mathbf{S^{-1}} \mathbf{C} \mathbf{S^{-1}}, \tag{5.10}$$

  where **S** is a diagonal matrix determined by the diagonal elements of the covariance matrix **C** such that $S_{ii} = \sqrt{C_{ii}}$. Each element of the correlation matrix represents the Pearson's coefficient between bins. If the Pearson's coefficient is near 0, then the two bins are not correlated and if the coefficient is near 1, then the two bins are strongly correlated.

- Panel D shows a χ^2/dof goodness of fit between the refolded and observed distributions as a function of iteration. A dotted line at $\chi^2/dof = 1.2$ signifies the iteration cutoff point.

- Panel E shows each iteration of the unfolding procedure refolded with the response matrix.

The observed distribution is also shown to illustrate how well the refolded distributions reproduce it.

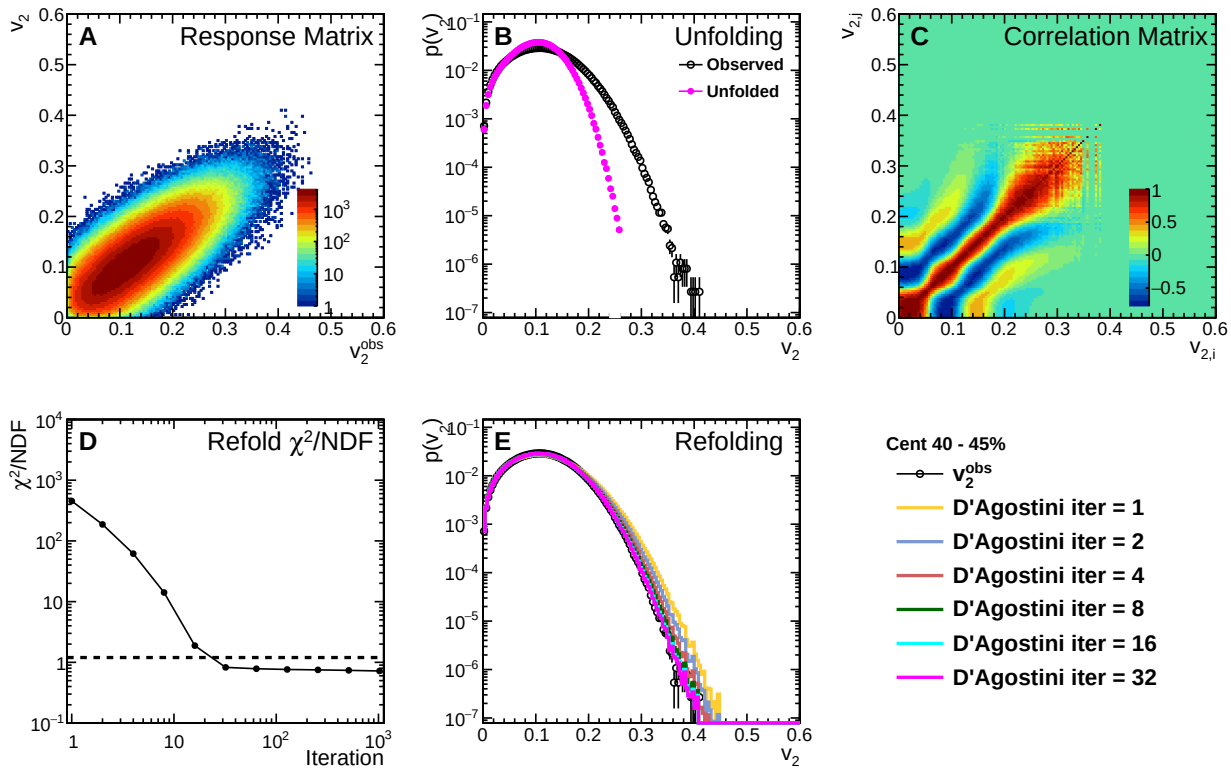

Figure 5.4: Example unfolding performance plots for a $p(v_2)$ for events in the 40–45% centrality bin. Panel A shows the response matrix obtained using the methods described in Secs. 5.2.1 and 5.2.1.1. Panel B shows both the observed and final unfolded distributions. Panel C shows the correlation matrix for the final unfolded distribution in panel B. Panel D shows a χ^2/NDF goodness-of-fit-between the refolded and observed distributions as a function of iteration. Panel E shows each iteration of the unfolding procedure refolded with the response matrix. The observed distribution is also shown to illustrate how well the refolded distributions reproduce it.

5.3 Event-shape engineering

Event-shape engineering is a type of event selection where events are characterized by their "shape" observed in the forward region. In CMS, the HF calorimeters are used to measure raw flow vectors,

with

$$
\begin{aligned}
q_{n,x}^{\mathrm{raw}} &= \frac{\sum_i w_i \cos n\phi_i}{\sum_i w_i}, \\
q_{n,y}^{\mathrm{raw}} &= \frac{\sum_i w_i \sin n\phi_i}{\sum_i w_i}, \\
\left|\vec{q}_n^{\mathrm{raw}}\right| &= \sqrt{\left(q_{n,x}^{\mathrm{raw}}\right)^2 + \left(q_{n,y}^{\mathrm{raw}}\right)^2},
\end{aligned}
\tag{5.11}
$$

where sums run over all towers in the HF and w_i is a weighting factor that is chosen as the E_{T} deposited in the i^{th} tower. Similar to the flow vectors in Eq. (5.1), the HF measured q-vectors are recentered to remove biases that result from non-uniform acceptance

$$
\begin{aligned}
\vec{q}_n^{\mathrm{det}} &= \frac{\sum_i^{N_{\mathrm{Events}}} \vec{q}_{n,i}^{\mathrm{raw}}}{N_{\mathrm{Events}}}, \\
\vec{q}_n^{\mathrm{obs}} &= \vec{q}_n^{\mathrm{raw}} - \vec{q}_n^{\mathrm{det}}.
\end{aligned}
\tag{5.12}
$$

By dividing into areas of equal statistics, the distribution of observed q-vectors in HF can be used to further classify events with the same centrality into bins of event shape. Figure. 5.5 shows the distribution of second-order q-vectors observed by the HF for mid-central collisions. Here, the distribution is divided into 10 slices of equal area to form 10% ellipticity bins. This allows for measurement of detailed correlations between initial-shape components that would otherwise be destroyed by event-averaging techniques. For example, the Glauber model predicts an anti-correlation between ε_2 and ε_3 which would propagate to an anti-correlation between measured v_2 and v_3 values [227]. This anti-correlation was first observed by ATLAS in PbPb collisions using event-shape engineering techniques [228]. Coupling the event-shape engineering event selection to unfolding allows for unprecedented selection in correlators to event shape, given the access to all of the moments of the unfolded $p(v_n)$ distribution.

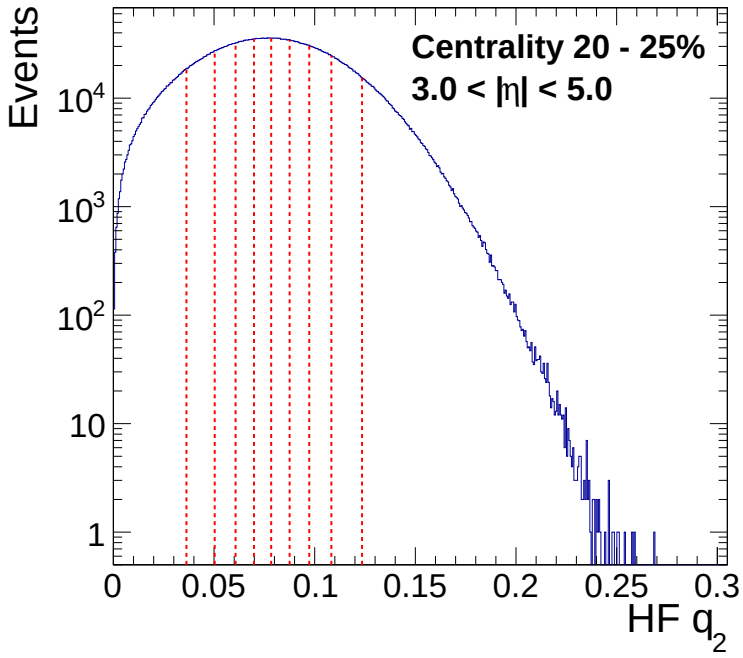

Figure 5.5: Second-order q-vectors as measured in the HF$\pm$ detectors for mid-central PbPb collisions. Dotted lines denote the division into 10 areas of equal statistics and so-called ellipticity bins.

Chapter 6

Systematic uncertainties and cross-checks

6.1 Systematic uncertainties

There are five primary sources of systematic uncertainty for the quantities studied in this analysis: vertex position, pileup contamination, track quality cuts, unfolding regularization, and response matrix uncertainty. Systematic uncertainties are determined separately for the bins of unfolded $p(v_2)$ distributions and the quantities extracted from each, namely the cumulant flow harmonics, ratios of higher-order cumulant flow harmonics, the elliptic flow skewness estimate with respect to the reaction plane, and the elliptic power law parameters. Each of the quantities are determined from the bin contents of the unfolded $p(v_2)$ distributions and are thus correlated. Studying each quantity independently suppresses these correlations and leads to a more robust extraction of the systematic uncertainties. Details of each systematic study are outlined in the following subsections.

6.1.1 Vertex position

The systematic biases that arise from the vertex z-position are investigated by splitting the current vertex cut into two scenarios. In the first scenario, the vertex position window is restricted to $|v_z| < 3.0$ cm, while the second window contains the remainder of possible vertex positions, $3.0 < |v_z| < 15.0$ cm. Each scenario is compared to the default vertex position selection, $|v_z| < 15.0$ cm

and deviations are quoted as systematic uncertainties.

Results of this study are reported in Figs. 6.1 – 6.5. For each centrality bin, observables are extracted from the unfolded $p(v_2)$ distributions for each of the three vertex windows and ratios of the observables for each of the systematic vertex windows relative to the nominal $|v_z| < 15.0$ cm window are determined. The trends observed in the ratios show how the position of the primary vertex biases the quantities extracted from $p(v_2)$ distributions. This bias is qualitatively understood by considering the construction of the response matrix. As the vertex z-position deviates further from $v_z = 0$, the track distributions in either side of the tracker will become more asymmetric in terms of number of particles. This, in turn leads to different smearing effects in each of the subevents and can bias the response function.

The systematic bias is relatively small for the extracted cumulants in Fig. 6.1, on the order of 1% for central to mid-central events. The ratios of higher order cumulants in Fig. 6.2 are the most stable in this study, and show variation of 0.1% for mid-central events. The least stable observable in this study is γ_1^{exp} in Fig. 6.3, showing variation up to 100% in central events. The behavior of γ_1^{exp} is expected to be the least stable in all systematic studies because of its complex dependence on multiple orders of cumulants, as described by Eq. (2.12). In addition, the bias on the elliptic power law parameters is shown in Fig 6.4. Here, all three parameters show a strong bias in central collisions, on the order of 20%, that becomes less significant toward peripheral collisions.

To assess the systematic uncertainty on the bins of the unfolded $p(v_2)$ distributions, the unfolded distributions from each systematic vertex window are first translated to have the same mean as the unfolded distributions in the default vertex window. Bin-to-bin ratios relative to the default case are calculated and the maximum deviation is taken to be the systematic uncertainty for each. To avoid point-to-point statistical fluctuations, the ratios are first smoothed to fit the general trend. The result of this study is shown in Fig. 6.5. Here, agreement amongst the three vertex windows is observed in the bulk regions of the unfolded distributions, while deviations become significant toward the low-statistics tails.

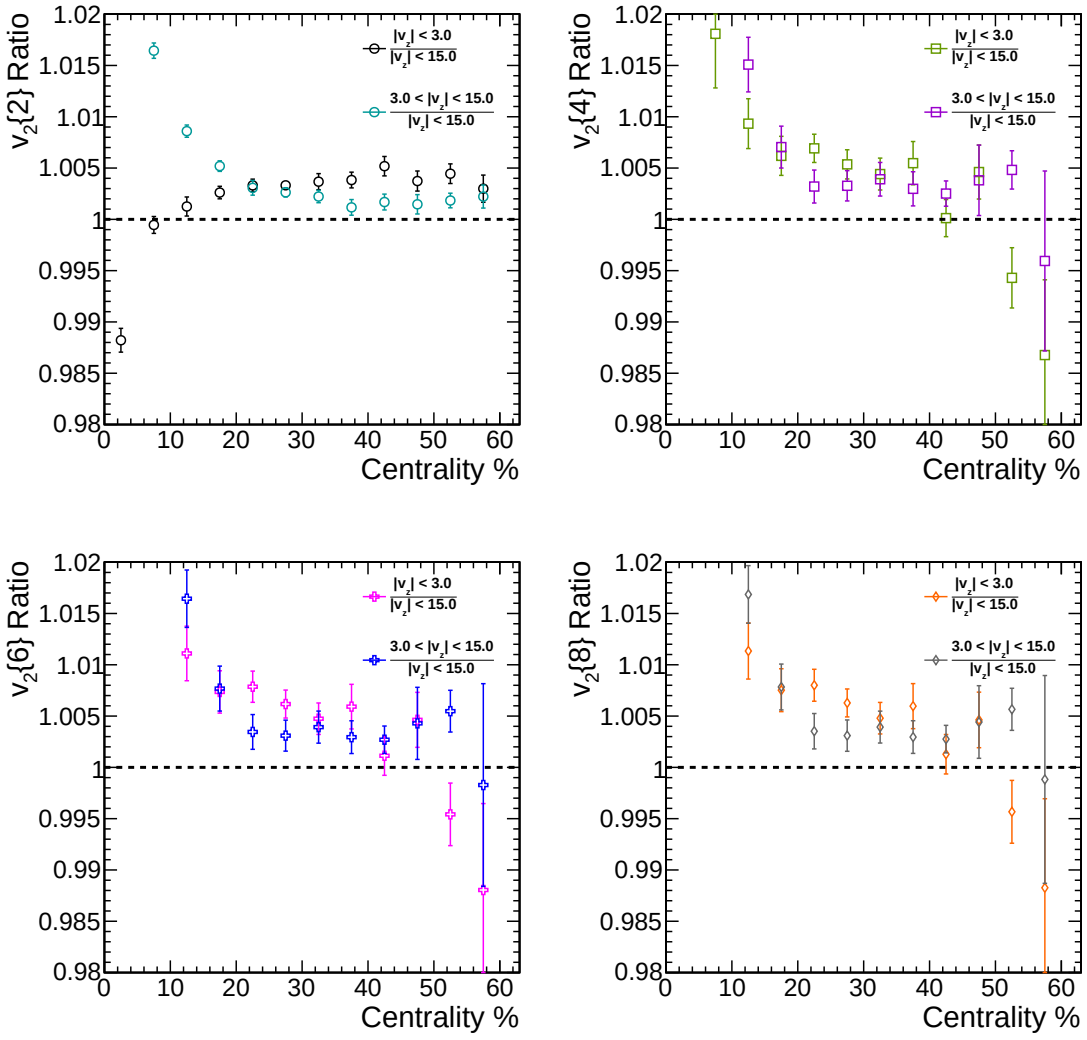

Figure 6.1: Bias on the cumulants extracted from $p\,(v_2)$ distributions for vertex selection windows relative to the default window $|v_z| < 15.0$ cm.

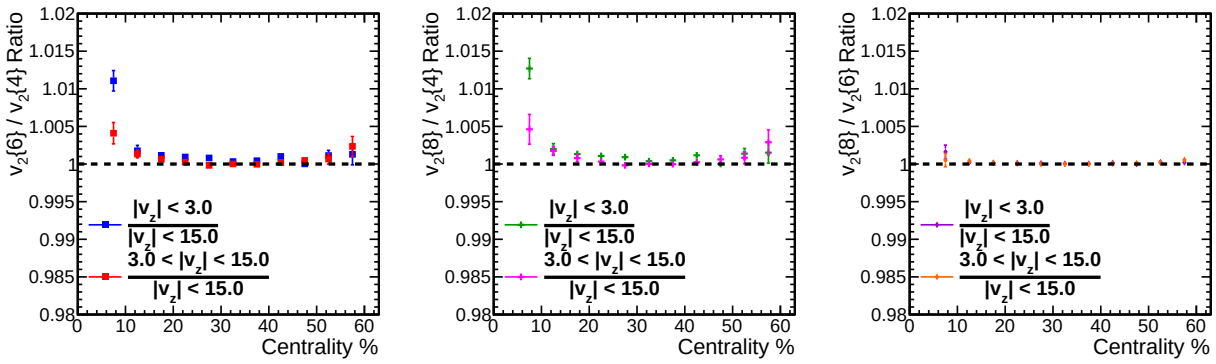

Figure 6.2: Biases on the ratio of higher order cumulants extracted from $p(v_2)$ distributions for vertex selection windows relative to the default window $|v_z| < 15.0$ cm. The ratios of higher order cumulants are the most stable in this study.

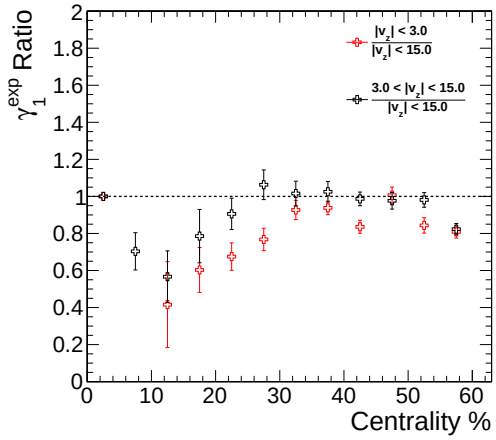

Figure 6.3: Biases on the skewness measure γ_1^{exp} of $p(v_2)$ distributions for vertex selection windows relative to the default window $|v_z| < 15.0$ cm. Skewness is the least stable observable in this study.

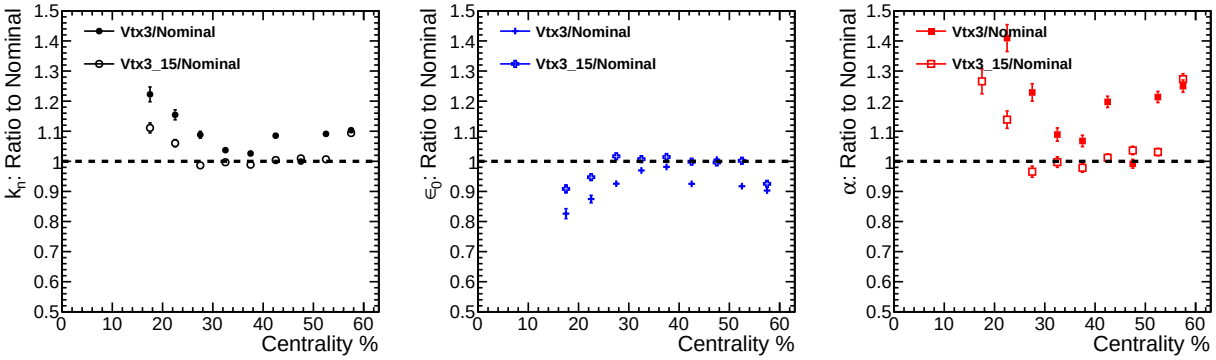

Figure 6.4: Biases on the parameters extracted from elliptic power law fits to the $p(v_2)$ distributions for vertex selection windows relative to the default window $|v_z| < 15.0$ cm.

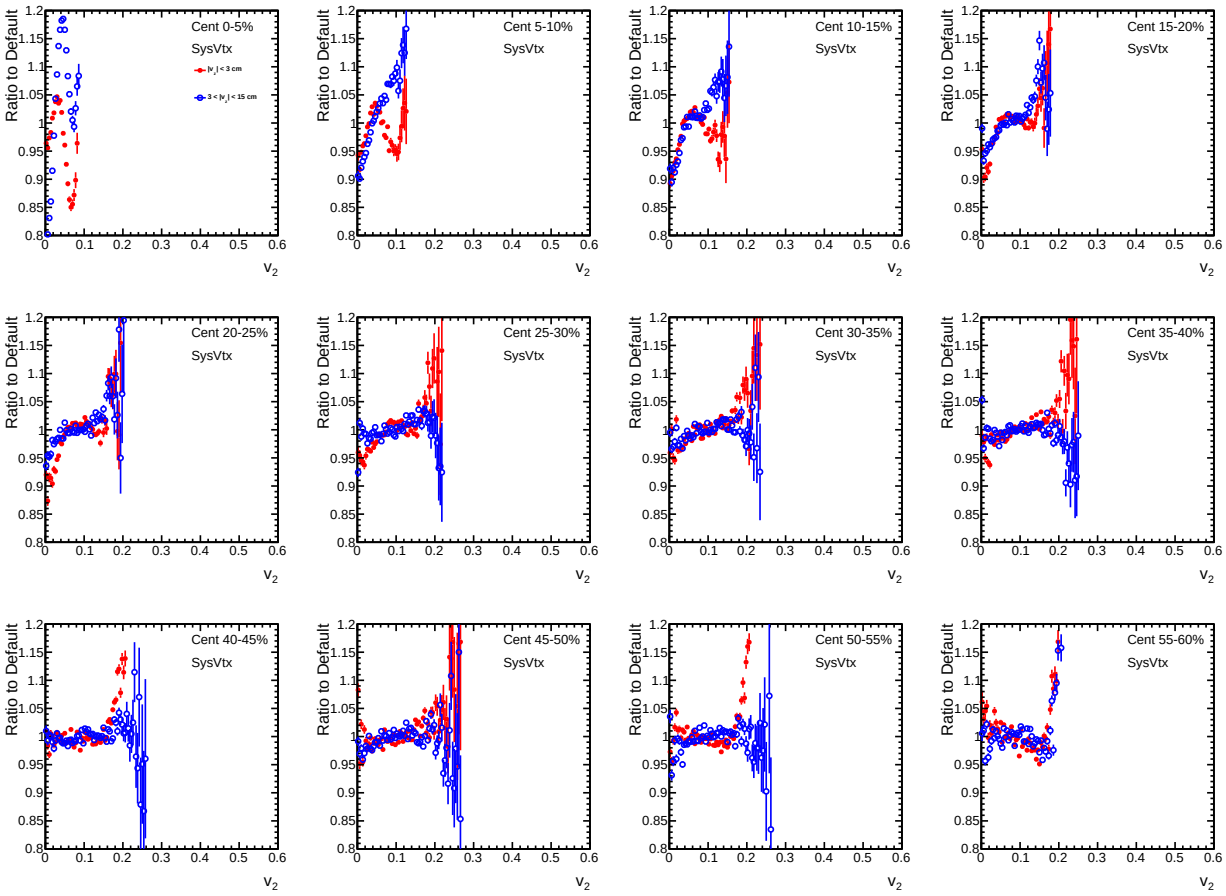

Figure 6.5: Systematic bias on the shape of $p(v_2)$ distributions that arises from the vertex position cut.

6.1.2 Pileup contamination

To assess the potential bias from residual pileup events on this analysis, the strength of the vertex-cluster compatibility filter is varied. By default, the filter cuts out the bottom 1% of poorly compatible vertices. For this study, the filter is re-tuned to drop out the bottom and 2% to further reject potential pileup events from the data sample. To achieve this new tune, the cluster compatibility quality scores described in Sec. 4.1 are revisited. Minimum bias events are re-analyzed without running the cluster compatibility filter and the cluster-vertex quality score for all collected events is inspected as a function of number of compatible vertex clusters, as illustrated in the left panel of Fig 6.6. To determine a new tune, events are separated into bins based on the number of compatible pixel clusters N_{Pixel} and distributions of quality scores are obtained for each. A lower bound for each quality score distribution is then chosen such that all events below correspond to the bottom 2% of poorly reconstructed vertices. The lower bounds are plotted as a function of N_{Pixel} in the center panel of Fig. 6.6 and are parametrized using a series of polynomials. This parametrization is then added to the vertex compatibility filter and drops all events with quality scores below the lower bounds, as shown in the right panel of Fig 6.6.

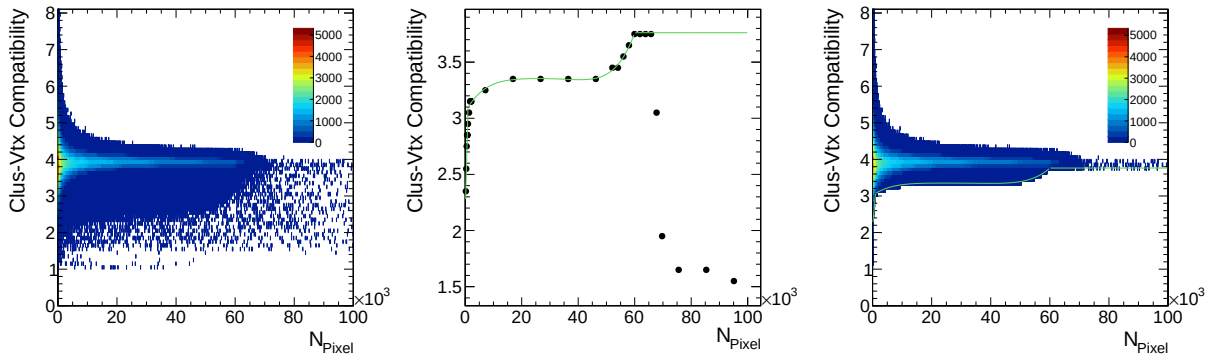

Figure 6.6: (Left) Cluster-vertex quality score for minimum bias events prior to running the cluster compatibility filter. (Center) Parametrization that determines the lower bound that drops the bottom 2% of poorly compatible vertices. (Right) Cluster-vertex quality score for minimum bias events after running the strengthened cluster compatibility filter.

Results of this study are reported in Figs. 6.7 – 6.11. For each centrality bin, observables are extracted from the unfolded $p(v_2)$ distributions for each of the cluster compatibility tunes and

ratios of the observables for the strengthened tune relative to the nominal tune are determined. The trends observed in the ratios show how pileup contamination biases the quantities extracted from $p(v_2)$ distributions. The bias is essentially negligible for the cumulants in Fig. 6.7, on the order of 0.1% for central events and less than 0.1% for the remaining centralities. The ratios of higher order cumulants in Fig. 6.8 show similar behavior as a function of centrality. The least stable observable in this study is γ_1^{exp} in Fig. 6.9, showing dramatic variation in central events. In addition, the bias on the elliptic power law parameters is shown in Fig 6.10. Here, all three parameters show a weak bias for all centralities, on the order of 2%.

To assess the systematic uncertainty on the bins of the unfolded $p(v_2)$ distributions, the unfolded distributions obtained using the strengthened cluster compatibility tune are first translated to have the same mean as the unfolded distributions obtained using the nominal tune. Bin-to-bin ratios relative to the nominal case are calculated and the maximum deviation is taken to be the systematic uncertainty for each. To avoid point-to-point statistical fluctuations, the ratios are first smoothed to fit the general trend. The result of this study is shown in Fig. 6.11. Here, agreement amongst the two pileup scenarios is observed in the bulk regions of the unfolded distributions, while deviations become significant toward the low-statistics tails.

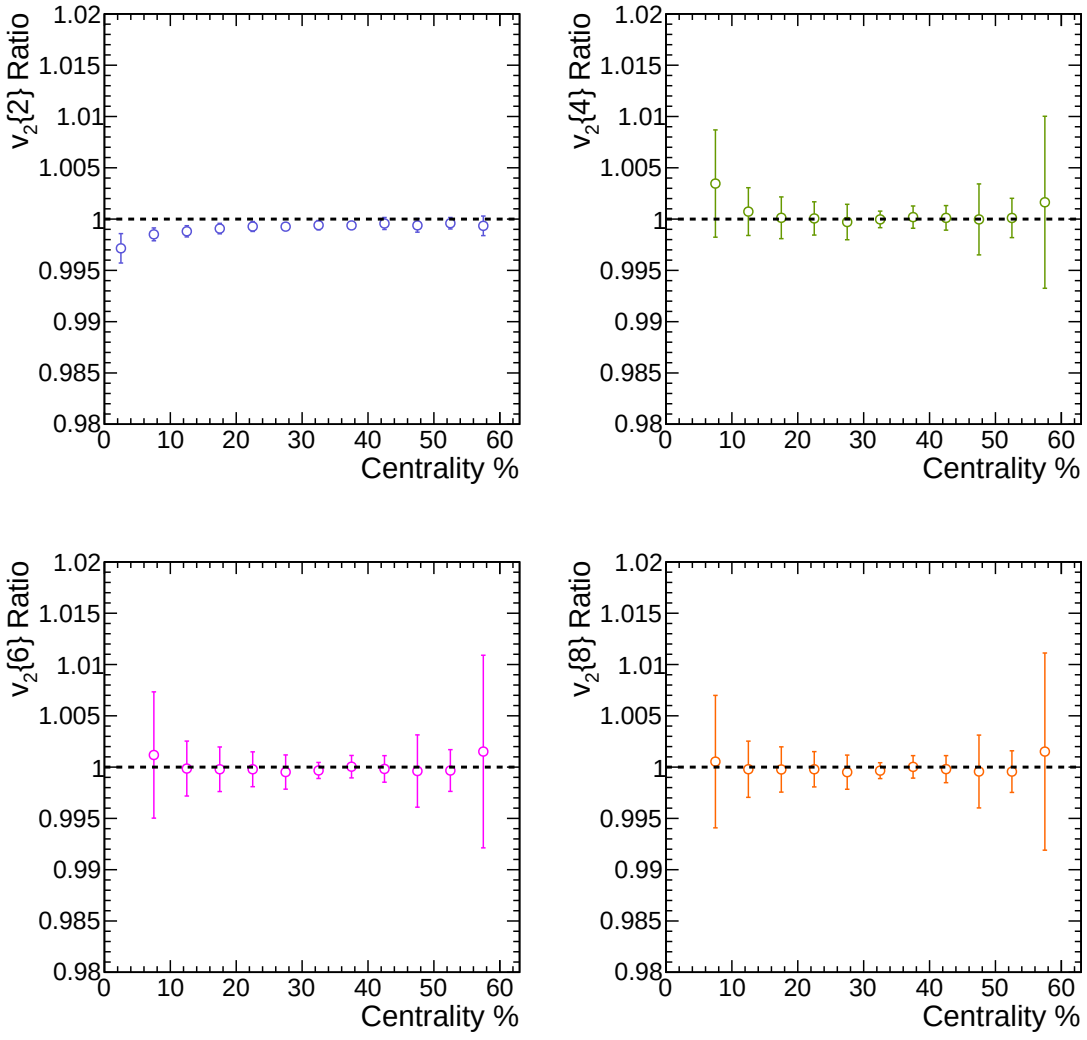

Figure 6.7: Bias on the cumulants extracted from $p(v_2)$ distributions for a strengthened cluster-compatibility tune relative to the default tune. Biases relative to the default selection are essentially negligible for most centralities and order of cumulants.

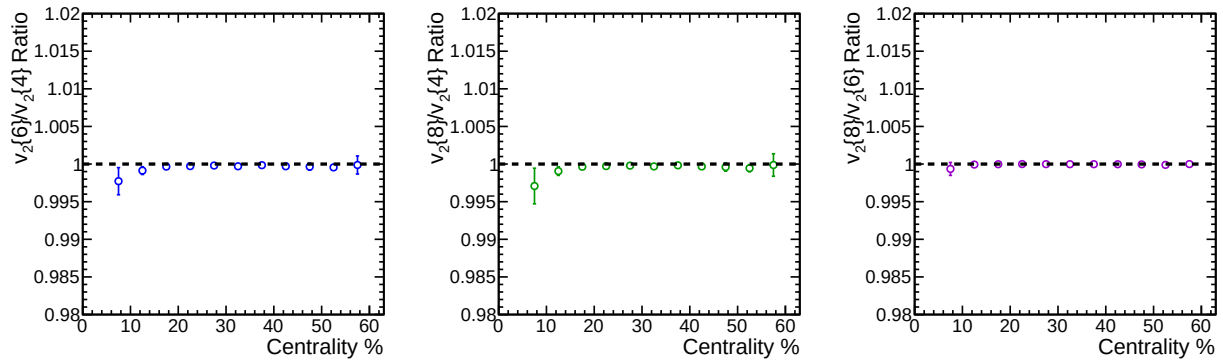

Figure 6.8: Bias on the higher-order cumulant ratios extracted from $p(v_2)$ distributions for a strengthened cluster-compatibility tune relative to the default tune. Biases relative to the default selection are essentially negligible for most centralities and order of cumulants.

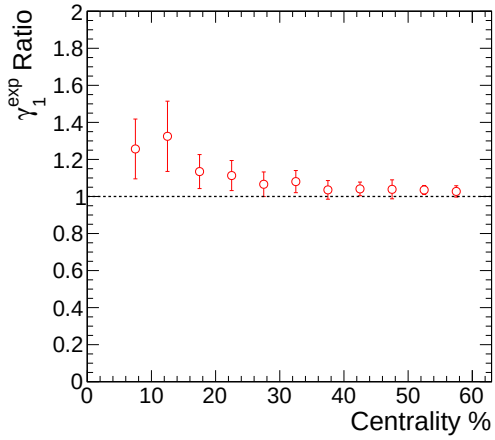

Figure 6.9: Bias on the skewness measure of $p(v_2)$ distributions for a strengthened cluster-compatibility tune relative to the default tune. Biases relative to the default selection are small for most centralities and order cumulants, but grow exponentially for central events.

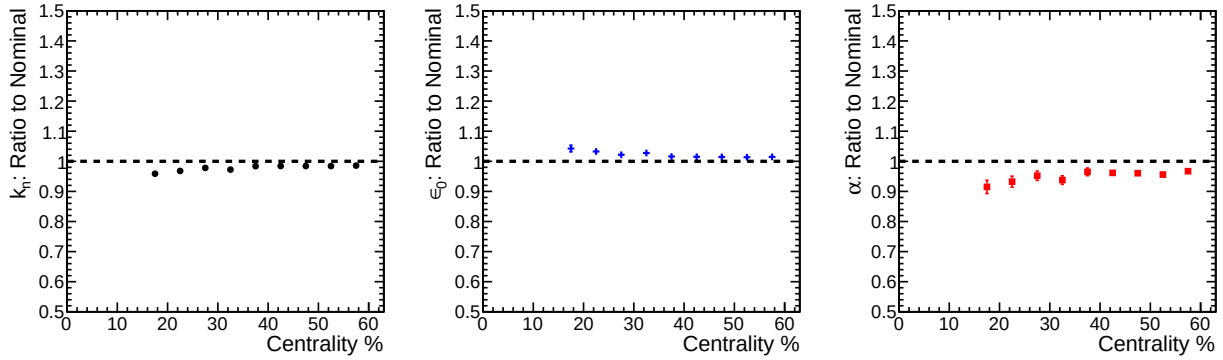

Figure 6.10: Biases on the parameters extracted from elliptic power law fits to the $p(v_2)$ distributions for a strengthened cluster-compatibility tune relative to the default tune.

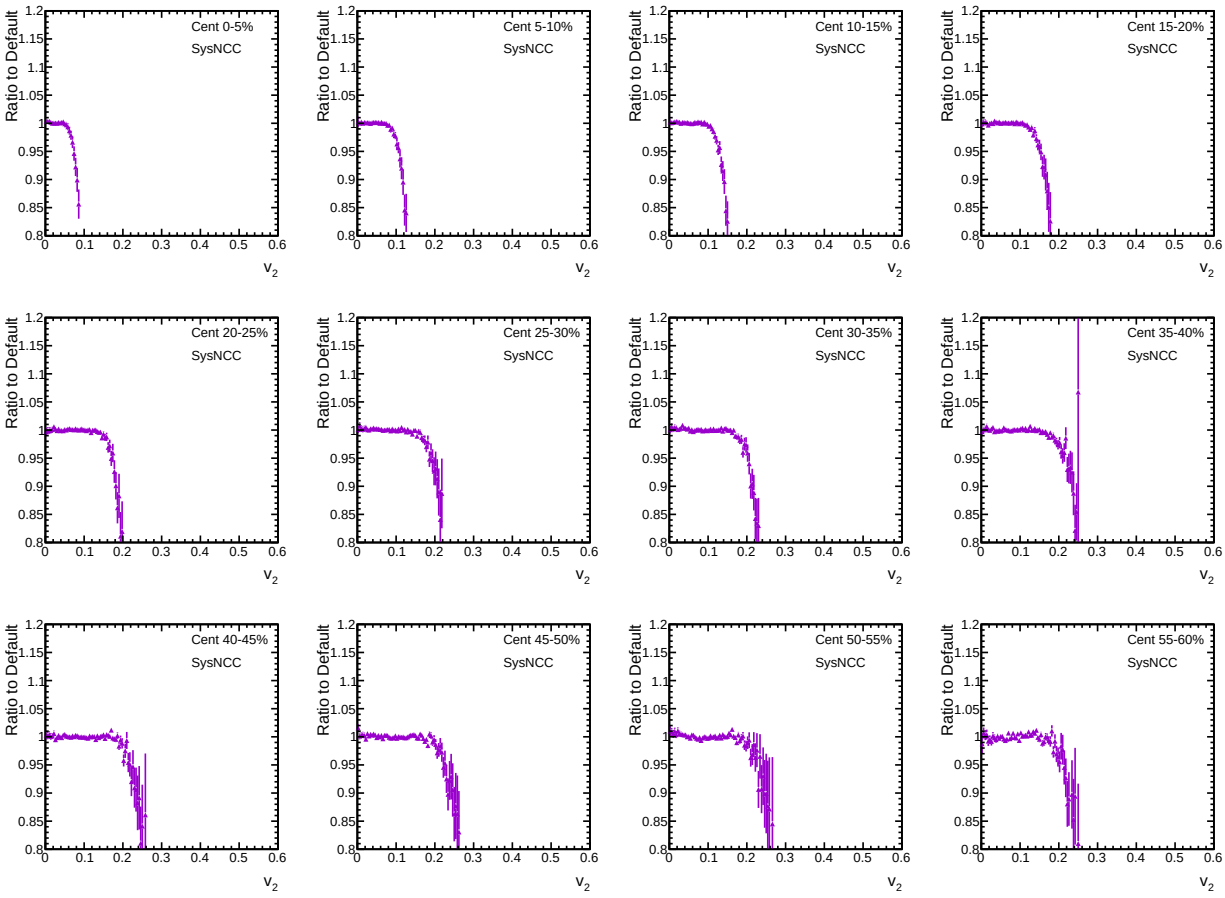

Figure 6.11: Systematic bias on the shape of $p(v_2)$ distributions that arises from pileup events.

6.1.3 Track quality cuts

To estimate the systematic bias that arises from misidentified tracks, the analysis is re-run with two new scenarios of track quality selection: "loose" and "tight." The strength of the track quality cuts will alter the probability of falsely identifying a track and, depending on the cut, will allow more or less misidentified tracks into the analysis. Outlines of the new scenarios for pixel and general tracks can be found in Tables 6.1 and 6.2, respectively.

Table 6.1: Systematic track quality cut scenarios for pixel tracks.

Track Quality	Loose Cut	Tight Cut
$\left\|d_z/\sigma_{d_z}\right\|$	< 10.0	< 6.0
$\chi^2/dof/N_{\text{Layers}}$	< 18.0	< 9.0

Table 6.2: Systematic track quality cut scenarios for general tracks.

Track Quality	Loose Cut	Tight Cut
$\left\|d_z/\sigma_{d_z}\right\|$	< 5.0	< 2.0
$\left\|d_0/\sigma_{d_0}\right\|$	< 5.0	< 2.0
$\sigma_{p_{\text{T}}}/p_{\text{T}}$	< 0.10	< 0.05

Results of this study are reported in Figs. 6.12 – 6.16. For each centrality bin, observables are extracted from the unfolded $p(v_2)$ distributions for each of the track quality cuts scenarios and ratios of the observables for each of the systematic track quality selections relative to the nominal track selection are determined. The trends observed in the ratios show how misidentified tracks bias the quantities extracted from $p(v_2)$ distributions. The bias is relatively small for the extracted cumulants in Fig. 6.12, on the order of 0.5% for all centralities. The ratios of higher order cumulants in Fig. 6.13 are the most stable in this study, and show variations less than 0.1% for all centralities. The least stable observable is γ_1^{exp} in Fig. 6.14, showing variation up to 5% in peripheral events. In addition, the bias on the elliptic power law parameters is shown in Fig 6.15. Here, the three parameters show a negligible bias, on the order of $< 1\%$.

To assess the systematic uncertainty on the bins of the unfolded $p(v_2)$ distributions, the unfolded distributions from each track quality selection are first translated to have the same mean as

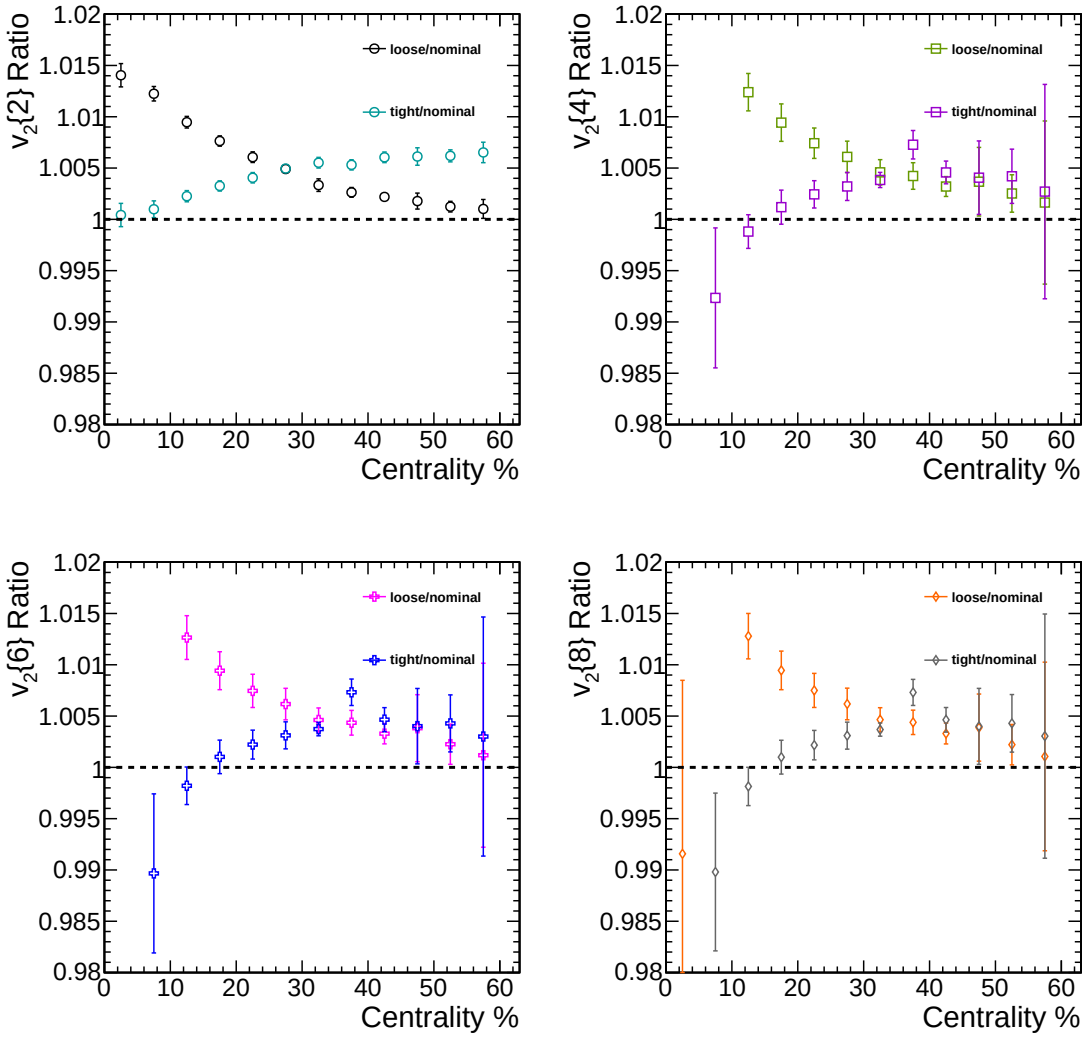

Figure 6.12: Bias on the cumulants extracted from $p(v_2)$ distributions for loose and tight track selections relative to the default track selection.

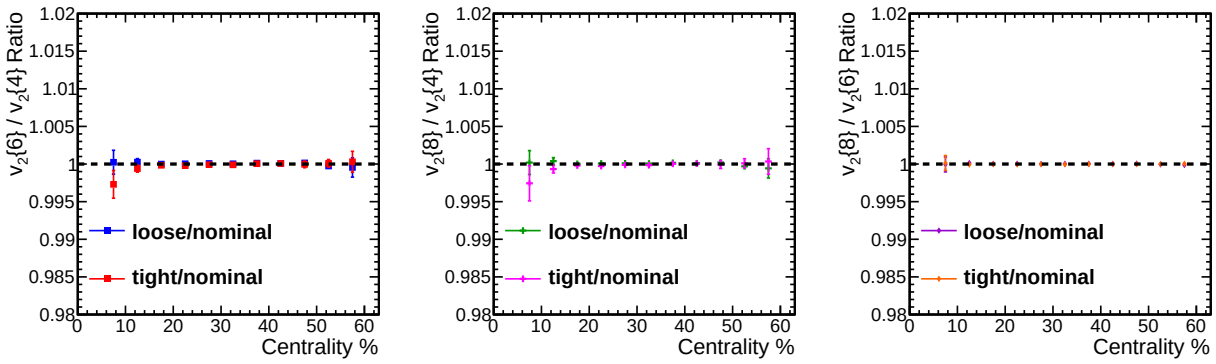

Figure 6.13: Biases on the ratio of higher order cumulants extracted from $p(v_2)$ distributions for loose and tight track selections relative to the default track selection. The ratios of higher order cumulants are the most stable in this study.

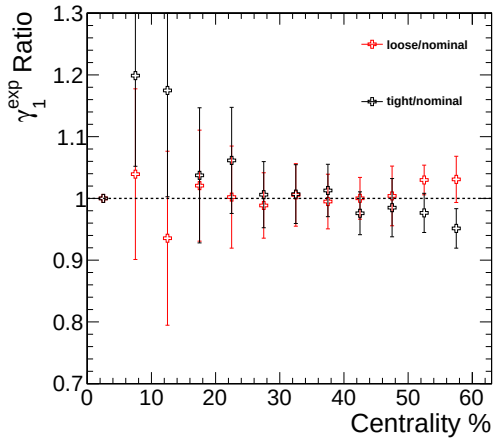

Figure 6.14: Biases on the skewness measure γ_1^{exp} of $p(v_2)$ distributions for loose and tight track selections relative to the default track selection. Skewness is the least stable observable in this study.

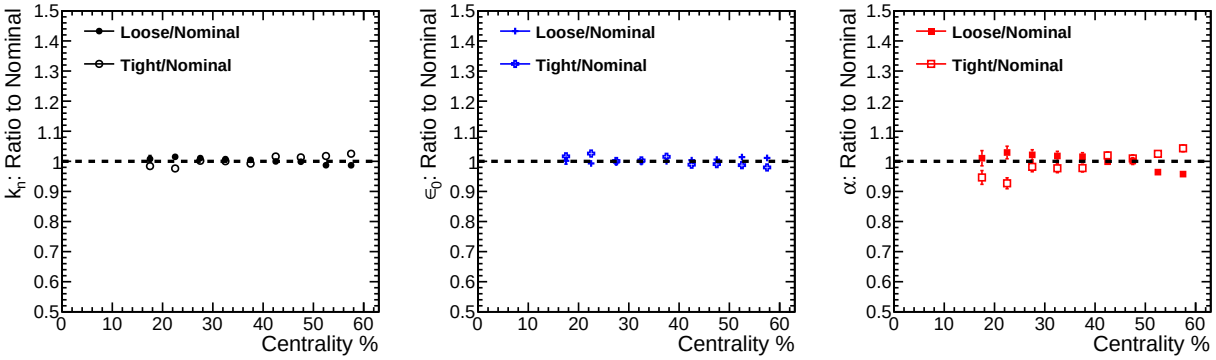

Figure 6.15: Biases on the parameters extracted from elliptic power law fits to the $p(v_2)$ distributions for loose and tight track selections relative to the default track selection.

the unfolded distributions in the nominal selection. Bin-to-bin ratios relative to the default case are calculated and the maximum deviation is taken to be the systematic uncertainty for each. To avoid point-to-point statistical fluctuations, the ratios are first smoothed to fit the general trend. The result of this study is shown in Fig. 6.16. Here, agreement amongst the three scenarios is observed in the bulk regions of the unfolded distributions, while deviations become significant toward the low-statistics tails. The distribution are biased in different directions representing the fact that misidentified tracks carry an average v_2 that contaminate the measured signal.

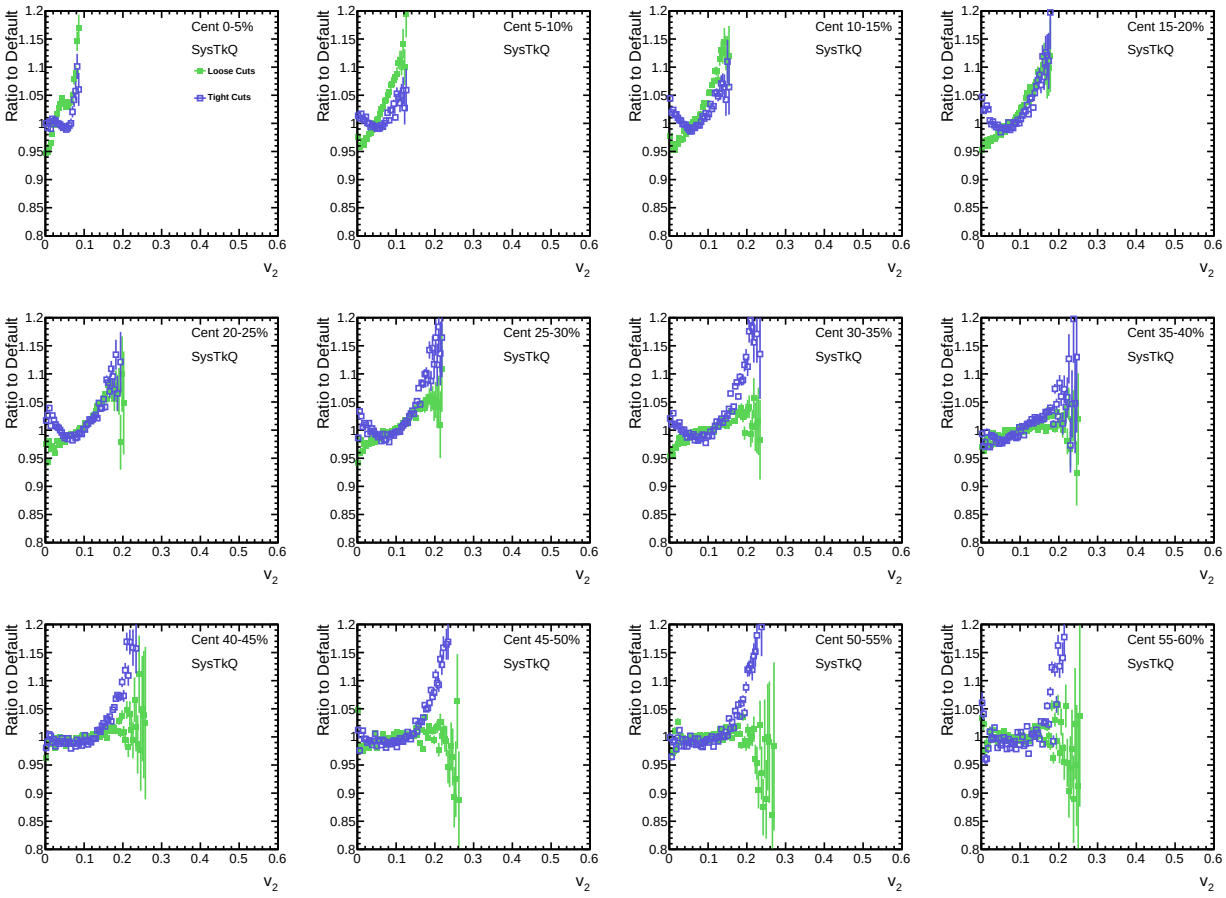

Figure 6.16: Systematic bias on the shape of $p(v_2)$ distributions that arises from the loosening/tightening the track selection.

6.1.4 Unfolding regularization bias

The choice of stopping iteration in the unfolding procedure in Sec. 5.2.2 can potentially bias the reported results. If too few iterations are used, the result is biased toward the initial prior distribution and if too many iterations are used, unphysical oscillations will manifest in the unfolded distribution. An estimate of the systematic bias from regularization can be obtained by varying the cutoff criteria for the χ^2/dof test statistic between the refolded and observed distributions. Figure 6.17 illustrates the refolding χ^2/dof behavior as a function of iteration for all centrality intervals used in this analysis. Similar behavior is seen for all plots: the χ^2/dof drops at a large rate for the first few iterations and then slows as the unfolding procedure starts to converge. As the choice in χ^2/dof that flags the procedure to stop iterating is arbitrary, the value was varied between 1.0 and 2.0 to explore how this affects the moments obtained from each unfolded distribution.

The results of this study are shown in Figs. 6.18 – 6.22. For each centrality bin, observables are extracted from the unfolded $p(v_2)$ distributions for various χ^2/dof cutoff values between 1.0 and 2.0 and ratios of the observables for each χ^2/dof scenario relative to the "best-case-scenario" where $\chi^2/dof \leq 1.0$ are determined. The trends observed in the ratios show how unfolding regularization can bias the quantities. The the extracted cumulants and ratios of higher order cumulants in Figs. 6.18 and 6.19 from are the most stable in all of these tests, and show variations of less than 0.1%. The least stable observable in these tests is $\gamma_1^{\rm exp}$ in Fig. 6.20, showing variation up to 30% in central and peripheral events. In addition, the bias on the elliptic power law parameters is shown in Fig 6.21. Here, all three parameters show a negligible bias for central collisions, which starts to become significant in peripheral collisions (on the order of 20%).

To assess the systematic uncertainty on the bins of the unfolded $p(v_2)$ distributions, the unfolded distributions obtained using various χ^2/dof cutoff values are first translated to have the same mean as the unfolded distributions obtained using the $\chi^2/dof \leq 1$ cutoff value. Bin-to-bin ratios relative to the $\chi^2/dof \leq 1$ case are calculated and the maximum deviation is taken to be the systematic uncertainty for each. To avoid point-to-point statistical fluctuations, the ratios are first smoothed to fit the general trend. The result of this study is shown in Fig. 6.22. Here, agree-

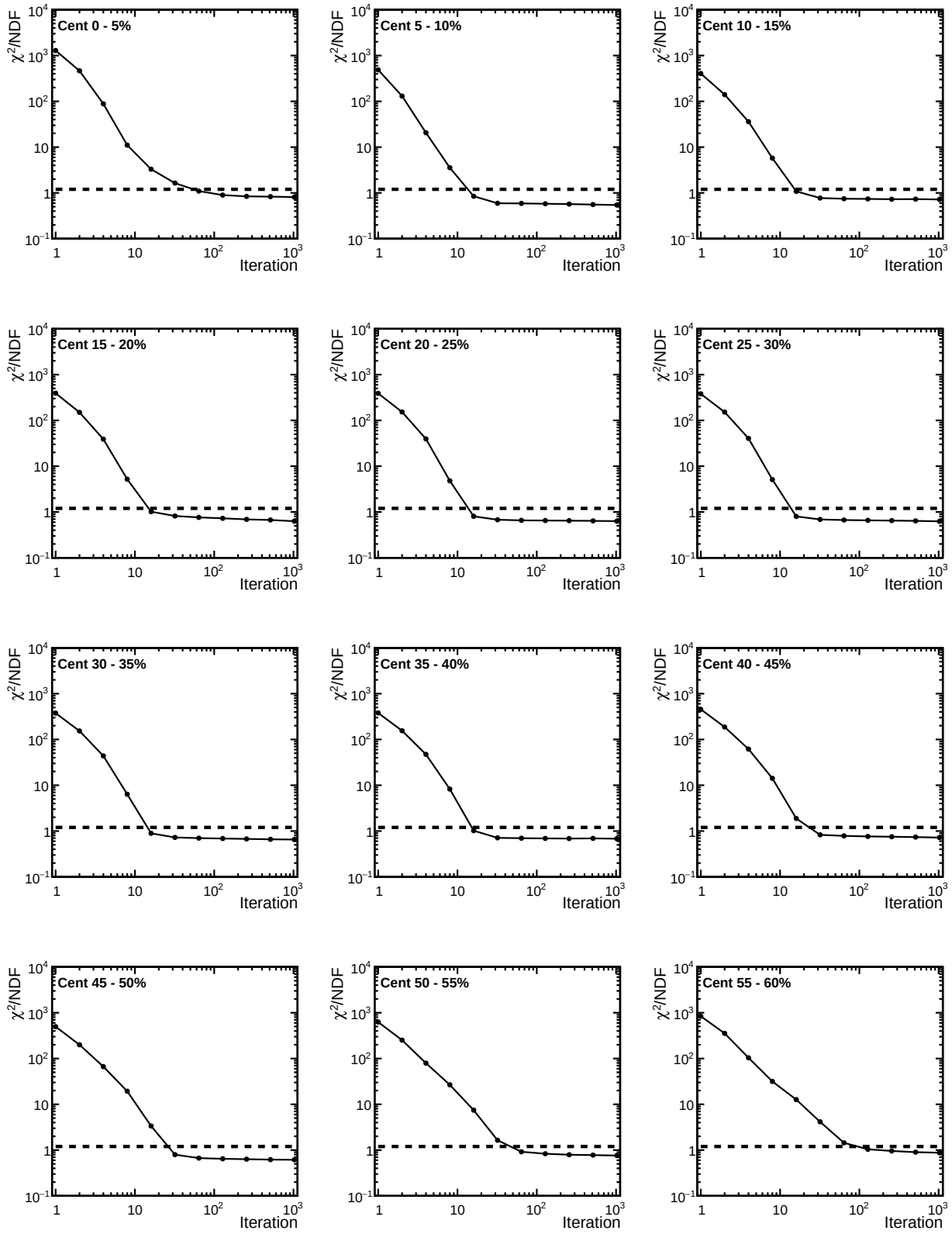

Figure 6.17: Refolding χ^2/dof behavior as a function of iteration for all centrality intervals used in this analysis. A dotted line at $\chi^2/dof = 1.2$ shows the default cutoff criteria for analysis.

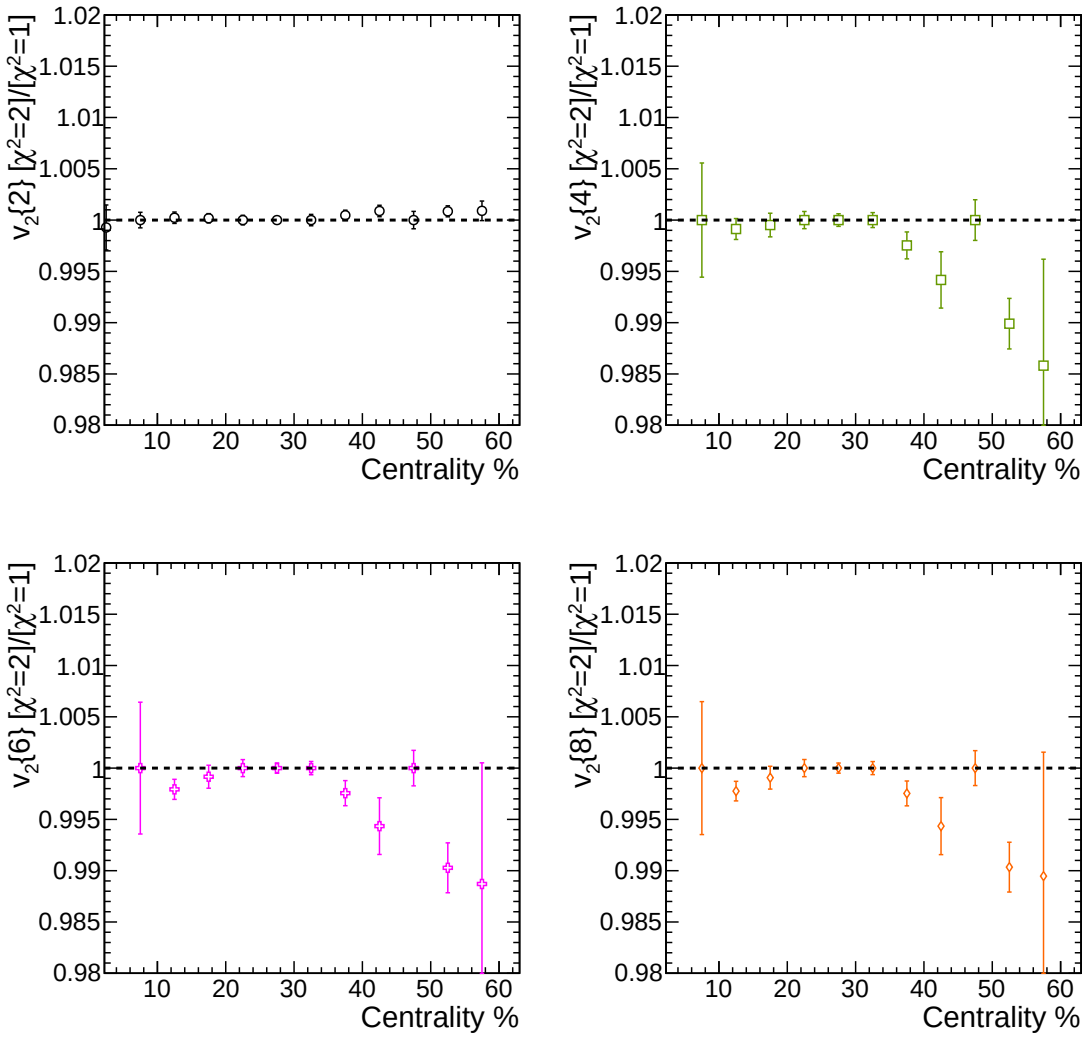

Figure 6.18: Ratio of the cumulants extracted from $p(v_2)$ distributions when the iteration cutoff criteria is $\chi^2/dof \leq 2$ to those extracted when the criteria is $\chi^2/dof \leq 1$.

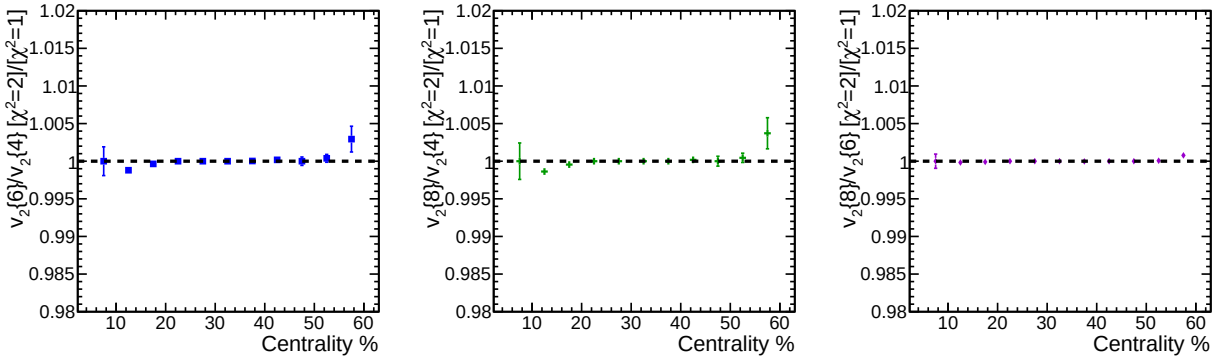

Figure 6.19: Ratio of the higher order cumulant ratios extracted from $p(v_2)$ distributions when the iteration cutoff criteria is $\chi^2/dof \leq 2$ to those extracted when the criteria is $\chi^2/dof \leq 1$.

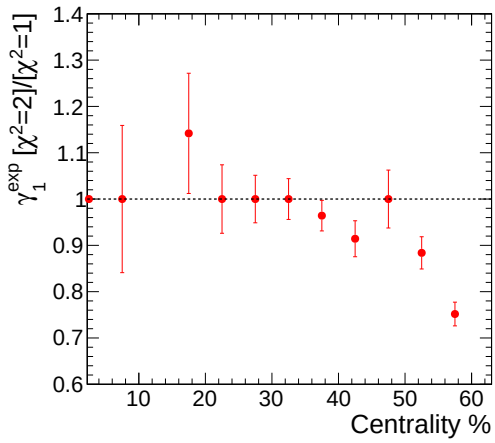

Figure 6.20: Ratio of γ_1^{exp} extracted from $p(v_2)$ distributions when the iteration cutoff criteria is $\chi^2/dof \leq 2$ to those extracted when the criteria is $\chi^2/dof \leq 1$. Larger variations are seen in this plots as a function of centrality. The systematic bias for regularization can be as large as 30% in cases where smearing is large and flow signal is small.

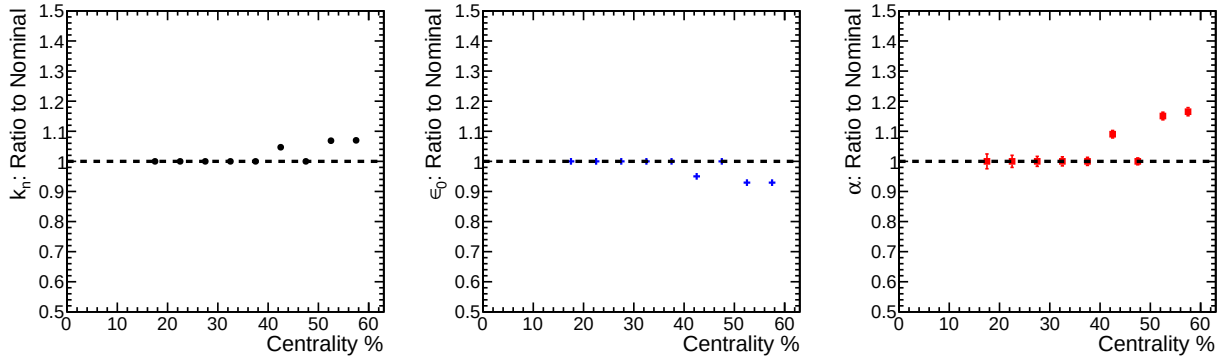

Figure 6.21: Biases on the parameters extracted from elliptic power law fits to the $p(v_2)$ distributions when the iteration cutoff criteria is $\chi^2/dof \leq 2$ to those extracted when the criteria is $\chi^2/dof \leq 1$.

ment amongst the two scenarios is observed in the bulk regions of the unfolded distributions, while deviations become significant toward the low-statistics tails. The tails are always biased to larger values indicating that the smearing effects have not been fully removed.

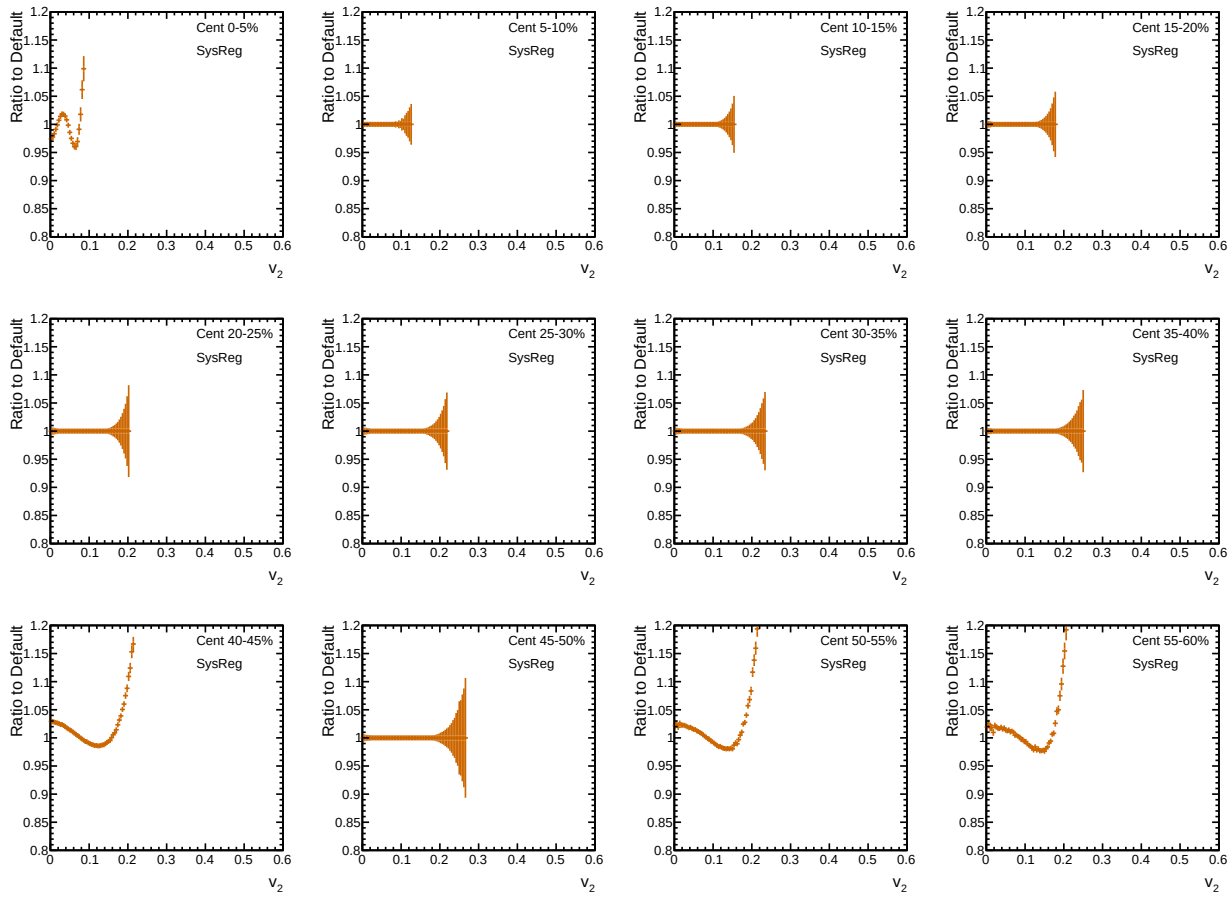

Figure 6.22: Systematic bias on the shape of $p(v_2)$ distributions that arises from regularized unfolding.

6.1.5 Response matrix uncertainty

To assess the potential bias from the choice in response matrix on the $p(v_2)$ distributions, the unfolding procedure is repeated using the Gaussian analytic response matrix described in Appendix B.1. The default choice in the analysis is to use the purely data-driven response matrix that does not assume an underlying functional form for the smearing effects. Given that for most centralities the distribution of smearing vectors can be described well with a Gaussian parametrization, the two approaches should give similar results. The differences in the two approaches are reported as as systematic uncertainty.

Results of this study are reported in Figs. 6.23 – 6.27. For each centrality bin, observables are extracted from the unfolded $p(v_2)$ distributions obtained using the default and Gaussian response matrices and ratios of the observables obtained using Gaussian response matrices relative to the default response matrix are determined. The trends observed in the ratios show how the choice in response matrix can bias the quantities. The cumulant bias shown in Fig. 6.23 and is on the order of 1% for most centralities. The bias in the ratios of higher-order cumulants is shown in Fig. 6.24 and exhibits a similar behavior as the cumulants. The least stable observable in this study is γ_1^{exp}, shown in Fig. 6.25, exhibiting similar behavior as the cumulants, but on a larger scale ($\sim 50\%$). In addition, the bias on the elliptic power law parameters is shown in Fig 6.26. Here, all three parameters show strong biases on the order of 50% in central and peripheral collisions. The bias is less significant in mid-central collisions, on the order of 1% for all parameters.

To assess the systematic uncertainty on the bins of the unfolded $p(v_2)$ distributions, the unfolded distributions obtained using the analytic Gaussian response matrix are first translated to have the same mean as the unfolded distributions obtained using the default response matrix. Bin-to-bin ratios relative to the default case are calculated and the maximum deviation is taken to be the systematic uncertainty for each. To avoid point-to-point statistical fluctuations, the ratios are first smoothed to fit the general trend. The result of this study is shown in Fig. 6.27. Here, agreement amongst the two response matrix scenarios is observed in the bulk regions of the unfolded distributions, while deviations become significant toward the low-statistics tails.

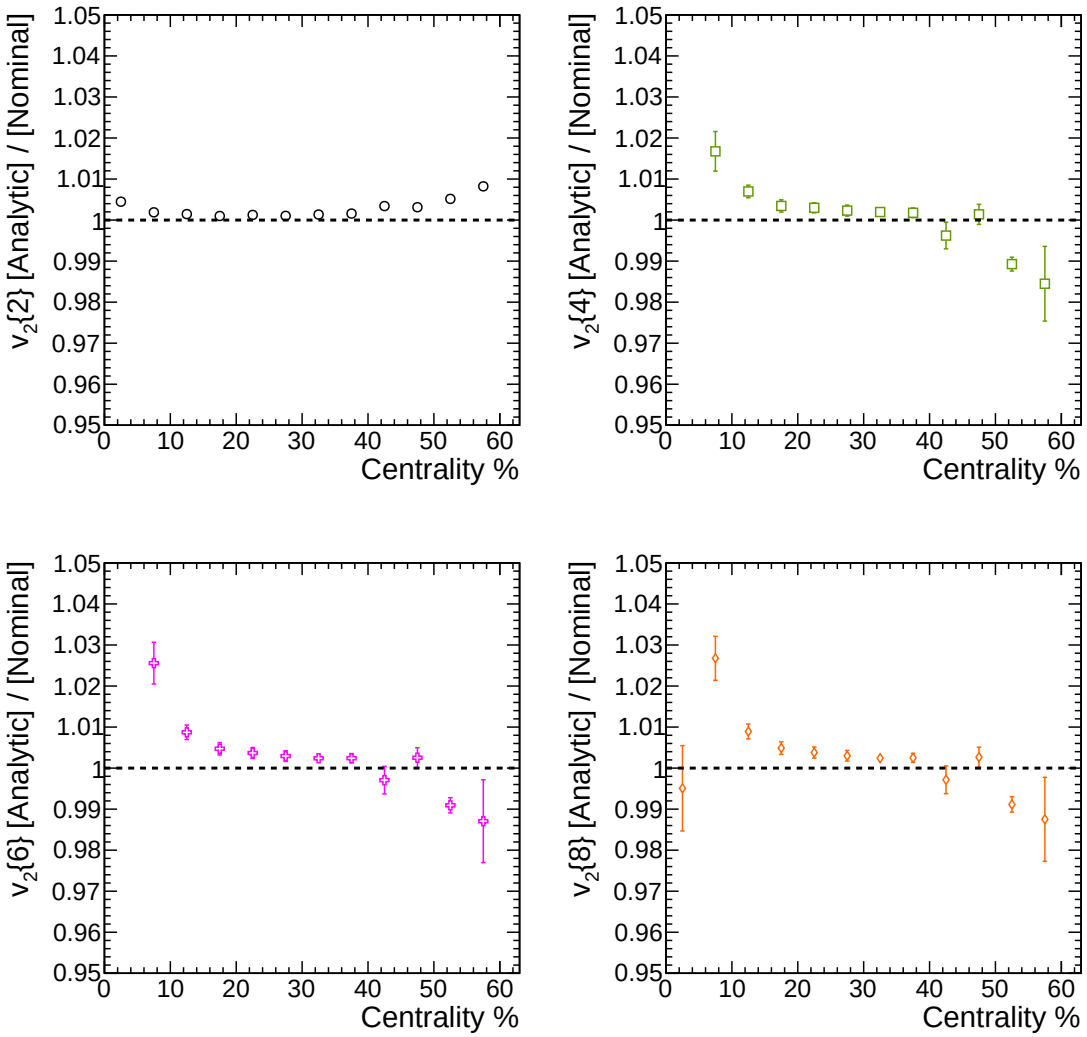

Figure 6.23: Bias on the cumulants extracted from $p(v_2)$ distributions obtained from Gaussian and data-driven unfolding.

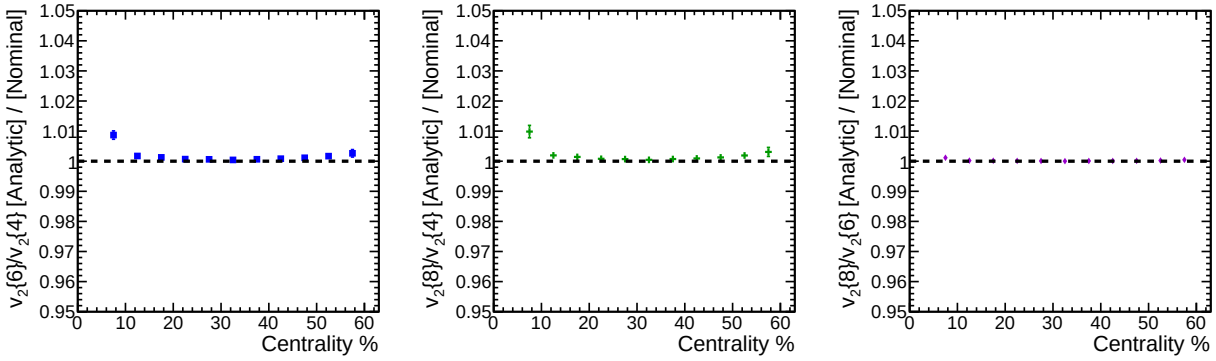

Figure 6.24: Bias on the higher-order cumulant ratios extracted from $p(v_2)$ distributions obtained from Gaussian and data-driven unfolding.

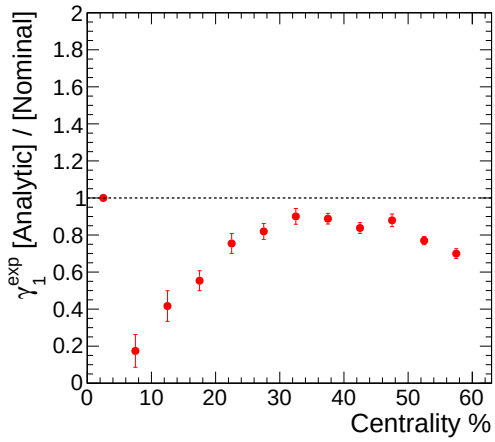

Figure 6.25: Bias on the skewness measure of $p(v_2)$ distributions for Gaussian unfolding relative to the default case.

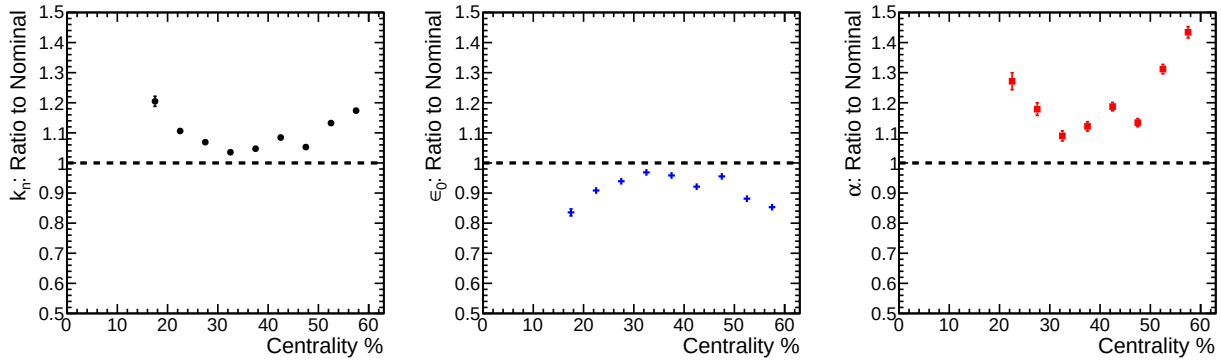

Figure 6.26: Biases on the parameters extracted from elliptic power law fits to the $p(v_2)$ distributions for Gaussian unfolding relative to the default case.

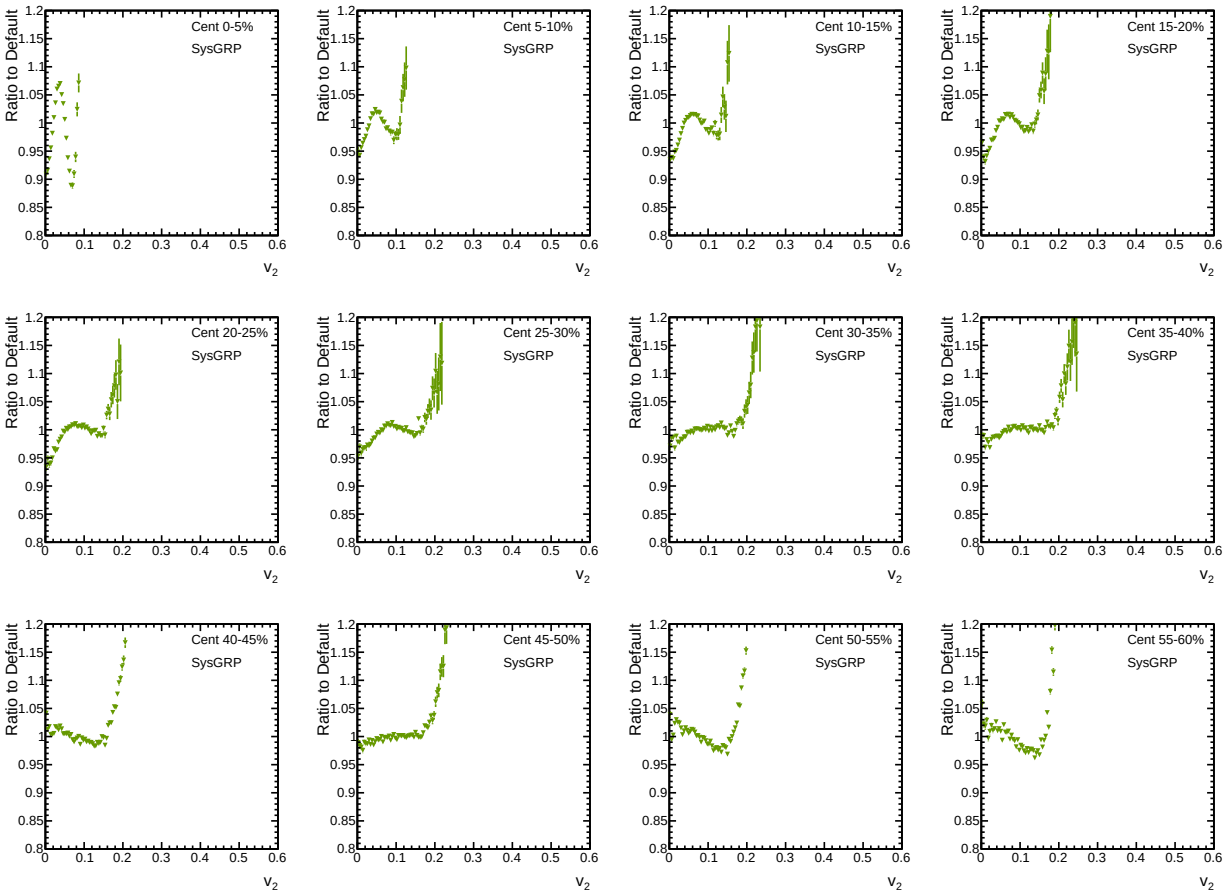

Figure 6.27: Systematic bias on the shape of $p(v_2)$ distributions that arises from the choice in response matrix.

In addition, since there is a finite amount of events used to build the response matrix in Sec. 5.2.1.1, there will be uncertainties on the individual matrix elements. By default, matrix element uncertainties are not propagated through unfolding iterations. The uncertainties on response matrix elements are considered to be a systematic uncertainty for the bins of the unfolded distributions, and have no effect on the quantities extracted from the distribution. It should be noted that the response matrix error propagation proposed in the original D'Agostini paper [220] underestimates this systematic uncertainty. The original implementation does not properly account for the fact that after the first iteration, the prior depends on the response matrix. The RooUnfold software package contains a corrected response matrix error propagation, as proposed in Ref. [225]. The resulting distributions from this additional error propagation contain identical bin contents to those run without, but with larger uncertainties. These propagated uncertainties are added in quadrature to the uncertainties obtained from the previous systematic studies to provide unfolded $p(v_2)$ distributions with statistical and systematic error bands. The final systematic $p(v_2)$ distributions are discussed in Sec. 6.1.6.

6.1.6 Systematic studies summary

The results of the systematic studies for quantities extracted from the unfolded $p(v_2)$ distributions are summarized in Table 6.3. An additional systematic uncertainty of 0.5% was placed on the cumulant values to account for the uncertainty in the tracking efficiencies. Total systematic uncertainties are determined by adding the contribution from each study in quadrature. Figure 6.28 presents the total systematic uncertainties on the bins of the unfolded $p(v_2)$ distributions. Total bin systematic uncertainties are obtained by adding the propagated matrix element uncertainties to the those obtained from the remaining systematic studies in quadrature. Systematic uncertainties are represented by gray bands.

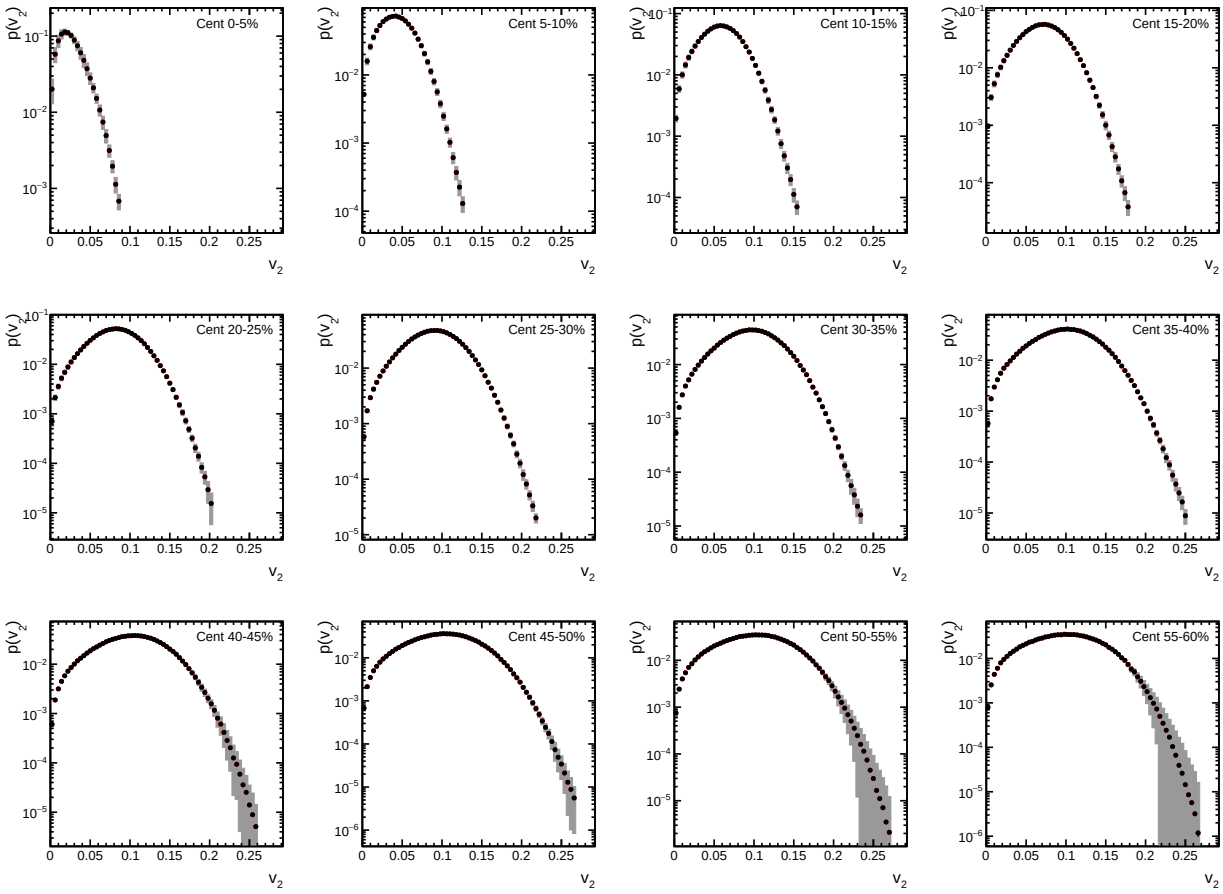

Figure 6.28: Final unfolded $p(v_2)$ distributions for 5% centrality intervals with statistical and systematic error bars. Systematic errors are represented by gray bands.

Table 6.3: Contribution from each systematic scale study. Systematic uncertainties reported as percentages.

	Source: Vertex Position Cuts							
	$v_2\{2\}$	$v_2\{4\}$	$v_2\{6\}$	$v_2\{8\}$	γ_1^{exp}	$v_2\{6\}/v_2\{4\}$	$v_2\{8\}/v_2\{4\}$	$v_2\{8\}/v_2\{6\}$
0–10%	1.6	4.1	4.5	4.5	106.9	0.9	1.1	0.1
10–20%	0.7	1.2	1.3	1.3	58.7	0.2	0.2	< 0.1
20–30%	0.3	0.6	0.7	0.7	23.6	0.1	0.1	< 0.1
30–50%	0.4	0.4	0.4	0.4	10.4	0.1	0.1	< 0.1
50–60%	0.4	0.9	0.7	0.7	16.5	0.1	0.2	< 0.1
	Source: Response Matrix Uncertainty							
	$v_2\{2\}$	$v_2\{4\}$	$v_2\{6\}$	$v_2\{8\}$	γ_1^{exp}	$v_2\{6\}/v_2\{4\}$	$v_2\{8\}/v_2\{4\}$	$v_2\{8\}/v_2\{6\}$
0–10%	0.2	1.7	2.4	2.5	81.8	0.6	0.6	< 0.1
10–20%	0.1	0.5	0.7	0.7	51.9	0.2	0.2	< 0.1
20–30%	0.1	0.3	0.3	0.3	21.7	0.1	0.1	< 0.1
30–50%	0.2	0.2	0.3	0.3	13.4	0.1	0.1	< 0.1
50–60%	0.7	1.5	1.2	1.1	26.2	0.2	0.2	< 0.1
	Source: Pileup Contamination							
	$v_2\{2\}$	$v_2\{4\}$	$v_2\{6\}$	$v_2\{8\}$	γ_1^{exp}	$v_2\{6\}/v_2\{4\}$	$v_2\{8\}/v_2\{4\}$	$v_2\{8\}/v_2\{6\}$
0–10%	0.1	0.3	0.1	0.1	27.9	0.2	0.3	< 0.1
10–20%	0.1	0.1	< 0.1	< 0.1	18.8	0.1	0.1	< 0.1
20–30%	0.1	< 0.1	< 0.1	< 0.1	9.4	< 0.1	< 0.1	< 0.1
30–50%	0.1	< 0.1	< 0.1	< 0.1	4.6	< 0.1	< 0.1	< 0.1
50–60%	0.1	< 0.1	0.1	0.1	3.1	< 0.1	< 0.1	< 0.1
	Source: Unfolding Regularization							
	$v_2\{2\}$	$v_2\{4\}$	$v_2\{6\}$	$v_2\{8\}$	γ_1^{exp}	$v_2\{6\}/v_2\{4\}$	$v_2\{8\}/v_2\{4\}$	$v_2\{8\}/v_2\{6\}$
0–10%	< 0.1	0.1	< 0.1	< 0.1	5.3	0.1	0.2	< 0.1
10–20%	< 0.1	0.1	0.2	0.2	20.1	0.1	0.1	< 0.1
20–30%	< 0.1	< 0.1	< 0.1	< 0.1	1.8	< 0.1	< 0.1	< 0.1
30–50%	< 0.1	0.2	0.2	0.2	4.6	< 0.1	< 0.1	< 0.1
50–60%	0.1	1.4	1.4	1.4	17.4	0.2	0.2	< 0.1
	Source: Track Quality Cuts							
	$v_2\{2\}$	$v_2\{4\}$	$v_2\{6\}$	$v_2\{8\}$	γ_1^{exp}	$v_2\{6\}/v_2\{4\}$	$v_2\{8\}/v_2\{4\}$	$v_2\{8\}/v_2\{6\}$
0–10%	1.2	2.1	2.1	2.1	20.3	0.2	0.2	< 0.1
10–20%	0.9	1.1	1.1	1.1	10.6	< 0.1	< 0.1	< 0.1
20–30%	0.6	0.7	0.6	0.6	2.5	< 0.1	< 0.1	< 0.1
30–50%	0.6	0.5	0.5	0.5	1.7	< 0.1	< 0.1	< 0.1
50–60%	0.6	0.4	0.4	0.4	3.9	< 0.1	< 0.1	< 0.1
	Source: Tracking Efficiencies							
	$v_2\{2\}$	$v_2\{4\}$	$v_2\{6\}$	$v_2\{8\}$	γ_1^{exp}	$v_2\{6\}/v_2\{4\}$	$v_2\{8\}/v_2\{4\}$	$v_2\{8\}/v_2\{6\}$
0–60%	0.5	0.5	0.5	0.5	< 0.1	< 0.1	< 0.1	< 0.1
	Total Systematic Uncertainty							
	$v_2\{2\}$	$v_2\{4\}$	$v_2\{6\}$	$v_2\{8\}$	γ_1^{exp}	$v_2\{6\}/v_2\{4\}$	$v_2\{8\}/v_2\{4\}$	$v_2\{8\}/v_2\{6\}$
0–10%	2.1	4.9	5.5	5.6	139.1	1.2	1.3	0.1
10–20%	1.1	1.7	1.9	1.9	83.7	0.3	0.3	< 0.1
20–30%	0.7	0.9	1.0	1.0	33.6	0.1	0.1	< 0.1
30–50%	0.8	0.7	0.7	0.8	18.6	0.1	0.1	< 0.1
50–60%	1.0	2.3	2.1	2.0	36.1	0.3	0.4	0.1

6.2 Cross-checks

6.2.1 Tracker p_{T} resolution

Differential flow measurements [97, 53] have shown a strong linear p_{T} dependence of v_2 harmonics at low p_{T}. Given the p_{T} resolution of the tracker [200], shown in Fig. 3.4, it is necessary to check the sensitivity of this analysis to biases from low p_{T} particles leaking into and out of the acceptance, which will alter the mean p_{T} of particles measured in this analysis. To study this potential bias, the analysis is re-run over minimum bias events, but with an additional 5% smearing in p_{T} added to each track. Ratios of the observables obtained to using the additionally smeared data relative to the nominal tracking results are determined and the results of this study are shown in Figs. 6.29 – 6.31 for each. There is no statistically significant bias present for observables across all centralities in this study. The typical resolution for the kinematic region explored in this analysis is on the order of 1% and the observation of stable results in this study is evidence that this analysis technique is not sensitive to the p_{T} resolution of the tracker. Therefore, tracker p_{T} resolution is not considered as a source of systematic uncertainty for this analysis.

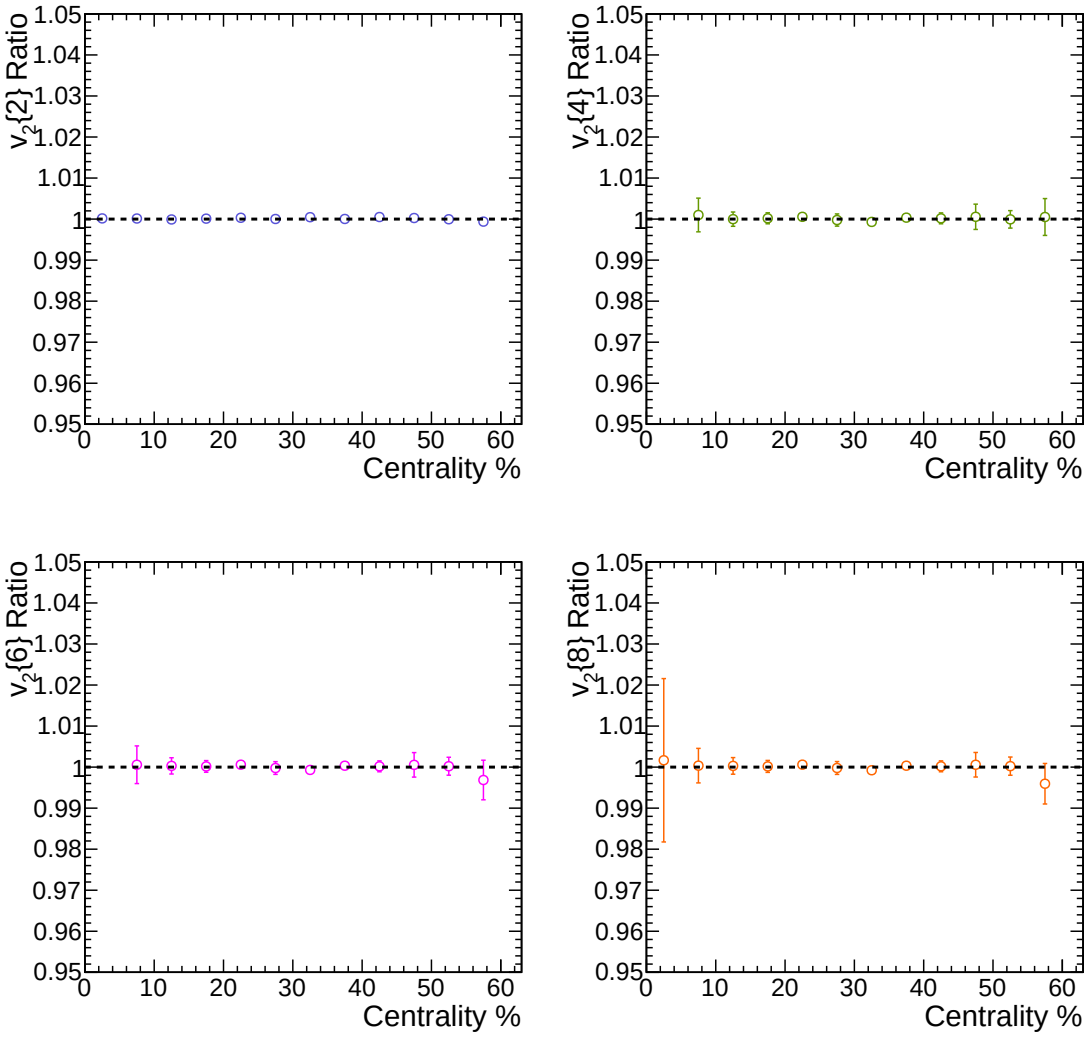

Figure 6.29: Systematic bias on the cumulants extracted from unfolded $p(v_2)$ distributions as a result of the tracker p_{T} resolution. Biases reported are ratios of the additionally smeared data relative to the nominal data selection.

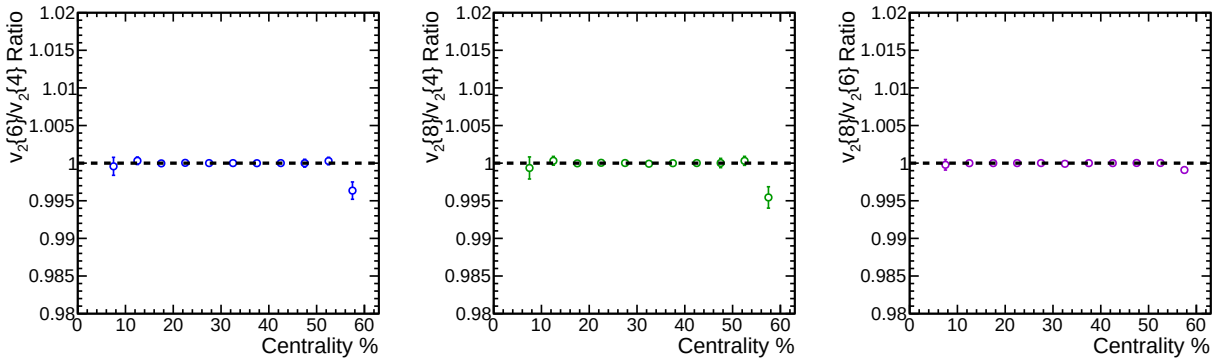

Figure 6.30: Systematic bias on the higher-order cumulant ratios extracted from unfolded $p(v_2)$ distributions as a result of the tracker p_{T} resolution. Biases reported are ratios of the additionally smeared data relative to the nominal data selection.

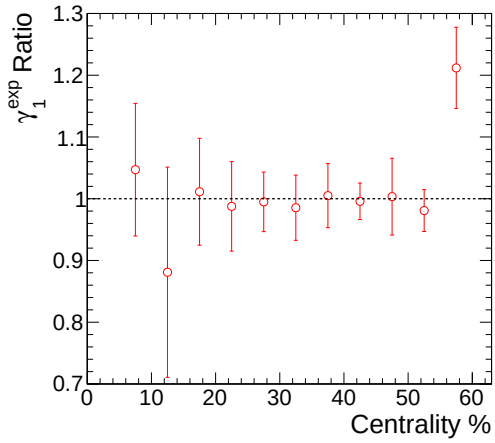

Figure 6.31: Systematic bias on the skewness extracted from unfolded $p(v_2)$ distributions as a result of the tracker p_{T} resolution. Biases reported are ratios of the additionally smeared data relative to the nominal data selection.

6.2.2 SVD unfolding

As an additional cross-check on the unfolding analysis, the unfolding procedure is repeated using a different approach to invert the response matrix. In this case, the observed flow distributions and response matrices are determined as outlined in Secs. 5.1 and 5.2.1, respectively. However, instead of using D'Agostini iteration to invert the response matrix, the SVD Tikhonov regularization [223] technique is used. In short, SVD unfolding is a least-squares approach that aims to minimize

$$\chi^2 = \left[p(v_{n,i}^{\text{obs}}) - K_{ij}p(v_{n,j})\right]^{\text{T}} V_{il}^{-1} \left[p(v_{n,l}^{\text{obs}} - K_{lk}p(v_{n,k})\right] + \delta P\left[p(v_n)\right], \tag{6.1}$$

where $p(v_{n,i}^{\text{obs}})$ is a vector that represents the observed distribution, $K_{ij} = p(v_{n,i}^{\text{obs}}|v_{n,j})$ is the response matrix, $p(v_{n,j})$ is a vector that represents the underlying flow behavior that minimizes this χ^2, $P\left[p(v_n)\right]$ is a penalty term that encourages physical solutions, and δ is a term that determines the penalty strength. The penalty term can be written as [229]

$$P\left[p(v_n)\right] = \left\| \mathbf{L} \begin{bmatrix} p(v_{n,1})/p_0(v_{n,1}) \\ p(v_{n,2})/p_0(v_{n,2}) \\ \vdots \\ p(v_{n,j})/p_0(v_{n,j}) \end{bmatrix} \right\|^2, \tag{6.2}$$

where $\mathbf{L}$ is a discretized second derivative operator, and $p_0(v_n)$ is the initial prior discussed in Sec. 5.2.2. This technique is regularized by the δ term, which is chosen as the number of significant elements in a rotated $p(v_{n,i}^{\text{obs}})$ vector that occurs during a singular-value decomposition of the response matrix [223].

Results of this cross-check are shown in Figs. 6.32 – 6.35. In this study, both the unfolded distributions and quantities extracted from each technique are compared. In the comparison of the unfolded distributions, shown in Fig. 6.32, the unfolded distributions from each technique are consistent in the bulk regions, but differ out at the tails for peripheral events. To further explore this deviation, the quantities extracted from each distribution for each technique are compared

in Figs. 6.33 – 6.35. For most centralities, the results are consistent within uncertainties, but deviations become statistically significant for peripheral events. The deviation can be described qualitatively by a phenomenon that occurs in the low-statistics tails of distributions obtained using the SVD unfolding technique. For mid-central to peripheral bins, the tails of the SVD unfolded distributions yield negative probabilities, which is clearly unphysical.

This negative probability effect is explored in further detail using a toy MC where there is complete control over the inputs to the unfolding procedure. The results of the toy MC study are shown in Fig. 6.36 where unfolded distributions obtained using both SVD and D'Agostini iteration unfolding are compared to the MC truth distribution. Even in a toy MC, the SVD bin contents yield negative probabilities at large v_2 values. This is a consequence of the effectiveness of each technique when bin contents in the observed distribution are small (< 10). The SVD approach is essentially a least-squares fit, which implies that low event counts are not treated correctly [223]. This often manifests as negative probabilities in unfolded distributions. Contrary to SVD, D'Agostini iteration is a MLE approach [220], which better handles low event counts and suppresses negative probability effects in unfolded distributions. Thus, D'Agostini iteration is a more robust unfolding technique for this analysis and discrepancies between the two approaches are not considered as a source of systematic uncertainty.

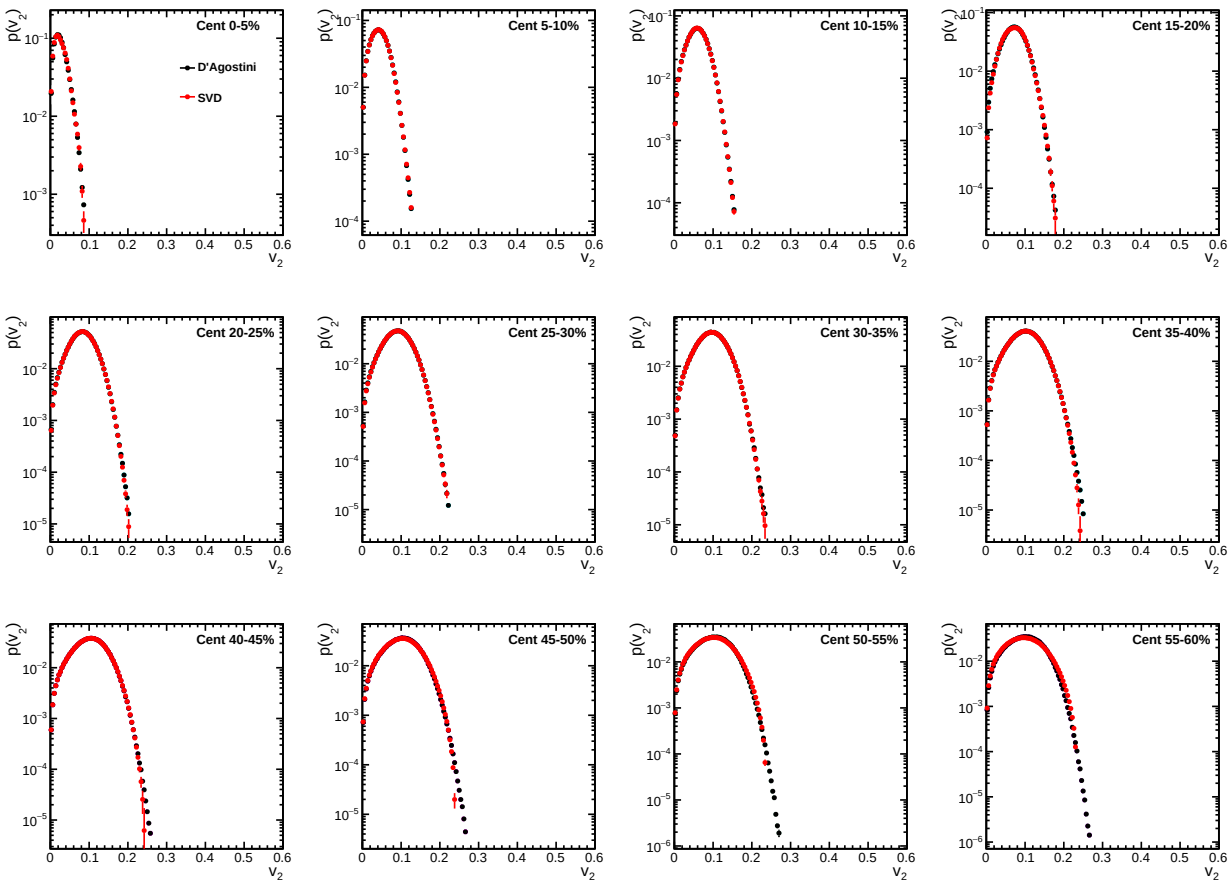

Figure 6.32: Final unfolded $p(v_2)$ distributions for 5% centrality intervals for both D'Agostini and SVD unfolding. D'Agostini unfolding has both statistical and systematic uncertainties while SVD unfolding has only statistical errors.

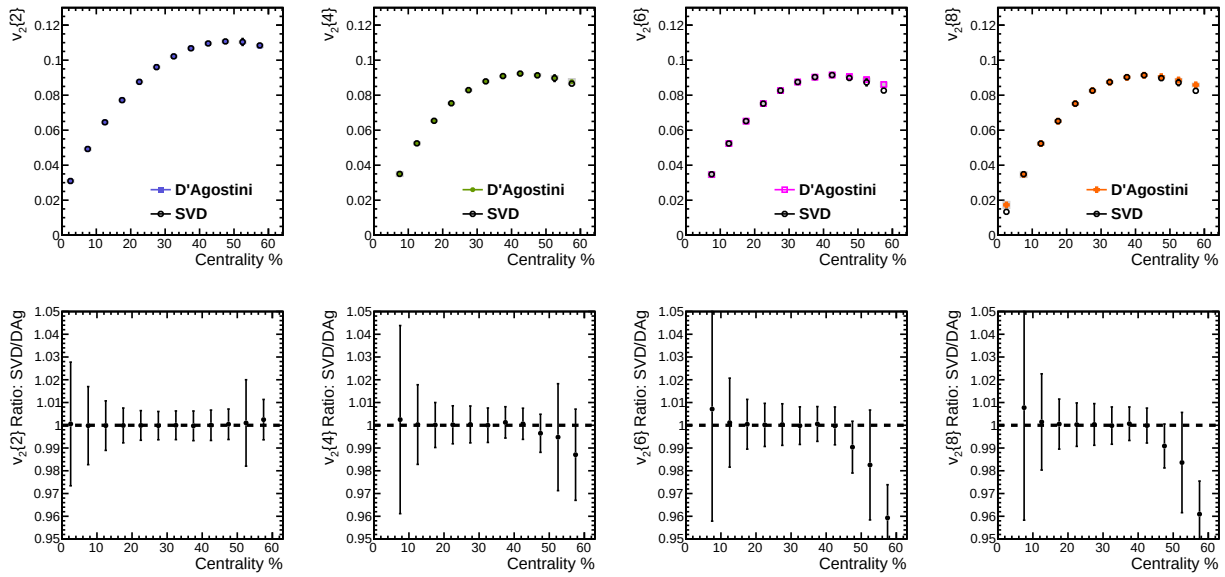

Figure 6.33: Cumulants extracted from $p(v_2)$ distributions obtained using both D'Agostini and SVD unfolding. D'Agostini unfolding has both statistical and systematic uncertainties while SVD unfolding has only statistical errors.

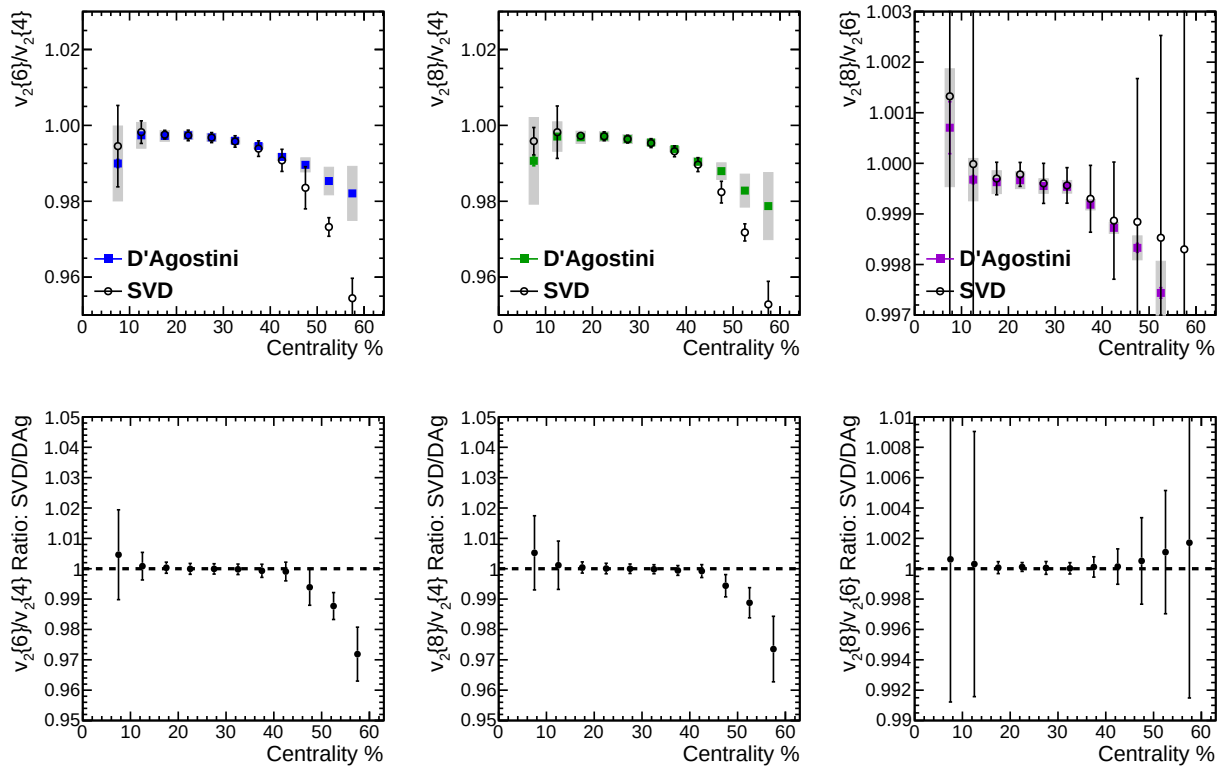

Figure 6.34: Higher-order cumulant ratios extracted from $p(v_2)$ distributions obtained using both D'Agostini and SVD unfolding. D'Agostini unfolding has both statistical and systematic uncertainties while SVD unfolding has only statistical errors.

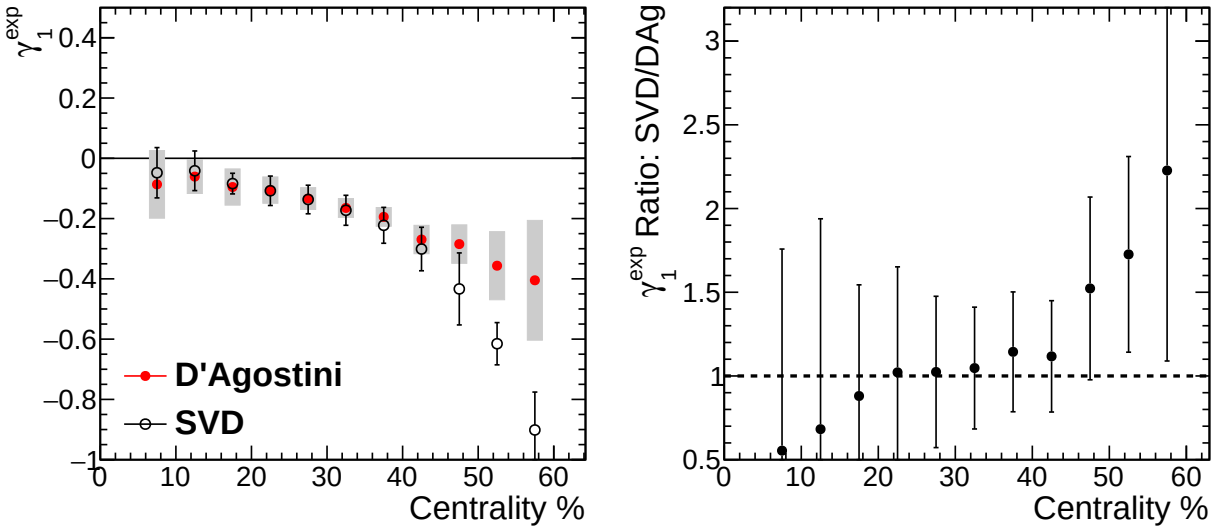

Figure 6.35: Skewness measure of $p(v_2)$ distributions obtained using both D'Agostini and SVD unfolding. D'Agostini unfolding has both statistical and systematic uncertainties while SVD unfolding has only statistical errors.

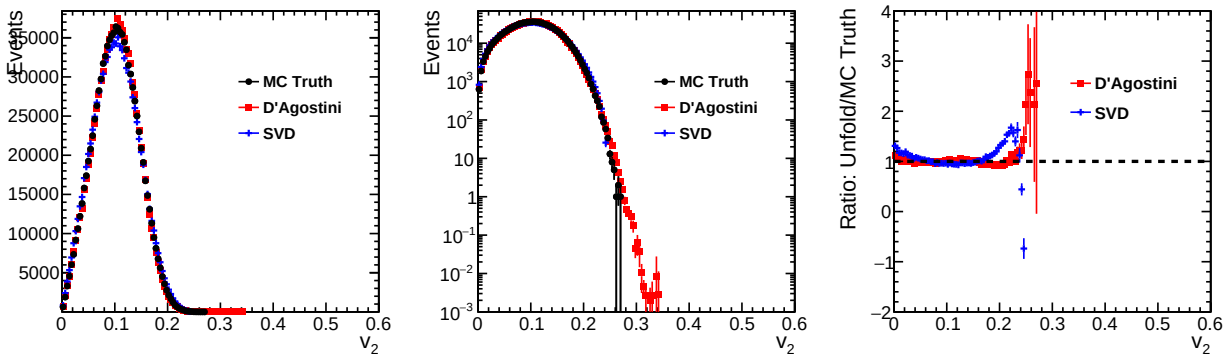

Figure 6.36: Toy MC unfolded $p(v_2)$ distributions obtained using both D'Agostini and SVD unfolding compared to the MC truth distribution. The first two panels show the same distributions, but on linear and semi-log scale respectively. The final panel shows the ratio of the unfolded distribution to the MC truth distribution and at large v_2 values the negative probabilities from SVD unfolding can be seen.

Chapter 7

Results

7.1 Cumulant elliptic flow harmonics

Cumulant elliptic flow harmonics are determined from the moments of the unfolded $p(v_2)$ distributions using Eqs. (2.4) and (2.7). Figure 7.1 shows the behavior of the cumulant flow harmonics for the four lowest, non-vanishing cumulant orders as a function of event centrality. For all centralities, the cumulant flow harmonics show the previously observed $v_2\{2\} > v_2\{4\} \approx v_2\{6\} \approx v_2\{8\}$ behavior [187, 188, 189]. However, a splitting between the higher-order cumulant flow harmonics is also evident in the peripheral bins. This splitting between the higher-order cumulant flow harmonics is explored further in Sec. 7.2.

In addition to obtaining cumulant flow harmonics from unfolded $p(v_2)$ distributions, cumulants can also be obtained using m-particle correlations using the right hand side of Eq. (2.4) and Eq. (2.7). To cross-check the unfolding analysis, a m-particle correlation analysis was run using the same event and track selection. The cumulant flow harmonic results for both analyses are reported in Fig. 7.2, where, for most centrality bins, the results are consistent amongst the two analysis techniques. However, significant deviations between the two approaches are observed in central bins, which is understood by each technique's sensitivity to non-flow.

The sensitivity to non-flow for each technique is studied using the HIJING event generator. By default, HIJING does not simulate flow effects and any flow signals measured in HIJING events

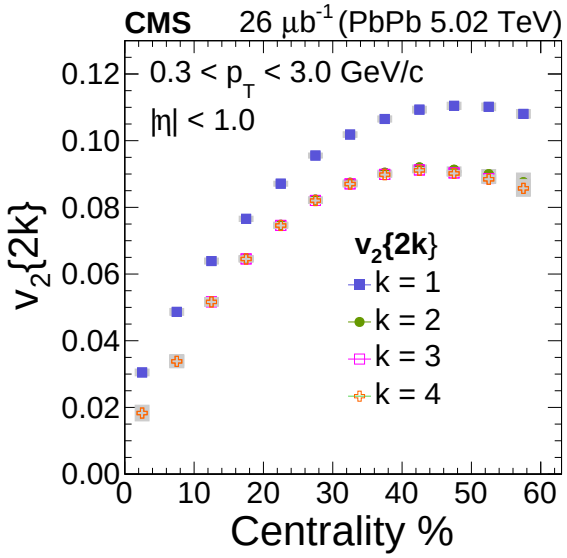

Figure 7.1: Cumulant values extracted from the unfolded $p(v_2)$ distributions exhibiting the expected $v_2\{2\} > v_2\{4\} \approx v_2\{6\} \approx v_2\{8\}$ behavior. Both statistical and systematic uncertainties are shown. A fine-level splitting of the higher-order cumulants becomes more pronounced in peripheral bins.

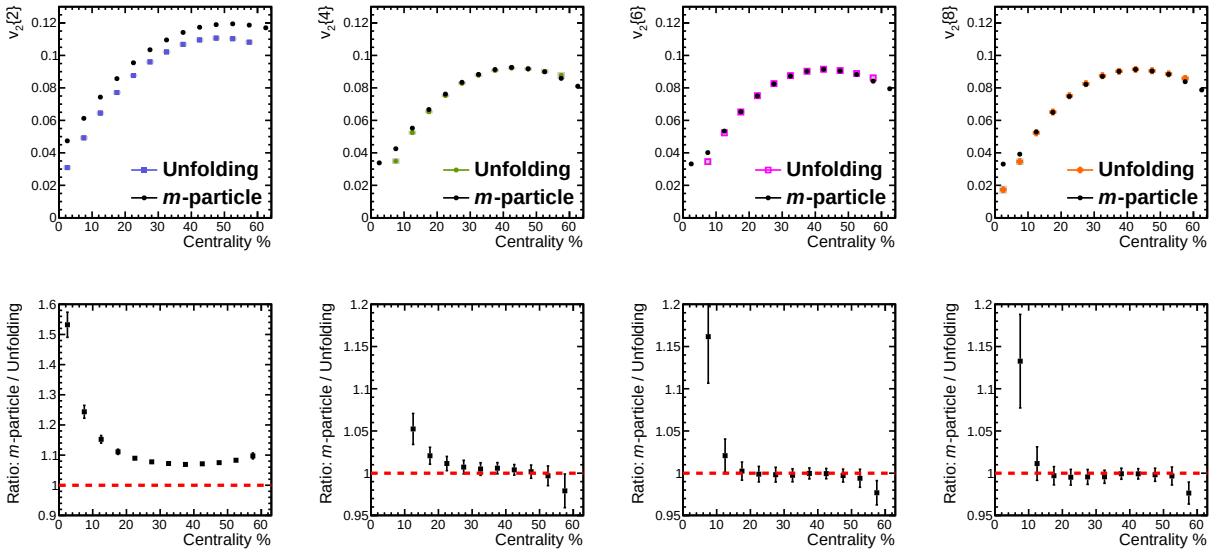

Figure 7.2: Comparison of cumulants extracted from unfolded $p(v_2)$ distributions to those obtained through multi-particle correlation measurements.

will be a result of non-flow correlations. A flow afterburner is run on top of HIJING events to impose a physical flow signal that largely preserves the underlying non-flow from event generation. Three studies are performed to assess the sensitivity to non-flow for m-particle cumulant flow harmonics and cumulant flow harmonics obtained from unfolded $p(v_2)$ distributions:

1. The "HIJING + flow" study: HIJING events are generated and a flow afterburner is applied that introduces a v_2 signal that fluctuates event-by-event. The v_2 fluctuations are parametrized by an elliptic power law distribution similar to the parametrizations found in Sec. 7.3 for mid-central collisions.

2. The "HIJING" study: HIJING events are generated and no afterburner is applied. If each analysis technique was completely insensitive to non-flow, one would expect the techniques to return cumulants with a value consistent with 0.

3. The "Flow" study: Events are generated using a toy MC that only accounts for event-by-event elliptic flow fluctuations. To be consistent, the elliptic flow fluctuations are parametrized using the same elliptic power law distribution from the HIJING + flow study.

Results from each of the non-flow studies are shown in Fig. 7.3. In all studies where there is a flow signal, the unfolding cumulant flow harmonics are statistically consistent with the MC truth. In cases where non-flow present, the m-particle correlations technique always returns cumulants larger than the unfolding results. This behavior suggests that the multi-particle cumulants are more sensitive to non-flow than the unfolding cumulants. When non-flow is removed, the two techniques converge on the same values, which are statistically consistent with the MC truth. The unfolding results in the HIJING study should only be interpreted qualitatively as the unfolded distribution is highly unstable. The unfolded distribution is illustrated in Fig. 7.4 and is the result of over 130 000 iterations. The unfolding behavior appears to be converging on a very small signal, with a very small width, similar to a Dirac delta Function. The extracted cumulants in this case are consistent with the bin width of the histogram representing the unfolded distribution. This issue arises because the unfolding technique inherently assumes smooth behavior for all iterations, but

in this case is attempting to unfold a delta function-like behavior. Regardless, results of the three MC studies provide evidence that the m-particle cumulant flow harmonics are more sensitive to non-flow than those obtained from unfolding. Therefore, the unfolding is a more robust technique for measuring cumulant flow harmonics.

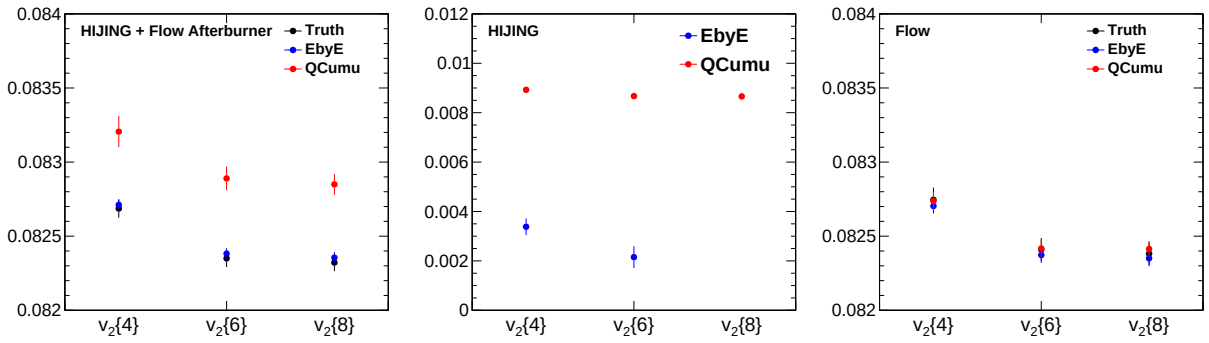

Figure 7.3: Comparison of cumulants extracted from unfolded $p(v_2)$ distributions to those obtained through multi-particle correlation measurements using the HIJING event generator. Results are compared to the truth values for scenarios where there are non-flow and flow signals, flow signals only, and non-flow signals only present in the generated events.

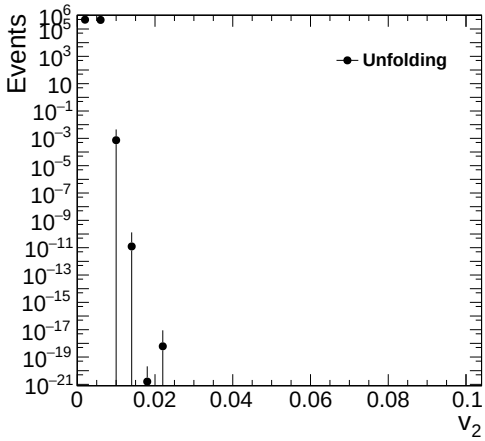

Figure 7.4: Final unfolded distribution for the HIJING study. Unlike the other studies that take on the order of 4 iterations to converge, this distribution is the result of 130 000 iterations. Unfolding results are unreliable in this case, as the procedure is trying to reproduce a distribution that has a small signal and essentially zero width.

7.2 Skewness of elliptic flow probability distributions

As was discussed in Chapter 2, the observation that $v_2\{4\} \approx v_2\{6\} \approx v_2\{8\}$ suggests that the elliptic flow fluctuations are nearly Gaussian in nature. However, a lifted degeneracy in the cumulant flow harmonics is expected based on non-Gaussian fluctuations in the initial state [178]. The emergent splitting of the higher-order cumulant flow harmonics in Fig. 7.1 is quantified further by inspecting ratios of differing-order cumulant flow harmonics. The ratios of the higher-order cumulant flow harmonics are shown in Fig. 7.5 as a function of event centrality. Here, the degeneracy is lifted in the higher-order cumulant flow harmonics such that $v_2\{4\} > v_2\{6\} > v_2\{8\}$, providing evidence of a deviation from the Gaussian model for elliptic flow fluctuations. In addition, the cumulant flow harmonics are extracted with such precision that a fine-level splitting between the $v_2\{6\}$ and $v_2\{8\}$ is observed on the order of 0.1% for the first time.

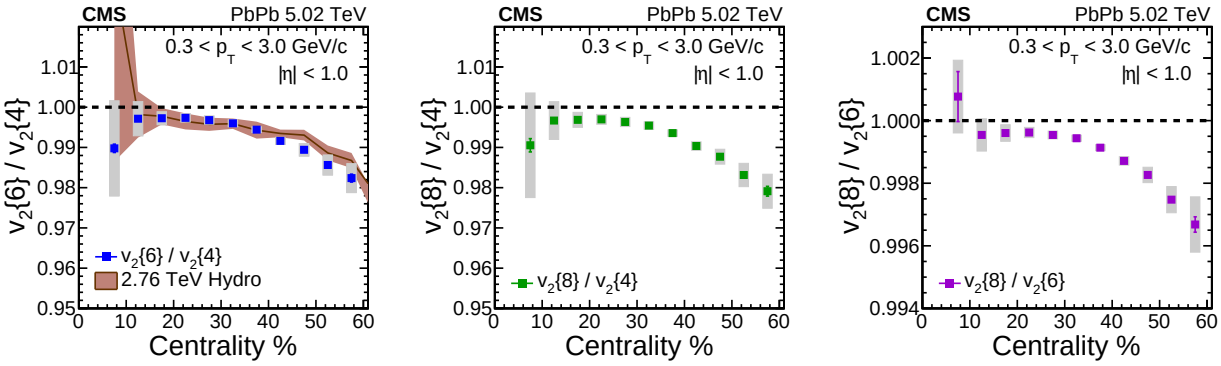

Figure 7.5: Ratios of higher-order cumulants with values obtained from the moments of the unfolded $p(v_2)$ distributions. Both statistical and systematic uncertainties are shown. Hydrodynamic predictions for 2.76 TeV from Ref. [178] are presented as a colored band and are compared to the measured $v_2\{6\}/v_2\{4\}$ ratio. Theory predictions are consistent to the measurement within uncertainties.

The primary finding in the hydrodynamic study in Ref. [178] was that the initial-state elliptic anisotropy probability distribution is skewed with respect to the reaction plane and that the elliptic flow response reflects this behavior. The results in Fig. 7.5 are further supported by the results in Fig. 7.6, where the cumulant flow harmonics are used to estimate the skewness of the elliptic flow probability distributions with respect to the reaction plane (γ_1^{exp}). Here, a statistically significant

negative skewness is observed for the same centralities that exhibit a splitting between the higher-order cumulant flow harmonics. A negative skewness is also consistent with the observed $v_2\{4\} > v_2\{6\} > v_2\{8\}$ ordering of the cumulant flow harmonics.

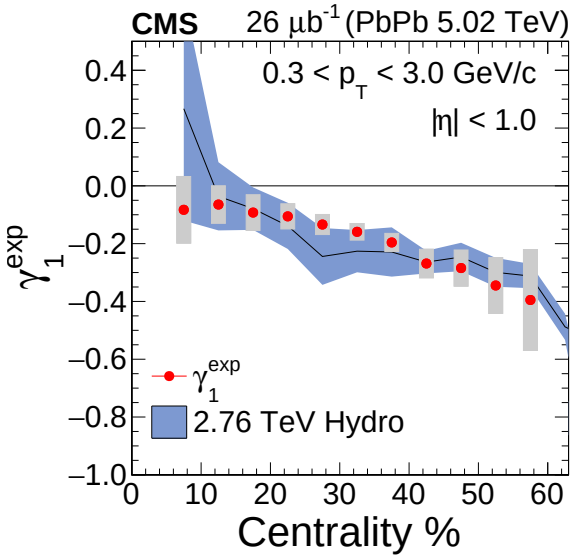

Figure 7.6: The estimated skewness for the unfolded $p(v_2)$ as determined from its cumulant flow harmonics with Eq. (2.12). Both statistical and systematic uncertainties are shown. Hydrodynamic predictions for 2.76 TeV from Ref. [178] are presented as a colored band and are compared to the measured skewness. Theory predictions are consistent to the measurement within uncertainties.

The results of the hydrodynamic study in Ref. [178] are available to compare to the measured $v_2\{6\}/v_2\{4\}$ and γ_1^{exp} values and are shown in the respective figures as colored bands. Within the study, event-by-event hydrodynamic calculations were performed using Monte-Carlo Glauber initial conditions for PbPb collisions at $\sqrt{s_{\text{NN}}} = 2.76$ TeV energies. The hydrodynamic calculations used an η/s value of 0.08 and assumed that the flow response was linear with a response coefficient of $\kappa = 0.21$. Elliptic flow harmonics were obtained for pions with $0.2 < p_{\text{T}} < 3.0$ GeV/c and were used to construct the cumulant flow harmonics and elliptic flow skewness. In addition, the 5.02 TeV $v_2\{6\}/v_2\{4\}$ and $v_2\{8\}/v_2\{4\}$ results are compared in Fig. 7.7 to previous measurements by the ATLAS collaboration in Ref. [189] for 2.76 TeV. In this comparison, the quantities measured by the ATLAS collaboration used a different track selection than those in the 5.02 TeV analysis. There, ATLAS selected tracks with $0.5 < p_{\text{T}} < 20$ GeV/c and $|\eta| < 2.5$. The hydrodynamic cal-

culations are consistent with the experimental results found at both beam energies. Since only small changes are expected for the initial-state eccentricities between 2.76 and 5.02 TeV [230], agreement between hydrodynamic predictions and different collision energies might be expected.

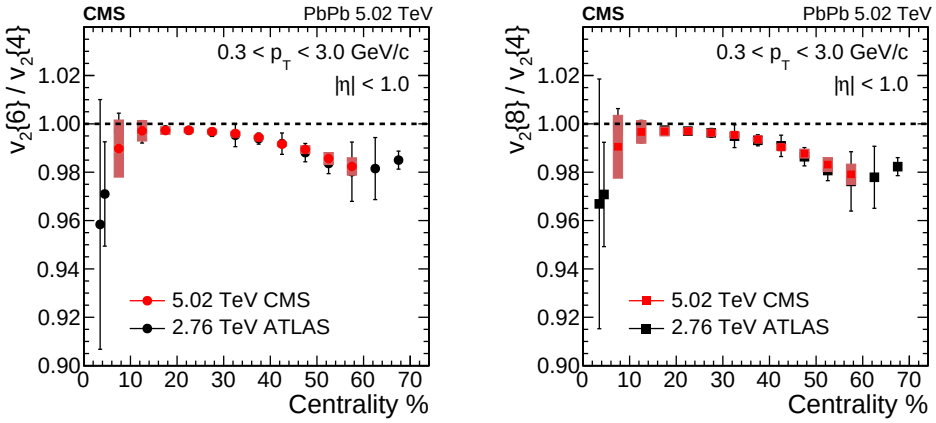

Figure 7.7: Ratios of higher-order cumulants with values obtained from the moments of the unfolded $p(v_2)$ distributions measured by CMS compared to those measured by ATLAS in Ref. [189]. Both statistical and systematic uncertainties are shown for CMS as error bars and bands respectively. ATLAS uncertainties are presented as statistical and systematic added in quadrature.

7.3 Parametrizing the elliptic flow probability distributions

To gain further insight on the nature of the elliptic flow fluctuations, unfolded $p(v_2)$ distributions are fitted with elliptic power law (Eq. (2.14)) and Bessel Gaussian (Eq. (2.3)) parametrizations. The elliptic power law fits are done by first rewriting Eq. (2.13) in terms of the flow coefficients assuming a linear flow response, with $v_n = k_n \varepsilon_n$. Figure. 7.8 demonstrates the fit results for 5% wide centrality bins for both the elliptic power law and Bessel-Gaussian parametrizations. Fit qualities are assessed by refolding the fits using the response function and determining a χ^2/dof goodness of fit with respect to the observed distribution. This is done to suppress biases in χ^2 due to the bin-to-bin correlations in the unfolded distributions. In all cases the elliptic power law parametrization better describes the fluctuations, yielding a χ^2/dof goodness-of-fit closer to 1 than for the Bessel-Gaussian. Fits are not shown below 15% centrality, as the fits do no converge below this limit.

The elliptic power law parametrization outperforms the Bessel Gaussian parametrization, as it is a more generalized function that naturally incorporates a finite skewness and has more free parameters than the Bessel Gaussian. In addition, the elliptic power law parameterization is a more attractive candidate for describing the fluctuation behavior, because the flow response coefficient k_n factorizes when fluctuations are non-Gaussian [191], meaning that it is a free parameter in the transformed elliptic power law parametrization. This implies that the response coefficient can be extracted from these fits without assuming a model for the initial-state conditions. When $p(v_2)$ distributions are fitted with a transformed Bessel Gaussian, the k_n parameters cannot be disentangled, resulting in the extraction of combined $k_n\langle v_n^{\mathrm{RP}}\rangle$ and $k_n\delta_{v_n}$ parameters. The centrality dependence of the response coefficient is of interest because viscous hydrodynamics predict that deviation from thermal equilibrium result in a reduced correspondence between initial spatial anisotropy and flow in peripheral collisions [231, 232]. A reliable extraction of the centrality dependence of the response coefficient therefore provides an independent measure of the viscosity of the medium.

The centrality dependence of parameters extracted from elliptic power law fits to the unfolded $p(v_2)$ distributions is shown in Fig 7.9. Here, the parameters extracted from the ATLAS $p(v_2)$

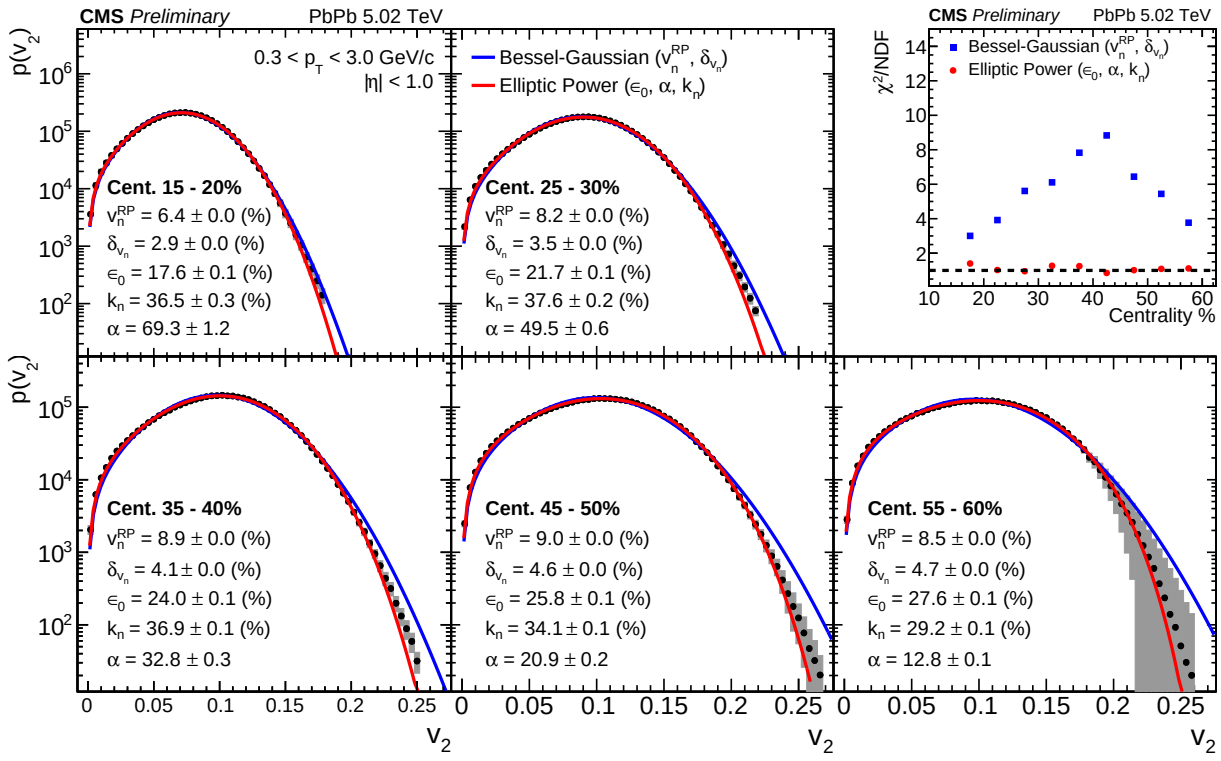

Figure 7.8: Elliptic power law (Eq. (2.14)) and Bessel-Gaussian (Eq. (2.3)) parametrizations fitted to unfolded $p(v_2)$ distributions. Parameters extracted from each fit are provided in each panel with respective statistical uncertainties. All parameters except α are reported as percentages. Fit performance, as measured by the smeared-space χ^2/dof goodness-of-fit, is presented as a function of centrality for each parametrization.

distributions and theoretical predictions from Ref. [183] are compared to the current analysis. Theoretical predictions are obtained using Glauber and IP-Glasma [172, 173] initial conditions, where the IP-Glasma model includes gluon saturation effects. The Glauber and IP-Glasma predictions for ε_0 and α parameters qualitatively capture the measured behavior, but deviate in magnitude. The behavior of the response coefficient for both the ATLAS and hydrodynamic predictions using $\eta/s = 0.19$ are in agreement with the current analysis. The consistency between the three independent measurements provides the first steps toward a model-independent method for extracting the response coefficients and the viscosity of the medium. The extracted parameters for the elliptic power law fits are provided in Table 7.1 with respective statistical uncertainties.

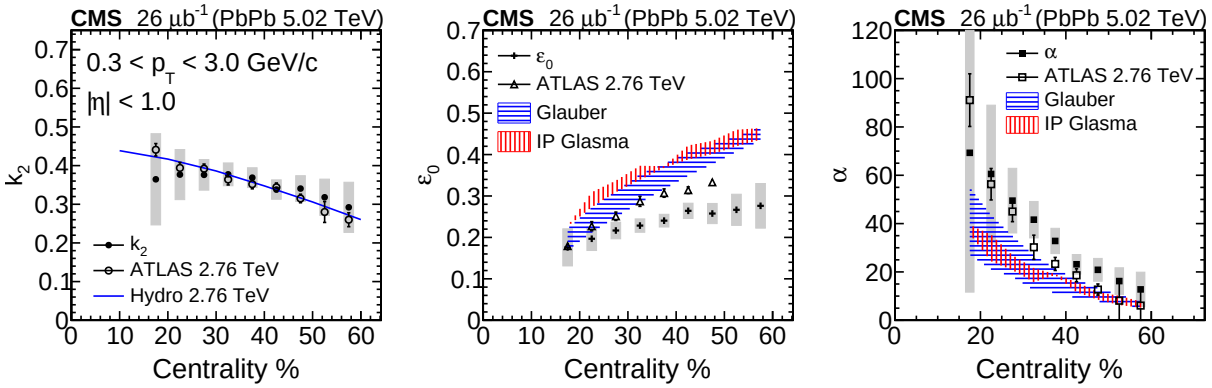

Figure 7.9: Centrality dependence of the parameters extracted from elliptic power law fits to the unfolded $p(v_2)$ distributions. Solid lines represent theoretical calculations from Ref. [183] using viscous hydrodynamics with Glauber initial conditions and an η/s value of 0.19 to determine the response coefficient (green line). In addition, the Glauber (blue lines) and IP Glasma (red lines) models were used to predict the α and ε_0 parameters. Parameters obtained from fits to the ATLAS unfolded $p(v_2)$ distributions for PbPb collisions at 2.76 TeV are plotted as open symbols.

Table 7.1: Parameters extracted from elliptic power law fits to unfolded $p(v_2)$ distributions.

Centrality	α	k_n	ε_0
15–20%	69.3 ± 1.2	0.3646 ± 0.0029	0.1759 ± 0.0014
20–25%	60.5 ± 0.9	0.3768 ± 0.0023	0.1967 ± 0.0012
25–30%	49.5 ± 0.6	0.3761 ± 0.0019	0.2166 ± 0.0011
30–35%	41.6 ± 0.4	0.3774 ± 0.0017	0.2285 ± 0.0010
35–40%	32.8 ± 0.3	0.3688 ± 0.0014	0.2404 ± 0.0009
40–45%	23.2 ± 0.2	0.3380 ± 0.0010	0.2641 ± 0.0007
45–50%	20.9 ± 0.2	0.3406 ± 0.0010	0.2576 ± 0.0007
50–55%	16.2 ± 0.1	0.3181 ± 0.0008	0.2666 ± 0.0006
55–60%	12.8 ± 0.1	0.2921 ± 0.0007	0.2762 ± 0.0005

7.4 Event-shape engineering

Moving beyond the elliptic flow harmonic, the triangular and quadrangular flow harmonic fluctuations are studied using a different analysis technique, event-shape engineering. The goal in this study is to look at detailed correlations between flow harmonics of different orders and their respective fluctuation behavior. The triangular and quadrangular flow fluctuations are expected to follow the Gaussian model of fluctuations [175] and the event-shape engineering technique will provide insights as to how the elliptic flow harmonic fluctuations influence these distributions.

Correlations between the moments of $p(v_n)$ distributions are obtained by coupling the event-shape selection to the unfolding technique. Here, $p(v_n)$ distributions for harmonics $n = 2$–4 are obtained for 5% wide centrality bins up to 60%. Within each centrality bin, events are further divided into 10% bins based on their ellipticity q_2 measured by the HF calorimeters. This event classification transforms a single centrality bin into 10 data points, allowing access to detailed correlations that are otherwise destroyed using event-averaging techniques. For each flow harmonic distribution, the first and second moments are extracted and correlated to spectrum-weighted average q_2 values. In addition, the moments of different-order harmonics are correlated using the same q_2 selection.

The correlations between the moments of elliptic flow probability distributions and event ellipticity are shown in Fig 7.10. Here, there is a clear linear correlation between the mean and RMS elliptic flow with event ellipticity. This measurement illustrates how flow is a global collective observable, in that flow measured in different regions with large separation yield a similar behavior. The elliptic flow standard deviation shows no strong correlation to event ellipticity, but does show a strong correlation with centrality. This observation implies that this quantity is correlated with system size. The correlation between the relative elliptic flow fluctuations $\sigma_{v_2}/\langle v_2 \rangle$ illustrates a two-fold effect: the negative correlation is a result of the positive correlation between mean elliptic flow and event ellipticity and no correlation between the fluctuations and event ellipticity.

Figures 7.11 and 7.12 show the correlation between triangular and quadrangular flow with event ellipticity, respectively. The expected anti-correlation between triangularity and ellipticity

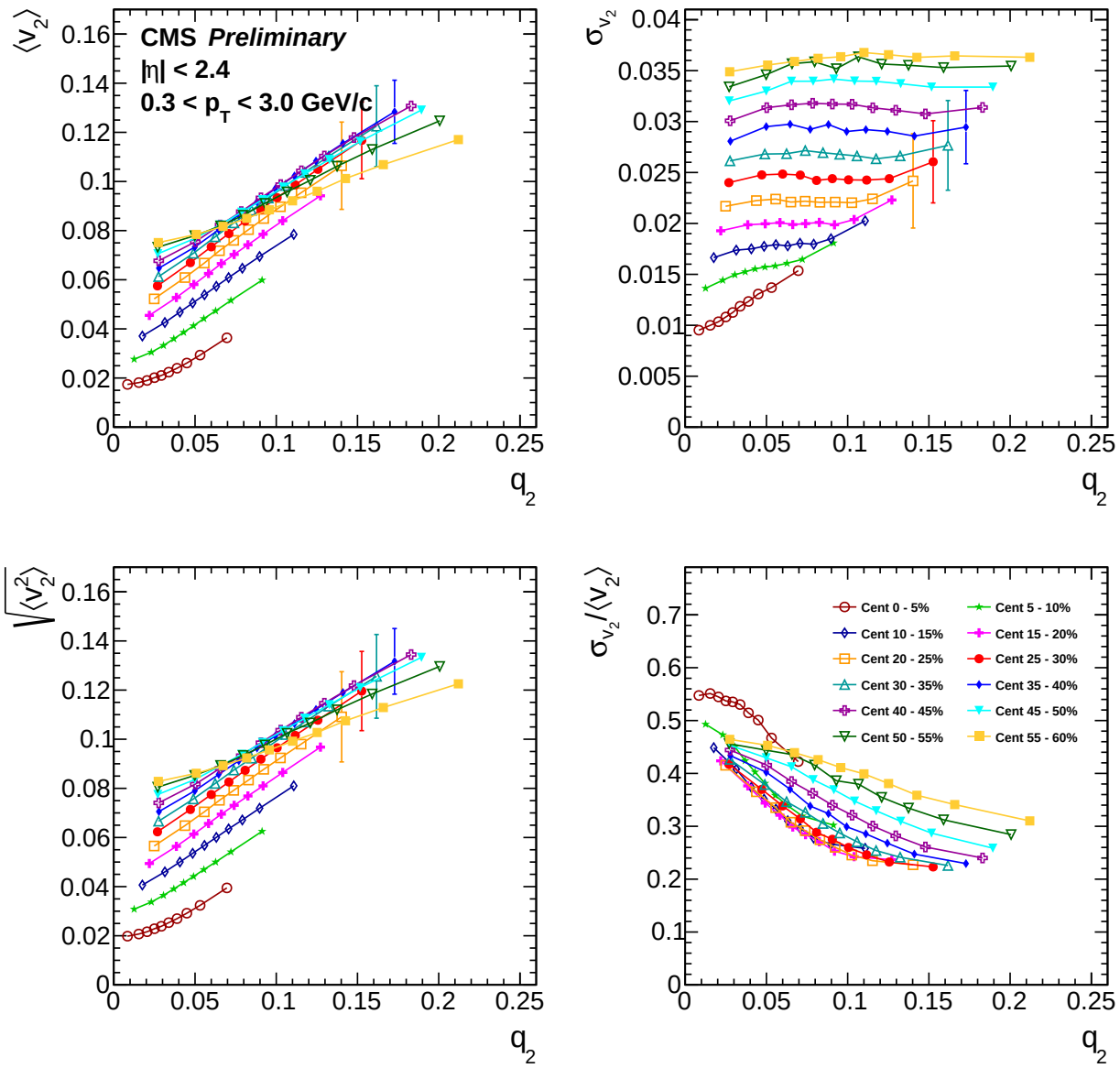

Figure 7.10: Moments (mean and variance) of $p(v_2)$ distributions correlated to event ellipticity. Only statistical errors are shown.

predicted by the Glauber model is captured in the mean, standard deviation, and RMS v_3 behavior with q_2 selection. In a similar vein, a clear non-linear correlation between quadrangular flow and event ellipticity is seen with the behavior of the mean, standard deviation, and RMS v_4 values with q_2 selection. This behavior is understood in that higher-order ($n > 3$) harmonics have two sources: the underlying initial state spatial anisotropy and the mixing of lower-order flow harmonics [233, 234, 235]. The relative fluctuations of both v_3 and v_4 values all hover around the same value of 0.5, regardless of centrality. This behavior is an indicator that flow harmonics with $n > 2$ arise from initial-state eccentricity fluctuations ($\langle v_n^{\mathrm{RP}} \rangle = 0$), which are Gaussian in nature. In this scenario, the relative fluctuations are predicted to be $\sigma / \langle v_n \rangle = \sqrt{4/\pi - 1} \approx 0.52$ [236], which arises from setting $\langle v_n^{\mathrm{RP}} \rangle = 0$ in Eq. (2.3) and finding the mean and variance of the distribution.

Figures 7.13 and 7.14 show the correlation between higher-order flow harmonics and elliptic flow. Here, the q_2 selection is "hidden" within the data points, where each point represents the $p(v_n)$ distribution moment for a single q_2 bin. The apparent "infinite correlation" between the σ_{v_3} and σ_{v_4} values with σ_{v_2} values is a consequence of elliptic flow fluctuations having no correlation with event ellipticity. This provides a clear picture of the underlying correlations between elliptic, triangular, and quadrangular flow described above.

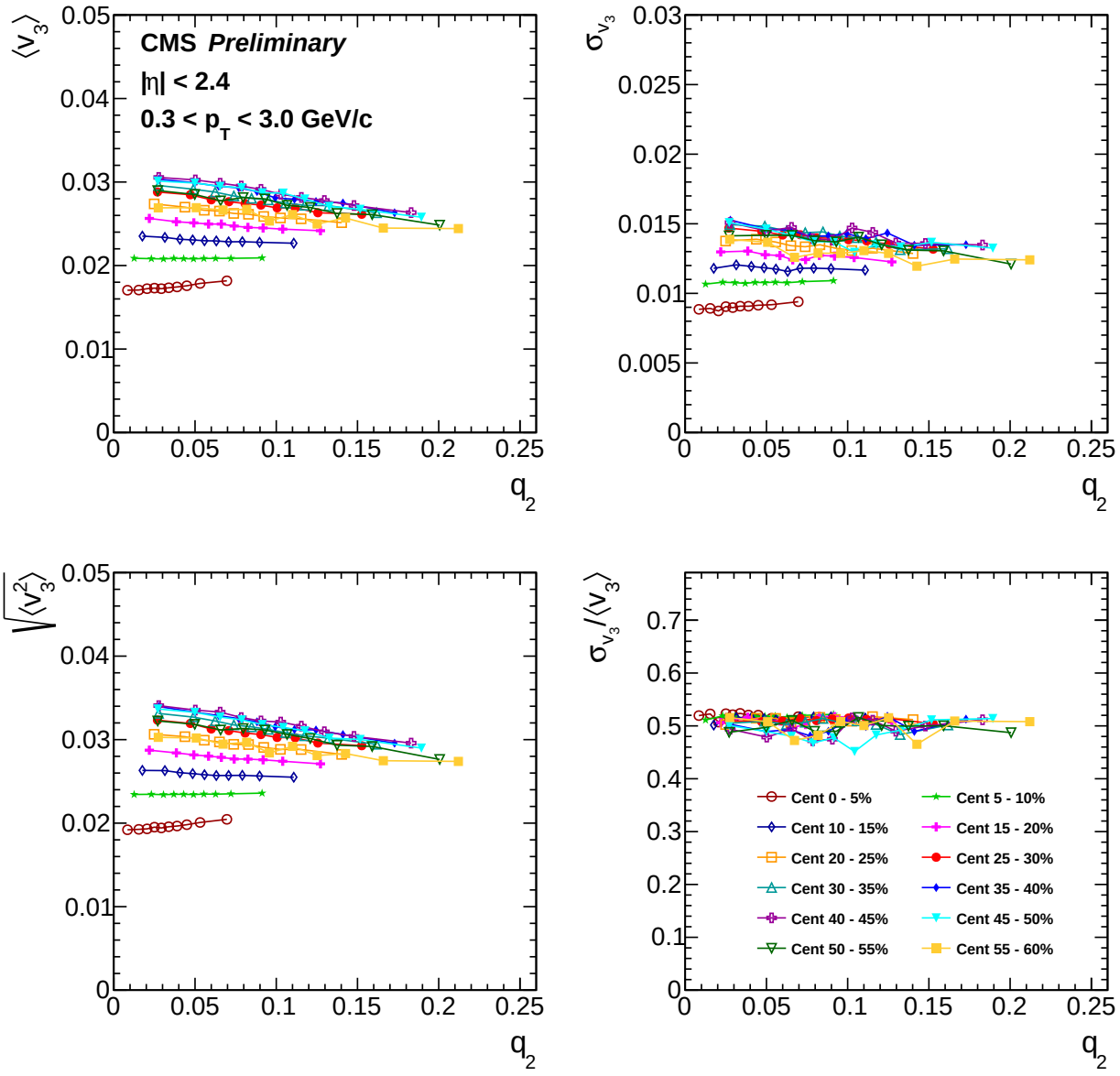

Figure 7.11: Moments (mean and variance) of $p(v_3)$ distributions correlated to event ellipticity. Only statistical errors are shown.

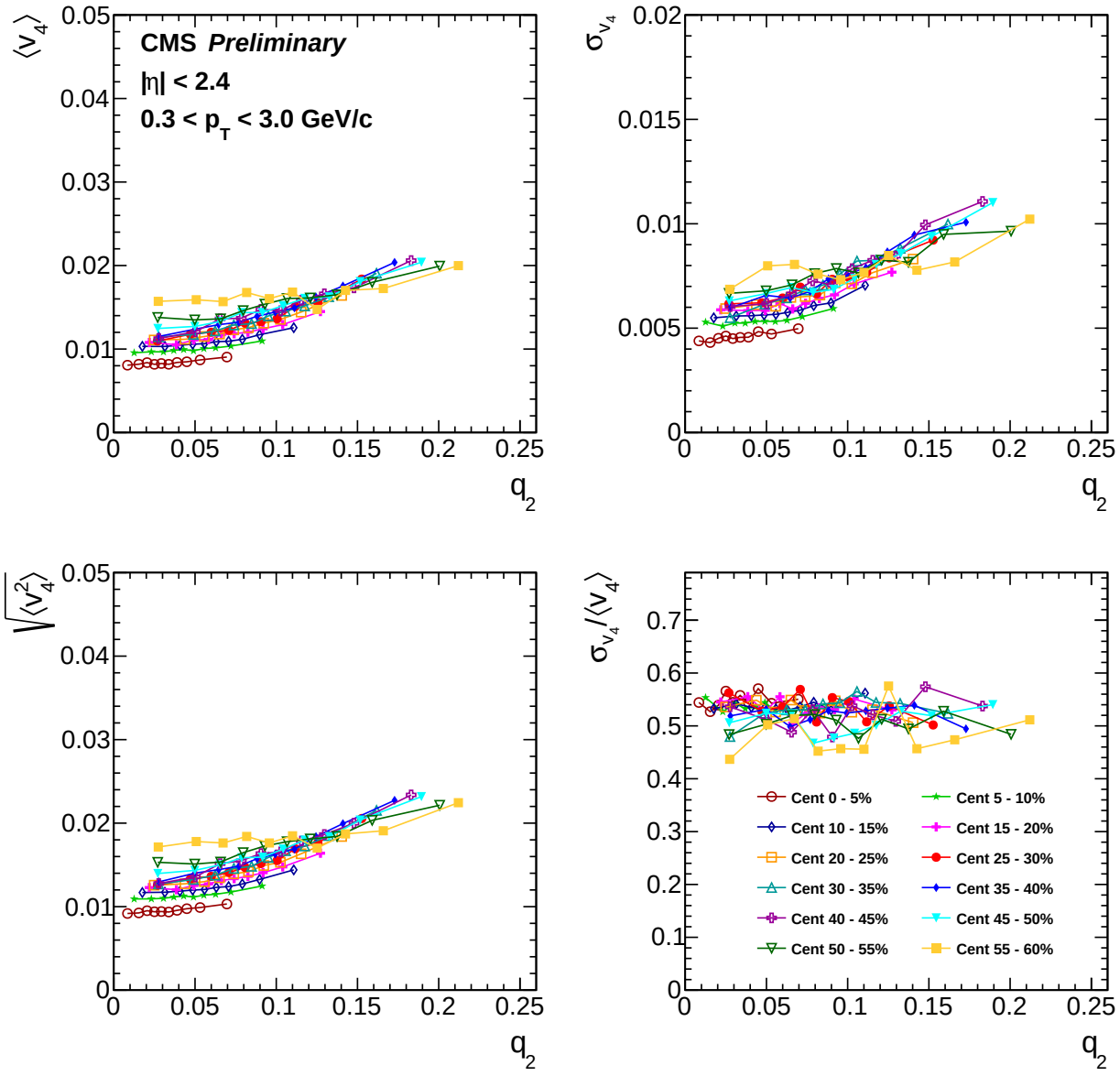

Figure 7.12: Moments (mean and variance) of $p(v_4)$ distributions correlated to event ellipticity. Only statistical errors are shown.

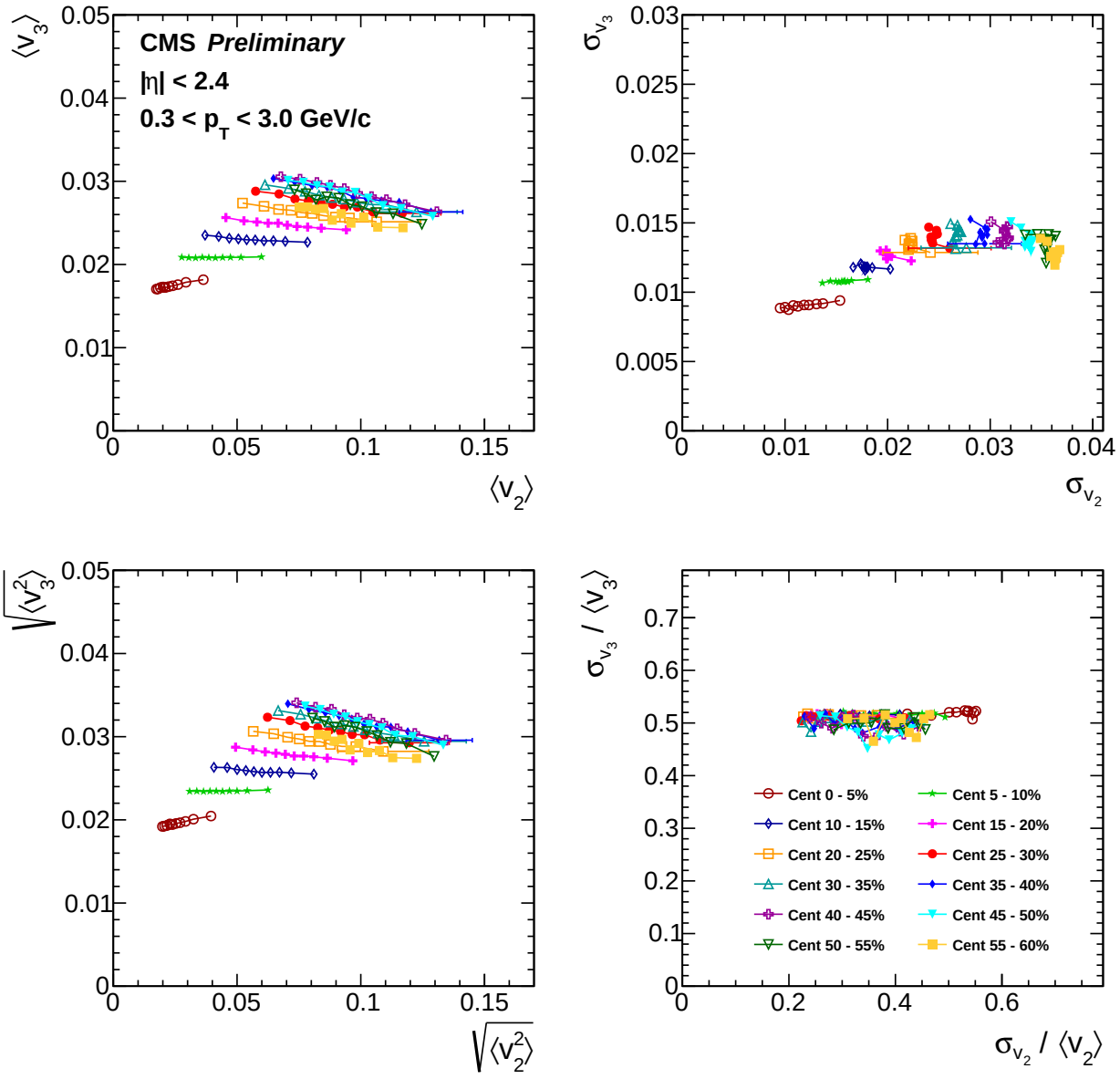

Figure 7.13: Moments (mean and variance) of $p(v_3)$ distributions correlated to moments of $p(v_2)$ distributions with identical q_2 selection. Only statistical errors are shown.

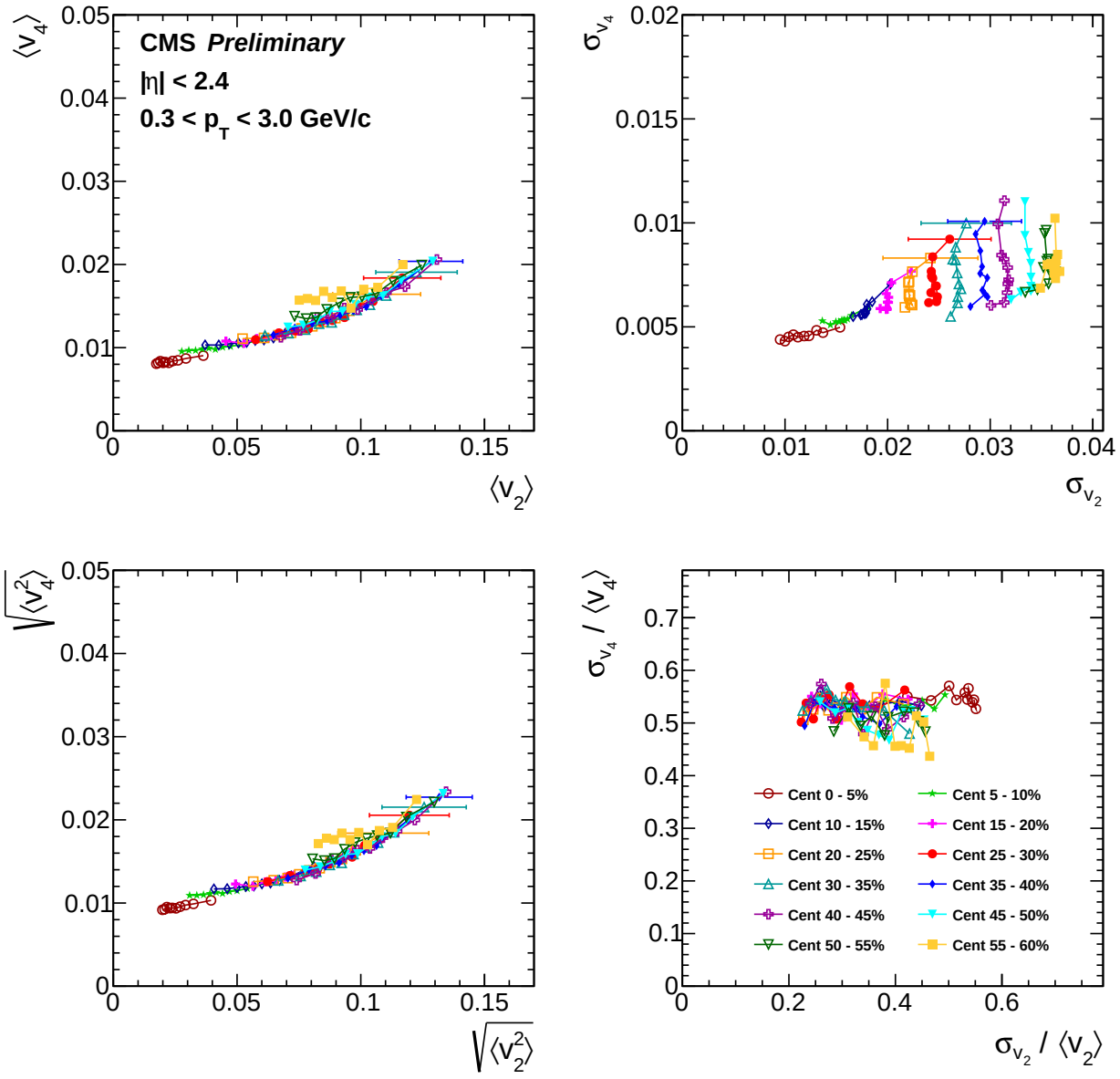

Figure 7.14: Moments (mean and variance) of $p(v_4)$ distributions correlated to moments of $p(v_2)$ distributions with identical q_2 selection. Only statistical errors are shown.

Chapter 8

Conclusions

In summary, this thesis seeks to answer the question of whether initial-state spatial anisotropy fluctuations can be quantified experimentally and how this information can be used to constrain the theoretical understanding of the physics governing the early stages of the QGP. To answer this question, probability distributions describing final-state flow harmonic fluctuation behavior for 5% wide centrality bins up to 60% were obtained for PbPb collisions at $\sqrt{s_{\mathrm{NN}}} = 5.02$ TeV and non-Gaussian behavior in the fluctuations of v_2 coefficients has been observed. Final-state flow fluctuation behavior was related to initial-state spatial anisotropy fluctuations through a cumulant expansion, fits using transformed eccentricity fluctuation parametrizations, and the event-shape engineering technique. To provide further constraints on the understanding of the initial state, predictions using state-of-the-art models for fluctuating initial conditions, which include effects from gluon saturation, were compared to the high precision measurements.

Cumulant flow harmonics were calculated from the moments of the elliptic flow probability distributions and a fine-structure splitting was observed between $v_2\{4\}$, $v_2\{6\}$, and $v_2\{8\}$ cumulants. In addition, the standardized skewness with respect to the reaction plane was estimated using the cumulant results and was found to have a negative value with a magnitude that increases with centrality. Both measurements are consistent with a breakdown in the Gaussian model of elliptic flow fluctuations. These precision measurements of the deviation from Gaussian behavior place

constraints on how the event-by-event fluctuation in the transverse profile of a collision is modeled. With this, it has been shown that the generally assumed isotropic 2D Gaussian behavior for initial-state spatial anisotropy fluctuations cannot replicate the final-state flow harmonic fluctuation behavior.

Bessel-Gaussian and elliptic power law parametrizations were fitted to the unfolded $p(v_2)$ distributions to gain further insight on the nature of the initial-state spatial anisotropy fluctuations. Both parametrizations assume a linear response between eccentricity and flow, but only the elliptic power law allows for a finite skewness. This flexibility allows the elliptic power law parametrization to provide a more accurate description of $p(v_2)$ (and ultimately $p(\varepsilon_2)$) distributions than the Bessel-Gaussian parametrization. This finding is consistent with the cumulant results. The transformed elliptic power fits to the unfolded $p(v_2)$ distributions provide additional discriminators to the underlying physics in the initial stages of heavy-ion collisions. The centrality dependence of the flow response coefficient k_2 provides a model-independent measure of the viscosity of the medium and therefore can be used to constrain underlying assumptions in models of the initial state. Thus, in addition to matching the predicted eccentricities to measured flow coefficients, the model viscosity must now also replicate the system size dependence of the response coefficients. Moreover, the centrality dependence of the inferred average eccentricity in the reaction plane (ε_0) and fluctuation magnitude (α) parameters from the elliptic power law fits provide powerful discriminators for competing models of the initial state. While the predictions from the Glauber and IP-Glasma models qualitatively matched the behavior of these parameters, they deviated in magnitude. Since the two approaches differ in the assumption of the contributions to the initial-state azimuthal anisotropy (participant nucleons and/or their substructures), they yield different values for the eccentricity harmonics. The quantitative disagreement between prediction and measurement provide grounds for further tuning of these models.

In addition, the underlying distributions of flow harmonics for orders $n = 2$–4 have been measured at mid-rapidity and correlated to event ellipticity as estimated at forward rapidity. Events were divided into 5% wide centrality and 10% wide ellipticity bins. The moments of each un-

derlying flow harmonic probability distribution were correlated to event ellipticity and, using the same event selection, were correlated to the moments of other-ordered flow harmonic distributions. The mean and RMS moments of $p(v_2)$ distributions exhibit a linear correlation with event ellipticity while the same moments from $p(v_3)$ distributions show a clear anti-correlation. The values of the relative fluctuations for $p(v_3)$ distributions are consistent with a fluctuations-only scenario, where the average v_3 value with respect to the reaction plane is 0 and any non-zero coefficients are the result of initial-state eccentricity fluctuations. In this scenario the relative fluctuations are predicted to have the value $\sigma_{v_3}/\langle v_3 \rangle = \sqrt{4/\pi - 1} \approx 0.52$. While the mean and RMS moments of $p(v_4)$ distributions show a clear non-linear correlation to event ellipticity, the relative fluctuations are consistent with a mean v_4 value with respect to the reaction plane of 0. These observations suggest that there are two contributions to the v_4 coefficient: initial-state eccentricity fluctuations and elliptic flow.

Perhaps the most interesting prospects for future study would be to extend this analysis technique to small systems like pp and pPb collisions. Measurement of the underlying distributions of flow harmonics can bring insight on the source of the anisotropies observed in these collision systems and help to answer the question on whether or not a small QGP droplet is formed. The number of particles produced in these collisions places a limiting factor on the success of unfolding. Particle production in pp and pPb collisions can be likened to peripheral PbPb collisions where statistical smearing effects are greatest. In addition, independent measurements in pp and pPb collisions have shown smaller flow signals. The combination of small flow signals and large smearing effects provides potential for a breakdown in the unfolding procedure. In order to extract meaningful $p(v_n)$ distributions in these small systems great care will be needed in choosing which events to analyze. With the access to higher collision energies, the smearing effects become less and less of an issue. Beyond the limiting factors with unfolding, the response matrix cannot currently be built for pPb collision systems, as they are asymmetric. A new procedure for determining the response matrix for pPb collisions must be defined before this analysis can be considered viable.

This thesis discusses some of the work done to improve detector calibrations for the CMS

silicon tracker. With the inclusion of dedicated heavy-ion tracker alignment and beamspot calibration workflows in the PCL, the quality of data collected by the CMS detector during heavy-ion operations has improved. This, in turn, has allowed for more robust physics analyses to be run immediately after data collection.

To conclude, significant work has been done to analyze and understand the role of initial-state eccentricity fluctuations in PbPb collisions. Studies performed using the HIJING event generator have indicated that the unfolding technique is a more robust method for removing non-flow effects from measurements than the standard m-particle correlations technique. The inclusion of the unfolding technique into standard flow analyses has provided an unprecedented degree of precision for measuring cumulant flow harmonics, which have been used to elucidate the finer structures of the underlying eccentricity probability distributions. Transformed initial-state eccentricity parametrizations fitted to unfolded $p(v_2)$ distributions have provided the first steps toward obtaining model-independent parameters that relate to the initial-state spatial anisotropy and viscosity of the medium created in ultrarelativistic heavy-ion collisions. Moreover, the union of the event-shape engineering and unfolding techniques has provided detailed insights on the nature of higher-order flow harmonic fluctuations and how they relate to initial-state eccentricity fluctuations.

References

[1] I. Arsene *et al.* (BRAHMS), Nucl. Phys. **A757**, 1 (2005), arXiv:nucl-ex/0410020 [nucl-ex] .

[2] K. Adcox *et al.* (PHENIX), Nucl. Phys. **A757**, 184 (2005), arXiv:nucl-ex/0410003 [nucl-ex] .

[3] B. B. Back *et al.*, Nucl. Phys. **A757**, 28 (2005), arXiv:nucl-ex/0410022 [nucl-ex] .

[4] J. Adams *et al.* (STAR), Nucl. Phys. **A757**, 102 (2005), arXiv:nucl-ex/0501009 [nucl-ex] .

[5] G. Aad *et al.* (ATLAS), Phys. Rev. Lett. **105**, 252303 (2010), arXiv:1011.6182 [hep-ex] .

[6] S. Chatrchyan *et al.* (CMS), Phys. Rev. **C84**, 024906 (2011), arXiv:1102.1957 [nucl-ex] .

[7] H. Fritzsch, M. Gell-Mann, and H. Leutwyler, Phys. Lett. **B47**, 365 (1973).

[8] D. J. Gross and F. Wilczek, Phys. Rev. Lett. **30**, 1343 (1973).

[9] H. D. Politzer, Phys. Rev. Lett. **30**, 1346 (1973).

[10] K. G. Wilson, Phys. Rev. **D10**, 2445 (1974), [,45(1974)].

[11] V. Khachatryan *et al.* (CMS), Eur. Phys. J. **C75**, 186 (2015), arXiv:1412.1633 [hep-ex] .

[12] S. Schaefer, *Proceedings, 30th International Symposium on Lattice Field Theory (Lattice 2012): Cairns, Australia, June 24-29, 2012*, PoS **LATTICE2012**, 001 (2012), arXiv:1211.5069 [hep-lat] .

[13] Z. Fodor and C. Hoelbling, Rev. Mod. Phys. **84**, 449 (2012), arXiv:1203.4789 [hep-lat] .

[14] Y. Nambu and G. Jona-Lasinio, Phys. Rev. **124**, 246 (1961).

[15] 796947, (2008), arXiv:0809.3137 [nucl-ex] .

[16] F. Karsch, *Lectures on quark matter. Proceedings, 40. International Universitätswochen for theoretical physics, 40th Winter School, IUKT 40: Schladming, Austria, March 3-10, 2001*, Lect. Notes Phys. **583**, 209 (2002), arXiv:hep-lat/0106019 [hep-lat] .

[17] S. Chatrchyan *et al.* (CMS), Phys. Rev. Lett. **109**, 152303 (2012), arXiv:1205.2488 [nucl-ex] .

[18] T. Matsui and H. Satz, Phys.Lett. **B178**, 416 (1986).

[19] J. Rafelski and B. Muller, Phys. Rev. Lett. **48**, 1066 (1982), [Erratum: Phys. Rev. Lett.56,2334(1986)].

[20] H. A. Grunder, W. D. Hartsough, and E. J. Lofgren, Science **174**, 1128 (1971).

[21] M. A. Bloomer, W. A. Love, and L. Waters, *Particles and nuclei. Proceedings, 12th International Conference, PANIC XII, Cambridge, USA, June 25-29, 1990*, Nucl. Phys. **A527**, 595 (1991).

[22] H. Satz, Phys. Rept. **403-404**, 33 (2004), arXiv:hep-ph/0405051 [hep-ph] .

[23] S. Ozaki, *Quark matter '90. Proceedings, 8th International Conference on Ultrarelativistic Nucleus Nucleus Collisions, Menton, France, May 7-11, 1990*, Nucl. Phys. **A525**, 125C (1991), [Conf. Proc.C900802V2,C900802V2:1106(1990)].

[24] G. Roland, K. Safarik, and P. Steinberg, Prog. Part. Nucl. Phys. **77**, 70 (2014).

[25] R. Vogt, *Ultrarelativistic heavy-ion collisions* (Elsevier, Amsterdam, 2007).

[26] A. Tawfik and A. G. Shalaby, Adv. High Energy Phys. **2015**, 186812 (2015).

[27] J. Breitweg *et al.* (ZEUS), Eur. Phys. J. **C7**, 609 (1999), arXiv:hep-ex/9809005 [hep-ex] .

[28] D. Kharzeev and M. Nardi, Phys. Lett. **B507**, 121 (2001), arXiv:nucl-th/0012025 [nucl-th] .

[29] L. D. McLerran, *Lectures on quark matter. Proceedings, 40. International Universitätswochen for theoretical physics, 40th Winter School, IUKT 40: Schladming, Austria, March 3-10, 2001*, Lect. Notes Phys. **583**, 291 (2002), arXiv:hep-ph/0104285 [hep-ph] .

[30] Y. V. Kovchegov, *Saturation the color glass condensate and the glasma: What have we learned from RHIC? Proceedings, Workshop, Upton, Brookhaven, USA, May 10-12, 2010*, Nucl. Phys. **A854**, 3 (2011), arXiv:1007.5021 [hep-ph] .

[31] S. Chatrchyan *et al.* (CMS), JHEP **08**, 141 (2011), arXiv:1107.4800 [nucl-ex] .

[32] B. Abelev *et al.* (ALICE), Phys. Rev. **C88**, 044909 (2013), arXiv:1301.4361 [nucl-ex] .

[33] N. Armesto, C. A. Salgado, and U. A. Wiedemann, Phys. Rev. Lett. **94**, 022002 (2005), arXiv:hep-ph/0407018 [hep-ph] .

[34] D. Kharzeev, E. Levin, and M. Nardi, Nucl. Phys. **A747**, 609 (2005), arXiv:hep-ph/0408050 [hep-ph] .

[35] J. Adam *et al.* (ALICE), Phys. Rev. Lett. **116**, 222302 (2016), arXiv:1512.06104 [nucl-ex] .

[36] N. Armesto and E. Scomparin, Eur. Phys. J. Plus **131**, 52 (2016), arXiv:1511.02151 [nucl-ex] .

[37] G. Policastro, D. T. Son, and A. O. Starinets, Phys. Rev. Lett. **87**, 081601 (2001), arXiv:hep-th/0104066 [hep-th] .

[38] P. Kovtun, D. T. Son, and A. O. Starinets, Phys. Rev. Lett. **94**, 111601 (2005), arXiv:hep-th/0405231 [hep-th] .

[39] U. Heinz, C. Shen, and H. Song, *Proceedings, 19th International Conference on Particles and Nuclei (PANIC 11): Cambridge, USA, July 24-29, 2011*, AIP Conf. Proc. **1441**, 766 (2012), arXiv:1108.5323 [nucl-th] .

[40] J.-Y. Ollitrault, Phys. Rev. **D46**, 229 (1992).

[41] B. Alver and G. Roland, Phys. Rev. **C81**, 054905 (2010), [Erratum: Phys. Rev.C82,039903(2010)], arXiv:1003.0194 [nucl-th] .

[42] H. Song, *Proceedings, 23rd International Conference on Ultrarelativistic Nucleus-Nucleus Collisions : Quark Matter 2012 (QM 2012): Washington, DC, USA, August 13-18, 2012*, Nucl. Phys. **A904-905**, 114c (2013), arXiv:1210.5778 [nucl-th] .

[43] D. Teaney and L. Yan, Phys. Rev. **C83**, 064904 (2011), arXiv:1010.1876 [nucl-th] .

[44] S. A. Voloshin, A. M. Poskanzer, A. Tang, and G. Wang, Phys. Lett. **B659**, 537 (2008), arXiv:0708.0800 [nucl-th] .

[45] L. Yan and J.-Y. Ollitrault, Phys. Rev. Lett. **112**, 082301 (2014), arXiv:1312.6555 [nucl-th] .

[46] Z. Qiu and U. W. Heinz, Phys. Rev. **C84**, 024911 (2011), arXiv:1104.0650 [nucl-th] .

[47] S. A. Voloshin, A. M. Poskanzer, and R. Snellings, (2008), arXiv:0809.2949 [nucl-ex] .

[48] D. A. Teaney, (2009), arXiv:0905.2433 [nucl-th] .

[49] A. M. Poskanzer and S. A. Voloshin, Phys. Rev. **C58**, 1671 (1998), arXiv:nucl-ex/9805001 [nucl-ex] .

[50] N. Borghini, P. M. Dinh, and J.-Y. Ollitrault, Phys. Rev. **C64**, 054901 (2001), arXiv:nucl-th/0105040 [nucl-th] .

[51] R. S. Bhalerao, N. Borghini, and J. Y. Ollitrault, Nucl. Phys. **A727**, 373 (2003), arXiv:nucl-th/0310016 [nucl-th] .

[52] N. Borghini, R. S. Bhalerao, and J. Y. Ollitrault, *Ultra-relativistic nucleus-nucleus collisions. Proceedings, 17th International Conference, Quark Matter 2004, Oakland, USA, January 11-17, 2004*, J. Phys. **G30**, S1213 (2004), arXiv:nucl-th/0402053 [nucl-th] .

[53] S. Chatrchyan *et al.* (CMS), Phys. Rev. **C89**, 044906 (2014), arXiv:1310.8651 [nucl-ex] .

[54] J. Adams *et al.* (STAR), Phys. Rev. Lett. **92**, 052302 (2004), arXiv:nucl-ex/0306007 [nucl-ex] .

[55] B. I. Abelev *et al.* (STAR), Phys. Rev. **C75**, 054906 (2007), arXiv:nucl-ex/0701010 [nucl-ex] .

[56] J. Adams *et al.* (STAR), Phys. Rev. **C72**, 014904 (2005), arXiv:nucl-ex/0409033 [nucl-ex] .

[57] S. S. Adler *et al.* (PHENIX), Phys. Rev. Lett. **91**, 182301 (2003), arXiv:nucl-ex/0305013 [nucl-ex] .

[58] S. Afanasiev *et al.* (PHENIX), Phys. Rev. Lett. **99**, 052301 (2007), arXiv:nucl-ex/0703024 [NUCL-EX] .

[59] A. Adare *et al.* (PHENIX), Phys. Rev. Lett. **98**, 162301 (2007), arXiv:nucl-ex/0608033 [nucl-ex] .

[60] A. Adare *et al.* (PHENIX), Phys. Rev. **C85**, 064914 (2012), arXiv:1203.2644 [nucl-ex] .

[61] B. B. Abelev *et al.* (ALICE), JHEP **06**, 190 (2015), arXiv:1405.4632 [nucl-ex] .

[62] H. Song, S. A. Bass, and U. Heinz, Phys. Rev. **C83**, 024912 (2011), arXiv:1012.0555 [nucl-th] .

[63] S. Chatrchyan *et al.* (CMS), Phys. Rev. Lett. **109**, 022301 (2012), arXiv:1204.1850 [nucl-ex] .

[64] D. d'Enterria, Landolt-Bornstein **23**, 471 (2010), arXiv:0902.2011 [nucl-ex] .

[65] R. A. Lacey, A. Taranenko, R. Wei, N. N. Ajitanand, J. M. Alexander, J. Jia, R. Pak, D. H. Rischke, D. Teaney, and K. Dusling, Phys. Rev. **C82**, 034910 (2010), arXiv:1005.4979 [nucl-ex] .

[66] J. Noronha-Hostler, B. Betz, J. Noronha, and M. Gyulassy, Phys. Rev. Lett. **116**, 252301 (2016), arXiv:1602.03788 [nucl-th] .

[67] A. Dumitru, F. Gelis, L. McLerran, and R. Venugopalan, Nucl. Phys. **A810**, 91 (2008), arXiv:0804.3858 [hep-ph] .

[68] B. Alver *et al.* (PHOBOS), Phys. Rev. Lett. **104**, 062301 (2010), arXiv:0903.2811 [nucl-ex] .

[69] B. I. Abelev *et al.* (STAR), Phys. Rev. **C80**, 064912 (2009), arXiv:0909.0191 [nucl-ex] .

[70] V. Khachatryan *et al.* (CMS), JHEP **09**, 091 (2010), arXiv:1009.4122 [hep-ex] .

[71] V. Khachatryan *et al.* (CMS), Phys. Rev. Lett. **116**, 172302 (2016), arXiv:1510.03068 [nucl-ex] .

[72] G. Aad *et al.* (ATLAS), Phys. Rev. Lett. **116**, 172301 (2016), arXiv:1509.04776 [hep-ex] .

[73] S. Chatrchyan *et al.* (CMS), Phys. Lett. **B718**, 795 (2013), arXiv:1210.5482 [nucl-ex] .

[74] G. Aad *et al.* (ATLAS), Phys. Rev. Lett. **110**, 182302 (2013), arXiv:1212.5198 [hep-ex] .

[75] B. Abelev *et al.* (ALICE), Phys. Lett. **B719**, 29 (2013), arXiv:1212.2001 [nucl-ex] .

[76] P. Bozek and W. Broniowski, Phys. Lett. **B718**, 1557 (2013), arXiv:1211.0845 [nucl-th] .

[77] E. Shuryak and I. Zahed, Phys. Rev. **C88**, 044915 (2013), arXiv:1301.4470 [hep-ph] .

[78] A. Bzdak, B. Schenke, P. Tribedy, and R. Venugopalan, Phys. Rev. **C87**, 064906 (2013), arXiv:1304.3403 [nucl-th] .

[79] K. Werner, I. Karpenko, and T. Pierog, Phys. Rev. Lett. **106**, 122004 (2011), arXiv:1011.0375 [hep-ph] .

[80] S. Gavin, L. McLerran, and G. Moschelli, Phys. Rev. **C79**, 051902 (2009), arXiv:0806.4718 [nucl-th] .

[81] A. Kovner and M. Lublinsky, Phys. Rev. **D83**, 034017 (2011), arXiv:1012.3398 [hep-ph] .

[82] E. Levin and A. H. Rezaeian, Phys. Rev. **D84**, 034031 (2011), arXiv:1105.3275 [hep-ph] .

[83] A. Dumitru, K. Dusling, F. Gelis, J. Jalilian-Marian, T. Lappi, and R. Venugopalan, Phys. Lett. **B697**, 21 (2011), arXiv:1009.5295 [hep-ph] .

[84] K. Dusling and R. Venugopalan, Phys. Rev. Lett. **108**, 262001 (2012), arXiv:1201.2658 [hep-ph] .

[85] K. Dusling and R. Venugopalan, Phys. Rev. **D87**, 054014 (2013), arXiv:1211.3701 [hep-ph] .

[86] T. Altinoluk, N. Armesto, G. Beuf, A. Kovner, and M. Lublinsky, Phys. Lett. **B751**, 448 (2015), arXiv:1503.07126 [hep-ph] .

[87] E. Wang and X.-N. Wang, Phys. Rev. **C64**, 034901 (2001), arXiv:nucl-th/0104031 [nucl-th] .

[88] B. Alver, M. Baker, C. Loizides, and P. Steinberg, (2008), arXiv:0805.4411 [nucl-ex] .

[89] M. L. Miller, K. Reygers, S. J. Sanders, and P. Steinberg, Ann. Rev. Nucl. Part. Sci. **57**, 205 (2007), arXiv:nucl-ex/0701025 [nucl-ex] .

[90] W. Broniowski, M. Rybczynski, and P. Bozek, Comput. Phys. Commun. **180**, 69 (2009), arXiv:0710.5731 [nucl-th] .

[91] S. S. Adler *et al.* (PHENIX), Phys. Rev. **C69**, 034910 (2004), arXiv:nucl-ex/0308006 [nucl-ex] .

[92] J. Adams *et al.* (STAR), Phys. Rev. Lett. **91**, 172302 (2003), arXiv:nucl-ex/0305015 [nucl-ex] .

[93] J. Adams *et al.* (STAR), Phys. Rev. Lett. **91**, 072304 (2003), arXiv:nucl-ex/0306024 [nucl-ex] .

[94] S. S. Adler *et al.* (PHENIX), Phys. Rev. Lett. **97**, 052301 (2006), arXiv:nucl-ex/0507004 [nucl-ex] .

[95] J. Adams *et al.* (STAR), Phys. Rev. Lett. **95**, 152301 (2005), arXiv:nucl-ex/0501016 [nucl-ex] .

[96] V. Khachatryan *et al.* (CMS), JHEP **04**, 039 (2017), arXiv:1611.01664 [nucl-ex] .

[97] S. Chatrchyan *et al.* (CMS), Phys. Rev. **C87**, 014902 (2013), arXiv:1204.1409 [nucl-ex] .

[98] M. Arneodo, Physics Reports **240**, 301 (1994).

[99] J. W. Cronin, H. J. Frisch, M. J. Shochet, J. P. Boymond, R. Mermod, P. A. Piroue, and R. L. Sumner, *High energy physics. Proceedings, 17th International Conference, ICHEP 1974, London, England, July 01-July 10, 1974*, Phys. Rev. **D11**, 3105 (1975).

[100] A. Adare *et al.* (PHENIX), Phys. Rev. **C88**, 024906 (2013), arXiv:1304.3410 [nucl-ex] .

[101] G. P. Salam, *2008 CTEQ-MCnet Summer School on QCD Phenomenology and Monte Carlo Event Generators (MCnet 08) (CTEQ 08) Debrecen, Hungary, August 8-16, 2008*, Eur. Phys. J. **C67**, 637 (2010), arXiv:0906.1833 [hep-ph] .

[102] S. Chatrchyan *et al.* (CMS), Phys. Lett. **B712**, 176 (2012), arXiv:1202.5022 [nucl-ex] .

[103] B. Abelev *et al.* (ALICE), JHEP **03**, 013 (2014), arXiv:1311.0633 [nucl-ex] .

[104] G. Aad *et al.* (ATLAS), Phys. Lett. **B719**, 220 (2013), arXiv:1208.1967 [hep-ex] .

[105] S. Chatrchyan *et al.* (CMS), Phys. Rev. Lett. **113**, 132301 (2014), [Erratum: Phys. Rev. Lett.115,no.2,029903(2015)], arXiv:1312.4198 [nucl-ex] .

[106] T. Sjöstrand, S. Mrenna, and P. Skands, JHEP **05**, 026 (2006), arXiv:hep-ph/0603175 [hep-ph] .

[107] I. P. Lokhtin and A. M. Snigirev, Eur. Phys. J. **C45**, 211 (2006), arXiv:hep-ph/0506189 [hep-ph] .

[108] B. Muller, J. Schukraft, and B. Wyslouch, Ann. Rev. Nucl. Part. Sci. **62**, 361 (2012), arXiv:1202.3233 [hep-ex] .

[109] L. Adamczyk *et al.* (STAR), Phys. Rev. Lett. **113**, 142301 (2014), arXiv:1404.6185 [nucl-ex] .

[110] A. Adare *et al.* (PHENIX), Phys. Rev. **C93**, 034904 (2016), arXiv:1509.04662 [nucl-ex] .

[111] D. V. Perepelitsa, Nuclear Physics A **904**, 669c (2013).

[112] B. Abelev *et al.* (ALICE), Phys. Rev. Lett. **109**, 112301 (2012), arXiv:1205.6443 [hep-ex] .

[113] J. Adam *et al.* (ALICE), Phys. Lett. **B753**, 41 (2016), arXiv:1507.03134 [nucl-ex] .

[114] J. Adam *et al.* (ALICE), Phys. Lett. **B754**, 81 (2016), arXiv:1509.07491 [nucl-ex] .

[115] J. Adam *et al.* (ALICE), JHEP **11**, 205 (2015), arXiv:1506.06604 [nucl-ex] .

[116] B. Abelev *et al.* (ALICE), JHEP **09**, 112 (2012), arXiv:1203.2160 [nucl-ex] .

[117] B. Abelev *et al.* (ALICE), Phys. Rev. Lett. **111**, 102301 (2013), arXiv:1305.2707 [nucl-ex] .

[118] B. B. Abelev *et al.* (ALICE), Phys. Rev. **C90**, 034904 (2014), arXiv:1405.2001 [nucl-ex] .

[119] J. Adam *et al.* (ALICE), JHEP **03**, 081 (2016), arXiv:1509.06888 [nucl-ex] .

[120] J. Adam *et al.* (ALICE), JHEP **03**, 082 (2016), arXiv:1509.07287 [nucl-ex] .

[121] J. Adam *et al.* (ALICE), JHEP **07**, 051 (2015), arXiv:1504.07151 [nucl-ex] .

[122] S. Chatrchyan *et al.* (CMS), JHEP **05**, 063 (2012), arXiv:1201.5069 [nucl-ex] .

[123] V. Khachatryan *et al.* (CMS), Phys. Rev. Lett. **116**, 032301 (2016), arXiv:1508.06678 [nucl-ex] .

[124] M. Gyulassy, I. Vitev, and X. N. Wang, Phys. Rev. Lett. **86**, 2537 (2001), arXiv:nucl-th/0012092 [nucl-th] .

[125] E. V. Shuryak, Phys. Rev. **C66**, 027902 (2002), arXiv:nucl-th/0112042 [nucl-th] .

[126] B. Alessandro *et al.* (NA50), Eur. Phys. J. **C39**, 335 (2005), arXiv:hep-ex/0412036 [hep-ex] .

[127] R. Arnaldi *et al.* (NA60 Collaboration), Phys. Rev. Lett. **99**, 132302 (2007).

[128] E. Scomparin (NA60), *Proceedings, 21st International Conference on Ultra-Relativistic nucleus nucleus collisions (Quark matter 2009): Knoxville, USA, March 30-April 4, 2009*, Nucl. Phys. **A830**, 239C (2009), arXiv:0907.3682 [nucl-ex] .

[129] A. Adare *et al.* (PHENIX), Phys. Rev. **C84**, 054912 (2011), arXiv:1103.6269 [nucl-ex] .

[130] B. I. Abelev *et al.* (STAR), Phys. Rev. **C80**, 041902 (2009), arXiv:0904.0439 [nucl-ex] .

[131] R. Vogt, Nucl. Phys. **A700**, 539 (2002), arXiv:hep-ph/0107045 [hep-ph] .

[132] B. Z. Kopeliovich and B. G. Zakharov, Phys. Rev. D **44**, 3466 (1991).

[133] D. C. McGlinchey, A. D. Frawley, and R. Vogt, Phys. Rev. **C87**, 054910 (2013), arXiv:1208.2667 [nucl-th] .

[134] K. J. Eskola, H. Paukkunen, and C. A. Salgado, JHEP **04**, 065 (2009), arXiv:0902.4154 [hep-ph] .

[135] D. de Florian, R. Sassot, P. Zurita, and M. Stratmann, Phys. Rev. **D85**, 074028 (2012), arXiv:1112.6324 [hep-ph] .

[136] P. Braun-Munzinger and J. Stachel, Phys. Lett. **B490**, 196 (2000), arXiv:nucl-th/0007059 [nucl-th] .

[137] R. L. Thews, M. Schroedter, and J. Rafelski, Phys. Rev. **C63**, 054905 (2001), arXiv:hep-ph/0007323 [hep-ph] .

[138] J. Adam *et al.* (ALICE), JHEP **05**, 179 (2016), arXiv:1506.08804 [nucl-ex] .

[139] B. Abelev *et al.* (ALICE), Phys. Rev. Lett. **109**, 072301 (2012), arXiv:1202.1383 [hep-ex] .

[140] E. Abbas *et al.* (ALICE), Phys. Rev. Lett. **111**, 162301 (2013), arXiv:1303.5880 [nucl-ex] .

[141] B. B. Abelev *et al.* (ALICE), Phys. Lett. **B734**, 314 (2014), arXiv:1311.0214 [nucl-ex] .

[142] B. B. Abelev *et al.* (ALICE), JHEP **02**, 073 (2014), arXiv:1308.6726 [nucl-ex] .

[143] B. B. Abelev *et al.* (ALICE), JHEP **12**, 073 (2014), arXiv:1405.3796 [nucl-ex] .

[144] J. Adam *et al.* (ALICE), JHEP **06**, 055 (2015), arXiv:1503.07179 [nucl-ex] .

[145] J. Adam *et al.* (ALICE), JHEP **11**, 127 (2015), arXiv:1506.08808 [nucl-ex] .

[146] J. Adam *et al.* (ALICE), Phys. Rev. Lett. **116**, 222301 (2016), arXiv:1509.08802 [nucl-ex] .

[147] B. B. Abelev *et al.* (ALICE), Phys. Lett. **B738**, 361 (2014), arXiv:1405.4493 [nucl-ex] .

[148] B. B. Abelev *et al.* (ALICE), Phys. Lett. **B740**, 105 (2015), arXiv:1410.2234 [nucl-ex] .

[149] S. Chatrchyan *et al.* (CMS), Phys. Rev. Lett. **107**, 052302 (2011), arXiv:1105.4894 [nucl-ex] .

[150] V. Khachatryan *et al.* (CMS), Phys. Rev. Lett. **113**, 262301 (2014), arXiv:1410.1804 [nucl-ex] .

[151] S. Chatrchyan *et al.* (CMS), JHEP **04**, 103 (2014), arXiv:1312.6300 [nucl-ex] .

[152] G. Aad *et al.* (ATLAS), Phys. Rev. **C92**, 034904 (2015), arXiv:1505.08141 [hep-ex] .

[153] G. Aad *et al.* (ATLAS), Phys. Lett. **B697**, 294 (2011), arXiv:1012.5419 [hep-ex] .

[154] R. Aaij *et al.* (LHCb), JHEP **07**, 094 (2014), arXiv:1405.5152 [nucl-ex] .

[155] R. Aaij *et al.* (LHCb), JHEP **02**, 072 (2014), arXiv:1308.6729 [nucl-ex] .

[156] V. Khachatryan *et al.* (CMS), Phys. Lett. B (2016), 10.1016/j.physletb.2017.04.031, arXiv:1611.01510 [nucl-ex] .

[157] M. Strickland, *Proceedings, 12th International Workshop on Hadron Physics: Bento Gonçalves, Rio Grande do Sul, Brazil, April 22-27, 2012*, AIP Conf. Proc. **1520**, 179 (2013), arXiv:1207.5327 [hep-ph] .

[158] A. Emerick, X. Zhao, and R. Rapp, Eur. Phys. J. **A48**, 72 (2012), arXiv:1111.6537 [hep-ph] .

[159] L. Grandchamp, S. Lumpkins, D. Sun, H. van Hees, and R. Rapp, Phys. Rev. **C73**, 064906 (2006), arXiv:hep-ph/0507314 [hep-ph] .

[160] C. F. von Weizsacker, Z. Phys. **88**, 612 (1934).

[161] E. J. Williams, Phys. Rev. **45**, 729 (1934).

[162] E. Abbas *et al.* (ALICE), Eur. Phys. J. **C73**, 2617 (2013), arXiv:1305.1467 [nucl-ex] .

[163] V. Khachatryan *et al.* (CMS), Submitted to: Phys. Lett. B (2016), arXiv:1605.06966 [nucl-ex] .

[164] V. Guzey, E. Kryshen, M. Strikman, and M. Zhalov, Phys. Lett. **B726**, 290 (2013), arXiv:1305.1724 [hep-ph] .

[165] C. Nonaka and S. A. Bass, Phys. Rev. **C75**, 014902 (2007), arXiv:nucl-th/0607018 [nucl-th] .

[166] T. Hirano, U. W. Heinz, D. Kharzeev, R. Lacey, and Y. Nara, Phys. Lett. **B636**, 299 (2006), arXiv:nucl-th/0511046 [nucl-th] .

[167] T. Hirano, U. W. Heinz, D. Kharzeev, R. Lacey, and Y. Nara, Phys. Rev. **C77**, 044909 (2008), arXiv:0710.5795 [nucl-th] .

[168] H. Petersen, J. Steinheimer, G. Burau, M. Bleicher, and H. Stocker, Phys. Rev. **C78**, 044901 (2008), arXiv:0806.1695 [nucl-th] .

[169] K. Werner, I. Karpenko, T. Pierog, M. Bleicher, and K. Mikhailov, Phys. Rev. **C82**, 044904 (2010), arXiv:1004.0805 [nucl-th] .

[170] H. Song, S. A. Bass, U. Heinz, T. Hirano, and C. Shen, Phys. Rev. Lett. **106**, 192301 (2011), [Erratum: Phys. Rev. Lett.109,139904(2012)], arXiv:1011.2783 [nucl-th] .

[171] S. Ryu, S. Jeon, C. Gale, B. Schenke, and C. Young, *Proceedings, 23rd International Conference on Ultrarelativistic Nucleus-Nucleus Collisions : Quark Matter 2012 (QM 2012): Washington, DC, USA, August 13-18, 2012*, Nucl. Phys. **A904-905**, 389c (2013), arXiv:1210.4588 [hep-ph] .

[172] B. Schenke, P. Tribedy, and R. Venugopalan, Phys. Rev. **C86**, 034908 (2012), arXiv:1206.6805 [hep-ph] .

[173] B. Schenke, P. Tribedy, and R. Venugopalan, *Proceedings, International Conference on the Initial Stages in High-Energy Nuclear Collisions (IS2013): Illa de Arousa, Galicia - Spain, September 8-14, 2013*, Nucl. Phys. **A926**, 102 (2014), arXiv:1312.5588 [hep-ph] .

[174] J. D. Bjorken, Phys. Rev. **D27**, 140 (1983).

[175] G. Aad *et al.* (ATLAS), JHEP **11**, 183 (2013), arXiv:1305.2942 [hep-ex] .

[176] N. Borghini, P. M. Dinh, and J.-Y. Ollitrault, Phys. Rev. **C63**, 054906 (2001), arXiv:nucl-th/0007063 [nucl-th] .

[177] N. Borghini, P. M. Dinh, and J.-Y. Ollitrault, in *International Workshop on the Physics of the Quark Gluon Plasma Palaiseau, France, September 4-7, 2001* (2001) arXiv:nucl-ex/0110016 [nucl-ex] .

[178] G. Giacalone, L. Yan, J. Noronha-Hostler, and J.-Y. Ollitrault, Phys. Rev. **C95**, 014913 (2017), arXiv:1608.01823 [nucl-th] .

[179] J. Schukraft, A. Timmins, and S. A. Voloshin, Phys. Lett. **B719**, 394 (2013), arXiv:1208.4563 [nucl-ex] .

[180] J. Jia, J. Phys. **G41**, 124003 (2014), arXiv:1407.6057 [nucl-ex] .

[181] R. S. Bhalerao, J.-Y. Ollitrault, and S. Pal, Phys. Lett. **B742**, 94 (2015), arXiv:1411.5160 [nucl-th] .

[182] L. Yan, J.-Y. Ollitrault, and A. M. Poskanzer, Phys. Rev. **C90**, 024903 (2014), arXiv:1405.6595 [nucl-th] .

[183] L. Yan, J.-Y. Ollitrault, and A. M. Poskanzer, Phys. Lett. **B742**, 290 (2015), arXiv:1408.0921 [nucl-th] .

[184] S. Voloshin and Y. Zhang, Z. Phys. **C70**, 665 (1996), arXiv:hep-ph/9407282 [hep-ph] .

[185] A. Rodríguez and C. Tsallis, Journal of Mathematical Physics **51**, 073301 (2010), arXiv:1003.2232 [cond-mat.stat-mech] .

[186] R. S. Bhalerao, M. Luzum, and J.-Y. Ollitrault, Phys. Rev. **C84**, 034910 (2011), arXiv:1104.4740 [nucl-th] .

[187] Q. Wang (CMS Collaboration), *Azimuthal anisotropy of charged particles from multiparticle correlations in pPb and PbPb collisions with CMS*, Tech. Rep. CMS-CR-2014-160 (CERN, Geneva, 2014).

[188] B. B. Abelev *et al.* (ALICE), Phys. Rev. **C90**, 054901 (2014), arXiv:1406.2474 [nucl-ex] .

[189] G. Aad *et al.* (ATLAS), Eur. Phys. J. **C74**, 3157 (2014), arXiv:1408.4342 [hep-ex] .

[190] H. Gronqvist, J.-P. Blaizot, and J.-Y. Ollitrault, (2016), arXiv:1604.07230 [nucl-th] .

[191] L. Yan, J.-Y. Ollitrault, and A. M. Poskanzer, Phys. Lett. B **742**, 290 (2015), arXiv:1408.0921 [nucl-th] .

[192] C. Adler *et al.* (STAR), Phys. Rev. **C66**, 034904 (2002), arXiv:nucl-ex/0206001 [nucl-ex] .

[193] M. Luzum and J.-Y. Ollitrault, Phys. Rev. **C87**, 044907 (2013), arXiv:1209.2323 [nucl-ex] .

[194] S. Chatrchyan *et al.* (CMS), Phys. Lett. **B716**, 30 (2012), arXiv:1207.7235 [hep-ex] .

[195] G. Aad *et al.* (ATLAS), Phys. Lett. **B716**, 1 (2012), arXiv:1207.7214 [hep-ex] .

[196] L. Evans and P. Bryant, JINST **3**, S08001 (2008).

[197] D. G. d'Enterria *et al.* (CMS), J. Phys. **G34**, 2307 (2007).

[198] O. S. Bruning, P. Collier, P. Lebrun, S. Myers, R. Ostojic, J. Poole, and P. Proudlock, (2004).

[199] S. Chatrchyan *et al.* (CMS), JINST **5**, T03012 (2010), arXiv:0911.4991 [physics.ins-det] .

[200] S. Chatrchyan *et al.* (CMS), JINST **9**, P10009 (2014), arXiv:1405.6569 [physics.ins-det] .

[201] S. Agostinelli *et al.* (GEANT4), Nucl. Instrum. Meth. **A506**, 250 (2003).

[202] D. Hufnagel, *Proceedings, 21st International Conference on Computing in High Energy and Nuclear Physics (CHEP 2015): Okinawa, Japan, April 13-17, 2015*, J. Phys. Conf. Ser. **664**, 032014 (2015).

[203] T. Miao, N. Leioatts, H. Wenzel, and F. Yumiceva, *Beam Position Determination using Tracks*, Tech. Rep. CMS-NOTE-2007-021 (CERN, Geneva, 2007).

[204] G. L. Bayatian *et al.* (CMS Collaboration), *CMS Physics: Technical Design Report Volume 1: Detector Performance and Software*, Technical Design Report CMS (CERN, Geneva, 2006) there is an error on cover due to a technical problem for some items.

[205] S. Chatrchyan *et al.* (CMS), JINST **8**, P04013 (2013), arXiv:1211.4462 [hep-ex] .

[206] S. Chatrchyan *et al.* (CMS), JINST **9**, P06009 (2014), arXiv:1403.2286 [physics.ins-det] .

[207] S. Chatrchyan *et al.* (CMS), JINST **3**, S08004 (2008).

[208] V. Blobel and C. Kleinwort, in *Advanced Statistical Techniques in Particle Physics. Proceedings, Conference, Durham, UK, March 18-22, 2002* (2002) pp. URL–STR(9), arXiv:hep-ex/0208021 [hep-ex] .

[209] V. Blobel, *Tracking in high multiplicity environments. Proceedings, 1st Workshop, TIME 2005, Zuerich, Switzerland, October 3-7, 2005*, Nucl. Instrum. Meth. **A566**, 5 (2006).

[210] J. Ocariz, in *Proceedings, 1st Asia-Europe-Pacific School of High-Energy Physics (AEPSHEP): Fukuoka, Japan, October 14-27, 2012* (2014) pp. 253–280, [,253(2014)], arXiv:1405.3402 [physics.data-an] .

[211] S. Chatrchyan *et al.* (CMS), JINST **3**, S08004 (2008).

[212] *The CMS muon project: Technical Design Report*, Technical Design Report CMS (CERN, Geneva, 1997).

[213] F. Thyssen (CMS), *Position sensitive detectors. Proceedings, 9th International Conference, PSD9, Aberystwyth, UK, September 12-16, 2011*, JINST **7**, C01104 (2012).

[214] E. Kuznetsova (CMS), *Proceedings, 2nd International Conference on Technology and Instrumentation in Particle Physics 2011: Chicago, Illinois, 9-14 Jun 2011*, Phys. Procedia **37**, 356 (2012).

[215] O. A. Grachov, M. J. Murray, A. S. Ayan, P. Debbins, E. Norbeck, Y. Onel, and D. G. d'Enterria (CMS), *Calorimetry in high energy physics. Proceedings, 12th International Conference, CALOR 2006, Chicago, USA, June 5-9, 2006*, AIP Conf. Proc. **867**, 258 (2006), [,258(2006)], arXiv:nucl-ex/0608052 [nucl-ex] .

[216] O. A. Grachov *et al.* (CMS), *Calorimetry in high energy physics. Proceedings, 13th International Conference, CALOR 2008, Pavia, Italy, May 26-30, 2008*, J. Phys. Conf. Ser. **160**, 012059 (2009), arXiv:0807.0785 [nucl-ex] .

[217] CMS Collaboration (CMS), *Particle-flow event reconstruction in CMS and performance for jets, taus, and E_{T}^{miss}*, CMS Physics Analysis Summary CMS-PAS-PFT-09-001 (2009).

[218] CMS Collaboration (CMS), *Commissioning of the particle-flow event reconstruction with the first LHC collisions recorded in the CMS detector*, CMS Physics Analysis Summary CMS-PAS-PFT-10-001 (2010).

[219] V. Khachatryan *et al.* (CMS), Eur. Phys. J. **C70**, 1165 (2010), arXiv:1007.1988 [physics.ins-det] .

[220] G. D'Agostini, Nucl.Instrum.Meth. **A362**, 487 (1995).

[221] W. H. Richardson, JOSA **62**, 55 (1972).

[222] L. B. Lucy, The astronomical journal **79**, 745 (1974).

[223] A. Hocker and V. Kartvelishvili, Nucl. Instrum. Meth. **A372**, 469 (1996), arXiv:hep-ph/9509307 [hep-ph] .

[224] J. Jia and S. Mohapatra, Phys. Rev. **C88**, 014907 (2013), arXiv:1304.1471 [nucl-ex] .

[225] T. Adye, in *Proceedings of the PHYSTAT 2011 Workshop, CERN, Geneva, Switzerland, January 2011, CERN-2011-006, pp 313-318* (2011) pp. 313–318, arXiv:1105.1160 [physics.data-an] .

[226] R. Brun and F. Rademakers, *New computing techniques in physics research V. Proceedings, 5th International Workshop, AIHENP '96, Lausanne, Switzerland, September 2-6, 1996*, Nucl. Instrum. Meth. **A389**, 81 (1997).

[227] P. Huo, J. Jia, and S. Mohapatra, Phys. Rev. **C90**, 024910 (2014), arXiv:1311.7091 [nucl-ex] .

[228] *Measurement of the correlation between elliptic flow and higher-order flow harmonics in Pb+Pb collisions at* $\sqrt{s_{\rm NN}}$*=2.76 TeV*, Tech. Rep. ATLAS-CONF-2014-022 (CERN, Geneva, 2014).

[229] V. Blobel, in *Advanced Statistical Techniques in Particle Physics. Proceedings, Conference, Durham, UK, March 18-22, 2002* (2002) pp. 258–267, arXiv:hep-ex/0208022 [hep-ex] .

[230] J. Noronha-Hostler, M. Luzum, and J.-Y. Ollitrault, Phys. Rev. **C93**, 034912 (2016), arXiv:1511.06289 [nucl-th] .

[231] S. A. Voloshin and A. M. Poskanzer, Phys. Lett. **B474**, 27 (2000), arXiv:nucl-th/9906075 [nucl-th] .

[232] H.-J. Drescher, A. Dumitru, C. Gombeaud, and J.-Y. Ollitrault, Phys. Rev. **C76**, 024905 (2007), arXiv:0704.3553 [nucl-th] .

[233] D. Teaney and L. Yan, Phys. Rev. **C86**, 044908 (2012), arXiv:1206.1905 [nucl-th] .

[234] L. Yan and J.-Y. Ollitrault, Phys. Lett. **B744**, 82 (2015), arXiv:1502.02502 [nucl-th] .

[235] J. Qian, U. W. Heinz, and J. Liu, Phys. Rev. **C93**, 064901 (2016), arXiv:1602.02813 [nucl-th] .

[236] W. Broniowski, P. Bozek, and M. Rybczynski, Phys. Rev. **C76**, 054905 (2007), arXiv:0706.4266 [nucl-th] .

Appendix A

Derivation of the cumulant flow harmonics

A.1 Moment and cumulant generating functions

The moments of a probability distribution are a set of quantities that describe its behavior. The n^{th}-order moment of a probability distribution is defined as

$$\langle x^n \rangle \equiv \int x^n p(x) dx. \tag{A.1}$$

If a random variable x is distributed according to a probability distribution $p(x)$, then its moments can be obtained using a moment-generating function. The moment-generating function for a random variable is defined as

$$M(k) \equiv \int e^{kx} p(x) dx, \tag{A.2}$$

which is interpreted as the expectation value of the random variable e^{kx}. To illustrate the source of each moment, the moment-generated function is expressed as a series:

$$\begin{aligned} M(k) &= \int \sum_{n=0}^{\infty} \frac{(xk)^n}{n!} p(x) dx, \\ &= \int p(x) dx + k \int x p(x) dx + \frac{1}{2!} k^2 \int x^2 p(x) dx + \ldots \\ &= 1 + k\langle x \rangle + \frac{k^2}{2!} \langle x^2 \rangle + \ldots \end{aligned} \tag{A.3}$$

Here, the n^{th}-order moment is obtained by differentiating the moment-generating function n times and setting $k = 0$. For example, the first moment is obtained by

$$\begin{aligned} \frac{d}{dk}M(k)\bigg|_{k=0} &= \int xp(x)dx + k\int x^2 p(x)dx + \mathscr{O}(k^2)\bigg|_{k=0} \\ &= \langle x \rangle, \end{aligned} \tag{A.4}$$

the second-oder moment is obtained by

$$\begin{aligned} \frac{d^2}{dk^2}M(k)\bigg|_{k=0} &= \int x^2 p(x)dx + \mathscr{O}(k)\bigg|_{k=0} \\ &= \langle x^2 \rangle, \end{aligned} \tag{A.5}$$

and so on.

Cumulants are an alternative set of quantities that can be used to describe the behavior of a probability distribution. Cumulants and moments of a probability distribution are directly related in that the moments determine the cumulants and *vice versa.* Cumulants are obtained using a cumulant-generating function, which is defined as the natural logarithm of the moment generating function

$$G(k) \equiv \log M(k). \tag{A.6}$$

In a similar approach, the source of each cumulant is illustrated through a series expansion of the cumulant-generating function:

$$G(k) = \sum_{n=0}^{\infty} C_n \frac{k^n}{n!}, \tag{A.7}$$

Here, the n^{th}-order cumulant C_n is obtained by differentiating the cumulant-generating function n

times and setting $k = 0$. For example, the first-order cumulant is obtained by

$$\begin{aligned} C_1 &= \frac{d}{dk} G(k) \Big|_{k=0} \\ &= \frac{d}{dk} \left[\log \left(M(k) \right) \right] \Big|_{k=0} \\ &= \frac{d}{dk} \left[\log \left(\int e^{kx} p(x) dx \right) \right] \Big|_{k=0} \\ &= \frac{\int x e^{kx} p(x) dx}{\int e^{kx} p(x) dx} \Big|_{k=0} \\ &= \frac{\int x p(x) dx}{\int p(x) dx} \\ &= \langle x \rangle, \end{aligned} \tag{A.8}$$

the second-oder cumulant is obtained by

$$\begin{aligned} C_2 &= \frac{d^2}{dk^2} \left[\log \left(\int e^{kx} p(x) dx \right) \right] \Big|_{k=0} \\ &= \frac{d}{dk} \frac{\int x e^{kx} p(x) dx}{\int e^{kx} p(x) dx} \Big|_{k=0} \\ &= \frac{\left(\int x^2 e^{kx} p(x) dx \right) \left(\int e^{kx} p(x) dx \right) - \left(\int x e^{kx} p(x) dx \right)^2}{\left(\int e^{kx} p(x) dx \right)^2} \Big|_{k=0} \\ &= \frac{\left(\int x^2 p(x) dx \right) \left(\int p(x) dx \right) - \left(\int x p(x) dx \right)^2}{\left(\int p(x) dx \right)^2} \\ &= \langle x^2 \rangle - \langle x \rangle^2, \end{aligned} \tag{A.9}$$

and so on. The first three orders of cumulants ($n = 1$–3) are equivalent to the respective orders of *central* moments ($\int (x - \langle x \rangle)^n p(x) dx$) for a probability distribution. The lowest-order cumulants are commonly referred to as the mean, the variance, and the skewness, respectively. The cumulants diverge from the central moments beyond $n = 3$.

A.2 Cumulant flow harmonics

The cumulant flow harmonics in Eqs. (2.8) and (2.7) are obtained by assuming that the fluctuation behavior is Gaussian and isotropic. In two dimensions, the Gaussian behavior is parametrized with

$$p(\vec{v}_n) = \frac{1}{2\pi\sigma_x\sigma_y}\exp\left[-\frac{\left(v_{n,x}-\langle v_n^{\mathrm{RP}}\rangle\right)^2}{2\sigma_x^2}-\frac{v_y^2}{2\sigma_y^2}\right], \tag{A.10}$$

where the coordinate system is chosen such that the $\hat{x}$ vector points in the direction of the reaction plane. Here, the average flow in the $\hat{y}$ direction is set to 0 in order to conserve parity [178]. Setting the transverse widths equal ($\sigma_x = \sigma_y = \sigma$) will make Eq. A.10 isotropic,

$$p(\vec{v}_n) = \frac{1}{2\pi\sigma^2}\exp\left[-\frac{\left|\vec{v}_n-\langle\vec{v}_n^{\mathrm{RP}}\rangle\right|^2}{2\sigma_{v_n}^2}\right], \tag{A.11}$$

Since this $p(\vec{v}_n)$ distribution is Gaussian, all cumulants above order 2 disappear in a cumulant expansion,

$$\begin{aligned} G(k) &\equiv \log\langle e^{\vec{k}\cdot\vec{v}_n}\rangle \\ &= k_x\langle v_n^{\mathrm{RP}}\rangle + \frac{k^2\sigma^2}{2}. \end{aligned} \tag{A.12}$$

Here, σ^2 denotes the variance of the distribution. However, in this isotropic Gaussian case, $\sigma_{v_n}^2 = \sigma^2$. Before calculating cumulant flow harmonics, Eq. (A.12) must be transformed to the laboratory frame, where the reaction plane angle is assumed to be uniformly distributed. This is achieved by exponentiating the right-hand-side of Eq. (A.12), making the substitution $\vec{k} = (k\cos\phi, k\sin\phi)$, and

integrating over the azimuthal dependence

$$\begin{aligned} G(k) &\equiv \log\left[\int_0^{2\pi}\frac{d\phi}{2\pi}\langle\exp\left(k\langle v_n^{\mathrm{RP}}\rangle\cos\phi+\frac{k^2\sigma^2}{2}\right)\rangle\right] \\ &= \log\left[\langle e^{\frac{k^2\sigma^2}{2}} I_0\left(k\langle v_n^{\mathrm{RP}}\rangle\right)\rangle\right] \\ &= \log I_0\left(k\langle v_n^{\mathrm{RP}}\rangle\right)+\frac{k^2\sigma^2}{2}. \end{aligned} \tag{A.13}$$

The m^{th}-order cumulant flow harmonic in the laboratory frame is then obtained using Eq. (2.6). The cumulant flow harmonic for $m=2$ is obtained with

$$\begin{aligned} \frac{d^2}{dk^2}\log I_0(kv_n\{2\}) &\equiv \left.\frac{d^2}{dk^2}\log G_n(k)\right|_{k=0} \\ \frac{v_n\{2\}^2}{2} &= \sigma^2+\frac{\langle v_n^{\mathrm{RP}}\rangle^2}{2} \\ v_n\{2\}^2 &= \langle v_n^{\mathrm{RP}}\rangle^2+2\sigma^2, \end{aligned} \tag{A.14}$$

the cumulant flow harmonic for $m=4$ is obtained with

$$\begin{aligned} \frac{d^4}{dk^4}\log I_0(kv_n\{4\}) &\equiv \left.\frac{d^4}{dk^4}\log G_n(k)\right|_{k=0} \\ -\frac{3v_n\{4\}^4}{8} &= -\frac{3\langle v_n^{\mathrm{RP}}\rangle^4}{8} \\ v_n\{4\}^4 &= \langle v_n^{\mathrm{RP}}\rangle^4, \end{aligned} \tag{A.15}$$

and so on. Continuing to higher orders will reproduce the results of Eq. (2.8).

Since the reaction plane is inaccessible in experiment, the findings of Eq. (2.8) are not practical in terms of a measurement. As was shown in Chapter 5 the distribution of flow harmonics can be measured and from it can be extracted its moments. Following the assumptions at the beginning of this section, integration of the isotropic 2D Gaussian of Eq. (A.11) over the azimuthal dependence yields the Bessel Gaussian distribution of Eq. (2.3). A moment expansion of this probability

distribution yields (for even-order moments):

$$\langle v_n^2 \rangle = \langle v_n^{\mathrm{RP}} \rangle^2 + 2\delta_{v_n}^2 \tag{A.16}$$

$$\langle v_n^4 \rangle = \langle v_n^{\mathrm{RP}} \rangle^4 + 8\langle v_n^{\mathrm{RP}} \rangle^2 \delta_{v_n}^2 + 8\delta_{v_n}^4 \tag{A.17}$$

$$\langle v_n^6 \rangle = \langle v_n^{\mathrm{RP}} \rangle^6 + 18\langle v_n^{\mathrm{RP}} \rangle^4 \delta_{v_n}^2 + 72\langle v_n^{\mathrm{RP}} \rangle^2 \delta_{v_n}^4 + 48\delta_{v_n}^2 \tag{A.18}$$

$$\langle v_n^8 \rangle = \langle v_n^{\mathrm{RP}} \rangle^8 + 32\langle v_n^{\mathrm{RP}} \rangle^6 \delta_{v_n}^2 + 288\langle v_n^{\mathrm{RP}} \rangle^4 \delta_{v_n}^4 + 768\langle v_n^{\mathrm{RP}} \rangle^2 \delta_{v_n}^6 + 384\delta_{v_n}^8 \tag{A.19}$$

The cumulant flow harmonics of Eq. (2.7) can now be derived by eliminating the δ_{v_n} term from Eqs. (A.16)– (A.19), solving each for $\langle v_n^{\mathrm{RP}} \rangle^m$, and then plugging the results into Eq. (2.8). In order to achieve a compact form, solutions are first derived for the lowest orders and then bootstrapped to higher orders. Solving for $\langle v_n^{\mathrm{RP}} \rangle^2$ in Eq (A.16) yields

$$\langle v_n^{\mathrm{RP}} \rangle^2 = \langle v_n^2 \rangle - 2\delta_{v_n}^2, \tag{A.20}$$

and plugging this into Eq. (2.8) gives

$$v_n\{2\}^2 = \langle v_n^2 \rangle - 2\delta_{v_n}^2 + 2\sigma^2. \tag{A.21}$$

Given the assumed isotropic Gaussian behavior, $\delta_{v_n}^2 = \sigma^2$ in this case, and the final result for the second-order cumulant flow harmonic is

$$v_n\{2\}^2 = \langle v_n^2 \rangle. \tag{A.22}$$

Before moving to higher orders, an expression for $\delta_{v_n}^2$ is needed in terms of the moments. To achieve this aim, Eq. (A.16) is rearranged such that

$$\delta_{v_n}^2 = \frac{1}{2}\left(\langle v_n^2 \rangle - \langle v_n^{\mathrm{RP}} \rangle^2 \right). \tag{A.23}$$

The fourth-order cumultant flow harmonic is determined by plugging Eq. (A.23) into Eq. (A.23) and solving for $\langle v_n^{\mathrm{RP}} \rangle^4$

$$\langle v_n^{\mathrm{RP}} \rangle^4 = 2\langle v_n^2 \rangle^2 - \langle v_n^4 \rangle. \tag{A.24}$$

Plugging this result into Eq. (2.8) then gives an expression for the fourth-order cumulant flow harmonic in terms of the moments

$$v_n\{4\}^4 = 2\langle v_n^2 \rangle^2 - \langle v_n^4 \rangle. \tag{A.25}$$

Repeating this procedure for increasing orders of cumulants and utilizing the results from the lower orders will yield the cumulant flow harmonics expressed in Eq. (2.7).

Appendix B

Analytic response matrices

B.1 Gaussian response matrix

For Gaussian smearing effects, the response function is built from a standard, 2D Gaussian distribution for vector quantities:

$$p\left(\vec{v}_n^{\,\mathrm{obs}}|\vec{v}_n\right) = \frac{1}{2\pi\delta_{v_n}^2}\exp\left[-\frac{\left(\vec{v}_n^{\,\mathrm{obs}}-\vec{v}_n\right)^2}{2\delta_{v_n}^2}\right], \tag{B.1}$$

where $\vec{v}_n^{\,\mathrm{obs}}$ is the observed (smeared) flow vector for the event, $\vec{v}_n$ is the true underlying flow vector for the event, and δ_{v_n} is the width of the smearing distribution. In general, flow analyses are more interested in the magnitude of the flow vector. In order to obtain a response function for the magnitude of flow, the 2D Gaussian is projected onto the radial direction. This is achieved by

transforming the 2D distribution to polar coordinates and integrating out the ϕ-dependence:

$$
\begin{aligned}
p\left(v_n^{\mathrm{obs}}|v_n\right) &= \frac{1}{2\pi\delta_{v_n}^2}\oint \exp\left[-\frac{\left(v_n^{\mathrm{obs}}\right)^2+(v_n)^2-2v_n^{\mathrm{obs}}v_n\cos\phi}{2\delta_{v_n}^2}\right] v_n^{\mathrm{obs}}d\phi\,, \\
p\left(v_n^{\mathrm{obs}}|v_n\right) &= \frac{v_n^{\mathrm{obs}}}{\delta_{v_n}^2}\exp\left[-\frac{\left(v_n^{\mathrm{obs}}\right)^2+(v_n)^2}{2\delta_{v_n}^2}\right] I_0\left(\frac{v_n^{\mathrm{obs}}v_n}{\delta_{v_n}^2}\right)\,,
\end{aligned}
\tag{B.2}
$$

where I_0 is the modified Bessel Function of the first kind. The width for this distribution is extracted from the average of the widths obtained from Gaussian fits to the x- and y-projections of the rescaled subevent difference distribution. These projections are themselves 1D Gaussian distributions centered at zero with equal widths. With Eq. B.2 fully parametrized, it can then be used to populate each element of the response matrix. Once the Gaussian response matrix is populated it can be used in the unfolding technique described in section 5.2.2.

B.2 Student's t-response matrix

The standard Student's t-distribution probability density function (PDF) is given as

$$
p(t) = \frac{\Gamma\left(\frac{\nu+1}{2}\right)}{\Gamma\left(\frac{\nu}{2}\right)\sqrt{\nu\pi}}\left(1+\frac{t^2}{\nu}\right)^{\frac{\nu+1}{2}}\,, \tag{B.3}
$$

where ν is the number of degrees of freedom and $\Gamma(x)$ is the gamma function. The mean of this distribution is always zero and its variance is driven solely by the number of degrees of freedom, which is always greater than one, $\sigma^2 = \nu/(\nu-2)$. With these features, the standard Student's t-distribution is too restrictive for this analysis. In this case, it is more attractive to use the non-standardized Student's t-distribution:

$$
p\left(t|\nu,\mu,\delta\right) = \frac{\Gamma\left(\frac{\nu+1}{2}\right)}{\Gamma\left(\frac{\nu}{2}\right)\delta\sqrt{\nu\pi}}\left[1+\frac{(t-\mu)^2}{\nu\delta^2}\right]^{\frac{\nu+1}{2}}\,, \tag{B.4}
$$

where the mean is no longer fixed at zero, but shifts to μ. The variance is no longer driven solely by the number of degrees of freedom and therefore able to be less than one, $\sigma^2 = \delta^2 \nu / (\nu - 2)$.

As was done with the Gaussian response function, one can build a Student's t-response function from a 2D non-standardized Student's t-distribution for vector quantities:

$$p\left(\vec{v}_n^{\,\mathrm{obs}} | \vec{v}_n\right) = \frac{\Gamma\left(\frac{\nu+1}{2}\right)}{\Gamma\left(\frac{\nu}{2}\right)\delta_{v_n}\sqrt{\nu\pi}} \left[1 + \frac{\left(\vec{v}_n^{\,\mathrm{obs}} - \vec{v}_n\right)^2}{\nu\delta_{v_n}^2}\right]^{\frac{\nu+1}{2}}. \tag{B.5}$$

Again, the interest is in the magnitude of flow, so this distribution is then projected onto the radial direction by integrating out the azimuthal dependence

$$p\left(v_n^{\mathrm{obs}} | v_n\right) = \frac{\Gamma\left(\frac{\nu+1}{2}\right)}{\Gamma\left(\frac{\nu}{2}\right)\delta_{v_n}\sqrt{\nu\pi}} \oint \left[1 + \frac{\left(v_n^{\mathrm{obs}}\right)^2 + (v_n)^2 - 2v_n^{\mathrm{obs}} v_n \cos\phi}{\nu\delta_{v_n}^2}\right]^{\frac{\nu+1}{2}} v_n^{\mathrm{obs}} d\phi. \tag{B.6}$$

In this case, the integral over the azimuthal variable cannot be determined analytically and therefore must be evaluated numerically. The number of degrees of freedom for each event class is set as the average particle multiplicity for that class minus one, $\nu = \langle N \rangle - 1$. Similar to the Gaussian response matrix approach, the width for this function can be obtained by Student's t-fits to the rescaled subevent difference distributions. This fully parametrized response function can be used to populate each element of the response matrix. Once the Student's t-response matrix is populated it can be used in the unfolding technique described in section 5.2.2.

Appendix C

Unfolding performance plots

C.1 D'Agostini unfolding

Here, the unfolding performance for all $p(v_2)$ distributions quoted in this analysis obtained using D'Agostini iteration unfolding is provided. Each figure has the following form:

- Panel A shows the response matrix obtained using the methods described in Secs. 5.2.1 and 5.2.1.1.
- Panel B shows both the observed and final unfolded distributions. The observed distribution is unfolded using the response matrix in panel A.
- Panel C shows the correlation matrix for the final unfolded distribution in panel B. The bin-to-bin correlations are a result of the unfolding procedure itself and the non-diagonal elements in the response matrix.
- Panel D shows a χ^2/NDF goodness of fit between the refolded and observed distributions as a function of iteration. A dotted line at $\chi^2/NDF = 1.2$ signifies the iteration cutoff point.
- Panel E shows each iteration of the unfolding procedure refolded with the response matrix. The observed distribution is also shown to illustrate how well the refolded distributions reproduce it.

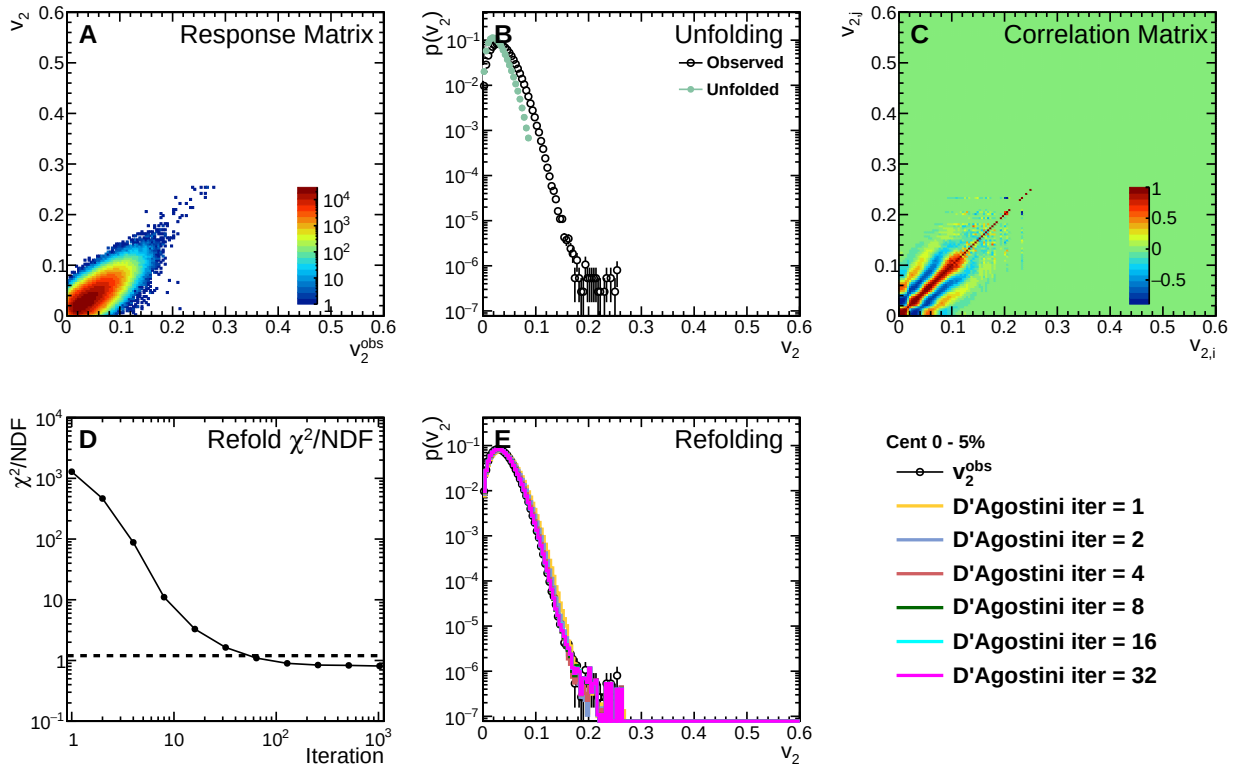

Figure C.1: $p\,(v_2)$ D'Agostini unfolding performance plots for events in the 0–5% centrality bin.

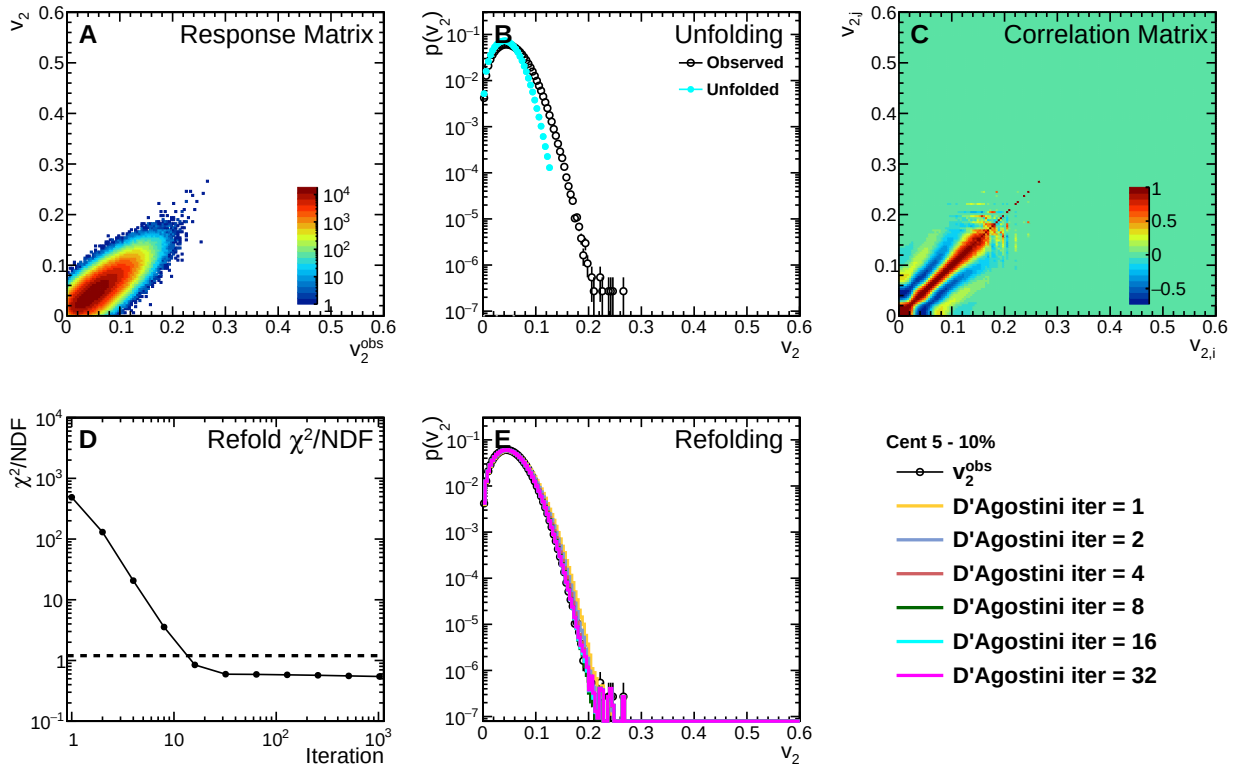

Figure C.2: $p(v_2)$ D'Agostini unfolding performance plots for events in the 5–10% centrality bin.

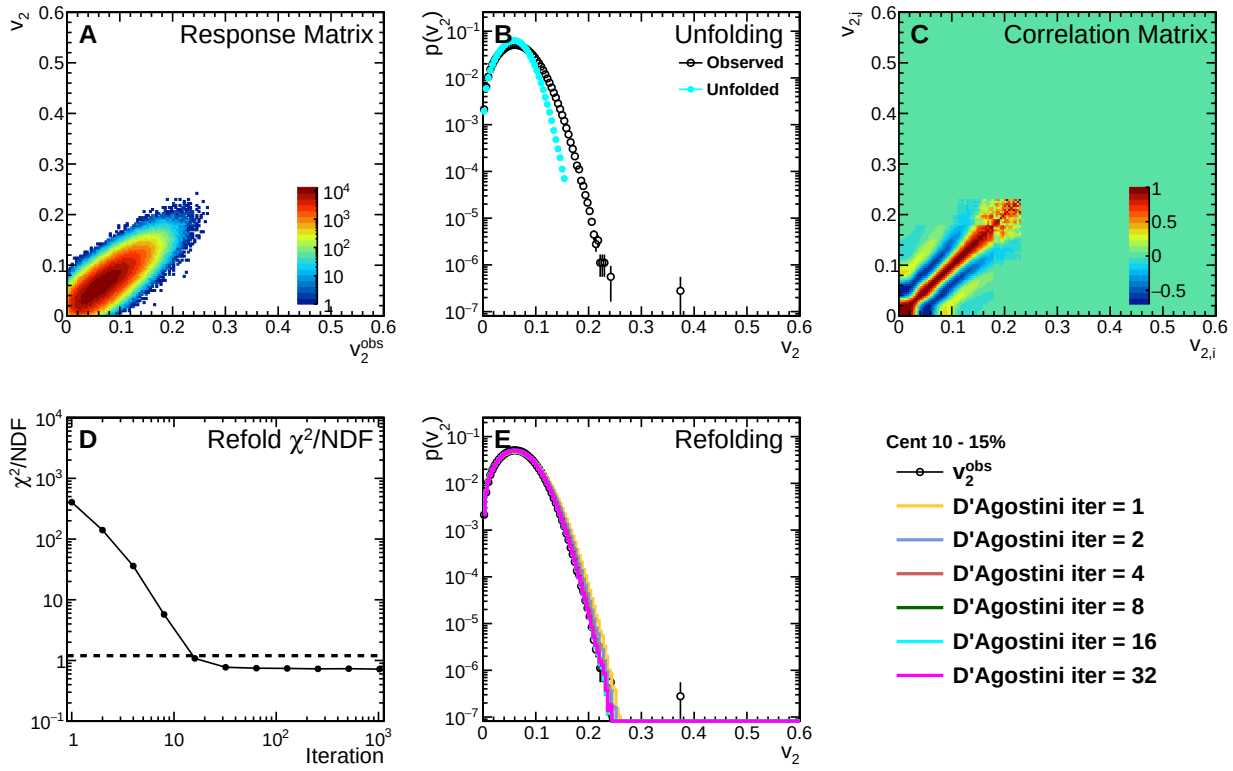

Figure C.3: $p(v_2)$ D'Agostini unfolding performance plots for events in the 10–15% centrality bin.

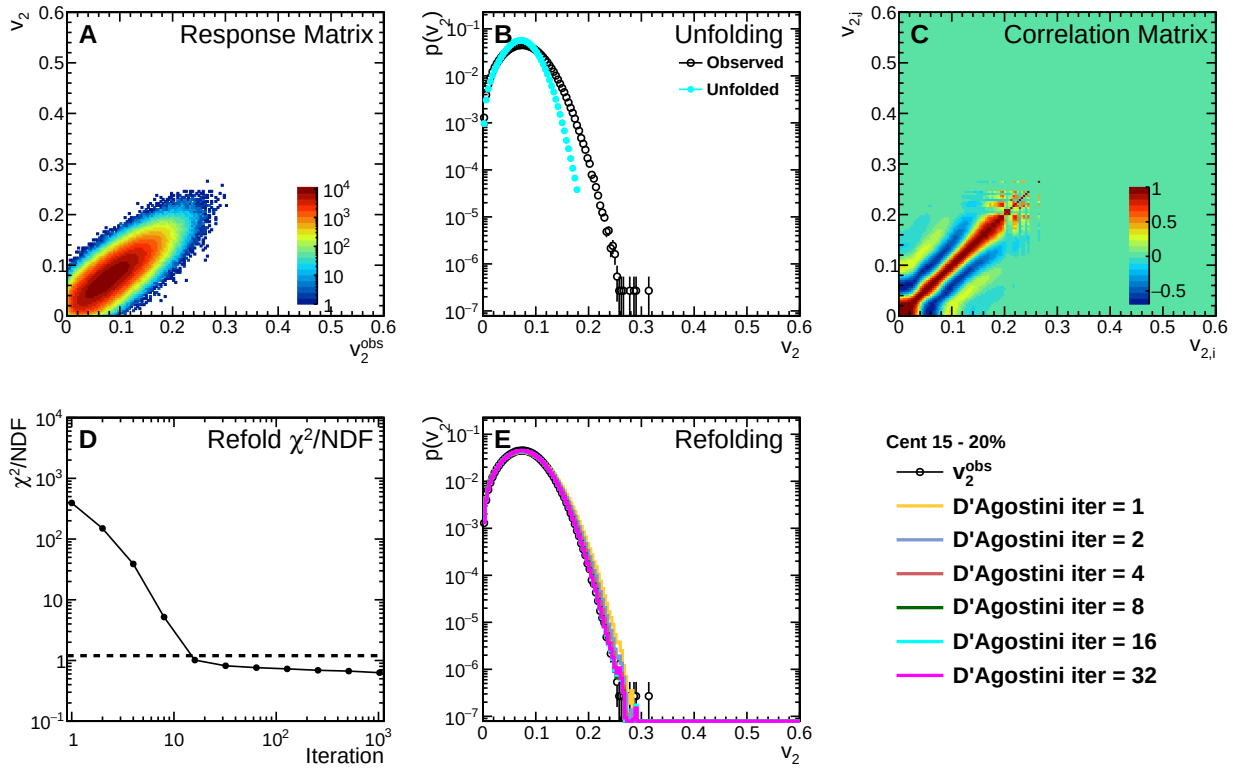

Figure C.4: $p(v_2)$ D'Agostini unfolding performance plots for events in the 15–20% centrality bin.

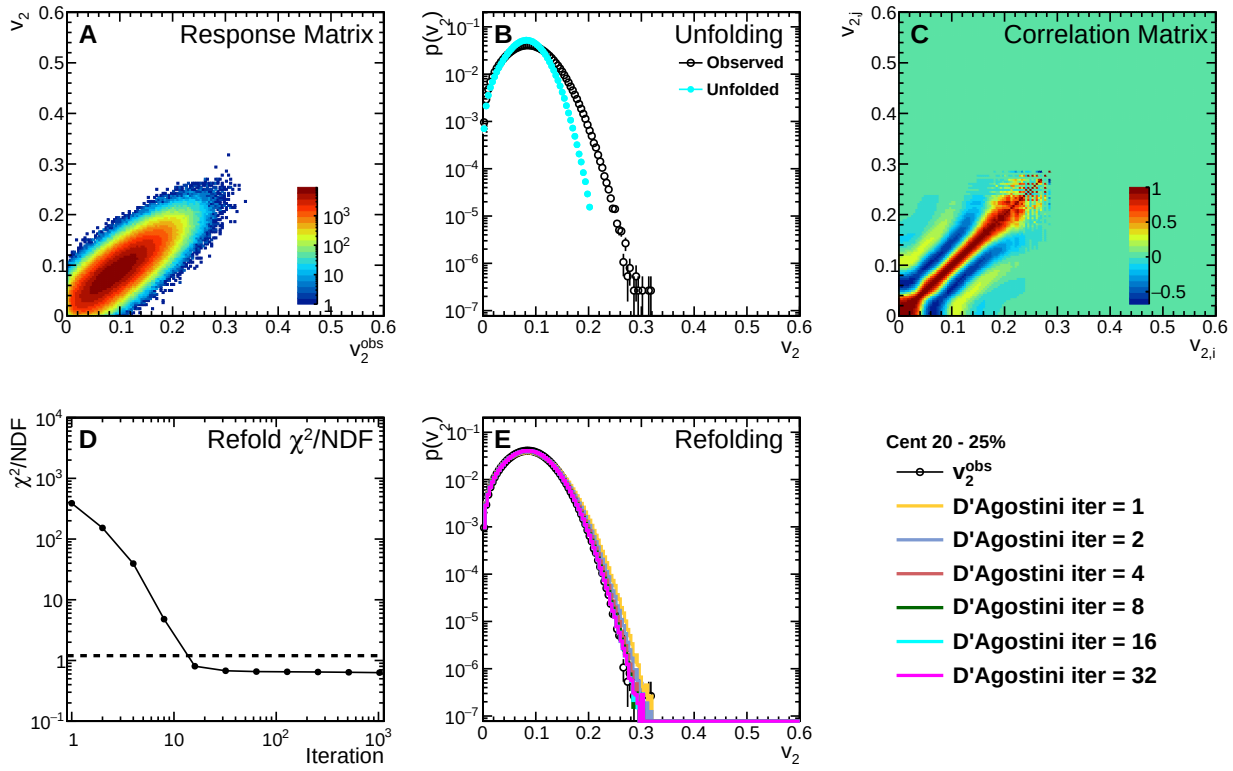

Figure C.5: $p(v_2)$ D'Agostini unfolding performance plots for events in the 20–25% centrality bin.

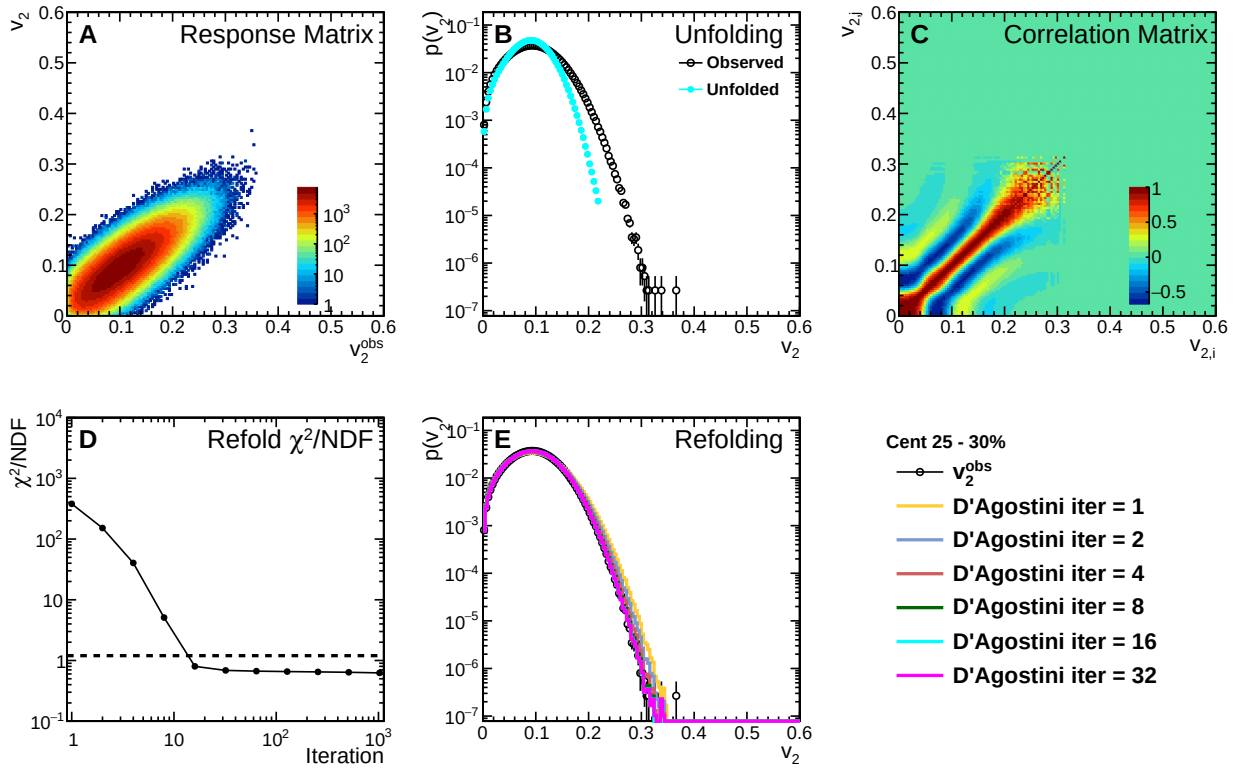

Figure C.6: $p(v_2)$ D'Agostini unfolding performance plots for events in the 25–30% centrality bin.

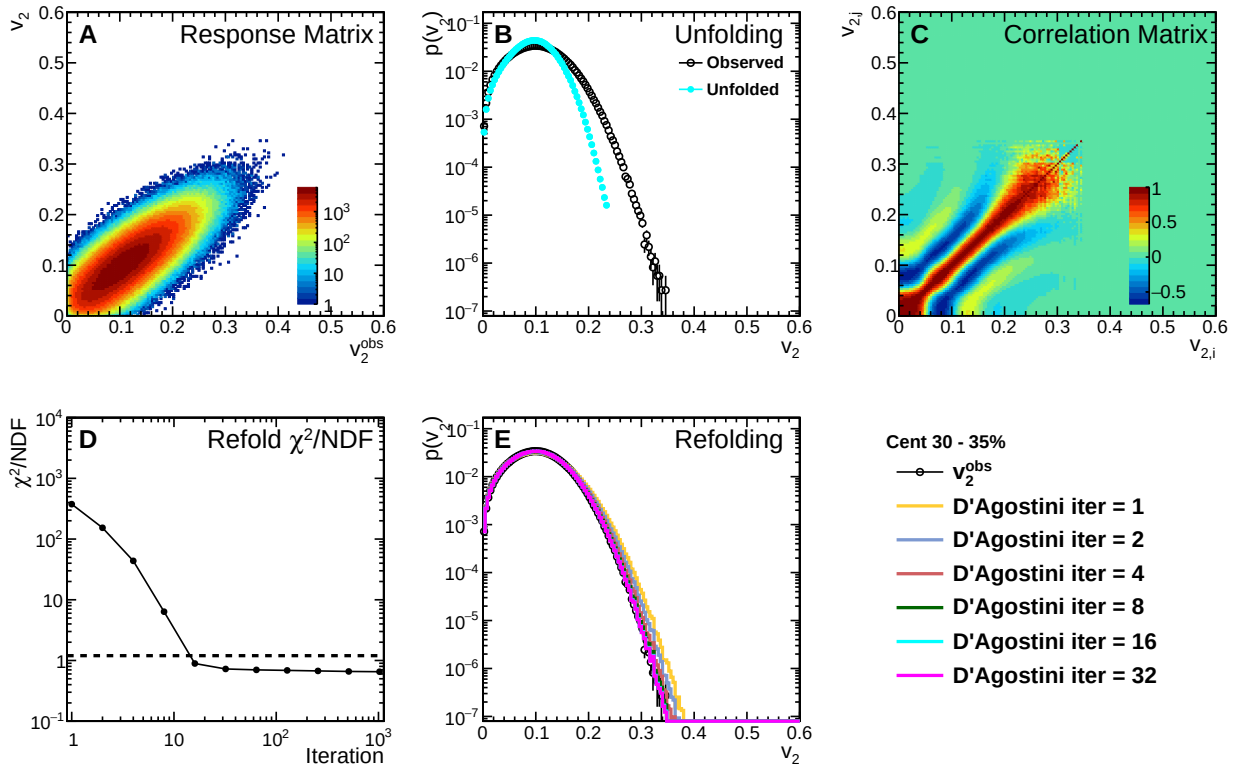

Figure C.7: $p(v_2)$ D'Agostini unfolding performance plots for events in the 30–35% centrality bin.

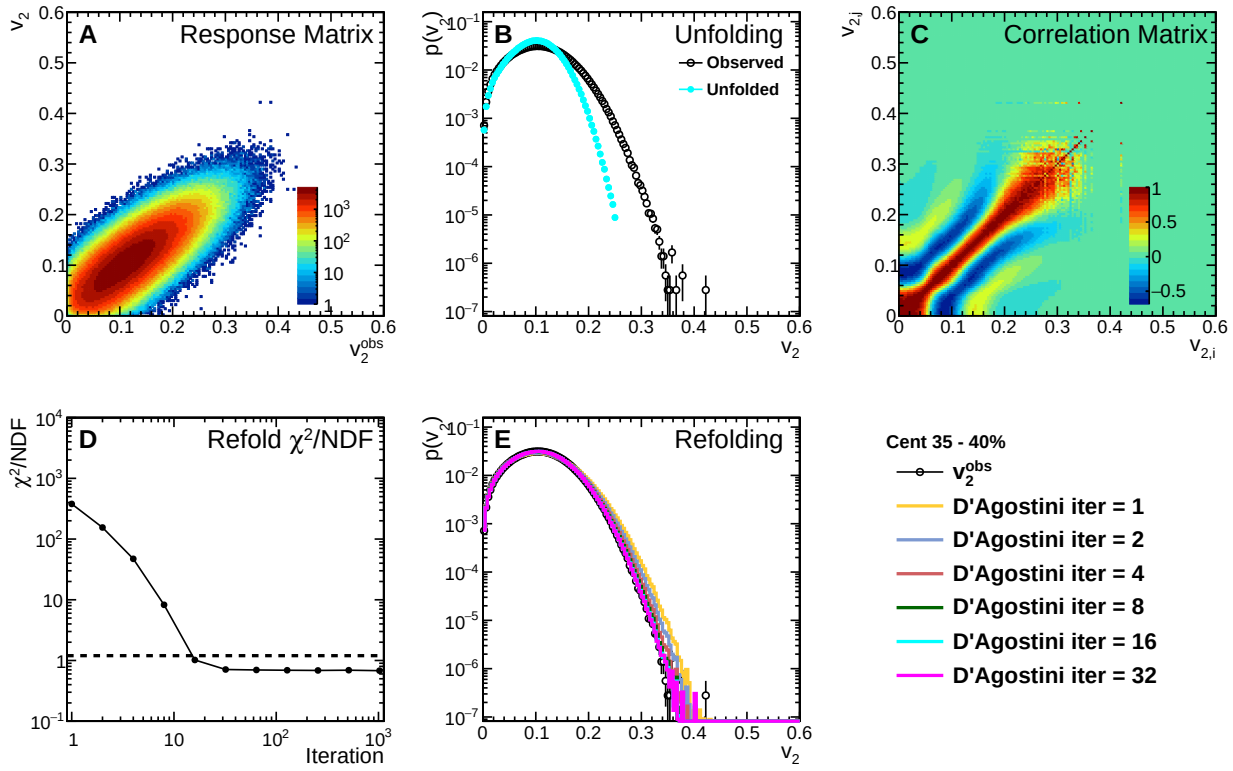

Figure C.8: $p(v_2)$ D'Agostini unfolding performance plots for events in the 35–40% centrality bin.

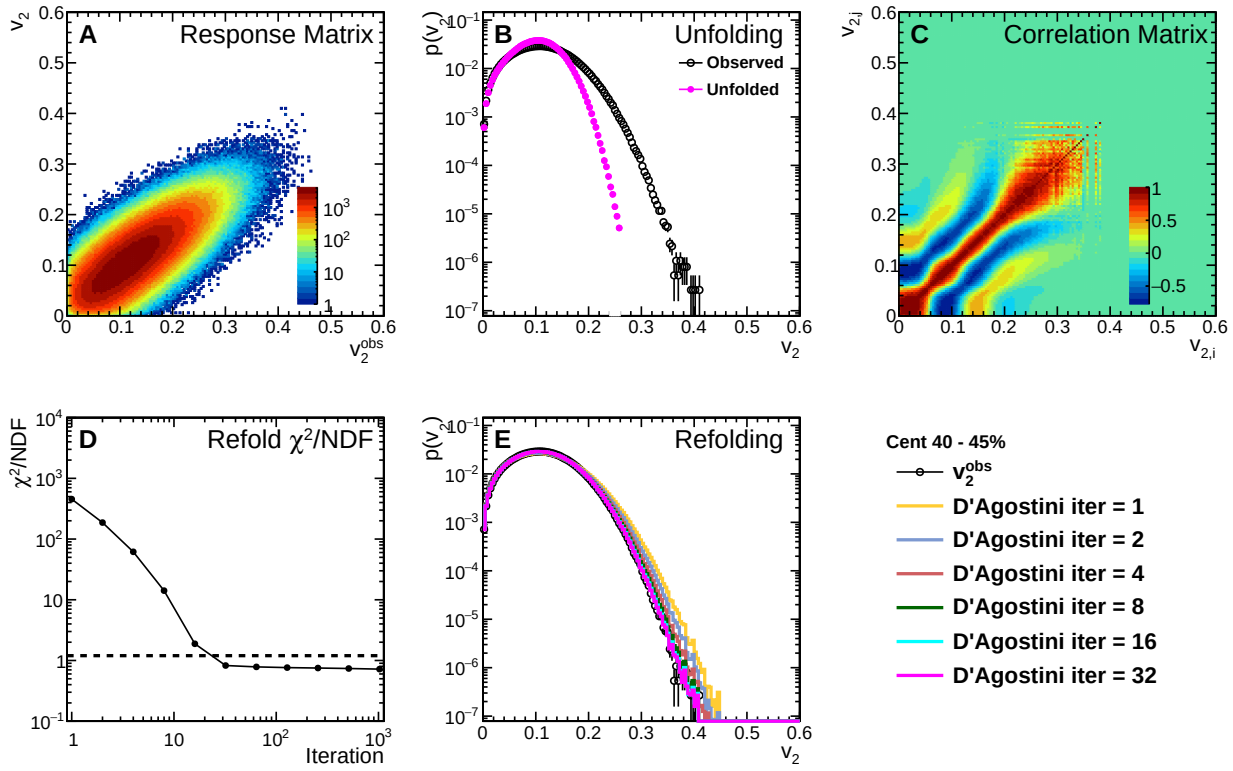

Figure C.9: $p(v_2)$ D'Agostini unfolding performance plots for events in the 40–45% centrality bin.

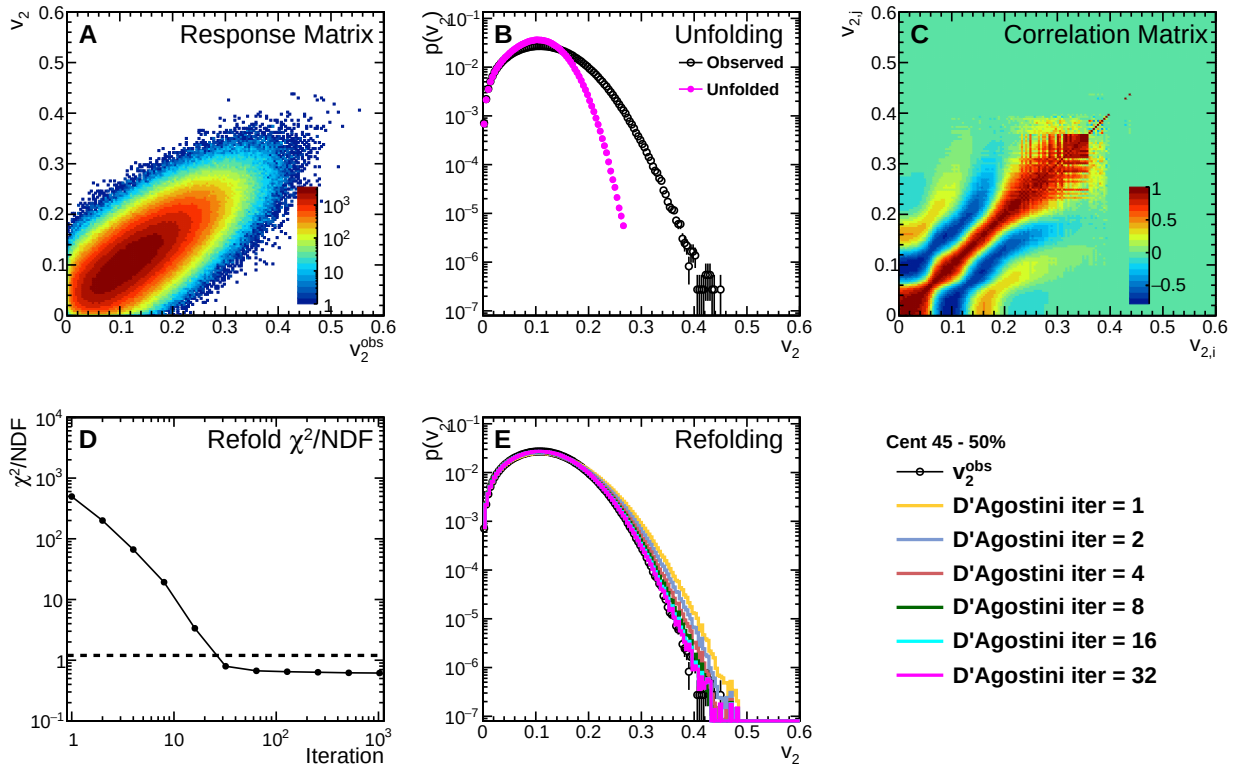

Figure C.10: $p(v_2)$ D'Agostini unfolding performance plots for events in the 45–50% centrality bin.

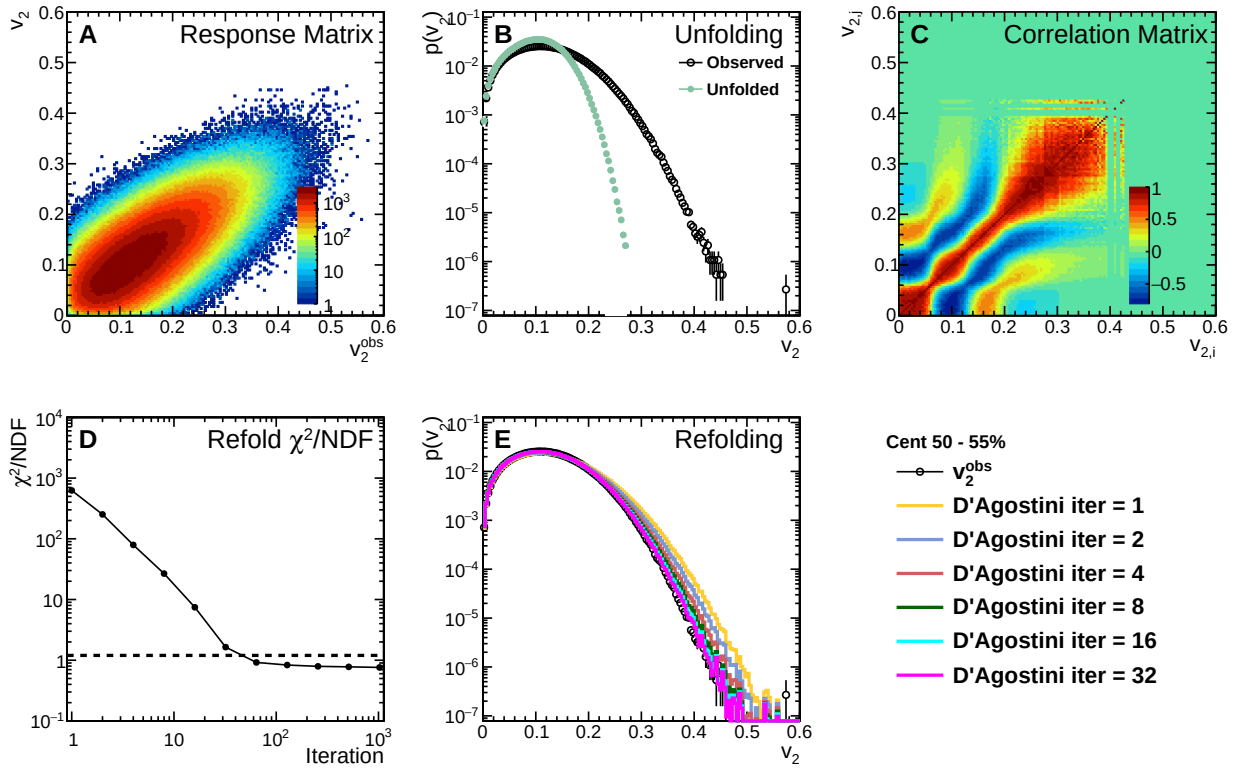

Figure C.11: $p(v_2)$ D'Agostini unfolding performance plots for events in the 50–55% centrality bin.

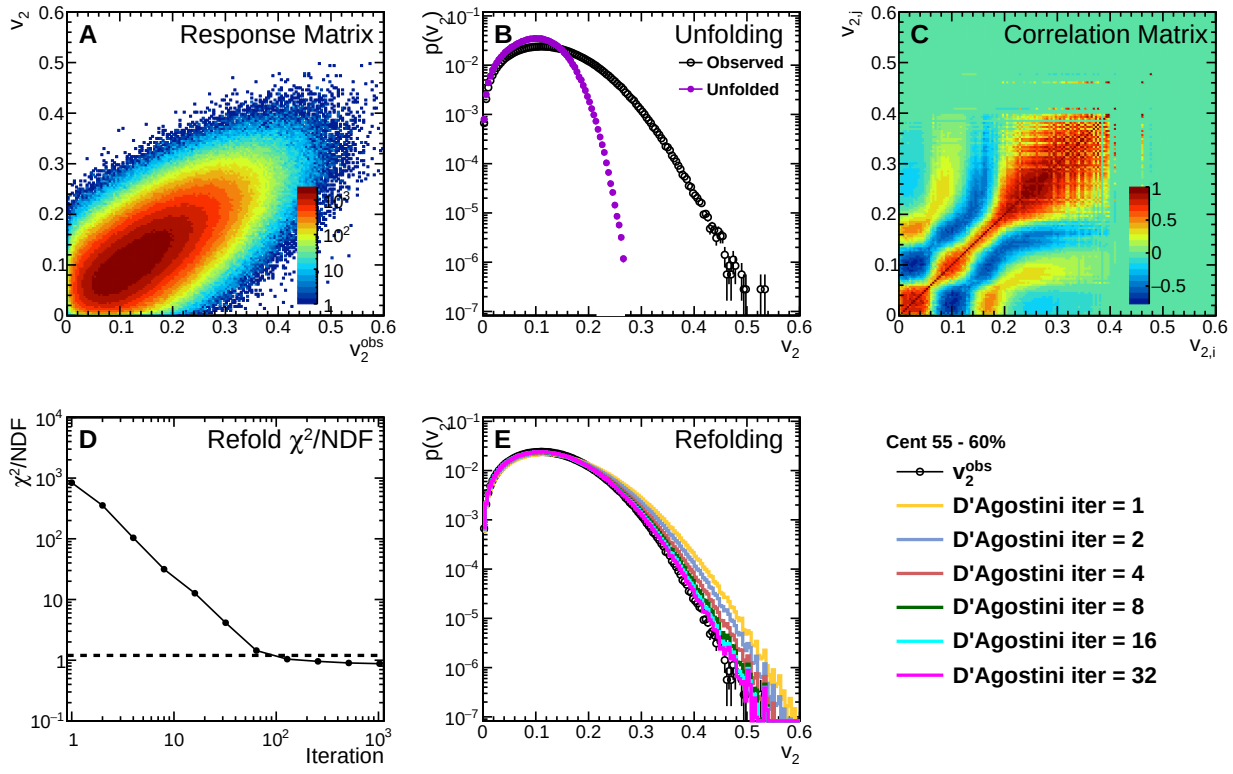

Figure C.12: $p(v_2)$ D'Agostini unfolding performance plots for events in the 55–60% centrality bin.

C.2 SVD unfolding

Here, the unfolding performance for all $p(v_2)$ distributions quoted in this analysis obtained using SVD unfolding is provided. Each figure has the following form:

- Panel A shows the response matrix obtained using the methods described in Secs. 5.2.1 and 5.2.1.1.
- Panel B shows both the observed and final unfolded distributions. The observed distribution is unfolded using the response matrix in panel A.
- Panel C shows the correlation matrix for the final unfolded distribution in panel B. The bin-to-bin correlations are a result of the unfolding procedure itself and the non-diagonal elements in the response matrix.
- Panel D shows a χ^2/NDF goodness of fit between the refolded and observed distributions as a function of iteration. A dotted line at $\chi^2/NDF = 1.2$ signifies the iteration cutoff point.
- Panel E shows each iteration of the unfolding procedure refolded with the response matrix. The observed distribution is also shown to illustrate how well the refolded distributions reproduce it.

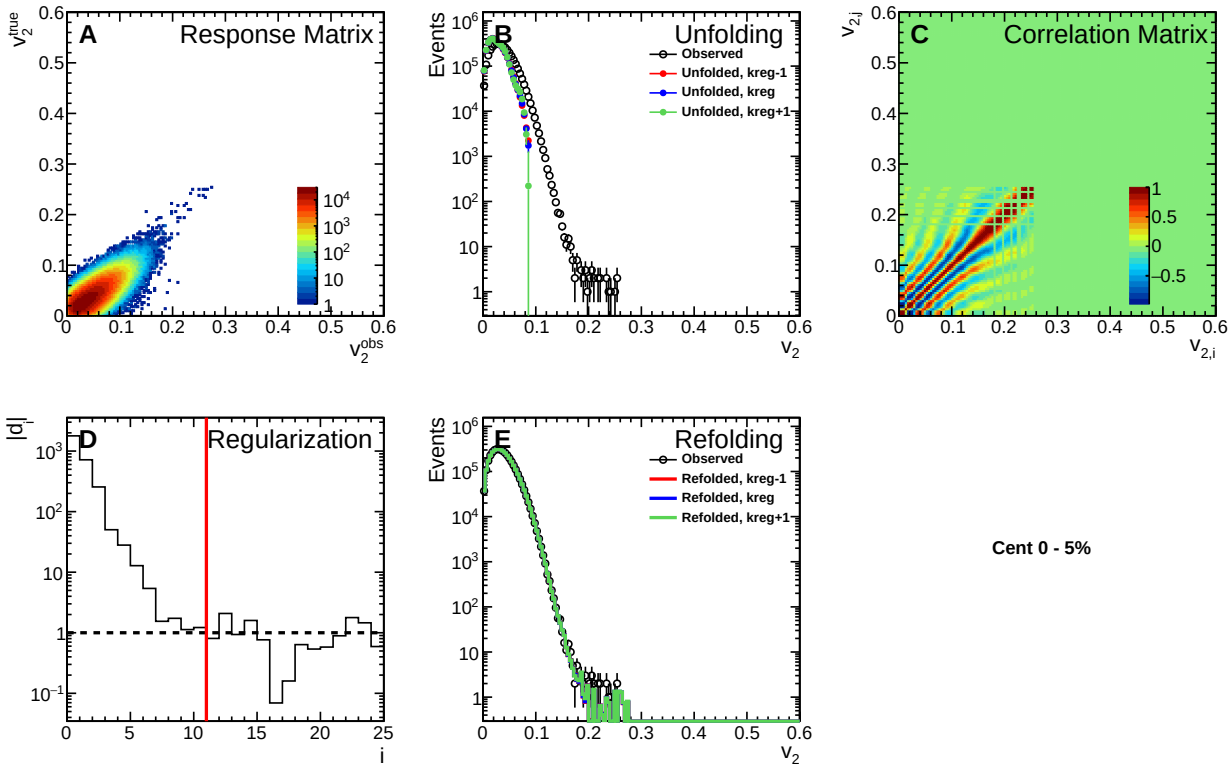

Figure C.13: $p(v_2)$ SVD unfolding performance plots for events in the 0–5% centrality bin.

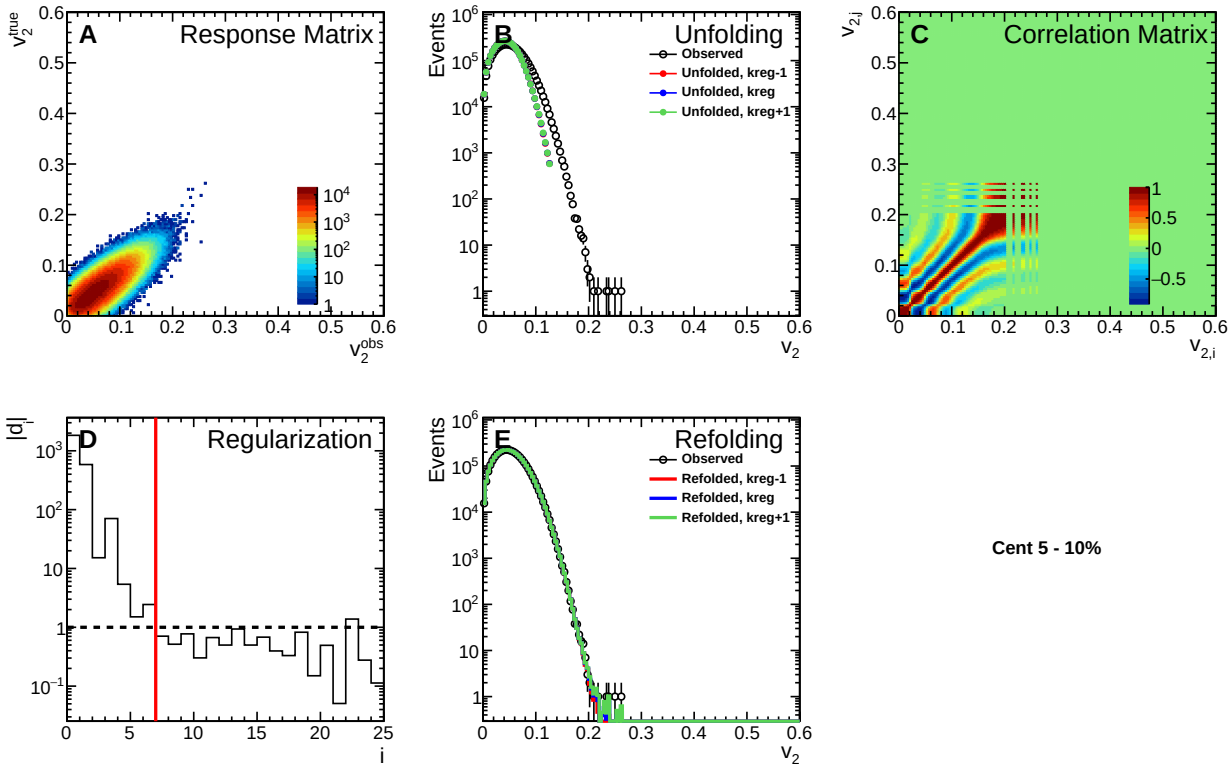

Figure C.14: $p(v_2)$ SVD unfolding performance plots for events in the 5–10% centrality bin.

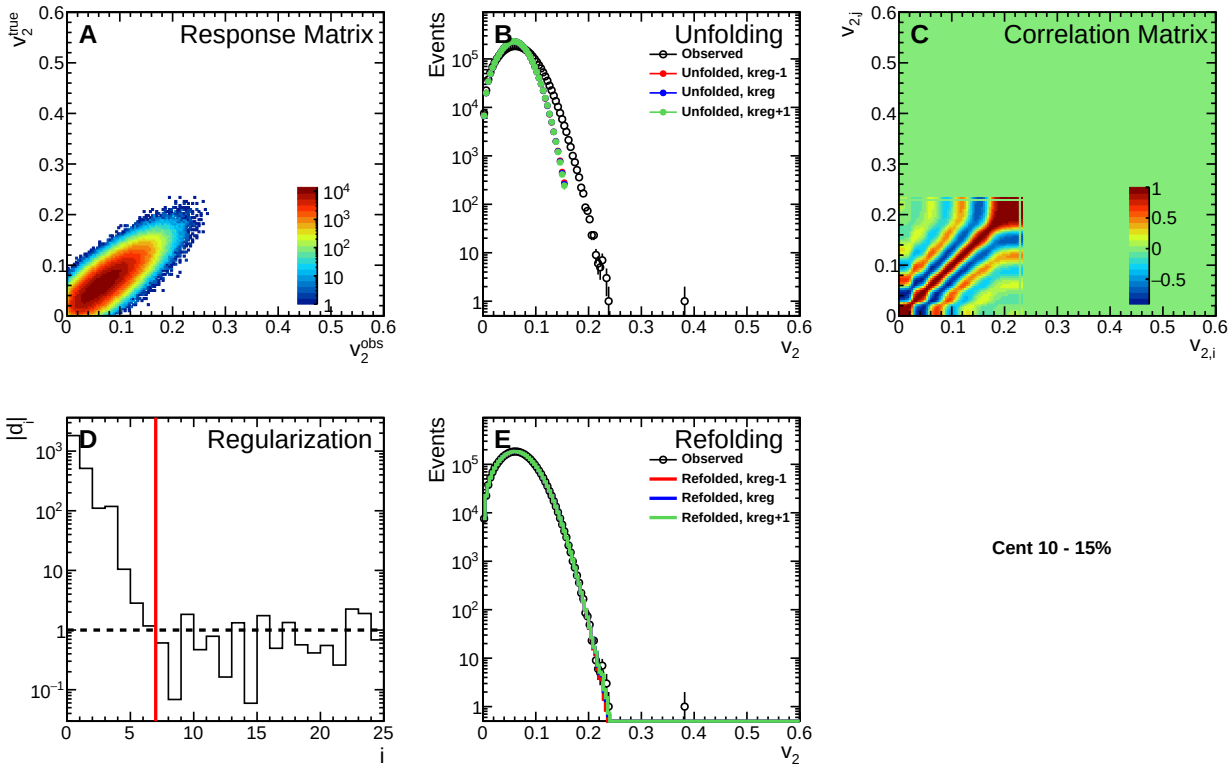

Figure C.15: $p(v_2)$ SVD unfolding performance plots for events in the 10–15% centrality bin.

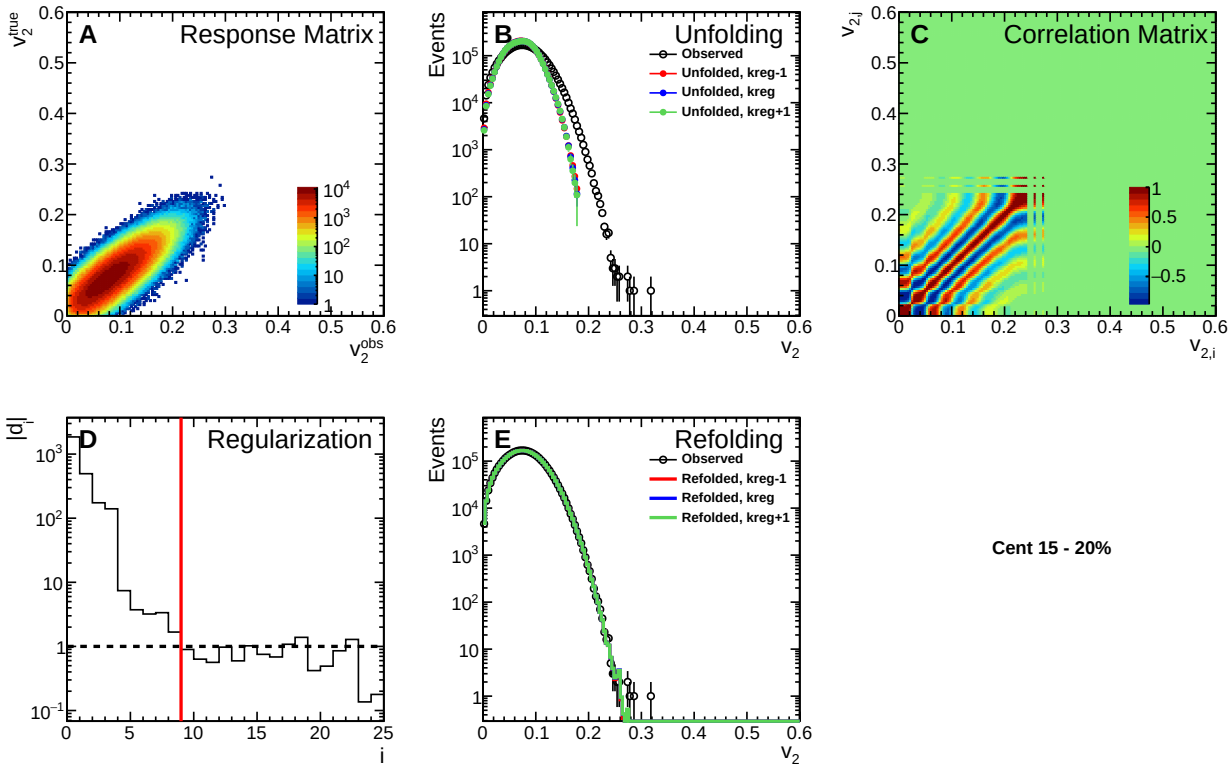

Figure C.16: $p(v_2)$ SVD unfolding performance plots for events in the 15–20% centrality bin.

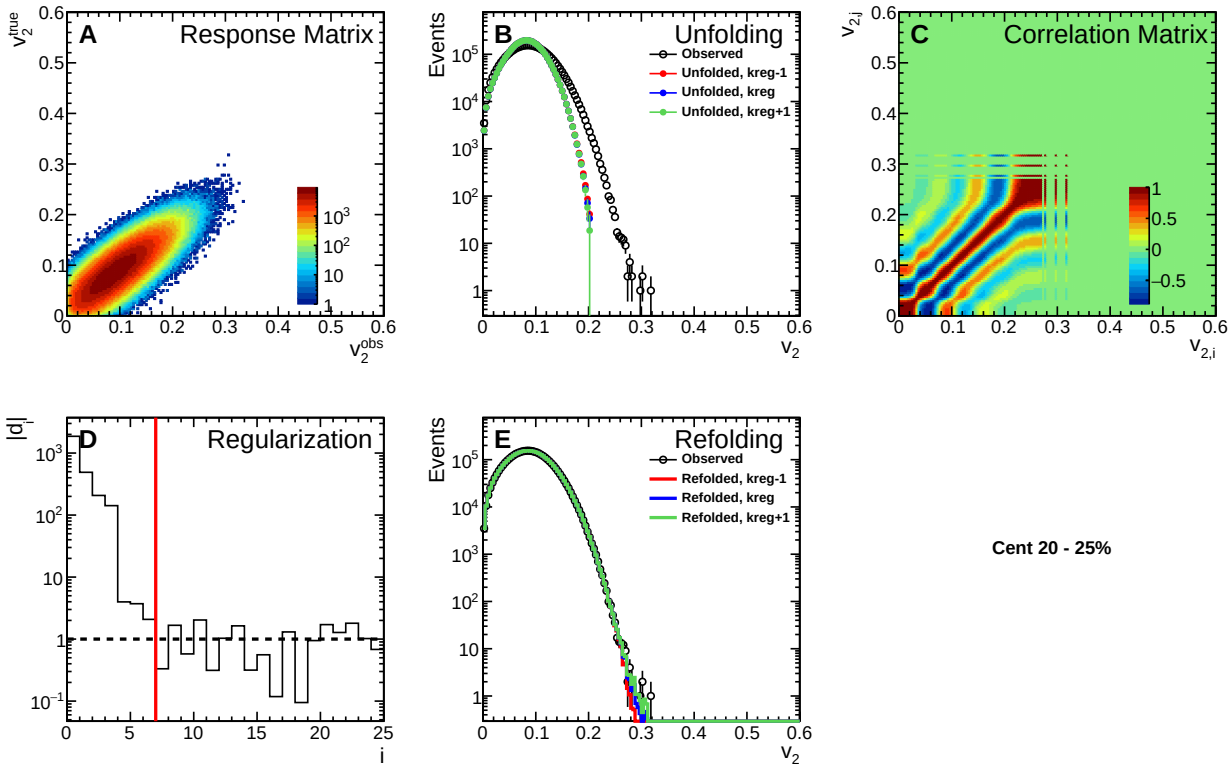

Figure C.17: $p(v_2)$ SVD unfolding performance plots for events in the 20–25% centrality bin.

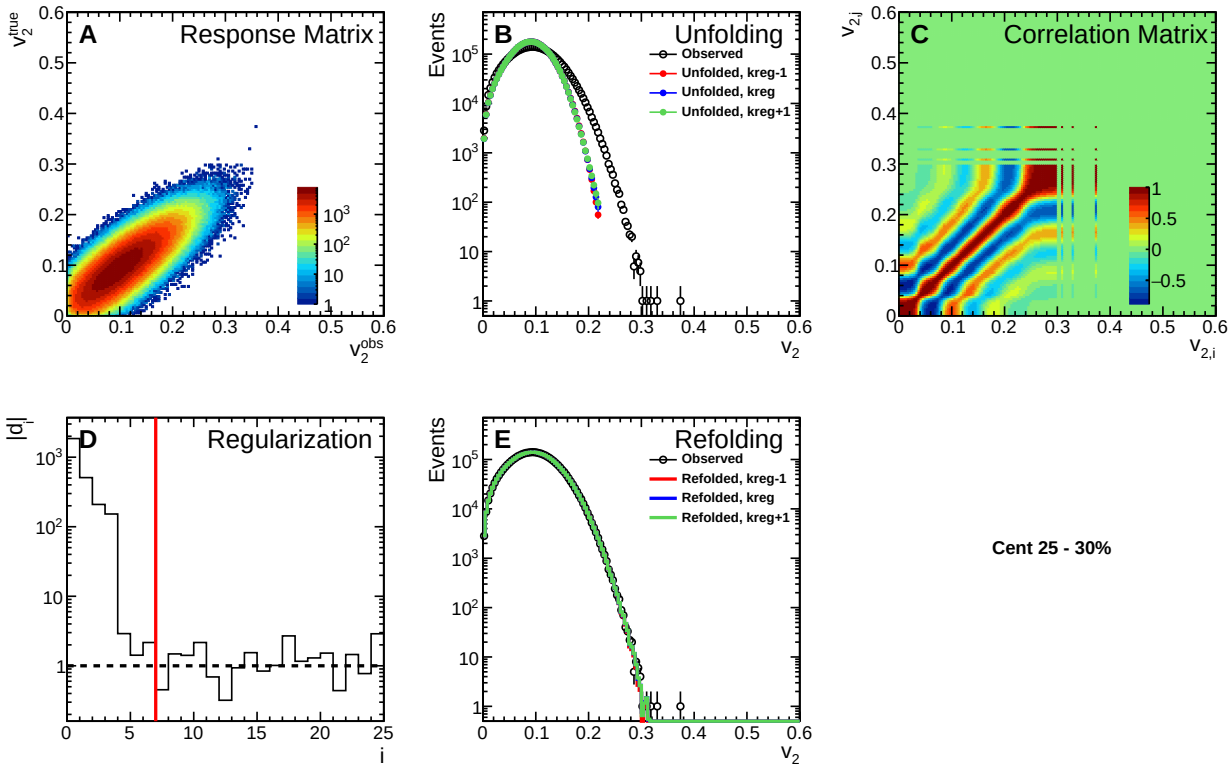

Figure C.18: $p(v_2)$ SVD unfolding performance plots for events in the 25–30% centrality bin.

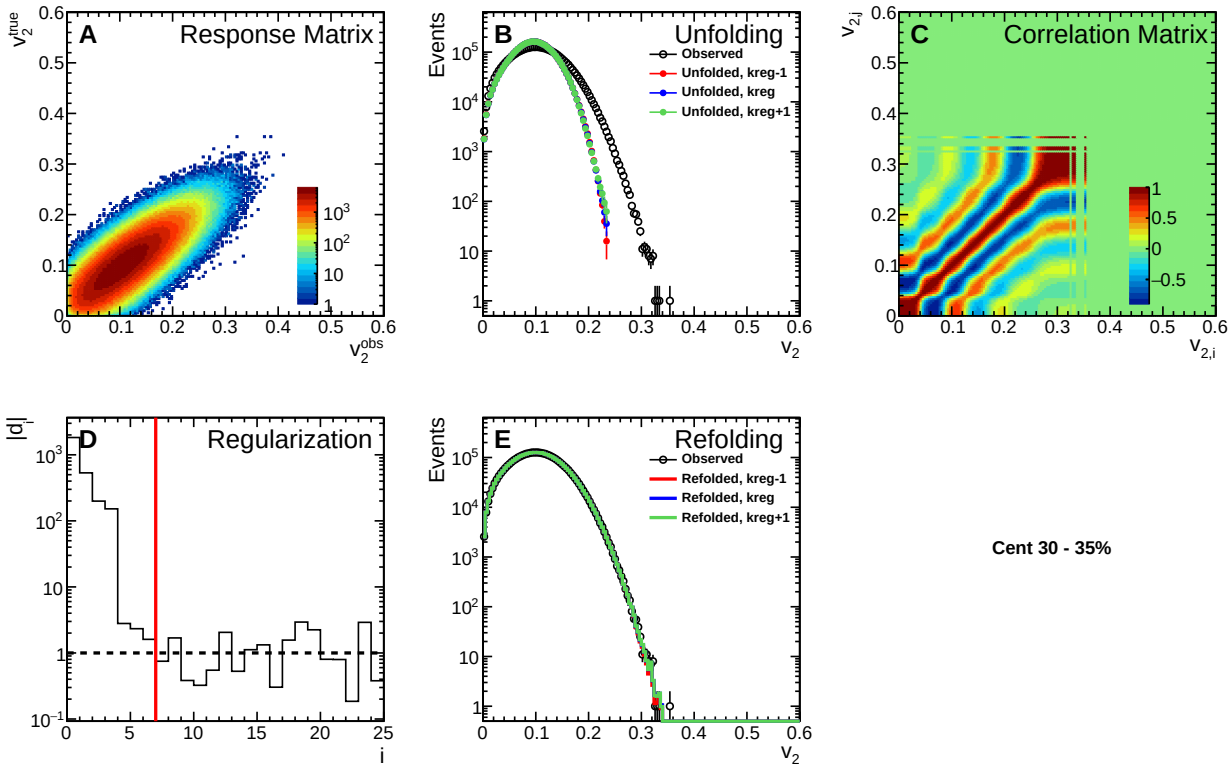

Figure C.19: $p(v_2)$ SVD unfolding performance plots for events in the 30–35% centrality bin.

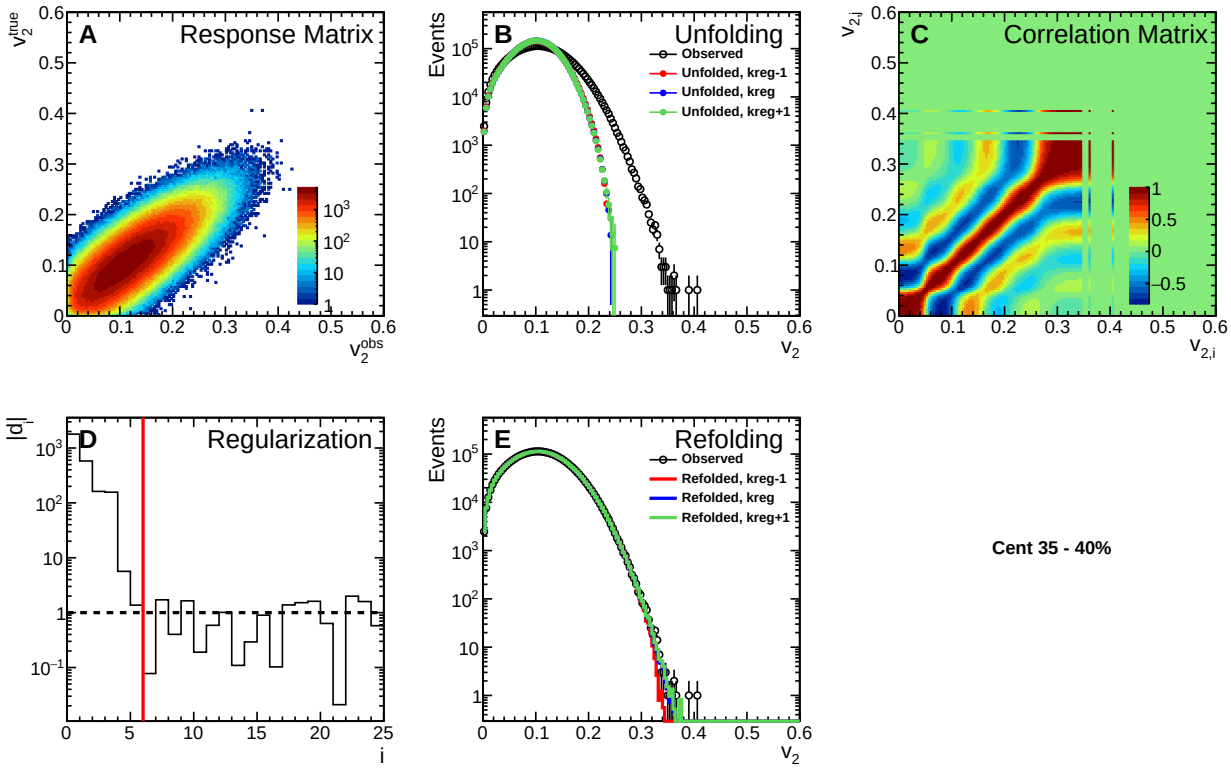

Figure C.20: $p(v_2)$ SVD unfolding performance plots for events in the 35–40% centrality bin.

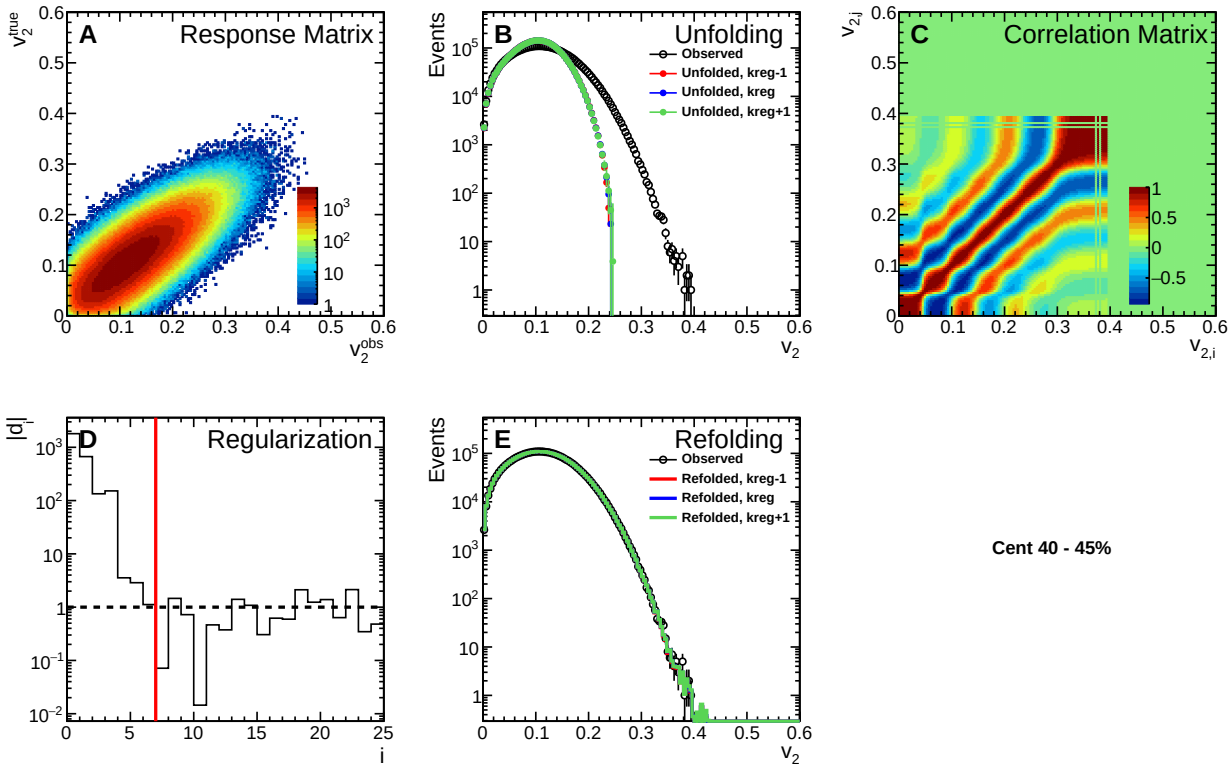

Figure C.21: $p(v_2)$ SVD unfolding performance plots for events in the 40–45% centrality bin.

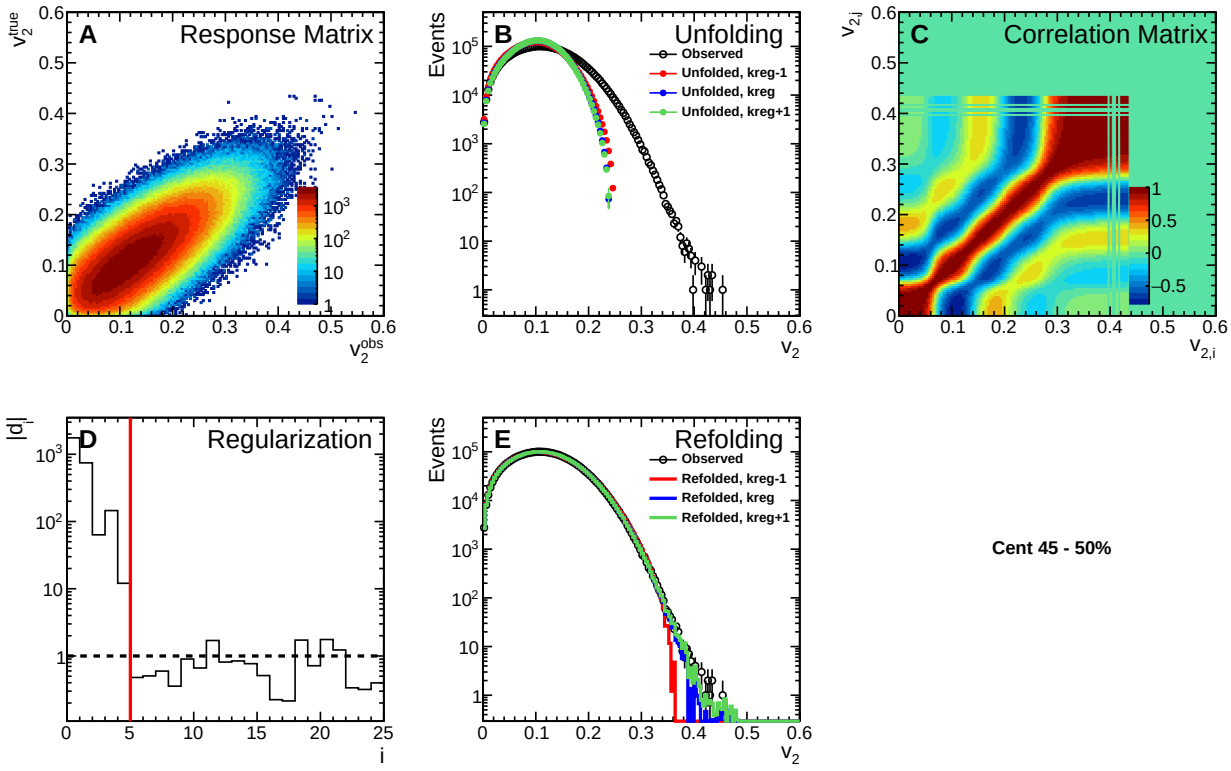

Figure C.22: $p(v_2)$ SVD unfolding performance plots for events in the 45–50% centrality bin.

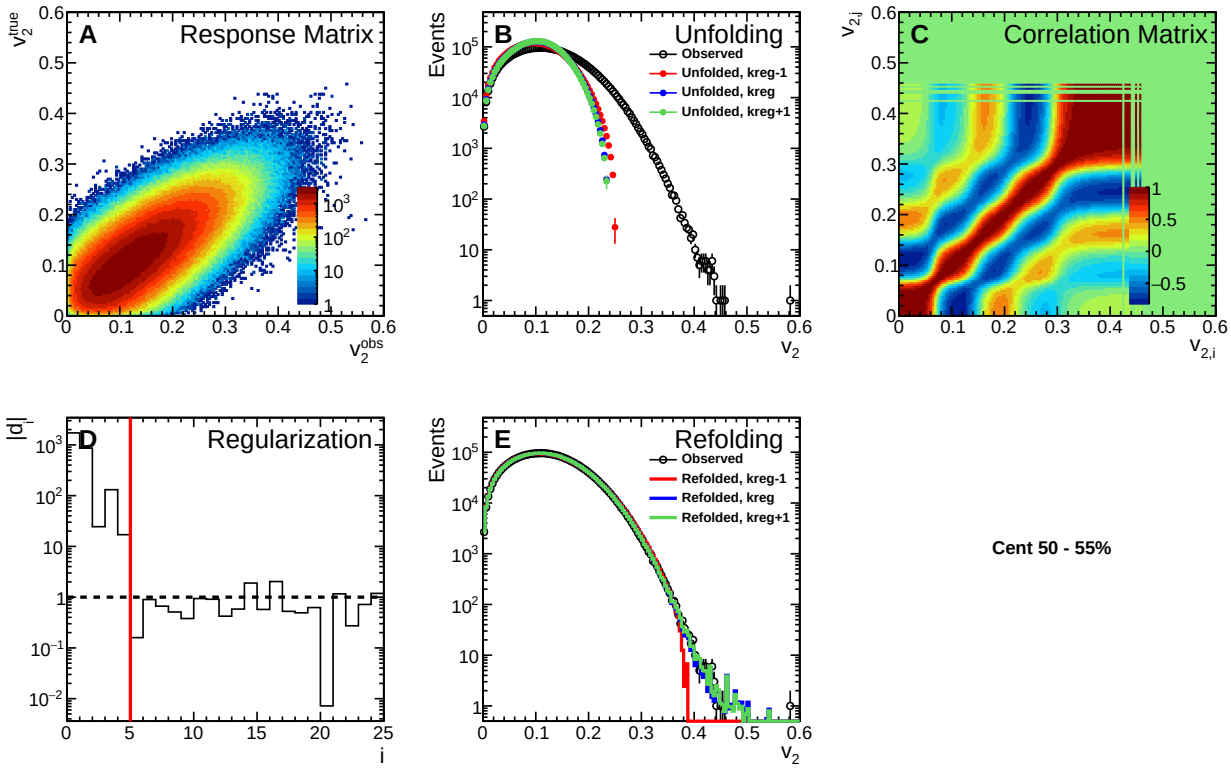

Figure C.23: $p(v_2)$ SVD unfolding performance plots for events in the 50–55% centrality bin.

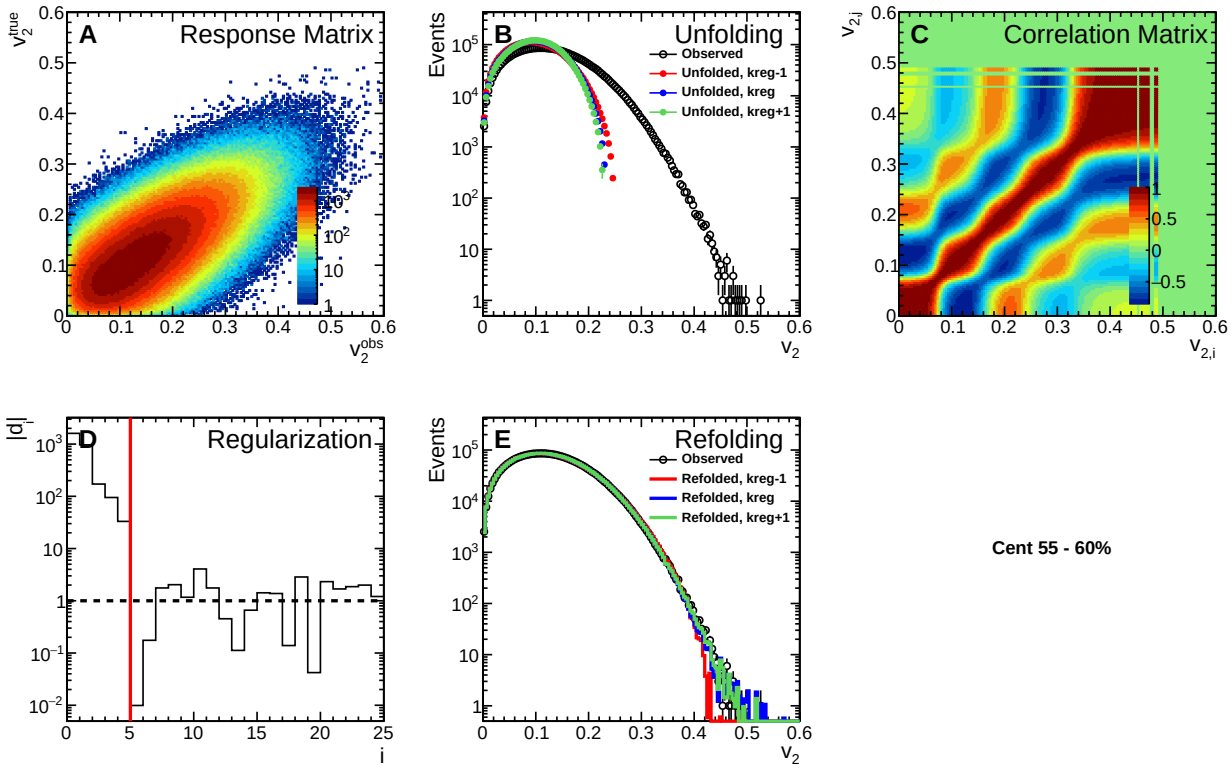

Figure C.24: $p(v_2)$ SVD unfolding performance plots for events in the 55–60% centrality bin.